ISSN 1811-1165 (Print)
ISSN 2413-2179 (Online)

EURASIAN PHYSICAL TECHNICAL JOURNAL

VOLUME 23, NO. 2(56), 2026

phtj.buketov.edu.kz

EURASIAN PHYSICAL TECHNICAL JOURNAL

p - ISSN 1811-1165
e - ISSN 2413-2179

Volume 23, No. 2(56), 2026

Journal Founder:

NON-PROFIT LIMITED COMPANY «KARAGANDA NATIONAL RESEARCH UNIVERSITY NAMED AFTER ACADEMICIAN YE.A. BUKETOV»

https://phtj.buketov.edu.kz

https://www.scopus.com/sourceid/21100920795

www.facebook.com/groups/1103109540750967

Registration Certificate No.4382-Zh, November 7, 2003.

Re-registration Certificate No.KZ32VPY00135738, November 28, 2025 issued by the Information Committee of the Ministry of Culture and Information of the Republic of Kazakhstan

Contact information:

Editorial board of EAPhTJ
(Build. 2, room 216)
Karaganda Buketov University
Universitetskaya St. 28, Karaganda,
Kazakhstan, 100024
Subscription index: 75240

Tel: +7(7212) 77-04-03
Fax: +7(7212) 35-63-98
E-mail: ephtj@mail.ru,
ephtj2021@gmail.com

Signed to print 16.06.2026
Format 60x84 1/8. Offset paper.
Volume 20.5 p.sh. Circulation 300 copies.
Order No. 80.

Printed in the Publishing House of Karaganda National Research University named after academician Ye.A. Buketov

Tel. +7 (7212) 35-63-16.
E-mail: printed@karnu-buketov.edu.kz

Eurasian Physical Technical Journal, 2026, Vol. 23, No. 2(56)

CONTENTS

.

Dear authors and readers!
Dear colleagues!

In the preface, we traditionally inform authors and readers about the latest important achievements of our journal. The Eurasian Journal of Physics and Engineering has been successfully accepted into the Directory of Open Access Journals (DOAJ), one of the leading international databases of high-quality open access journals. The journal's inclusion in the DOAJ confirms its compliance with international standards of scientific publication, transparency of editorial processes, and the principles of open access to scientific research. This achievement represents an important step toward increasing the journal's international visibility, expanding its readership and author base, and strengthening its position in the global scientific community.

Furthermore, as you are aware, based on the 2025 results, the journal ranks in the Q3 quartile across all scientific fields, reaching a peak percentile of 29% in Energy (previously 25%). Percentiles improved slightly in other fields: Physics and Astronomy – 28% (previously25%); Materials Science 20% (previously 18%) and Engineering – 26% (the same).

The Cite Score Tracker, which is directly related to the number of citations an article receives, has demonstrated a stable value of 1.4 in recent months.

According to statistics, to articles published in 2023-2024 170 citations were made in 2025. In total, 64 articles from 109 articles published in 2023-2024 were cited, accounting for 58.7%, with self-citations accounting for 11.8%. But the remaining 45 articles were not cited at all.

We hope each author can contribute to improving the dynamics of this important citation indicator. All journal indicators in the Scopus database, including the h-index of authors, are determined by the number of citations! Cite and be cited in articles published in Eurasian Physical Technical Journal!

Allow me to present to you a brief announcement of the articles in this issue articles.

The Materials Science section of this issue presents new, original research results on the properties of materials exposed to aggressive influences. Accelerated tests to determine the tribological characteristics of castings revealed that the use of Ni, Ti, and Mo as alloying additives provides casting hardness of up to 340–400 HB. In a study by Ukrainian scientists, a unified analytical model was developed to describe the deformation resistance of metals during thermoplastic processing and to evaluate the behavior of the surface layer under complex thermomechanical loading. Researchers at our university presented the results of a study on the microhardness and corrosion resistance of a number of protective coatings applied to the surface of D16 alloy products. It was demonstrated that a double protective coating consisting of a chromium nitrite layer applied over a chromium layer exhibits satisfactory hardness (HV = 236) and corrosion resistance.

The "Energy" section presents the results of research aimed at solving current energy problems using alternative energy sources. On the base of modern software, researchers from Almaty conducted a numerical study of the influence of blade geometry on the aerodynamic characteristics of a three-bladed Darrieus vertical-axis wind turbine. Joint research by authors from Astana and Uzbekistan is focused on finding methods for efficient processing of organic matter and biogas production. Specifically, the influence of mixing intensity and mode on gas exchange, heat transfer, and substrate decomposition during anaerobic digestion were studied. Researchers from Al-Farabi National University have modeled bifacial photovoltaic cells based on a single-diode model. Test results, including both typical operating conditions and a configuration with enhanced rear-side reflectivity, demonstrated the high potential of bifacial modules for increasing power generation and the overall energy efficiency of photovoltaic systems.

The "Engineering" section presents the results of developing innovative research methods aimed at improving the efficiency of technical devices and technologies. The article by Petropavlovsk authors is devoted to studying the durability criteria for a rod-type deep-well pump and determining the relationship between valve efficiency and the structural and material characteristics of the ball-and-seat assembly. The feasibility of using modern structural materials and new designs with elastic-damping valve properties while simultaneously improving valve tightness is substantiated. Authors from Astana examines the dynamic characteristics and improvements to control methods for pulsed impact mechanisms used in high-performance hydraulic systems.

A logical structure for generating the input signal X(t) is developed, ensuring more precise synchronization of dynamic processes. A paper by a representative of the Institute of Engineering Thermophysics, National Academy of Sciences of Ukraine, Kyiv, Ukraine, demonstrates that reliable diagnostics of such a laminar-turbulent transition is only possible using a combination of developed methods. The data obtained allow prediction of the location of the wake-induced transition and the intensification of heat transfer in the preceding pseudolaminar boundary layer. The article by authors from Tashkent proposes an approach to intelligent diagnostics of fiber-optic information transmission system elements based on the parameters of digital monitoring of optical modules. A structural diagram of a hardware-software device is proposed, providing continuous data collection, their adaptive processing, and the formation of real-time prognostic estimates.

The first two articles in the "Physics and Astronomy" section are devoted to studying the patterns of complex interactions at the microscopic level. One article defines the boundary between diffusion and convective regimes and identifies the parameters controlling the convective regime. The novelty lies in reconstructing the spatiotemporal evolution of isoconcentration fields for binary mixtures at different pressures and correlating the structures of convective flows with the observed regime transitions. The second article presents the results of an experimental study of the absorption properties of water cryocrystals for carbon monoxide, carbon dioxide and methane molecules under high vacuum and ultra-low temperature conditions (13–200 K). The results confirm the potential of water cryostructures for promising applications in decarbonization, environmental monitoring, and gas storage technologies.

This section contains articles devoted to the study of astrophysical phenomena of the macro-world and space. The study of young stellar objects as indicators of the formation of stars and planetary systems is a priority area of modern astrophysics. Authors studied of the N22 dust bubble region using data from the Wide-Field Infrared Survey Explorer space telescope in the near- and mid-infrared ranges: W1 (3.4 μm), W2 (4.6 μm), W3 (12 μm), and W4 (22 μm). Next article devoted study the distribution of dark matter in the halos of the spiral galaxies ESO3050090, ESO4880049, and ESO0140040 using their observed rotation curves. A statistical comparison between the King and Plummer profiles was performed using the Bayesian Information Criterion. The results of this work clarify how effectively the halo models under consideration reproduce the observed kinematics and highlight the ability to distinguish alternative dark matter density profiles. Another paper considers a new generalized Higgs inflation scenario, in which inflation occurs near a symmetric point of the "Mexican hat" potential, unlike standard Higgs inflation. The advantage of such models in the broad landscape of inflationary theories is their simplicity: no special scalar fields are assumed to exist solely to explain inflation, since both the Higgs and Peccei-Quinn fields are motivated by considerations of particle physics. Last work presents an analysis of variable stars based on archival photometric data obtained with a Schmidt camera at the Fesenkov Astrophysical Institute during the period from 1960 to 1989. The detected objects are cross-matched with existing catalogs of variable stars and modern astrometric and photometric databases, allowing the compilation of an extended set of stellar parameters for studies of stellar variability and long-term photometric evolution.

We sincerely thank our editorial board members, reviewers, authors, and all contributors whose efforts have supported the development of Eurasian Physical Technical Journal.

We hope the presented articles will not only be interesting but also useful in preparing new publications for researchers, teachers, graduate students, and postgraduates.

Please remember to cite the articles published in our journal.

And we look forward to seeing you among our readers and authors in the future.

With respect and hope for fruitful collaboration,
Editor-in-Chief, Professor Sakipova S.E.
June, 2026

EURASIAN PHYSICAL TECHNICAL JOURNAL

2026, Volume 23, No. 2 (56)

https://doi.org/10.31489/2026N2/6-12

Received: 07/02/2026 Revised: 21/04/2026 Accepted: 26/06/2026 Published online: 30/06/2026

Original Research Article

UDC 539.043

WEAR RESISTANCE OF CAST IRON PARTS PRODUCED BY LOST FOAM CASTING

Yeszhanov G.S., Kuzembyev S.B.*, Abdrakhmanova S.T., Zhanshuakova R.M.

Sh. Ualikhanov Kokshetau University, Kokshetau, Kazakhstan

*Corresponding author: ksb_mlp@mail.ru

Abstract. *The article addresses the pressing issue of improving the wear resistance of cast iron parts manufactured by lost foam casting. Using a friction wedge as an example, the current state of wear-resistant components for railway rolling stock is analyzed. A methodology for accelerated testing to determine the tribological characteristics of castings is presented, based on specimen wear under conditions of external surface contact. The results of wear resistance tests conducted on samples of friction wedges are reported, enabling an assessment of component service life. Measures implemented to improve the lost foam casting process technology are also described. It is effective for casting parts weighing 10 to 20 kg, ensuring uniformity of chemical composition and the necessary stability of cast iron properties. The use of Ni, Ti, and Mo as alloying additives ensures casting hardness of up to 340 to 400 HB.*

Keywords: castings; wear resistance, lost foam casting, testing; friction wedge; tribological properties; casting.

1. Introduction

Kazakhstan, ranking ninth in the world by territory, is the largest country globally without direct access to the ocean. Therefore, overland transportation is vitally important for the country. Its significance is further increased by the extremely uneven distribution of settlements and population. Despite the fact that the total length of highways (about 96,000 km) significantly exceeds that of railways (over 16,000 km), rail transport has been and remains the primary mode of freight transportation, accounting for slightly less than three quarters of the total freight turnover. Consequently, the problem of improving the operational reliability of railway rolling stock and, accordingly, reducing downtime due to repairs remains highly relevant.

Particular attention should be paid to the running bogies of freight cars. The weak point in this system is the friction vibration damper assembly (Fig. 1). It consists of two friction wedges (1) installed between the inclined surfaces of the ends of the bolster (5) and the friction plates (2) mounted on the columns (4) of the bogie side frame. The wedges rest on springs (3). Changes in the condition of the damper components during operation—especially wear—affect the duration of maintenance intervals of freight car bogies.

The influence of stable wedge operation on service life is associated with the friction force it generates to damp vertical and horizontal vibrations of the railcar body. As a result of wear of the working surfaces of the friction wedge, the friction force gradually decreases over time, which leads to an increase in the dynamic forces acting on the railcar and the track [1, 2, 3].

Wear of the wedge or its improper installation in the vibration damper assembly leads to cracking, fracture, excessive raising or lowering of the wedge relative to the supporting surface of the bolster, and results in loss of elasticity and wear of the mating components. As a result, the damping of railcar vibrations is impaired. This, in turn, causes increased loads and accelerated wear of other components (wheelset flanges, axle boxes, etc.), ultimately leading to the necessity of removing the railcar from service for repair. The most common defects of the vibration damper assembly are excessive wear of the wedge working surfaces and wear of the mating surfaces (springs, etc.).

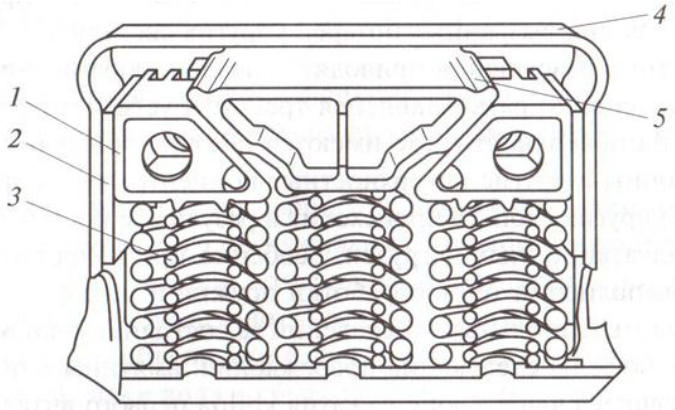

Fig.1. The main element determining the operability of the assembly is the friction wedge (Fig. 2 *a*) [1].

A review of the literature revealed a unique case of excessive wear (Fig. 2 *b*) [4]. According to GOST 34503-2018, friction wedges may be manufactured from cast iron (grey and ductile) as well as from various grades of cast steel. The standard specifies durability requirements for wedges, characterized by the duration of a defined stage of operation. The wedge must "ensure a service life not less than the designated operating life of the freight car bogie from the start of operation to its first scheduled overhaul or between scheduled overhauls" [5]. Based on service life and a scheduled maintenance interval of 250,000 km, friction wedges are divided into two classes. A wedge capable of ensuring a mileage not exceeding this limit is assigned to Class 2. A wedge capable of ensuring a greater mileage (but not exceeding 1 million km) is assigned to Class 1 [5].

a) b)

Fig.2. Friction wedge (*a*) and a case of its excessive wear (*b*).

The operation of the friction pair "wedge–plate" occurs under dry friction conditions [6] and is characterized by intense abrasive wear. Despite this, the wedge must ensure at least one scheduled maintenance interval of the freight car bogie before replacement [7]. According to [8], depending on their chemical composition, friction wedges provide service life in the range from 120,000 km to 500,000 km. Other studies indicate that wedges made of grey cast iron grade SCh25 exhibit wear that prevents further operation already at a mileage of about 100,000 km [1, 9]. It should be noted that GOST 34503-2018 recommends the use of cast iron grades SCh30 and SCh35. The use of other materials is permitted only if the requirements of the standard are met. Apparently, in the cited case involving SCh25 cast iron, this requirement was not satisfied.

The stages of operation of freight cars and their running bogies are determined by maintenance mileage intervals. The standards for performing the first depot repair of freight cars of any type are established in the *Regulations on the System of Maintenance and Repair…* [7], approved by the Commonwealth of Independent States countries. With a few exceptions, this standard is 210,000 km. Already at the first repair, the friction wedge is usually replaced. From the standpoint of the theory of reliability of technical systems, this is consistent with the durability of the friction wedge as an element of a friction assembly. In other words, its wear resistance can serve as a criterion for determining the service mileage [8]. Indeed, a linear relationship between the service life of the friction wedge and the mileage parameters of freight cars has been established [10]. At present, a number of cast irons have been developed for friction wedges that are complex-alloyed with combinations of various elements, ranging from traditional chromium to rare-earth metals [11-13]. These materials ensure a service mileage of 250,000 km or more, and some of them have already been implemented in production.

Friction wedges are usually manufactured by casting in disposable sand molds. Such molds are very inexpensive but do not provide high geometric accuracy. The wedge is a critical component of the assembly; however, wedge castings are not subjected to machining, except for the removal of feeder remnants. Therefore, the wedges must be cast within the specified dimensional tolerances, which is not always achievable when using disposable sand–clay molds. To improve geometric accuracy, the use of alternative, more advanced technologies is desirable.

The aim of this work is to develop a material and a technology for the serial production of a friction wedge capable of providing a service mileage of more than 500,000 km.

2. Materials and Research Methods

Grey cast iron grade SCh35 was selected as the base material. It is more technologically efficient in production than ductile iron, the melting technology of which is labor-intensive and requires the use of expensive modifiers. Compared with steels, grey cast iron exhibits higher frictional properties. In addition, cast iron castings do not require strengthening heat treatment. However, experimental data obtained in our studies conducted in 2019–2020 revealed, first, a wide scatter in the hardness of wedges in service (grey cast iron), ranging from 100 to 240 HB (according to GOST, the hardness of SCh35 cast iron is HB = 210–275), as well as a scatter in other mechanical properties of the castings and a coefficient of variation of service life equal to 0.67. This indicates instability either in the chemical composition or in the material structure, both of which equally determine mechanical and operational properties. Consequently, despite the above, either the composition and structure of grey cast iron require further optimization, or they are unstable due to imperfections in the production technology. Therefore, it is necessary to study not only the influence of a wide range of alloying elements, additives, and modifiers, but also the technology of their application. As an example, treatment of the same alloy with the same modifier in a furnace, in a ladle, and in a mold yields different results. Second, the main reason for failure of the friction assembly is wear of the contact surfaces between the wedge and the friction plate. This confirms the well-known dependence of the service life of a friction wedge on wear. Wear is a complex physic mechanical process accompanied by chemical and thermal phenomena. It is determined by the type of wear and loading, the material, geometry and surface condition, as well as other factors [14].

In our case, we are dealing with dry friction of flat surfaces under sliding conditions with an intensive cyclic load. The material of the cast part is unstrengthened grey cast iron without mechanical machining, and there is also a possibility of oxidation. Wear debris is not removed. The roughness of the contacting untreated surfaces with relative movement/sliding due to the applied external force should also be taken into account [15]. The choice of the wear testing methodology was based on the advantages of evaluating wear in terms of reduced duration and cost of these studies, which makes it possible to avoid shutdown and disassembly of units under actual operating conditions of the rolling stock fleet.

The use of statistical data on the reliability of cast iron components of railcar bogies proved impossible due to the limited amount of reliable information. The fact is that castings of these products already represent finished parts. This means that the possibility of influencing their surface layers by mechanical and thermal treatments—to create compressive stresses, the required surface roughness and hardness, as well as to remove defective structures—is excluded. When using new materials for vibration damping unit parts, full-scale bench tests are recommended to evaluate their frictional properties [16]. When preparing such products for serial production, a large body of statistical data is required, whereas in practice only a pilot batch of castings is

usually available. Moreover, to register the wear rate of the surfaces of castings weighing more than 10 kg (the wedge mass is 10.5 kg), an operating time of at least 500–1000 hours and significant labor input are required.

Thus, the problem arises of developing an accelerated method for studying the wear of the working surfaces of a friction wedge under foundry shop conditions. At the same time, experiments must be carried out under conditions that most strongly affect the wear of the working surfaces. Solving this problem is inextricably linked to conducting a large number of experiments to reveal the mechanism of surface property formation in castings, as well as to obtain and systematize data on the wear resistance of the objects under study.

A solution was found in the use of cast pilot specimens as test sections of the wedge. To achieve the closest possible correspondence to real operating conditions, a fixture was developed that allows adjustment of the duration and the force of interaction between the friction surfaces. In addition, based on the considerations outlined above, a guidance document entitled *"Methodology for Evaluating the Wear Resistance of Castings Made of Cast Iron Alloys"* was developed, which establishes a method for assessing surface wear parameters of castings. It is based on testing specimens by wear on a test rig according to the "roller–block" scheme. The roller material was U8A steel with a hardness of 280–300 HB.

The cast iron was melted in an induction furnace of the PPU-0.16 type. The technology for producing grey cast iron castings by the lost foam casting (LFC) method was developed. Compared with conventional sand–clay mold casting, LFC makes it possible to obtain higher-quality castings with improved dimensional and geometric accuracy. In order to reduce material consumption, surface alloying of the castings in the mold was applied.

Specimens for tribological testing were cast iron blocks in the form of square bars 50 mm in length and 15 mm in width. This geometry was chosen based on the need to conduct a large number of multivariate tests in order to ensure the required confidence level.

The choice of the testing method and a custom-made laboratory setup meets the above-mentioned environmental and friction conditions. Reproduction of operating regimes using this methodology was ensured by the requirements of tribological testing for parts having a complex elemental composition due to the combination of base and alloying or modifying elements: C, O, Mn, Mg, Si, Ca, Fe, Ni, Cu, Mo, V, Co, Cr, Ti, and B. The investigations included determination of hardness, as well as qualitative and quantitative analysis of the surface chemical composition before and after testing.

3. Results and Discussion

Friction pair tests were carried out at a constant sliding speed of 0.5 m/s under moderate heating conditions. The test duration for one contact pair was 0.2 h. Each experimental series included at least three tests. The surface wear per unit sliding distance was adopted as the evaluation criterion. Visual examination of the specimen surfaces revealed no signs of plastic deformation; the surfaces remained smooth, without adhesion or material buildup. Dark inclusions were observed on the block surfaces, indicating phase heterogeneity; no brittle structural constituents were detected. As follows from Table 1, the chemical composition of the contact surfaces of the specimens after testing does not differ from the initial composition.

Table 1. Chemical composition of the surface of sample SCH35 before (1) and after (2) testing.

Sample	Content of elements, in fractions							
	C	Si	Mn	Cr	Cu	Ni	P	S
No. 1	2,83	1,56	0,97	0,22	0,37	0,13	0,12	0,09
No. 2	2,83	1,56	0,97	0,22	0,37	0,13	0,12	0,09

This indicates that no oxidation of the component surfaces occurs during operation. Table 2 shows the results of wear resistance tests. The influence of the alloying element on the hardness of the specimens is clearly observed. At the same time, the hardness of all specimens falls within the range acceptable for friction wedges, namely 230–444 HB. Once again, the dependence of wear resistance on hardness is confirmed.

Table 2. Results of tribological wear tests.

Technological scheme	Sample material	Hardness, HB	Wear resistance, μm/hour
Basic option	SCH35	285	9,5
Technology No. 1	Mo = 0,6 %	340	7,1
Technology No. 2	Ni = 0,4 %	360	6,6
Technology No. 3	Ti = 0,3 %	420	4,6

The positive results of the study demonstrate the prospects for their application in the production of castings for railway transport. This approach makes it possible to predict the service life of friction wedges (Fig. 3). For example, at a wear rate of 2.5 to 5 μm/h, the service life of this component may reach 300,000–400,000 km, which is achievable through the implementation of certain casting technologies using appropriate alloying additions. In this regard, it is recommended that the working surfaces of both the friction wedge and the friction plate of a freight car bogie have the same hardness.

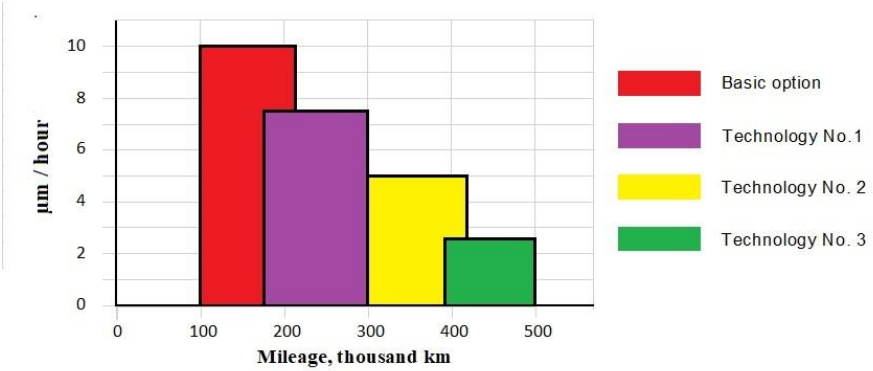

Fig.3. Wear rate of samples (friction wedge) under steady-state friction conditions.

The choice of gray cast iron as the base material was determined by the results of developing the LFC technology. Options for casting the wedge from ductile (nodular) and gray cast iron were considered. Pilot batches of castings were produced under industrial conditions. Patterns were made from granulated expanded polystyrene by foaming in heated molds. The finished casting patterns and elements of the gating system were bonded into a single cluster and coated with an anti-stick (refractory) paint (Fig. 4).

Fig.4. Block of friction wedge models.

After the coating had dried, the patterns were placed in flasks and molded with dry fine-grained sand. The molds were evacuated and then poured on a foundry conveyor with the vacuum pump operating continuously. Subsequent operations were carried out in the same manner as in conventional sand casting. The casting technologies for gray and ductile iron differed only in that the latter was produced by treating the liquid superheated iron with a powdered modifier in the ladle prior to pouring the molds.

Castings made of ductile iron were characterized by increased hardness and required heat treatment—quenching followed by tempering—to improve the microstructure. In addition, a surface defect, a shrinkage cavity, was observed on some of the castings (Fig. 5 *a*, *b*). The initial solution was a conventional one—the installation of a riser (Fig. 5 *c*). However, this led to increased material consumption and additional labor associated with riser removal and surface cleaning of its remnants. An alternative measure was then applied: the use of chills. Installing them directly on the casting proved to be impractical due to the appearance of chill imprints on the casting surface and the risk of metal adhesion. The final solution was to place the chills on the pattern (Fig. 5 *d*). After this modification, the defect was no longer observed. Nevertheless, the labor intensity of manufacturing the product still increased. In addition, during LGM, the nature of the formation of sound signals is preserved, which affects fatigue from receiving castings [17].

a *b* *c* *d*

Fig.5. Sink (*a, b*) on the wedge casting, riser (*c*) and refrigerators (*d*).

Pilot batches of gray cast iron castings demonstrated an almost complete absence of defects and satisfactory service properties (hardness and tensile strength) without additional labor input. Therefore, gray cast iron was selected for subsequent studies of wear resistance.

4. Conclusion

The research results demonstrated the effectiveness of the LFC for producing castings with a mass of 10–20 kg, ensuring uniformity of chemical composition and the required stability of cast iron properties.

The use of Ni, Ti, and Mo as alloying additions provides casting hardness in the range of 340–400 HB.

Changes in the physic mechanical condition of the casting surface after alloying resulted in a 1.4–1.5-fold increase in wear resistance compared with the baseline variant (serial parts), which corresponds to an increase in the service mileage of friction wedges up to rejection by 70–85 thousand km.

Conflict of interest statement. The authors declare that the re-search was conducted in the absence of any commercial or financial relationships that could be construed as a potential conflict of interest.

CRediT author statement.
Yeszhanov G.S.: Conceptualization, Investigation; Writing – original draft preparation; **Kuzembayev S.B.**: Methodology; Writing – review and editing, Supervision, **Abdrakhmanova S.T.:** Resources, Validation; **Zhanshuakova R.M.**: Data curation, Visualization. The final manuscript was read and approved by all authors

Statement on the use of Artificial Intelligence.
The authors declare that no artificial intelligence tools were used to generate scientific content, results, or conclusions of this article.

Data Availability Statement
The data that has been used is confidential.

References

1. Turakulov, M. R., Tursunov, N. K., Yunusov, S. Z. (2024). Friction wedge of vibration dampers for freight car bogies made of synthetic cast iron. *Universum: Technical Sciences*, *2*, 119. https://doi.org/10.32743/UniTech.2024.119.2.16806 [in Russian]
2. Corrêa, P. H. A., Ramos, P. G., Fernandes, R., Kurka, P. R. G., dos Santos, A. A. (2023). Effect of primary suspension and friction wedge maintenance parameters on safety and wear of heavy-haul rail vehicles. *Wear, (524–525), 204748.* https://doi.org/10.1016/j.wear.2023.204748
3. Ashtiani, I. H., Rakheja, S., Ahmed, AKW. (2016). Influence of friction wedge characteristics on lateral response and hunting of freight wagons with three-piece bogies. *Proceedings of the Institution of Mechanical Engineers, Part F: J. Rail and Rapid Transit, 231(8),* 877–891. https://doi.org/10.1177/0954409716647095
4. Severe wear of vibration damper wedges. Freight car bogie. (2025, November 15). *YouTube*. https://www.youtube.com/watch?v=nrF4Nw_W48E [in Russian]
5. Federal Agency on Technical Regulation and Metrology. (2019). *GOST 34503–2018: Friction wedges of freight car bogies. General technical specifications*. Moscow. https://meganorm.ru/1/4293732/4293732606.pdf [in Russian]
6. Wu, Q., Cole, C., Spiryagin, M. (2021). Characterising stochastic friction in railway draft gear. *Vehicle System Dynamics, 60 (6),* 1-13. https://doi.org/10.1080/00423114.2021.1889003.
7. Regulations on the system of maintenance and repair of freight cars admitted for operation on public railway lines in international traffic. (2020). *Electronic fund of legal and regulatory technical documentation*. http://docs.cntd.ru/document/902326053 [in Russian]
8. Gabets, A. V., Markov, A. M., & Gabets, D. A. (2016). Improving the reliability of critical components of railway rolling stock. *Polzunovsky Almanac*, *4*, 111–116. https://e.lanbook.com/journal/issue/302213 [in Russian]
9. Artamonov, E. I. (2008). Study of wear characteristics and review of friction wedges designs for selecting their rational configuration. *Science and progress of transport. Bulletin of the Dnipropetrovsk National University of Railway Transport, 23*, 6-10. https://cyberleninka.ru/article/n/issledovanie-osobennostey-iznosa-i-obzor-konstruktsiy [in Russian]
10. Kovrigina, I. V., Bolshakov, R. S., & Yakovleva, Y. S. (2023). Determination of freight car mileage depending on the degree of friction wedge wear. *Young Science of Siberia*, *electronic scientific journal*, *1(19)*, 1-6. https://ojs.irgups.ru/index.php/mns/article/view/1093 [in Russian]
11. Gabets, A. V. (2014). Special modified cast iron grade ChMN-35M for friction wedges of freight car bogies. *Bulletin of the Research Institute of Railway Transport, 6,* 46-49. https://elibrary.ru/download/elibrary_23234226_47136208.pdf [in Russian]
12. Butorin, S. M., Efimov, V. P. (2017). Friction wedges of freight bogies with increased service life between repairs. *Bulletin of the St. Petersburg State University of Railway Engineering, 4*, 605-614. https://cyberleninka.ru/article/n/ friktsionnye-klinya-gruzovyh-telezhek-s-povyshennym-mezhremont [in Russian]
13. Turakulov, M. R., Tursunov, N. K., Yunusov, S. Z. (2024). Friction wedge of the vibration damper of freight car bogies made of synthetic cast iron. *Universum: technical sciences*, *(119) 2*, 31-35. https://doi.org/10.32743/UniTech.2024.119.2.16806 [in Russian]
14. Wakelin, R. J. (1974). Tribology: The friction, lubrication, and wear of moving parts. *Annual Review of Materials Research, 4*, 221-253. https://doi.org/10.1146/annurev.ms.04.080174.001253
15. Khairaliyev, S., Kaishubayeva, N., Kapayeva, S., Bergander, M. J., Dzhundibayev, V. (2023). Coefficient of friction at rest of rough surfaces. *Eurasian phys. tech. j., 20(2(44)), 12-19.* https://doi.org/10.31489/2023No2/12-19
16. Sukhov, A. V., Borshch, B. V., Gabets, A. V. (2015). Evaluation of frictional properties in friction pairs of a wedge damper of a freight car bogie. *Bulletin of the Research Institute of Railway Transport, 2,* 32-37. https://doi.org/10.21780/2223-9731-2015-0-2-32-37 [in Russian]
17. Chakherlou, T. N., Mahdinia ,Y. V., Akbari, A. (2011). Influence of lustrous carbon defects on the fatigue life of ductile iron castings using lost foam process. *Materials & Design, 32(1),* 162-169. https://www.sciencedirect.com/science/article/abs/pii/S0261306910003900

AUTHORS' INFORMATION

Yeszhanov, Galikhan S. – Candidate of Technical Sciences, Associate Professor, Sh.Ualikhanov Kokshetau University, Kokshetau, Kazakhstan, https://orcid.org/0009-0006-0617-1662; algabas1998@mail.ru

Kuzembayev, Serik B. – Doctor of Technical Sciences, Professor, Sh.Ualikhanov Kokshetau University, Kokshetau, Kazakhstan; Scopus ID: 6507600024, https://orcid.org/0000-0003-2515-6696; ksb_mlp@mail.ru

Abdrakhmanova, Saule T. – Master of Eng., Senior lecturer, Sh.Ualikhanov Kokshetau University, Kokshetau, Kazakhstan; https://orcid.org/0009-0008-8793-9542; saule_abdrahmanova.janzakova@mail.ru

Zhanshuakova, Raushan M. – Master (Eng.), Senior Lecturer, Sh.Ualikhanov Kokshetau University, Kokshetau, Kazakhstan; https://orcid.org/0000-0001-9999-7020; raumadetovna@gmail.com

EURASIAN PHYSICAL TECHNICAL JOURNAL

2026, Volume 23, No. 2 (56)

https://doi.org/10.31489/2026N2/13-21

Received: 08/02/2026 Revised: 23/04/2026 Accepted: 26/06/2026 Published online: 30/06/2026

Original Research Article

UDC 531.43; 621.8

A UNIFIED ANALYTICAL MODEL FOR DEFORMATION RESISTANCE OF METAL UNDER THERMOPLASTIC PROCESSING CONDITIONS

Tsyganov V.[1*], Sheyko S.[2], Hrechanyi O.[2], Vasilchenko T.[2], Hrechana A.[2]

[1] National University Zaporizhzhia Polytechnic, Zaporizhzhia, Ukraine
[2] Zaporizhzhia National University, Zaporizhzhia, Ukraine
*Corresponding author: tsyganov705@gmail.com

Abstract. *A unified analytical framework is developed to describe the deformation resistance of metals under thermoplastic processing conditions. The proposed approach is based on the Hansel-Spittel constitutive equation and establishes a direct relationship between yield stress and the key thermomechanical parameters of deformation, including strain, strain rate, and temperature. An analytical solution of the spatial plasticity problem is obtained using harmonic functions, enabling the determination of stress intensity at any point within the deformation zone. The formulation integrates the Huber-Mises plasticity criterion with frictional and geometric factors, resulting in a closed-form expression that links the local stress strain state to process parameters. The model accounts for non-uniform and multi-stage deformation characteristic of rolling and contact loading processes. Its applicability is demonstrated for thermoplastic loading of surface layers in tribological contacts, where deformation resistance plays a decisive role in wear and fatigue damage accumulation. The developed analytical model provides an efficient tool for predicting energy-force parameters and assessing surface layer behavior under complex thermomechanical loading. The proposed framework can be directly applied in engineering calculations, process optimization, and the design of metal forming and tribological systems.*

Keywords: deformation resistance; thermoplastic processing; plasticity theory; tribological contact; surface layer damage.

1. Introduction

In thermoplastic processing of metallic materials, including rolling, forging, and contact loading in tribological systems, deformation resistance is one of the key parameters governing energy consumption, force characteristics, and the resulting service performance of components. Accurate prediction of deformation resistance is essential for the rational design and optimization of metal forming processes, as well as for assessing wear and fatigue damage in surface layers subjected to complex loading conditions [1].

Deformation conditions play a decisive role in shaping both the mechanical response of the material and the evolution of its microstructure. Variations in strain, strain rate, and temperature directly affect hardening, recovery, and dynamic recrystallization processes, which in turn determine the stress strain state within the deformation zone. As a result, reliable models describing the dependence of deformation resistance on thermomechanical parameters are required to ensure adequate prediction of energy-force parameters and material behavior under real processing conditions.

In recent years, numerical simulation methods, particularly finite element modeling, have become widely used for analyzing thermoplastic deformation processes [2, 3]. However, the accuracy of such simulations strongly depends on the quality of the constitutive description of the material. In addition to precise

characterization of physical and chemical properties, it is necessary to establish analytical relationships that adequately reflect the evolution of mechanical characteristics during deformation. In many engineering applications, the absence of closed-form solutions complicates rapid parametric analysis and limits the applicability of numerical models at early design stages.

Deformation resistance is commonly treated as a rheological characteristic of metals, representing the stress required to sustain plastic flow under specific thermomechanical conditions [4, 5]. In technological processes such as continuous rolling, this parameter determines the stress level in the deformation zone and significantly influences the mechanical properties of the final product. Therefore, the development of physically substantiated and mathematically tractable models for deformation resistance remains an important engineering task.

Existing experimental and semi-empirical approaches provide valuable insights into the dependence of yield stress on deformation parameters; however, the reported results are often inconsistent, particularly with respect to strain rate sensitivity and temperature effects [6]. Moreover, many available models are limited to monotonic deformation paths and do not fully capture the non-uniform and multi-stage nature of real industrial processes [7, 8]. Under such conditions, yield stress may increase, decrease, or remain nearly constant depending on the balance between hardening and softening mechanisms, highlighting the need for more flexible constitutive descriptions.

The rolling process represents a generalized case of thermoplastic loading, characterized by spatially non-uniform stress and strain distributions within the deformation zone. For sheet and section rolling, as well as for contact loading in tribological joints, an analytical solution of the three-dimensional plasticity problem is particularly valuable, as it allows the stress state to be evaluated at any material point rather than relying on averaged parameters.

2. Materials and methods

The most common methods of theoretical research of technological processes of processing metals by pressure, both hot and cold, are mathematical and simulation modeling.

At each moment of the technological process of rolling, especially in a continuous process, the metal is in completely different deformation and stress states at a single point of the deformation center [9, 10]. This leads to inhomogeneity of the physical and mechanical properties of the metal, ambiguity in determining the power parameters of the process, energy consumption.

Theirs is known complex nature of the metal flow curve, presented in Fig. 1 [11].

The dependence is characterized by the growth of σ_s from the yield strength σ_0 to a certain peak value σ_p corresponding to the peak deformation ε_p, then σ_s decreases to the steady-state stress σ_y, at which the equilibrium of the hardening and dynamic recrystallization processes occurs.

On the other hand, the flow curve of the metal also indicates the nature of the change in austenite. In the area of hardening, before the deformation value ε_p is reached, grain refinement occurs, the density of dislocations in the substructure increases, after which the process of dynamic recrystallization develops intensively, and according to, the size of the austenite grain depends exclusively on the stress σ_y.

In his scientific work A. Nadai proposed an equation for determining the resistance to deformation of a metal, taking into account temperature, relative deformation, hardening in time, stress changes, depending on the deformation rate taking into account the viscosity of the metal. The authors in work [11] considered the positive and negative sides of this equation, and established that the laws necessary for solving the equation proposed by A. Nadai are quite complex and require improvement. Thus, in practical applications, the determination of σs relies on experimental data, which are presented as discrete values corresponding to specific deformation conditions and steel grades or as approximated dependencies that represent these experimental results.

In various works, experimental studies were carried out that determined the dependence of the yield strength σ_T, yield stress σ_p on the thermomechanical parameters of the process of plastic impact (degree, speed and temperature of deformation). Based on the results of these experimental studies, the authors Cook P.M., Nikolaev V.O. and others [12] proposed their own options for determining the dependence of the flow stress of a metal on the deformation rate. The data presented in the technical literature regarding the dependence of deformation resistance on strain rate for steels are often inconsistent, making it difficult to draw definitive conclusions about the influence of various factors. An inaccurate mathematical representation of yield stress during the design of technological processes can lead to significant errors in calculating the forces and moments involved in plastic deformation.

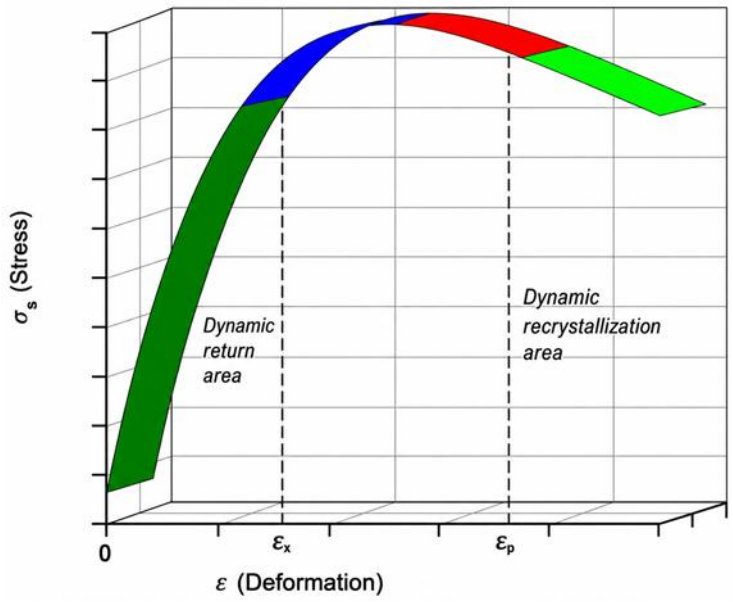

Fig.1. The general view of the flow curve of steel in the presence of dynamic recrystallization

A key distinction between yield strength and yield stress lies in their definition: yield strength characterizes the stress level at which plastic deformation begins under initial loading, whereas yield stress is determined throughout the loading process. The yield stress serves as an indicator of the material's rheological behavior. As a result, existing models and dependencies do not fully capture the rheological properties of the material. Depending on deformation conditions, yield stress may not only increase with greater strain but also decrease or remain constant.

In this context, the present study aims to develop a unified analytical model describing metal deformation resistance under thermoplastic processing conditions. The proposed approach is based on the Hansel-Spittel constitutive equation and is combined with an analytical solution of the spatial plasticity problem using harmonic functions. By integrating the Huber-Mises plasticity criterion with frictional and geometric factors, a closed form relationship between the local stress strain state and thermomechanical processing parameters is established. The developed framework is intended for practical engineering applications, including prediction of energy-force parameters and assessment of surface layer behavior in metal forming and tribological systems.

3. Results and discussion

A preliminary review of mathematical models proposed by various researchers revealed that the Hansel-Spittel equation is the most suitable for determining yield stress under varying thermomechanical conditions. This equation effectively represents the relationship between stress and thermomechanical parameters, accommodating diverse variations in their values:

$$\sigma_p = \alpha_1 \varepsilon^{\alpha_2} \exp\left(\frac{\alpha_3}{\varepsilon}\right) \exp(\alpha_4 \varepsilon)(1+\varepsilon)^{\alpha_5 T} u^{\alpha_6} u^{\alpha_7 T} T^{\alpha_8} \exp(\alpha_9 T), \quad (1)$$

where $\alpha_1 ... \alpha_9$ – empirical coefficients, ε – relative deformation, T – temperature, u – deformation rate

In case of small deformations (ε = 0.2...0.3), the yield strength increases strongly as the deformation increases. At moderate deformation levels, the increase in yield strength becomes less pronounced, and in some cases, it may even decline with further straining. A distinctive feature of this approximation is that the derived formula allows for consideration of the rheological properties of various steel grades. The relationship between yield stress and deformation can exhibit different trends – it may increase, decrease, or remain constant. This formula enables the calculation of energy parameters and yield stress at any point within the deformation zone.

Moreover, it is necessary to take into account that the inhomogeneity of the deformed state is the main feature of metal products shaped by pressure processes. As a result, the metal of the product has different

mechanical properties and fatigue resistance in its volume. This is important because, in each model, separate elements or zones usually correspond to service characteristics. Thus, for accurate forecasting, it is essential to analyze the deformation of individual material points throughout the entire product volume rather than relying on averaged deformation characteristics. The intensity of tangential stress is used as an indicator [13]:

$$\tau_i = \frac{1}{\sqrt{6}}\sqrt{(\sigma_x - \sigma_y)^2 + (\sigma_y - \sigma_z)^2 + (\sigma_z - \sigma_x)^2 + 6(\tau_{xy}^2 + \tau_{yz}^2 + \tau_{zx}^2)} \quad (2)$$

where σ_x, σ_y, σ_z, τ_{xy}, τ_{yz},τ_{xz} – normal and tangential stresses in space

Real technological processes are characterized by a multi-stage, non-monotonic nature of strain intensity with complex loading. In the theory of small deformations, it is proven that the deformed state of any material point is completely determined by six components: three main components, intensity and type of deformation. At the same time, the total shear deformation is a quantitative characteristic of the degree of change in the shape of the particle under consideration, which is expressed as a dependence through the main components of the deformation [14]:

$$D_i = \sqrt{\frac{2}{3}}\sqrt{(\varepsilon_x - \varepsilon_y)^2 + (\varepsilon_y - \varepsilon_z)^2 + (\varepsilon_z - \varepsilon_x)^2 + \frac{3}{2}(\gamma^2 + \gamma)} \quad (3)$$

where ε_x ,ε_y,ε_z – degree of deformation in space, γ – shear strain

In general, for finite (significant) deformation, the intensity equation is preserved. For multi-operational (multi-pass) processes Smirnov-Aliaev G.A. proposed a mathematical equation according to which the total (resulting) degree of deformation for the entire technological process is defined as the arithmetic sum of the degrees of deformation of individual operations, the values of which, in the case of a monotonous course of the deformation process, are numerically equal to the intensity of the main deformations. At the same time, it was noted that the intensity is a scalar quantity and the only comparable characteristic of the change in shape, allowing to determine the work spent on it.

Approximate theoretical calculations, based on the estimation of the amplitude of the change in the potential energy of the nucleus during the movement of the dislocation, showed that the minimum tangential stress necessary for the movement of the dislocation is equal to:

$$\tau_n = \frac{2G}{k} e^{-\frac{2\pi}{k}\frac{a}{b}}, \quad (4)$$

where a – distance between adjacent sliding planes, b – size of a structure element

This formula indicates that as a increases and b decreases, the value of τ_n becomes smaller. It is established that the value of a is the maximum for densely packed atomic planes, and the smallest value of b corresponds to the most densely packed directions.

Thus, checking the condition $\tau_i > \tau_n$, it is possible to talk about the possibility of dislocation movement. Dislocations that ensure plastic displacement along the directions and planes of the densest atoms are especially mobile. Preventing sliding in these planes in any way, it is possible to cause ego in those planes where the packing of atoms is less dense.

The most clearly marked relationship between metal deformation resistance and thermoplastic processing conditions impact on the surface layer is manifested in the contact interaction in the conditions of friction of parts in tribo-joints. It is obvious that under contact conditions of loading, the near-surface layers of the material are damaged more than the deep ones.

With repeated loading, fatigue microcracks appear on the surface even in the absence of contact loads and are located in the active sliding planes, in which the maximum shear stresses act. The accumulation of defects leading to the formation of microcracks is determined by the characteristic features of the main structural elements of the material. Under the action of multiple impulse loads, the original structure of the deformable material changes significantly. The subsurface zone, extending from a few to several hundred micrometers in depth, consists of a plastically deformed material layer characterized by specific crystallite size and orientation.

The processes of friction and wear, as well as the destruction of the surface layers of the tribocoupling, are determined by the dynamic nature of the application of loads in contact, the amplitudes of mutual displacements, which create specific conditions of contact interaction. At the same time, the majority of tribocoupling work under the conditions of complex three-dimensional dynamic loading: impact and sliding in two mutually perpendicular directions with the effect of both high and low temperatures. Such a complex

of loading conditions causes a complex tense state of the surface layers of contacting pairs. This explains the limited capabilities of the general principles of friction theory, as well as the majority of experimental research results.

As preliminary studies have shown [15-17], complex three-dimensional loading (impact and slip in two mutually perpendicular directions) creates conditions for the formation of surface layer fragments with relatively easy passage of dislocations through these crystallites to their boundaries. This contributes to lowering the level of external stresses required for the action of the rotational plasticity mechanism in the analyzed structures. As a result, a surface layer with a more uniform texture is formed, which is accompanied by increased wear. A change in the nature of loading leads to a change in the state of the surface layer and, as a consequence, a change in the wear resistance of the tribocoupling.

The features and specificity of the mechanism of plastic deformation during friction under multicomponent loading have not yet made it possible to develop the physical foundations and reveal the patterns of surface destruction. Research on the structure and properties of surfaces in tribocoupling components reveals the complexity and variety of surface phenomena involved.

The general case of a diagram of vertical surface and horizontal subsurface cracks during friction with three-dimensional dynamic loading is shown in Fig. 2 [17].

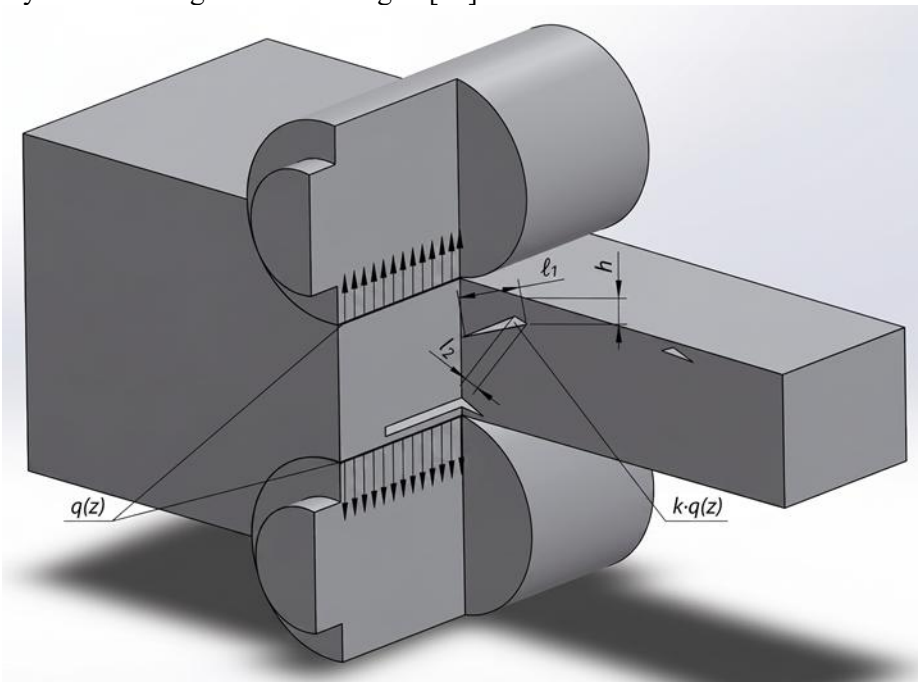

Fig. 2. Scheme cracks arrangement during friction with three-dimensional dynamic loading: l_1 – conditional length of the defect, l_2 – conditional width of the defect, h – depth of the defect, kq(z) – conditional area of the defect, q(z) – normal alternating stress (rolling stress)

The surface is loaded with normal alternating stress q(z) under impact loading and tangential stresses τ_x and τ_y under reciprocating sliding in two mutually perpendicular directions of the counter-specimen.

Studies using microscopic methods have shown that as a result of plastic deformation, a developed cellular structure oriented along the friction direction is formed in the surface layers. Fracture is initiated by the cell faces perpendicular to the sliding direction, and the initial crack passes along these faces. Therefore, with relative sliding of surfaces, the initiation of differently oriented cracks is possible [18-19]. Especially in the case of friction with sliding in two mutually perpendicular directions.

Overall, the development and propagation of microcracks under cyclic loading are heavily influenced by both the material's structural condition and the number of loading cycles N. To describe the development of microstructurally short cracks, the equation presented in [20] is applicable:

$$\frac{db}{dN} = C(\Delta\gamma)^m(d-b) \tag{5}$$

where b – crack depth; $\Delta\gamma$ – shear strain range; d – characteristic size of a structure element; C and m – experimentally determined material constants.

It follows from this equation that as the crack grows to the grain size, its speed decreases down to zero. At stresses above the endurance limit, the crack does not stop, but only slows down its growth or may stop for some time.

Moreover, the nature of deformation accumulation under the action of multiple pulse and pulsating loads is approximately the same. Thus, under impact loading, the dependence of contact deformation on the number of cycles is nonlinear with three sections: in the first section – the hardening stage (approximately up to N = 20) contact deformation occurs; in the second section, slow accumulation of contact deformation at an approximately constant speed (up to N = 103 ... 104); in the third section, a significant increase in deformation and intense destruction of the surface are observed [21].

It has been established [22] that wear under impact loading is a nonlinear function of the number of cycles and normal stress:

$$W = BN^n\sigma^m, \tag{6}$$

where B, n, m – coefficients determined experimentally.

In this case, the normal stress σ and the maximum contact pressure N are determined by the impact force, which in turn depends on the speed, geometry of the contact and the properties of the material.

Cyclic stresses lead to the occurrence of fatigue damage, both on the surface and at some depth. Surface fatigue occurs as a result of the normal collisions between microroughnesses, which generate tangential stresses beneath the roughness features, extending to a depth roughly corresponding to the height of the protrusions (in the micrometer range). The maximum tangential stress acts under the protrusion:

$$\tau'_m = \left(E'/\pi^2\right)\varphi, \tag{7}$$

where E' – reduced modulus of elasticity; φ – angular coefficient of protrusion.

It is obvious that microscopic (second kind) maximum shear stresses can indeed be the cause of the formation of embryonic cracks under the surface. The contact area between two bodies is influenced by the prevailing conditions:

$$\begin{cases} \tau_{xy} = -q(z)\sqrt{\psi_x^2 + \psi_y^2} + \left(E'_m/\pi^2\right)\varphi, \\ \sigma_z = -q(z) \end{cases} \tag{8}$$

Based on the solution of plane problems in analytical form presented in works [14, 23, 24], it is necessary to comply with the formulas:

$$\tau_{xz} = k_1 \cdot \sin A_1\Phi_1,\ \tau_{yz} = k_2 \cdot \sin A_2\Phi_2, \tag{9}$$

where A_1 and A_2 – constants that determine the parameters of a plastic medium; Φ_1 and Φ_2 – unknown coordinate functions determined by the solution of the problem; k_1, k_2 – resistance to plastic shear deformation along the X and Y axes, depending on the coordinates of the deformation zone:

$$k_1 = C_{\sigma 1} \cdot \exp\theta'_1,\ k_2 = C_{\sigma 2} \cdot \exp\theta'_2, \tag{10}$$

where $C_{\sigma 1}$, $C_{\sigma 2}$ – constants that determine the dimension of shear resistance in the directions of the X and Y axes; θ_1, θ_2 – coordinate unknown functions determined by solving the problem along the same axes. Based on the equilibrium equation, we obtain analytical dependencies for normal stresses. The components of the stress tensor have the form:

$$\begin{aligned} \sigma_x &= -2 \cdot C_{\sigma 2} \cdot \exp\theta'_2 \cdot \cos A_2\Phi_2 - C_{\sigma 3} \cdot \exp\theta'_3 \cdot \cos A_3\Phi_3 + C, \\ \sigma_y &= -C_{\sigma 2} \cdot \exp\theta'_2 \cdot \cos A_2\Phi_2 - 2 \cdot C_{\sigma 3} \cdot \exp\theta'_3 \cdot \cos A_3\Phi_3 + C, \\ \sigma_z &= -3 \cdot C_{\sigma 2} \cdot \exp\theta'_2 \cdot \cos A_2\Phi_2 - 3 \cdot C_{\sigma 3} \cdot \exp\theta'_3 \cdot \cos A_3\Phi_3 + C, \\ \tau_{yz} &= C_{\sigma 2} \exp\theta'_2 \cdot \sin A_2\Phi_2, \\ \tau_{zx} &= C_{\sigma 3} \exp\theta'_3 \cdot \sin A_3\Phi_3 \end{aligned} \tag{11}$$

The integral characteristic of the stress state of a point is the intensity of normal stresses according to equation (2). Substituting (11) into (2), we obtain an equation convenient for conducting analysis:

$$\sigma_i = \sqrt{3} \cdot \sqrt{\left(C_{\sigma 2} \cdot \exp\theta'_2\right)^2 + \left(C_{\sigma 3} \cdot \exp\theta'_3\right)^2 + \left(C_{\sigma 2} \cdot \exp\theta'_2 cos A_2\Phi_2\right)\left(C_{\sigma 3} \cdot \exp\theta'_3 cos A_3\Phi_3\right)} \tag{12}$$

Based on the condition of plastic deformation, in accordance with the Huber-Mises hypothesis on the equality of the intensity of normal stresses and yield stress, it is possible to write in relative values:

$$\frac{\sigma_i}{\sigma_T} = \frac{\sigma}{\sigma_T}, \tag{13}$$

where σ – yield stress; σ_T – yield stress in unhardened condition.

On the one hand, we have a characteristic of the stress state of the medium, depending on the friction coefficient, the shape factor, on the other, a physical quantity determined by the degree and speed of deformation, temperature, chemical composition. Thus, the Huber-Mises plasticity condition is a link that allows us to establish a connection between the parameters of the stress state of a point and the thermomechanical characteristics of the process.

Taking into account all of the above and the results of the experimental part, we finally get:

$$\sigma_p=0{,}00008\varepsilon^{0{,}52}\exp\left(\frac{-0{,}00016}{\varepsilon}\right)\exp(1{,}114\varepsilon)\,(1+\varepsilon)^{-0{,}0034T}\cdot \tag{14}$$

$$\cdot\dot{\varepsilon}^{-0{,}217}\dot{\varepsilon}^{0{,}00034T}T^{2{,}97}\exp(-0{,}00495T)$$

The obtained equation allows us to connect the parameters of the stress state of a point (friction coefficient, shape expresfactor) with the thermomechanical parameters of the process (degree, speed and temperature of deformation). Thus, an analytical connection has appeared that directly connects the factors of production and loading [24-25]. By setting the parameters of the stress state, with known coefficients α_i, it is possible to determine, using different calculation methods, the thermomechanical parameters of the process.

The proposed analytical model can be directly applied in engineering practice for the rapid estimation of deformation resistance and energy-force parameters in thermoplastic metal processing. The closed-form relationships obtained allow efficient parametric analysis without extensive numerical simulations, making the approach suitable for preliminary process design, optimization of rolling and forming regimes, and assessment of surface layer behavior in tribological contacts. The model can also be integrated into computational workflows as a constitutive sub-model, improving the accuracy and reliability of engineering calculations under complex thermomechanical loading conditions.

When performing the experimental part of the study using a Gleeble 3800 thermomechanical simulator, cylindrical specimens of microalloyed steel 10HFTBch with a diameter of 10 mm and a height of 12 mm were used. The samples were placed in a sealed chamber, where air was evacuated to create a vacuum environment in order to prevent oxidation during high-temperature deformation.

During thermomechanical loading, yield stress and logarithmic strain were recorded at predefined deformation intervals. The temperature of the central region of the specimens was monitored using thermocouples. The maximum temperature reached during hot deformation was 952 °C, ensuring deformation within the austenitic region. To analyze microstructural evolution during thermomechanical processing of microalloyed steel 10HFTBch, phase transformation behavior during continuous cooling after plastic deformation was investigated. The specimens in the as-delivered condition were heated to 950 °C and subjected to 30% plastic deformation in the austenitic region below the recrystallization temperature, while the deformation rate did not exceed 100 s^{-1}. Subsequently, the samples were cooled to 20 °C. To evaluate the effect of prior plastic deformation on subsequent structural formation, the specimens were reheated to 950 °C under identical thermal conditions.

Analysis of the results of calculating the intensity of normal stresses from the parameters of shape and friction coefficient shows that it is possible to increase this parameter compared to unhardened metal. There is an increase in this indicator by 1.13...2.0 times [17]. This means that, based on the Huber-Mises's hypothesis, the physical quantity, that is, the yield strength, also increases by 1.13...2.0 times. With an increase in the friction coefficient and shape parameters, we determine the yield stress, which in this case, through the temperature factor and recrystallization diagrams, makes it possible to establish structural transformations corresponding to a given stress state. The experimental data obtained from these thermomechanical tests were used to calibrate and validate the proposed universal analytical model describing metal deformation resistance under thermoplastic processing conditions.

4. Conclusions

A unified analytical model describing the dependence of metal deformation resistance on thermoplastic processing conditions has been developed. The proposed formulation combines the Hansel-Spittel constitutive equation with an analytical solution of the spatial plasticity problem, enabling a closed-form description of the stress strain state under non-uniform and multi-stage deformation.

The integration of the Huber-Mises plasticity criterion with frictional and geometric factors provides a direct analytical link between local stress intensity and the key thermomechanical parameters of the process,

including strain, strain rate, and temperature. This approach allows deformation resistance to be evaluated at any point within the deformation zone, overcoming the limitations of averaged or purely empirical models.

The developed framework is particularly effective for analyzing thermoplastic loading of surface layers in rolling and tribological contact conditions, where complex stress states govern wear and fatigue damage accumulation. The analytical nature of the solution makes it suitable for rapid parametric studies and preliminary engineering calculations without the need for extensive numerical simulations.

Overall, the proposed model enhances the accuracy of energy-force parameter prediction and provides a practical tool for process optimization, material behavior assessment, and the design of metal forming and tribological systems operating under complex thermomechanical loading conditions.

Conflict of interest statement
The authors declare that they have no conflict of interest in relation to this research, whether financial, personal, authorship or otherwise, that could affect the research and its results presented in this paper.

CRediT author statement
Tsyganov V.: Conceptualization, Resources; **Sheyko S.:** Methodology, Supervision; **Hrechanyi O.:** Project administration, Writing – review & editing, **Vasilchenko T.:** Data Curation, **Hrechana A.:** Writing - Original Draft. The final manuscript was read and approved by all authors.

Statement on the use of Artificial Intelligence.
The authors declare that no artificial intelligence tools were used to generate scientific content, results, or conclusions of this article.

Data Availability Statement
The data that support the findings of this article are openly available.

References

1 Rakhadilov, B.K. Satbaeva, Z.A., Kozhanova, R.S., Kowalewski, P., Bayatanova, L.B., Kalitova, A.A. (2022). Effect of the structure formed after bulk and surface hardening on the hardnessand wear resistance of 20Cr2Ni4A steel. *Eurasian Physical Technical Journal*, 19, 1(39), 20–25. . https://doi.org/10.31489/2022no1/20-25.

2 Kapoor, R. (2017). Severe Plastic Deformation of Materials. *Materials Under Extreme Conditions*, 717–754. https://doi.org/10.1016/b978-0-12-801300-7.00020-6

3 Bronkhorst, C. A., Ghosh, S. (2017.) Integrated Computational Structure-Material Modeling of Deformation and Failure under Extreme Conditions. *International Journal of Fracture*, 1-2(208), 1–3. https://doi.org/10.1007/s10704-017-0253-8

4 Eremin, E.N., Guchenko, S.A., Yurov, V.M. (2020). Wear resistance and tribological properties of high entropy coatings CrNiTiZrCu. *Eurasian phys. tech. j*., 17(1(33), 13–18. DOI: 10.31489/2020No1/13-18.

5 Hoboken, N.J. (2013). Elements of Plastic Deformation. Metal Failures. *John Wiley & Sons*, *Inc*., 59–79. doi: 10.1002/9781118671023.ch3

6 Sheyko, S., Tsyganov, V., Hrechanyi, O., Vasilchenko, T., & Hrechana, A. (2023). Determination of the optimal temperature regime of plastic deformation of micro alloyed automobile wheel steels. *Research on Engineering Structures and Materials*, 10(1), 331-339. https://doi.org/10.17515/resm2023.49me0428tn

7 Zheng, H. X., Chen, C. Y. (2012). Research on Interface Critical Fracture of Different Materials Based on Critical Fracture Curve. *Applied Mechanics and Materials*, 204-208, 3090–3093. https://doi.org/10.4028/www.scientific.net/amm.204-208.3090

8 Sheyko, S., Tsyganov, V., Hrechanyi, O., Vasilchenko, T., Vlasov, A. (2023). Mechanical property investigation of welded joints in 10HFTBch steel for the automobile wheel production. *Materials Letters: X*, 17, 100181. https://doi.org/10.1016/j.mlblux.2023.100181

9 Mikulski, Z., & Lassen, T. (2022). Probabilistic models for the fatigue resistance of welded steel joints subjected to constant amplitude loading. *International Journal of Fatigue*, 155, 106626 https://doi.org/10.1016/j.ijfatigue.2021.106626

10 Oginskyy, Y.K. (2011). The force pattern in the deformation zone at steady rolling process. *Metallurgical and Mining Industry*, 3(1), 10–14. https://www.metaljournal.com.ua/assets/Uploads/attachments/Oginskyy-10.pdf

11 Sheyko, S., Belokon. Y., Hrechanyi .O., & Vasilchenko, T. (2024). *Thermoplastic Processing of Structural Metallic Materials.* Springer Nature Switzerland, X, 112 p. https://doi.org/10.1007/978-3-031-73896-8

12 Pavlenko, D. V., Belokon', Y. O., Tkach, D. V. (2020). Resource-Saving Technology of Manufacturing of Semifinished Products from Intermetallic γ-TiAl Alloys Intended for Aviation Engineering. *Materials Science*, 6, 908–914. https://doi.org/10.1007/s11003-020-00386-1

13 Chigirinsky, V., Naumenko, O. (2020). Invariant differential generalizations in problems of the elasticity theory as applied to polar coordinates. *Eastern-European Journal of Enterprise Technologies*, 5, 7 (107), 56–73. https://doi.org/10.15587/1729-4061.2020.213476

14 Chigirinsky, V., Naizabekov, A., Lezhnev, S., Kuzmin, S., Naumenko, O. (2022). Solving applied problems of elasticity theory in geomechanics using the method of argument functions of a complex variable. *Eastern-European Journal of Enterprise Technologies*, 5, 7 (119), 105–113. https://doi.org/10.15587/1729-4061.2022.265673

15 Tsyganov, V. V. (2023). Features of mechanics destruction tribounitsat difficult dynamic loading. *Eurasian Physical Technical Journal*, 20, 2 (44), 99–105. https://doi.org/10.31489/2023no2/99-105

16 Tsyganov, V.V., Sheiko, S.P., Sakipov, K.E. (2022.) Features of estimation wearproofness tribojoints by work of electron output. *Eurasian Physical Technical Journal*, 19, 3 (41), 78 – 83. https://doi.org/10.31489/2022No3/78-83

17 Tsyganov, V.V., Sheyko, S.P., Hrechanyi ,O., Vasilchenko, T. (2024). Modeling the plastic deformation state of the contact surface during friction. *Eurasian Physical Technical Journal*, 21, 3(49), 63–70. https://doi.org/10.31489/2024no3/63-70

18 Trukhanska, O. (2020). Technological methods of increasing wear resistance and durability of details. *Engineering, Energy, Transport Aic.*, 4(111), 109-115. https://doi.org/10.37128/2520-6168-2020-4-12

19 Tsybanev, G. V. (2013). Application of the deformation criterion to the description of short fatigue crack growth. *Strength of Materials,* 45(1), 28–34. https://doi.org/10.1007/s11223-013-9429-2

20 Miller, K. J. (1988). The behaviour of short fatigue cracks and their initiation. *Mechanical behaviour of materials V*., 1357–1381. https://doi.org/10.1016/b978-0-08-034912-1.50183-1

21 Belodedenko, S., Grechany, A., Yatsuba, A. (2018). Prediction of operability of the plate rolling rolls based on the mixed fracture mechanism. *Eastern-European Journal of Enterprise Technologies*, 7 (91), 4-11, https://doi.org/10.15587/1729-4061.2018.122818

22 Morozov, E.M., Zernin, M.V. (1999). *Contact problems of fracture mechanics.* Mechanical engineering, 544 (in Russian). https://doi.org/read.in.ua/book253007.

23 Volokitina, I.E., Panin, E.A., Volokitin, A.V., Fedorova, T.D., Latypova, M.A., Makhmutov, B.B. (2025). Investigation of the stress-strain state during new combined deformation technology. *Eurasian Physical Technical Journal*, 22, 2 (52), 109–120. https:// doi.org/10.31489/2025N2/109-120

24 Chigirinsky, V., Volokitina, I. (2024). Additional effect on the deformation zone during plastic metal flow. *Engineering Solid Mechanics*, 2 (12), 113–126. https://doi.org/10.5267/j.esm.2023.11.001

25 Georgiev, G., Argirov, Y., Mechkarova, T., Spasova, D., Stoyanova, A. (2021). Study of the durability of ferritic - austenitic steel samples after cyclical fatigue impact. *IOP Conference Series: Materials Science and Engineering*, 1037(1), 012036. https://doi.org/10.1088/1757-899x/1037/1/012036

AUTHORS' INFORMATION

Tsyganov, Volodimir Vasilievich – Doctor of Techn. Sciences**,** Professor, National University Zaporizhzhia Polytechnic, Zaporizhzhia, Ukraine; Scopus Author ID: 56712109100; https://orcid.org/0000-0001-5682-7005**;** tsyganov705@gmail.com

Sheyko, **Sergey Petrovich –** PhD, Associate Professor, Department of Metallurgical Equipment**,** Zaporizhzhia National University, Zaporizhzhia, Ukraine; Scopus Author ID: 23095863300; https://orcid.org/0000-0001-5761-4263; ss6309113@gmail.com

Hrechanyi, Oleksii – PhD, Associate Professor, Department of Metallurgical Equipment**,** Zaporizhzhia National University, Zaporizhzhia, Ukraine; Scopus Author ID: 57219488722; https://orcid.org/0000-0003-0524-4998; hrechanyi@znu.edu.ua

Vasilchenko, Tetiana – PhD, Associate Professor, Department of Metallurgical Equipment**,** Zaporizhzhia National University, Zaporizhzhia, Ukraine; Scopus Author ID: 54415072500; https://orcid.org/0000-0002-0340-3900; vasilchenko@znu.edu.ua

Hrechana, Anastasiia – Specialist, **Scientific** Laboratory of the Latest Technologies of the Educational and Scientific Production Center "Metalspetsproekt"**,** Zaporizhzhia National University, Zaporizhzhia, Ukraine; Scopus Author ID: 58196088100; https://orcid.org/0000-0002-9650-3475; hrechana@znu.edu.ua

EURASIAN PHYSICAL TECHNICAL JOURNAL

2026, Volume 23, No. 2 (56)

https://doi.org/10.31489/2026N2/22-34

Received: 07/02/2026 Revised: 23/05/2026 Accepted: 28/06/2026 Published online: 30/06/2026

Original Research Article

UDC 539.232, 620.193; 669.2.8

CORROSION-RESISTANT COMPLEX-STRUCTURED COATINGS FOR ALUMINIUM ALLOYS

Guchenko S.A.[1], Seldyugaev O.B.[1], Karstina S.G.[1], Danilov M.B.[2], Afanasyev D.A.[1]*

[1] Buketov Karaganda National Research University, Karaganda, Kazakhstan
[2] LLP «Astaldo», Karaganda, Kazakhstan
*Corresponding author: a.d.afanasyev2@gmail.com

Abstract. *This paper presents the results of a study of the microhardness and corrosion resistance of a number of protective coatings applied to the surface of D16 alloy products. Various protective coatings (chromium, chromium nitrite, and a chromium nitrite layer with a chromium layer deposited on top) are proposed, each with varying degrees of Vickers microhardness (from HV = 80 to HV = 1114) and corrosion resistance. A chromium layer deposited on the surface of D16 alloy is shown to have very low hardness (HV = 80). A chromium nitrite layer deposited on the surface of D16 alloy is determined to have high hardness (HV = 655), but very low corrosion resistance. A double protective coating consisting of a chromium nitrite layer deposited on top of a chromium layer is shown to have satisfactory hardness (HV = 236) and corrosion resistance. It was found that the introduction of a highly hard layer between the surface of a D16 alloy part and an external chromium layer exceeds the surface hardness of the D16 alloy parts several times. It was shown that treating protective chromium-containing coatings with active oxygen species significantly increases the corrosion resistance and hardness of these coatings.*

Keywords: coating, microhardness, corrosion, corrosion resistance, chromium, chromium nitrite.

1. Introduction

Metal corrosion is one of the main processes leading to the destruction of metal structures and machine parts [1]. Under certain external conditions, the corrosion process can either accelerate or slow down. Land areas bordering seas and oceans are zones of increased corrosion due to the aggressive chemical composition of sea air [2, 3]. Halogen ions are the main factors in the destruction of metal products in seawater and in the atmosphere of coastal areas [4, 5]. One of the most widely used classes of metal alloys is duralumin alloys. Products made from these alloys are lightweight compared to steel parts and have sufficient strength [6].

Aluminium alloy D16 (duralumin, duralumin) belongs to the group of duralumin alloys with a high copper content. Close analogues of alloy D16 are 2024, $AlCu_4Mg_1$, $AlCuMg_1$, AA2024, AA2124. Alloy D16 is similar in composition to the group of aluminium-magnesium alloys - magnalium's of the AMg1.5 type (AMg-aluminium-magnesium alloys). The percentage of magnesium in the D16 sample is 1.2-1.8%, which allows this alloy to be classified as belonging to the AMg1.5 group of alloys (Table 1) [7]. The D16 alloy, which has a low density and high strength for aluminium alloys (Table 2) [8-10], is widely used in various fields of technology, such as aircraft construction [11]. In [10], it is noted that magnesium in AMg alloys is present in the form of Mg_2Al_4 groups, which are a rhombic subsystem of aluminium cells. It has been shown that the more aluminium cells contain Mg_2Al_4 groups, the higher the mechanical strength of the alloy. In AMg1.5 group alloys, the number of cells containing this group averages 18% of the total number of

aluminium cells [10]. It has been shown that a 1% increase in the number of cells containing the Mg_2Al_4 group in an aluminium alloy increases the strength of the aluminium alloy by 5.83 MPa. It has been shown that the structural formula of the Mg_2Al_4 compound is a rhombic system (Figure 1, a). Replacing two aluminium atoms in the rhombic subsystem with magnesium atoms significantly increases the strength of the alloys [10].

Table 1. Chemical composition of magnalium alloys (wt.%)

	Al	Mn	Cr	Ti	Cu	Zn	Mg	Fe	Si
D16	90,9-94,7	0,3-0,9	0.1%	0.155	3,8-4,9	0.25%	1,2-1,8	0.5%	0.5%
D16*	91.8%	91.8%	0.1%	0.155	4.3%	0.25%	1.6%	0.5%	0.5%
AMg1,5	96,45-98,9%	0,1%;	0,1%	-	0,2%;	0,25%;	1,1-1,8%	0,5%	0,5%
D19	91,095-94%	0,5-1%	0.1%	0.1	3.8-4.3	0.1	1.7-2.3%	0,5%	0,5%

* Calculated mass percentages of elements in alloy D16 based on the assumption that the number of copper atoms in alloy D16 is equal to the number of magnesium atoms.

Alloy D16 differs from the simple AMg1.5 alloy in that it has a significantly higher copper content, which leads to a significant increase in strength and hardness (Table 2). In the D16 alloy, the number of magnesium atoms is approximately equal to the number of copper atoms. In the D19 alloy, which is an improved version of the D16 alloy, the number of copper and magnesium atoms is actually equal, which has increased the impact strength of this alloy [12]. Considering that aluminium atoms are trivalent, while magnesium and copper atoms are divalent, it was concluded that in the D16 alloy, aluminium cells contain the $MgAl_4Cu$ group instead of the Mg_2Al_4 group. One magnesium atom in the rhombic subsystem of the aluminium lattice is replaced by a copper atom (Figure 1, b).

Table 2. Mechanical characteristics of aluminium alloys

	Tensile strength, MPa	Yield strength, MPa	Brinell hardness (HB), Kgs/mm^2	Vickers hardness (HV)
Pure aluminium	70	25	25	26.31579*
AMg1	140	50	30	31.57895*
AMg2	170	80	45	47.36842*
AMg3	200	100	58	61.05263*
AMg4	250	120	75	78.94737*
AMg5	280	150	65	68.42105*
AMg6	320	160	100	105
D16	440	300	114*, 125 [7]	120 [13], 132*
D19	460	340	125 [7]	132*

* Data is given in accordance with the formula HB=0.95* HV.

Increasing the copper content in the D16 alloy created a problem in that it reduced corrosion resistance. At the same time, the D16 alloy does not have a sufficiently high surface hardness (according to Vickers, HV = 120-132, Table 2). It is known that products made from the D16 alloy have insufficient corrosion resistance to seawater [14]. To protect against corrosion damage, these products are usually coated with protective coatings, such as varnishes [15], which creates problems during their use. For example, over time, protective varnishes deteriorate and flake off; protective coatings, such as bitumen, can also ignite.

However, the corrosion resistance of these alloys is low, and therefore various research groups are working to increase the corrosion resistance of products made from these alloys. One way to improve corrosion resistance is to apply inorganic protective coatings to aluminum alloy products [1]. In this case, it is important to increase the hardness of the protective coatings. Technologies for strengthening the surface layers of parts and creating protective coatings with high physical, mechanical, and chemical properties are a widely researched topic. These methods are discussed in the review article [1].

For example, reviews [16] the most promising innovative technology for surface hardening of aluminium alloys – plasma electrolytic oxidation (PEO). It considers the possible conditions and mechanisms for the formation of protective coatings on the surface of aluminium alloys. The influence of the main parameters of PEO treatment (electrical parameters, electrolyte composition and concentration, influence of alloying elements) on the structure and properties of oxide-ceramic coatings is studied. The qualitative characteristics of the surface layer of samples and finished products made of aluminium alloys demonstrated the effectiveness

of the PEO technology, which allows obtaining ceramic coatings with high hardness, strength, and increased wear and corrosion resistance.

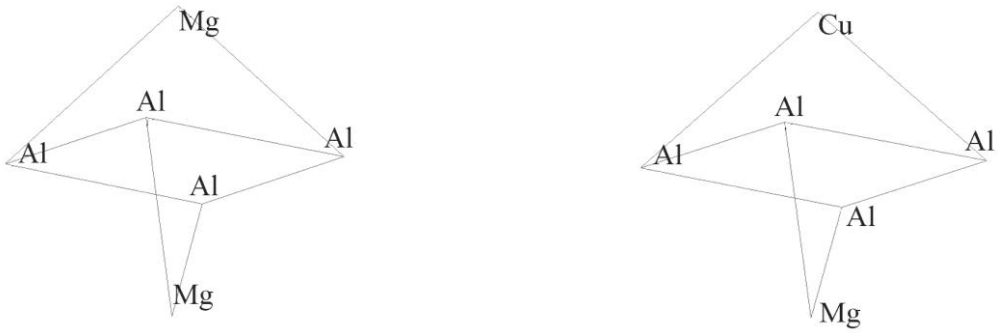

a) b)

Fig.1. Diagram of the possible arrangement of atoms in an elementary cell: a) Rhombic subsystem of the AMg alloy containing a solid solution in the form of Al_4Mg_2; b) Rhombic subsystem of the AMg alloy containing a solid solution in the form of $MgAl_4CuMgAl_4Cu$.

Possible areas of application for highly effective technologies for applying protective PEO coatings to the surfaces of aluminium alloy products are proposed. Another example of the development of protective coatings is the work [17]. It proposes a new method of high-dose ion implantation of chromium and oxygen ions for the anti-corrosion treatment of VNS-5 aviation steel. The resulting protective layer of chromium oxide with a thickness of up to 100 nm is rich in Cr and poor in Fe, which slows down oxidation. The results of the work showed an improvement in corrosion resistance without compromising mechanical properties, which is especially useful for marine vessel parts.

The aim of this work was to develop protective coatings for aluminium alloys based on chromium, which are both corrosion-resistant and highly durable. The cathodic sputtering method was used for production, followed by additional oxidation of the protective coating. This made it possible to obtain coatings with increased hardness and corrosion resistance.

2. Materials and experimental details

The study used samples of D16 aluminum alloy measuring 15 mm × 10 mm × 4 mm. Before being loaded into the working chamber, the samples were degreased in isopropyl alcohol. In the working chamber, before coating, the surface of the samples was ionically cleaned using a plasma source with a hot cathode (PINK) [18]. In order to increase the corrosion resistance of the surface of the D16 samples, chromium or chromium nitride with a thickness of 2 μm was applied to their surface. Chrome target ERKh 99.95 (TU 14-22-138-2000) were used. When chromium films were applied to the surface of the chromium nitride film, the thickness was 0.5 μm. The films were applied by cathodic sputtering with an accelerating voltage of 1000 volts on the measuring setup described in [18, 19]. The chromium films were obtained in an argon atmosphere with a chamber pressure of 0.5 Pa. During the process of obtaining chromium nitride coatings, the working gas in the working chamber is changed from argon to nitrogen. The working gas pressure in the chamber was 0.5 Pa.

Samples with protective coatings were placed in a working chamber and heated to 185 °C in an atmosphere for 12 hours, while the atmosphere was exposed to ultraviolet (UV) radiation. More details on the treatment method are provided in articles [10, 20].

For the purposes of this article, the following abbreviations were chosen for the names of samples subjected to various treatments:

D16_X – a layer of chromium sprayed onto the surface of a product made of D16 alloy;

D16_X_U12 – a layer of chromium sprayed onto the surface of a product made of D16 alloy and then exposed to air for 12 hours, subjected to UV radiation (further processed samples);

D16_(N+X) – surface of the D16 alloy covered with a layer of chromium nitride;

D16_(N+X)_U12 – surface of the D16 alloy covered with a layer of chromium nitride and then subjected to 12 hours of treatment;

D16_(N+X)_X – a layer of chromium nitride is sprayed onto the surface of the D16 alloy, then a layer of chromium is applied to the chromium nitride layer;

D16_(N+X)_X_U12 – a layer of chromium nitride is sprayed onto the surface of the D16 alloy, then a layer of chromium is applied to the chromium nitride layer and subjected to 12 hours of treatment.

In these designations: X – application of a chromium film to the surface of the sample, U12 – treatment of the sample surface with ultraviolet radiation for 12 hours, N+X – chromium nitride films applied with the addition of nitrogen to the working chamber. A schematic representation of the process of applying protective coatings and the process of their treatment is shown in Figure 2.

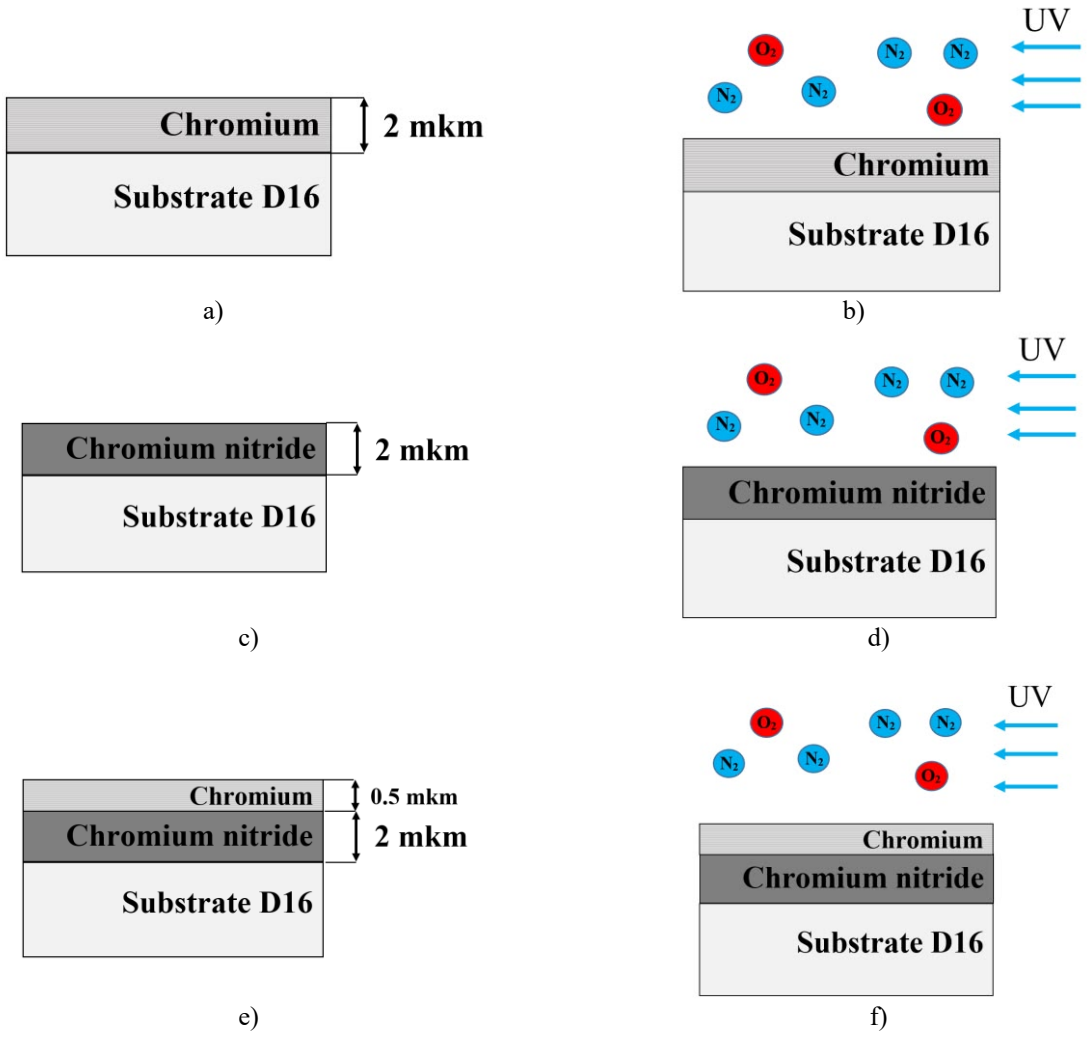

Fig.2. Schematic representation of the process of applying protective coatings and the process of their treatment: a) D16_X; b) D16_X_U12; c) D16_(N+X); d) D16_(N+X)_U12; e) D16_(N+X)_X; f) D16_(N+X)_X_U12.

The surface morphology of the synthesized films was investigated using a scanning electron microscope (SEM) (MIRA 3LMU, TESCAN) fitted with an energy-dispersive X-ray analyser (EDX, INCAPentaFET x3, Oxford Instruments, UK).

The microhardness of the obtained samples was measured using an HVS-1000A microhardness tester. A load of 100 g was used. The enlarged surface areas were also analyzed using an optical microscope of the HVS-1000A microhardness tester. Next, to test corrosion resistance using the method described in article [10], samples D16 and D16, coated with various protective films, were placed in a test solution simulating the corrosive effect of seawater for a control period (72 hours). A 5% solution of iodine in ethanol was used as the test solution. The mass of the sample was measured before and after placement in the solution. The results are given as mass percentages of mass loss, where the mass of the sample before placement in the solution is taken as 100%. Information is also provided in the form of the number of atoms lost from the surface of the samples as a result of corrosion. For this purpose, the mass loss was divided by the mass of one atom of the protective coating. The mass of samples was measured on electronic scales RADWAG AS 60/220.R2 with an accuracy

of 10^{-4} grams. The area of corrosion damage was estimated from measurements of areas affected by corrosion and without corrosion, obtained using an HVS-1000A optical microscope microhardness tester.

Image scaling and the subsequent measurement of structural elements were carried out in ImageJ following preliminary calibration using a reference object.

3. Results and discussion

3.1 Surface morphology of protective coatings based on chromium and chromium nitride

The surface morphology of the D16_(N+X), D16_(N+X)_U12, D16_(N+X)_X and D16_(N+X)_X_U12 samples is shown in Figures 3, a-d. Figures 3, a-d show the formation of a uniform structure on the surface of the D16 samples. The films are homogeneous, free from cracks and significant defects. Particles ranging in size from 50 nm to 2.5 μm are also present on the film surface. However, their proportion is not significant compared with the film surface without particles. The formation of particles is associated with the film deposition parameters and the use of an industrial cathodic metal sputtering system [18]. Treatment of the samples in an oxygen atmosphere under UV irradiation does not lead to significant changes in the film structure.

The map of elemental distribution across the sample surface on the Figure 4 shows the formation of a homogeneous film with no changes in stoichiometric composition across the sample surface. The remaining samples exhibit similar film quality on the surfaces of the D16 samples. EDX analysis determined the stoichiometric composition of the films to be $Cr_{2.7}N$. UV treatment of the film surfaces does not result in any change to their stoichiometric composition.

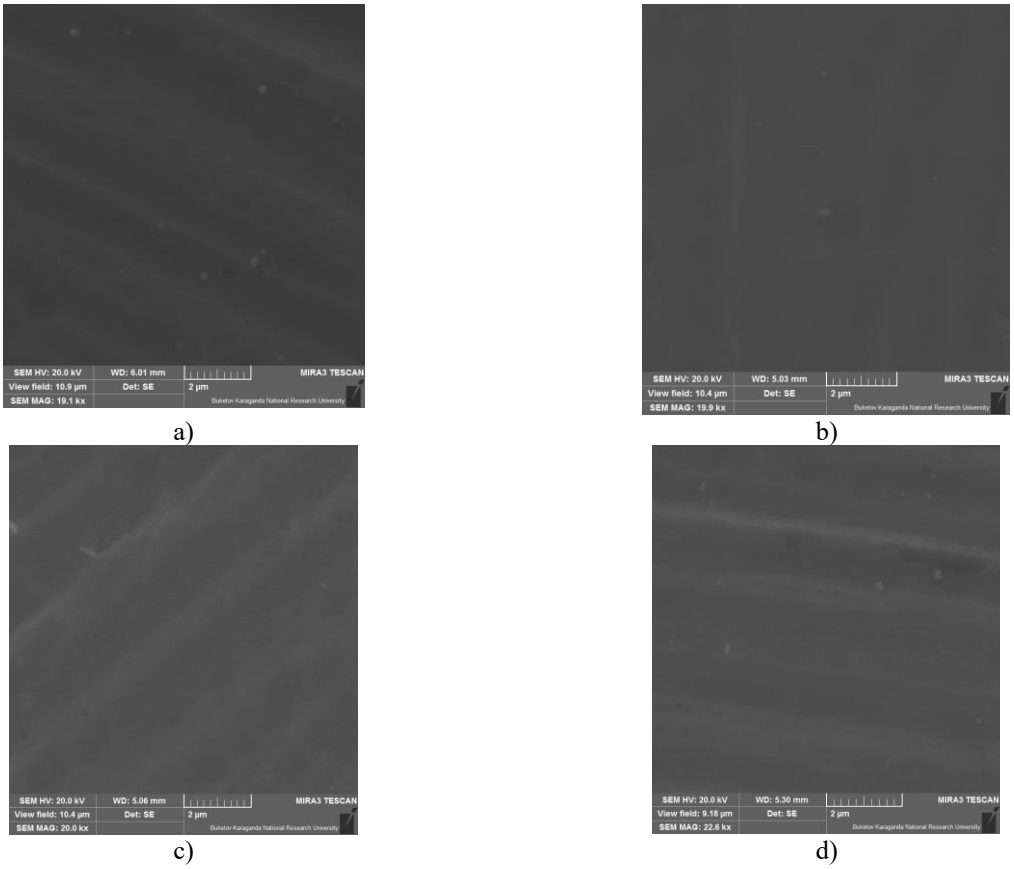

Fig.3. Surface morphology of coatings obtained by SEM: a) D16_(N+X); b) D16_(N+X)_U12; c) D16_(N+X)_X; d) D16_(N+X)_X_U12.

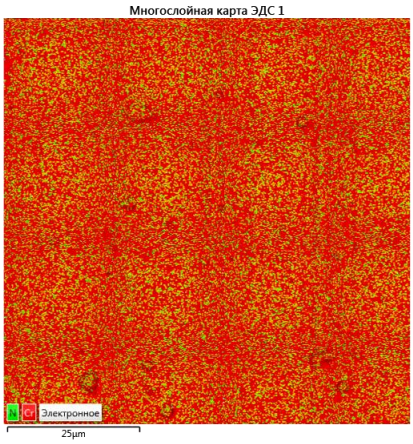

Fig.4. Map of distribution of elements on the sample surface of D16_(N+X).

3.2 Chromium-based protective coatings treated with ultraviolet light

Initially, in order to increase corrosion resistance, the surface of sample D16 was coated with a 2 μm layer of chromium. Next, to test corrosion resistance using the method specified in [10], samples D16 without additional protective coatings and D16 coated with chromium were placed in a test solution for a control period. The experiment showed a significant reduction in the corrosion rate in the test solution. The number of atoms lost by the D16 sample as a result of applying a layer of chromium to the surface decreased by 1.65 times (Table 3). However, a significant decrease in the surface hardness of the sample coated with pure chromium (1.5 times) was also recorded.

Table 3. Summary information on the loss of atoms in the samples studied, the area of corrosion damage, and the microhardness of D16 samples without coatings and with various protective coatings.

Number of ator lost by the surface due to corrosion	D16	D16_X	D16_X_U12	D16_(N+X)	D16_(N+X)_ U12	D16_(N+X) _X	D16_(N+X)_ X_U12
Number of ator lost by the surface due to corrosion	$9{,}868*10^{20}$	$5{,}992*10^{20}$	$4{,}072*10^{20}$	--	---	$5{,}611*10^{20}$	$4{,}19*10^{20}$
Surface hardne according to Vickers (HV)	150	80	120	655	1114	236	350
Area of corrosion damage*	-	30%	5%	53% .	6%;	23%	12%
Sample mass loss (%)	-	2,66%	1,81%	4,12 %	2,56%	2,49 %	1,86%

* Determined as a percentage of the total area of the micrograph at 160x magnification.

In [20], a significant increase in the corrosion resistance of martensitic stainless steel X17 was revealed as a result of treating the surface of stainless-steel samples with ozone (ozone was generated by exposing oxygen molecules in the air to ultraviolet radiation). It was shown that the corrosion resistance of martensitic stainless steel X17 increased by 71% due to a significant increase in the number of chromium-oxygen-chromium bonds (the oxygen content on the surface increased 5.71 times from 0.7 to 4 mass percent). Based on the results of [20], it was assumed that the corrosion resistance of D16 samples coated with chromium could increase after prolonged treatment of the surface of these samples with air exposed to UV radiation.

To verify this assumption, D16 alloy samples coated with a 2 μm thick layer of chromium were treated with air containing active oxygen species (AOS) at a temperature of 185°C for 12 hours. Each of the sample surfaces of D16_X and D16_X_U12 was treated for 12 hours. As a result of corrosion resistance testing, it was found that the corrosion rate of D16 samples coated with chromium and further processed by AOS decreased

by 32% in mass compared to the corrosion rate of D16 alloy samples coated with chromium (1.47 times) (Table 3). At the same time, the surface hardness of the samples coated with chromium and further processed by AOS increased by 33%.

Figure 5 shows photographs of D16 alloy samples coated with a layer of chromium after being kept in the test solution for a control period of time. There is a large difference in the area of damage to the D16 alloy samples. On samples coated with chrome and treated with AOS D16_X_U12, a dozen pinpoint corrosion pits are observed. On the surface of the sample coated with chrome D16_X without further treatment, moderate corrosion damage is observed: the number of pinpoint pits is an order of magnitude greater than on the sample subjected to prolonged treatment AOS.

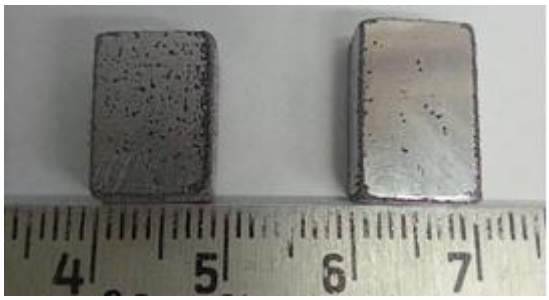

Fig.5. Photographs of D16 alloy samples with a protective chrome film after exposure to the test solution for the control time. On the left is a D16 sample coated with a layer of chrome. On the right is a D16 alloy sample coated with a layer of chrome and then subjected to 12 hours of treatment with air exposed to UV radiation.

Figure 6 shows micrographs of the surface of D16 alloy samples after exposure to the test solution for the control time. It is clearly visible that the total area of corrosion damage has significantly decreased on the D16_X_U12 sample, which was subjected to prolonged treatment. For these samples, the size of individual corrosion lesions has significantly decreased. The area of a single corrosion lesion is 5% of the studied area of the treated sample D16_X_U12 and 30% of the sample area D16_X if no treatment was performed. On average, the radius of individual lesions on ozonated samples D16_X_U12 decreased 6 times compared to samples D16_X coated with chromium without further treatment. Also, on the treated samples D16_X_U12, there are no destruction channels outside the main corrosion ulcer. It can be seen that outside the corrosion ulcers, the surface microstructure has practically not been affected. The absence of damage to the surface microstructure indicates that the destruction of the chrome-coated surface begins with isolated foci, which increase in area and depth over time. Iodine ions interact with chromium atoms and D16 alloy atoms at the edges of the primary corrosion hole, gradually increasing its area.

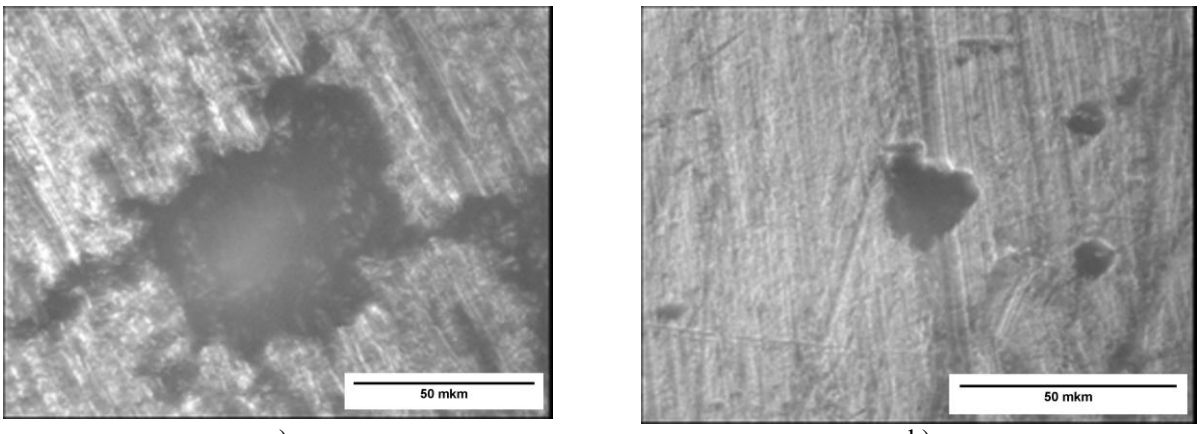

a) b)

Fig.6. Samples D16_X and D16_X_U12 after exposure to the test solution for the control time: a) D16_X; b) D16_X_U12. Samples magnified 160 times.

Considering the above, it can be concluded that samples coated with a layer of chromium D16_X without further processing can be used in an atmosphere containing halogen ions in the absence of abrasive particles in the atmosphere.

3.2 Protective coatings based on chromium nitride

There is often a need to use products made of D16 alloy in an atmosphere containing abrasive particles and chemically active vapors. It is known that after applying coatings (chromium nitride) to metal products, the surface hardness of the products increases significantly [21]. It was assumed that coating the samples with a layer of chromium nitride would increase the surface hardness of products made of D16 alloy, which would expand the technological application of this alloy. For example, increasing the surface hardness of products will allow them to be used in sandy desert conditions, where the atmosphere contains abrasive impurities. To test this hypothesis, a 2 μm thick chromium nitride coating was applied to the D16 sample using cathodic sputtering.

Studies of the obtained D16_(N+X) samples showed a significant increase in the surface hardness of the D16_(N+X) samples to HV100g = 655. Next, a study of the corrosion resistance of the D16_(N+X) samples was conducted. The D16_(N+X) samples were placed in a test solution for a control period. The experiment showed that the mass loss of the D16_(N+X) sample was 4.12% of the sample mass (Table 3). The surface of the D16_(N+X) sample became reddish. This fact indicates the destruction of the chromium nitride coating and the destruction of the upper layers of the surface of the D16 alloy sample (the red color of the surface indicates the release of copper from the D16 alloy structure). In addition to significant mass loss, significant corrosion damage was found on the surface of the test sample (Figure 7). Micrographs at 160x magnification showed that the corrosion process created wide areas of continuous damage between slightly damaged areas (Figure 8, a). The total area of corrosion damage was 53%.

Fig.7. Samples D16_(N+X) and D16_(N+X)_U12 after exposure to the test solution for the control time: on the left is sample D16_(N+X); on the right is sample D16_(N+X)_U12.

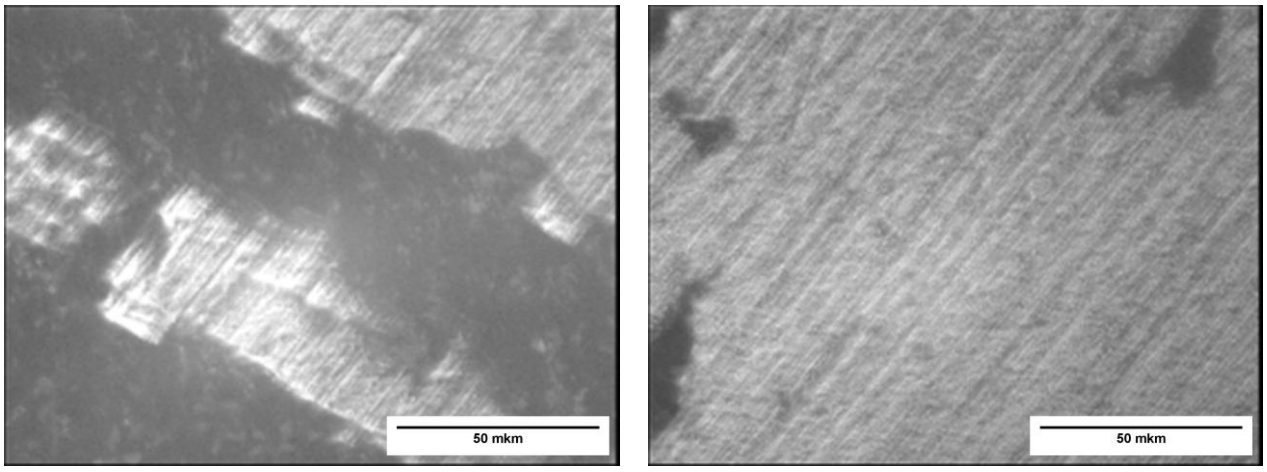

a) b)

Fig.8. Micrographs of the surface of samples D16_(N+X) and D16_(N+X)_U12 after exposure to the test solution for the control time: a) D16_(N+X); b) D16_(N+X)_U12. Magnification 160x.

Thus, severe damage to the micro- and macrostructure of the surface of samples D16_(N+X) was observed when these samples were placed in the test solution. For samples D16_(N+X), a significant increase in hardness leads to a significant decrease in corrosion resistance (Table 4). Products coated with chromium

nitride D16_(N+X) can be used in atmospheres containing abrasive particles but no halogen ions. For example, chromium nitride coating cannot be used in products used in seaports.

In [20], it was shown that an increase in the number of chromium-oxygen-chromium chemical bonds leads to a significant increase in the corrosion resistance of X17 stainless steel. Considering that the chromium-nitrogen coating applied to the surface of D16 alloy samples contains chromium in a basic valence state of 3, it was assumed that converting chromium to a higher valence state (from 4 to 6) would create additional chemical bonds in the coating. As a result of the increase in the density of chromium chemical bonds in the coating (chromium nitride), the corrosion resistance of the D16_(N+X) coating will increase. To activate the additional valence of chromium, active oxygen molecules were used, generated by the effect of ultraviolet radiation on oxygen molecules in the air (ultraviolet irradiation time 12 hours). The D16_(N+X) samples were subjected to 12 hours of UV radiation treatment at a temperature of 185°C. As a result, a significant increase in the hardness of the D16_(N+X) samples to HV = 1114 was recorded (a very significant increase in hardness). As a result of additional oxidation, the surface hardness of the D16_(N+X)_U12 sample increased 1.7 times at low loads.

However, a significant increase in surface brittleness was also observed. Under loads exceeding 50 grams, cracks formed around the test area. This fact prevents the use of this coating in cases of high loads, but does not prevent its use in atmospheres containing abrasive particles. Corrosion resistance testing showed a significant reduction in the corrosion process of samples coated with chromium nitride and then subjected to prolonged exposure to active forms of oxygen (D16_(N+X)_U12). A 2.56% loss in sample mass was recorded as a result of exposure to the test solution for the control time (Table 3). In other words, additional oxidation of the chromium nitride surface increased corrosion resistance by a factor of 1.61. Visually, there are no corrosion pits on the surface of the treated sample D16_(N+X)_U12 (Figure 7). The colour of the surface has not changed, and no reddish tint has appeared. With identical sample sizes, mass loss decreased by 37.8% (1.61 times) for D16_(N+X)_U12 samples. Figure 6, b shows a micrograph of the D16_(N+X)_U12 samples after the control time in the test solution. The micrograph shows that outside the corrosion pits, the surface microstructure has not changed. The total area of corrosion damage is no more than 6%.

3.3 Protective layered coatings based on chromium nitride and chromium layer

Applying a chromium nitride coating to the surface of alloy D16 revealed a significant increase in hardness to HV=655, but at the same time, corrosion resistance decreased significantly (Table 3). It was assumed that additional spraying of a chromium layer over the chromium nitride layer would increase the corrosion resistance of the product surface and, at the same time, the high hardness of the chromium nitride layer would increase the hardness of the applied chromium layer.

To test this hypothesis, a chromium nitride coating plus an additional 0.5 μm thick chromium layer was applied to sample D16 by cathodic spraying. Studies of the obtained samples D16_(N+X)_X showed a surface hardness of $HV_{100\ g}$=236. This hardness is significantly lower than the surface hardness of the D16_(N+X) samples, which is HV = 655, but 1.6 times higher than the surface hardness of the D16 alloy, which is HV = 150, and 3 times higher than the surface hardness of the D16_X samples, which is HV = 80 (Table 3).

The presence of a high-hardness surface under the chromium layer in sample D16_(N+X)_X HV = 655 resulted in the hardness of the chromium coating becoming significantly greater than HV = 240, which is the hardness of the chromium coating layer applied directly to the surface of alloy D16 (D16_X) HV=80.

At the same time, the chromium film applied to the surface with high hardness - chromium nitride HV=655 - protects the hard layer of chromium nitride HV=655 from the effects of halogen ions contained in seawater. Next, the corrosion resistance of the D16_(N+X)_X samples was studied. The experiment showed that during the control period, the mass loss of the D16_(N+X)_X sample was 2.49% of the sample mass (Table 3). The loss of atoms from the surface of sample D16_(N+X)_X decreased by 1.76 times compared to the surface of alloy D16 (Table 3). Figure 9 shows the appearance of sample D16_(N+X)_X after exposure to the test solution for the control period. Severe pitting is observed for this sample. However, there is no reddish tint on the surface, which indicates that the top layer of chromium and the layer of chromium nitride were not completely destroyed and corrosion on the surface of the D16 alloy did not begin.

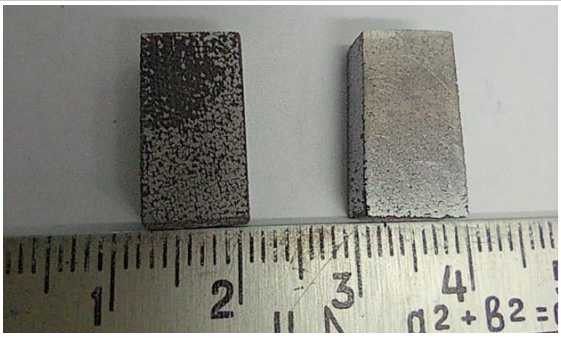

Fig.9. Samples of alloys D16_(N+X)_X and D16_(N+X)_X_U12 after exposure to the test solution for the control time. On the left is sample D16_(N+X)_X. On the right is sample D16_(N+X)_X_U12.

Micrographs at 160x magnification (Fig. 10) showed that the corrosion process created narrow zones of continuous damage between undamaged areas. The total area of the surface damaged by corrosion is 23% of the total surface area (Figure 10, a), which is 2.3 times less than the area of corrosion damage on the surface covered with chromium nitride and not subjected to ozonation. At a magnification of 160, a pattern of surface corrosion damage similar to that of chromium-nitrogen layer corrosion is observed, but the width of the damaged areas is significantly smaller. Thus, a decrease in damage to the micro- and macrostructure of the surface of D16 alloy samples coated sequentially with a layer of chromium nitride and a layer of chromium was observed when these samples were placed in the test solution. That is, additional spraying of a 0.5-micron-thick chromium layer onto the D16_(N+X) sample increases the corrosion resistance of D16 samples with a pre-applied chromium-nitrogen coating by 1.65 times (by 40%). At the same time, the final surface hardness of the D16_(N+X)_X samples is 1.57 times greater than HV=236 (36% greater) than the surface hardness of the D16 alloy samples HV=150. Also, the surface hardness of D16_(N+X)_X samples is 3 times greater (by 200%) than the surface hardness of D16_X.

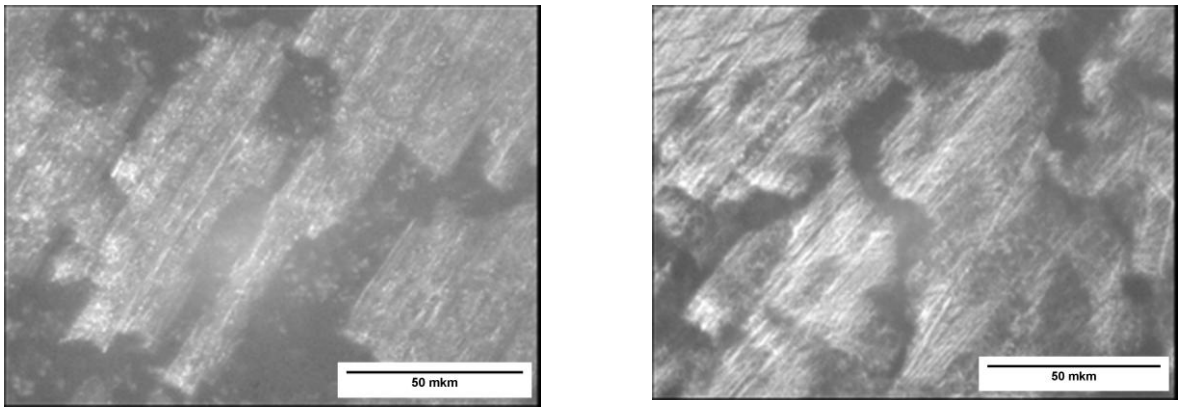

a) b)

Fig.10. Micrographs of the surface of samples D16_(N+X) _X and D16_(N+X)_X_U12 after exposure to the test solution for the control time. a) CD16_(N+X)_X; b) D16_(N+X)_X_U12. Magnification 160.

Based on the results of our experiments, we can conclude that in order to create an anti-corrosion coating of chromium with high surface hardness, it is necessary to place a layer of a substance with high hardness between the surface of the D16 alloy product and the top layer of chromium. The surface structure is as follows:

1) the bottom layer of D16 alloy with a hardness of HV=150;

2) the second layer of a substance with high hardness, in our case a layer of chromium nitride with a hardness of HV=655;

3) the third layer of chromium applied over the chromium nitride layer to protect the chromium nitride layer from corrosion. The final surface hardness is HV=240.

Products made of D16 alloy, coated sequentially with layers of chromium nitride and chromium (D16_(N+X)_X), can be used in atmospheres containing abrasive particles and atmospheres containing halogen ions, for example in seaports.

Considering that the AOS surface treatment of D16_X samples resulted in a significant increase in corrosion resistance (Table 3), the surface of D16_(N+X)_X samples was also treated with AOS for 12 hours. As a result of surface oxidation, an increase in the hardness of the D16_(N+X)_X coating to HV= 350 was recorded, and the hardness under low loads increased by 1.47 times.

However, a significant increase in surface brittleness was also observed: under loads exceeding 50 grams, cracks formed around the indentation zone. This fact prevents the use of this coating in cases of high loads, but does not prevent its use in atmospheres containing abrasive particles, such as sand particles in the desert.

Corrosion resistance testing showed a significant reduction in the corrosion process of D16 alloy samples coated with chromium nitride plus pure chromium, subjected to prolonged exposure to active forms of oxygen (12 hours): samples D16_(N+X)_X_U12. A mass loss of 1.86% was recorded for the sample as a result of exposure to the test solution during the control test. Before oxidation, there was a 2.49% loss in the surface mass of the D16_(N+X)_X samples (Table 3). That is, additional oxidation of the surface of the D16_(N+X)_X samples increased the corrosion resistance of the surface by 1.34 times (by 25%).

Visually, after the control time in the test solution, a small amount of fine pitting is present on the surface of sample D16_(N+X) _X_U12 (Figure 9, b). The colour of the sample surface has not changed, and no reddish tint has appeared. Outside the corrosion pits, the microstructure of the surface of sample D16_(N+X)_X_U12 did not change (Figure 10, b). The total area of corrosion damage on sample D16_(N+X)_X_U12 is no more than 12% of the total study area, which is 1.92 times less than the area of corrosion damage on the surface of D16_(N+X)_X. Compared to the surface of sample D16_(N+X)_X, the total area of affected areas on the oxidized surface of sample D16_(N+X)_X_U12 decreased by 48%.

In summary, the following conclusions can be drawn:

1. As a result of treating the surface of D16_(N+X)_X samples with air exposed to UV radiation, the surface hardness increased from HV=236 to HV=350 (1.48 times).

2. The corrosion resistance of the surface of samples D16_(N+X)_X as a result of AOS treatment increased by 1.34 times. The total area of corrosion damage as a result of surface treatment decreased by 1.7 times.

4. Conclusions

In summary, the following conclusions can be drawn:

1. Films of chromium and chromium nitride deposited by cathodic sputtering onto the surface of a D16 alloy specimen form a smooth, uniform surface with good adhesion to the D16 alloy surface. These films are free from cracks.

2. Spraying a layer of chromium onto the surface of alloy D16 significantly increases the corrosion resistance of the surface (by 39%), but at the same time significantly reduces the hardness of the surface (by 46%). The D16_X coating cannot be used in conditions where there are abrasive particles in the space surrounding the product. This D16_X, D16_X_U12 coating is acceptable for use in sea fog conditions.

3. Spraying a layer of chromium nitride onto the surface of the D16 alloy greatly increases the surface hardness – 4.3 times that of the D16 alloy surface.

At the same time, the corrosion resistance of the surface is significantly reduced (by 35%). Products with a D16_(N+X) chromium nitride coating cannot be used in sea fog conditions, but can be used in sandy desert conditions.

4. Treating the sputtered chromium nitride layer with air exposed to ultraviolet radiation significantly increases hardness by 41% and corrosion resistance by 62% compared to the untreated chromium nitride layer. These D16_(N+X)_U12 products are suitable for use in sea fog conditions and in the presence of abrasive particles in the atmosphere.

5. It was found that in order to increase the hardness of the chrome-coated surface, it is necessary to place a layer of a substance with very high hardness, for example, a layer of chromium nitride with a hardness of HV=655, between the surface of the D16 alloy and the chrome layer. This will increase the hardness of the surface layer of chrome by 3 times, from HV=80 to HV=236.

6. A layer of chrome sprayed over a layer of chromium nitride reduces the corrosion rate of the product D16_(N+X) by 38%.

7. Treating the chrome layer applied to the surface of the chromium nitride with air exposed to UV radiation increases the hardness of the top chrome layer by 32% to HV=350. Oxidation of the chrome surface also increases the corrosion resistance of the chrome layer by 25%.

8. In marine climates and in the presence of strong winds, it is recommended to use D16_(N+X) _X_U12 products made of D16 alloy, coated with a layer of chromium nitride, on top of which there is a layer of additionally oxidized chromium.

Conflict of interest statement

The authors declare that they have no conflict of interest in relation to this research, whether financial, personal, authorship or otherwise, that could affect the research and its results presented in this paper.

CRediT author statement

Guchenko S.A.: investigation, writing - original draft; **Seldyugaev O.B.:** conceptualization, writing - review & editing; **Karstina S.G.:** investigation, writing - review & editing; **Danilov M.B.:** investigation, formal analysis; **Afanasyev D.A.:** visualization, writing - review & editing. The final manuscript was read and approved by all authors.

Statement on the use of Artificial Intelligence.

The authors declare that no artificial intelligence tools were used to generate scientific content, results, or conclusions of this article.

Data Availability Statement

The data that support the findings of this article are openly available.

Acknowledgements

The authors are grateful to Tuleuov S.D. for assistance in preparing the article.

References

1 Yelwa, J.M., Musa, H., Fasanya, O.O., Yahaya, J.Y. (2025). Corrosion-resistant coatings: advances in deposition methods, nanostructures, and self-healing films. *Academia Mat. Science*, 2, 1-30. https://doi.org/10.20935/AcadMatSci7829

2 Sun, S., Zheng, Q., Li, D., Wen, J. (2009). Long-Term Atmospheric Corrosion Behaviour of Aluminum Alloys 2024 and 7075 in Urban, Coastal, and Industrial Environments. *Corrosion Science*, 51, 719–727. https://doi.org/10.1016/j.corsci.2009.01.016

3 Yanin, E.P. (2020). *Corrosion as a Source of Environmental Pollution.* Moscow, 112 p. [In Russia] Available at: http://intranet.geokhi.ru/DocLib5/publications/1_Yanin_Korrozia.pdf

4 Zhang, S.X., Wang, Y.A., Li, S.Y., Wang, Z.F., Chen, H.C., Yi, L., Chen, X., Yang, Q.H., Xu, W.W., Wang, A.Y. (2023). Concerning the stability of seawater electrolysis: a corrosion mechanism study of halide on Ni-based anode. *Nat. Com*., 14, 1, 4822. https://doi.org/10.1038/s41467-023-40563-9

5 Umoren, S.A., Solomon, M.M. (2015). Effect of halide ions on the corrosion inhibition efficiency of different organic species - A review. *J. of Industrial and Engineering Chem*., 21, 81-100. https://doi.org/10.1016/j.jiec.2014.09.033

6 Rao, M.S., Nayeem, S., Kiran, N.V.S.G.S., Gowthami, K., Krishnaraj, J. (2024). An examination and characterization study of the aluminum alloy Duralumin (AA2014). *J. of Physics: Conf. Series*, 2837, 1, 012086-012086. https://doi.org/10.1088/1742-6596/2837/1/012086

7 GOST 4784-2019. Aluminium and wrought aluminium alloys. Grades (State Standard 4784-2019.). Publishing House of Standards, Moscow. Available at: https://files.stroyinf.ru/Data2/1/4293728/4293728395.pdf?ysclid=m2sxpac9co349327183

8 Sun, Yi., Grebenikov, O.G., Li, Ch. (2021). Analysis of Force Distribution of Four Rows of Bolts in Aircraft Fitting. *Int. J. of Aerospace Eng.,* 9962645. https://doi.org/10.1155/2021/9962645

9 Shveikin, V.P., Kamantsev, I.S., Pugacheva, N.B., Zadvorkin, S.M., Senaeva, E.I., Razinkin, A.V., Maltseva, T.V., Kalinina, N.A., Bykova, T.M., Skorynina, P.A., Putilova, E.A. (2023). Application of microindentation to the evaluation of strain distribution over the section of extruded aluminum alloy bars. *Diagnostics, Resource and Mechanics of materials and structures*, 6, 45-64. https://doi.org/10.17804/2410-9908.2023.6.045-064

10 Guchenko, S.A., Seldyugaev, O.B., Fomin, V.N., Afanasyev, D.A. (2025). Prediction of corrosion resistance of magnalias. *Eurasian phys. tech. j.,* 22, 2 (52), 97-108. https://doi.org/10.31489/2025N2/97-108

11 Yurov, V.M., Goncharenko, V.I., Oleshko, V.S., Ryapukhin, A.V. (2023). Calculating the Surface Layer Thickness and Surface Energy of Aircraft Materials. *Inventions*, 8, 3, 66. https://doi.org/10.3390/inventions8030066

12 Prigunova, A., Neduzhyi, A. (2022). Structural aluminum alloys of the Al−Cu−Mg and Al−Zn−Mg−Cu systems in aircraft construction. Review. *Casting processes,* 151, 54-73. https://doi.org/10.15407/plit2023.01.054

13 Panchenko, Yu.M., Strekalov, P.V., Chesnokov, D.V., Zhirnov, A.D., Zhilikov, V.P., Karimova, S.A., Tararaeva, T.I. (2010). Dependence of D16 alloy corrosion resistance on salinity and meteorological parameters of the coastal atmosphere. *Aviation Materials and Technologies*, No. 3 (16). Available at:

https://cyberleninka.ru/article/n/zavisimost-korrozionnoy-stoykosti-splava-d16-ot-zasolennosti-i-meteoparametrov-viewer

14 Kozlova, A.A., Kondrashov, E.K., Deev, I.S. (2016). Protective properties of paint and lacquer coatings based on a fluorine-containing film-forming material. *Protection of Metals and Phys. Chem. of Surfaces*, 52(7), 1181-1186. https://doi.org/10.1134/S207020511607011X

15 Gnedenkov, A.S., Sinebryukhov, S.L., Marchenko, V.S., Nomerovskii, A.D., Ustinov, A.Yu., Fattah-alhosseini, A., Gnedenkov, S.V. (2025). Efficient and smart hybrid coatings for active corrosion protection of magnesium alloys. *J. of Magnesium and Alloys*, 13, 9, 4475-4499. https://doi.org/10.1016/j.jma.2025.07.017

16 Semin, V., Cherkasov, A., Savkin, K., Shandrikov, M., Khabibova, E. (2025). Corrosion Performance of Chemically Passivated and Ion Beam-Treated Austenitic-Martensitic Steel in the Marine Environment. *J. Manuf. Mater. Process*, 9, 5, 167. https://doi.org/10.3390/jmmp9050167

17 Berdibekov, A.T., Laurinas, V.Ch., Dolya, A.V., Gruzin, V.V., Guchenko, S.A., Baltabekov, A.S. (2023). Possibility of using inexpensive steel protected by deposited vacuum-arc coatings as a basis for parts and tools coating technology. *Bull. Karaganda Univ. Ser.: Phys.*, 4(112), 91–95. https://doi.org/10.31489/2023ph4/91-95

18 Guchenko, S.A. (2012). Production, structure, and properties of multiphase ion-plasma coatings. *Bull. Karaganda Univ. Ser.: Phys.*, 4(68), 12–25. https://phs.buketov.edu.kz/apart/srch/2012_physics_4_68_2012.pdf

19 Baikenov, M.I., Seldyugaev, O.B., Guchenko, S.A., Afanasyev, D.A. (2024). Reason of pitting corrosion of martensitic steel in sea water. *Eurasian phys. tech. j.,* 21, 1(47), 38-48. https://doi.org/10.31489/2024No1/38-48

20 Grudinin, V.A., Bleykher, G.A., Sidelev, D.V. (2022). Magnetron deposition of chromium nitride coatings using a hot chromium target: Influence of magnetron power on the deposition rate and elemental composition. *Surface and Coatings Technology*, 433, 128120(11). https://doi.org/10.1016/j.surfcoat.2022.128120

AUTHORS' INFORMATION

Guchenko, S.A. – Master (Sci.), Research Fellow, Buketov Karaganda National Research University, Karaganda, Kazakhstan; https://orcid.org/0000-0002-9954-5478; guchen@mail.ru

Seldyugaev, O.B. – Candidate of chemical sciences, Junior Research Fellow, Buketov Karaganda National Research University, Karaganda, Kazakhstan; https://orcid.org/0009-0004-9729-1015; oleg.seldyugaev@gmail.com

Karstina, S.G. – Doctor of Physical and Mathematical Sciences, Professor, Buketov Karaganda National Research University, Karaganda, Kazakhstan; https://orcid.org/0000-0001-8425-681X; skarstina@mail.ru

Danilov, M.B. – B.(Mech.Eng.), Workshop chief, LLP «Astaldo», Karaganda, Kazakhstan; Mishadanilov92@gmail.com; https://orcid.org/0009-0005-9201-8404

Afanasyev, D.A. – Ph.D, Professor, Buketov Karaganda National Research University, Karaganda, Kazakhstan; https://orcid.org/0000-0002-0437-5315; a.d.afanasyev2@gmail.com

EURASIAN PHYSICAL TECHNICAL JOURNAL

2026, Volume 23, No.2 (56)

https://doi.org/10.31489/2026N2/35-46

Received: 12/015/2025 Revised: 29/04/2026 Accepted: 26/06/2026 Published online: 30/06/2026

Original Research Article

UDC 533.0.01; 621.548.5

ANALYSIS OF AERODYNAMICS OF AN ASYMMETRIC DARRIEUS WIND TURBINE WITH THREE-BLADES

Manatbayev R.[1], Kalassov N.[1], Seydulla Zh.[1], Isataev M.[1], Baizhuma Zh.[1], Kuykabayeva A.[1], Rasul K.[1]*

Al-Farabi Kazakh National University, Almaty, Kazakhstan
*Corresponding author: kozhash@list.ru

Abstract. *This paper presents a comprehensive numerical investigation of the aerodynamic performance of a three-bladed vertical-axis Darrieus wind turbine equipped with asymmetric airfoil blades, with the primary aim of evaluating the influence of blade geometry on torque generation and overall aerodynamic efficiency. The study focuses on a detailed analysis of rotor flow behavior, including the spatial distributions of velocity and pressure fields, the formation and evolution of flow separation zones, and the development of a turbulent wake structure downstream of the rotor over a wide range of operating conditions. Numerical simulations were carried out using the Reynolds-Averaged Navier–Stokes equations coupled with the k–ω SST turbulence model, which provides reliable prediction of near-wall flow behavior, adverse pressure gradients, and unsteady aerodynamic effects typical for vertical-axis wind turbines. The obtained results demonstrate that the asymmetric blade profiles interact more effectively with the incoming airflow at moderate tip speed ratio values, leading to improved torque characteristics and a noticeable reduction in negative torque regions. In particular, the maximum average torque coefficient was observed at tip speed ratio values close to 2.5, where the aerodynamic performance of the rotor reached its optimum due to balanced lift and drag forces acting on the blades. At higher tip speed ratio values, despite the stabilization of the flow structure and reduction of large-scale vortical formations, a decrease in aerodynamic efficiency was identified, and the findings of this study provide a scientific basis for optimizing blade geometry and selecting efficient operating regimes in the design of Darrieus-type vertical-axis wind turbines with asymmetric airfoils.*

Keywords: Vertical-axis wind turbine; Darrieus rotor; asymmetric airfoil; aerodynamic performance; torque coefficient; tip speed ratio.

1. Introduction

Increasing global warming and growing concerns about environmental degradation are prompting many countries to reduce their dependence on fossil fuels and transition to clean energy sources. Wind energy holds a special place among renewable energy sources due to its abundant reserves, inexhaustible nature, and low environmental impact. Modern scientific research in this field demonstrates that wind energy has high potential to complement or replace traditional energy sources. Wind turbines are the primary technical devices for the efficient use of wind energy. A wind turbine is a complex engineering system designed to convert the kinetic energy of atmospheric airflow into mechanical energy and then into electrical energy [1]. Its operating principle is based on the coordinated control of aerodynamic forces and energy conversion processes, which determines the overall efficiency and energy productivity of the system. Depending on their axis of rotation, wind turbines can be divided into horizontal-axis wind turbines (HAWT) and vertical-axis wind turbines (VAWT) [2]. Horizontal-axis wind turbines (HAWT) are currently the most widely used wind turbines in large

wind farms due to their high efficiency [3]. However, vertical-axis wind turbines (VAWT) have distinct advantages. They are particularly suitable for use in turbulent or urban environments. Vertical-axis wind turbines (VAWTs) have not yet been fully studied [4]. This is mainly due to the fact that the aerodynamic characteristics of vertical-axis wind turbines are more complex than those of horizontal-axis wind turbines. However, VAWT offer unique advantages, including ease of design and maintenance [5], the ability to operate in any wind direction without the need for expensive turning mechanisms [6], low noise levels, and suitability for installation in urban areas [7, 8]. Recent recognition of the structural and aerodynamic advantages of vertical-axis wind turbines has led to a revival of this trend and the need for extensive scientific research [9-11]. One of the key elements determining the efficiency of the Darie wind turbine is the blade profile. Symmetrical and asymmetrical profiles are used in design practice, each with its own advantages and disadvantages. Symmetrical blades have identical upper and lower surfaces, while asymmetrical blades have different upper and lower surfaces. Asymmetrical blades are more efficient than symmetrical ones in areas with low and variable wind speeds due to their high starting torque and self-starting capability. Asymmetrical blades have been extensively studied in recent years to improve the aerodynamic performance of vertical-axis wind turbines and offer several significant advantages over symmetrical profiles. Therefore, another effective solution for increasing the power of vertical-rotor wind turbines is the development of specialized airfoils for such turbines, as they can significantly impact wind energy efficiency and the flow field around the blade [12]. Asymmetric airfoils, characterized by a curved shape, improve the aerodynamic performance of wind turbines under various conditions. For example, [13] showed that by optimizing the angle of asymmetric blades, performance at low wind speeds can be significantly improved.

The growing interest in asymmetric blades is explained by their ability to control complex flow processes. Asymmetric geometry balances aerodynamic loads during the positive and negative half-periods of the rotor, preventing flow interruption or stall. At the same time, such modifications can improve the maximum power factor (Cp) of the rotor not only at medium speeds but also in low- tip speed ratio (TSR) regimes. For example, [14–15] demonstrated that an asymmetric blade profile not only improves self-starting performance compared to a symmetric blade profile but also increases (Cp) by up to 26.83%. This makes vertical-axis wind turbines suitable for regions with low wind speeds, thereby expanding their application range.

Asymmetric and modified blades for vertical-axis Darrieus wind turbines have been shown to improve aerodynamic efficiency in low-TSR regimes [16–19]. Experimental and numerical analyses confirm that blade geometry directly influences the formation of pressure, velocity, and torque fields. These results support the relevance of in-depth numerical studies of asymmetric blades.

Thus, the literature review demonstrates that the use of asymmetric blades can significantly improve the aerodynamic performance of vertical-axis Darrieus wind turbines.

2. Methodology

2.1 Model geometry

Figure 1 shows the geometric model of an asymmetric three-bladed Darrieus wind turbine. In this study, the aerodynamic characteristics of an asymmetric three-bladed Darrieus vertical-axis wind turbine were analyzed using numerical simulation methods. The primary objective of the study was to evaluate the impact of asymmetric blade geometry on rotor performance and determine the aerodynamic efficiency under various operating conditions.

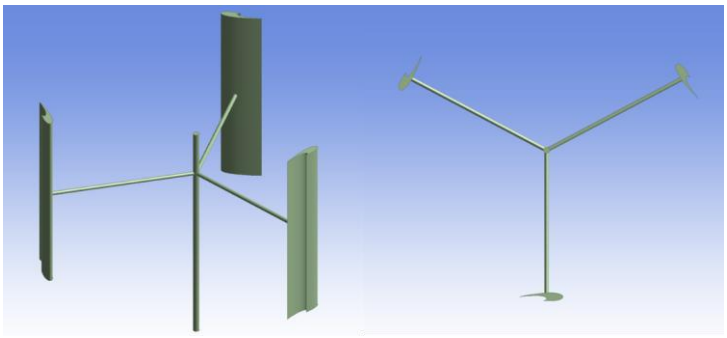

Fig.1. Asymmetric three-bladed Darrieus wind turbine.

The object of the study was an asymmetric configuration of a three-bladed Darrieus rotor. The blade shape was achieved by modifying the aerodynamic profiles to improve the interaction of the rotor with the wind flow at different phases. Table 1 shows the geometric parameters of the vertical-axis Darrieus turbine; this data is taken from the article [20]. As shown in Figure 2, a rectangle and a cylinder were chosen as the computational domain. We consider the rectangle as a stationary domain, and the cylinder as a moving domain. This approach allowed us to accurately represent the flow around the rotor and the interaction of the airflow with its blades. Table 2 shows the geometric parameters of the computational domain, taken from [20].

Table 1. Geometrical parameters of the vertical-axis Darrieus turbine.

Parameter	Mean
Aerodynamic profile	NACA 0021
Number of blades (N)	3
Chord length (C)	0,04 m
Rotor diameter (D)	3 m
Relative density of the turbine (σ)	0,3

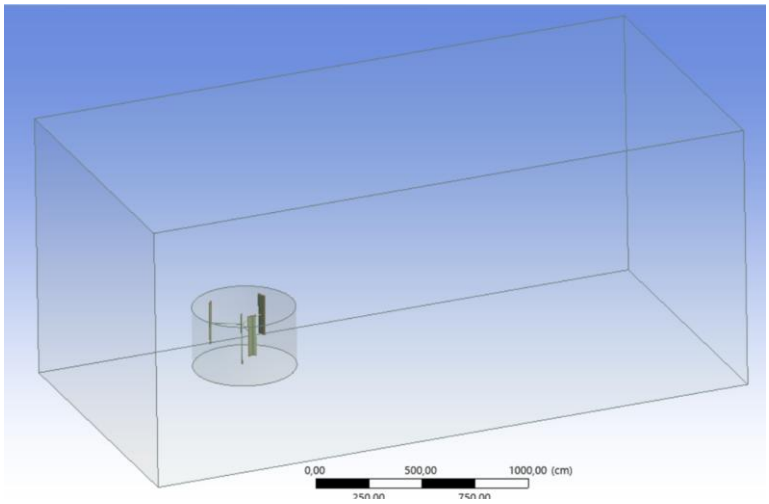

Fig.2. Computational domain of an asymmetric three-bladed Darrieus wind turbine.

Table 2. Geometric parameters of the computational domain for modeling the aerodynamics of an asymmetric three-bladed Darrieus wind turbine.

Parameter	Mean
Rotor diameter	D
Moving domain diameter	1,5D
Distance from the rotor center to the left border	20D
Distance from the rotor center to the right border	40D
Distance from the rotor center to the upper and lower boundaries	10D

One way to improve the Darrieus rotor is to introduce controlled geometric asymmetry into the blade configuration. Geometric modification improves the aerodynamic interaction of the blade with the airflow, expands the range of operating angles of attack, and increases torque stability. This study proposes the design of a three-bladed asymmetric Darrieus wind turbine, where the asymmetry is formed based on a combination of NACA0021 airfoils [21–24]. By trimming the main airfoil to a smaller airfoil, we obtain a modified NACA0021 blade, shown in Fig3.

This approach allows for the redistribution of loads along the arc of rotation, altering the blade's thickness, surface area, and local aerodynamic curvature. This improves the lift-to-drag ratio, potentially increasing the rotor's power factor. Furthermore, the proposed geometric design reduces vibration loads and torque fluctuations, a crucial factor for low-power vertical-axis wind turbines.

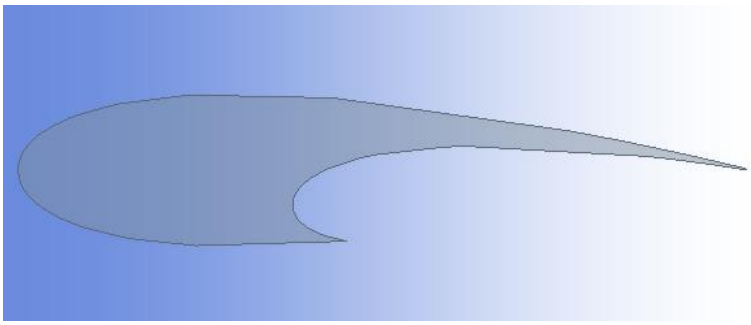

Fig.3. Asymmetrical blade NACA 0021

To provide a quantitative description of the blade geometry and to improve the reproducibility of the numerical model, the coordinate data of the NACA 0021 profile were analyzed. The chord length in the coordinate file is equal to 400 coordinate units and was scaled to the chord length used in the numerical model, C = 0.04 m. The maximum profile thickness obtained from the coordinates is tmax/C = 0.2100, which corresponds to the NACA 0021 airfoil. The maximum thickness is located at xt/C = 0.3014. The main geometrical parameters extracted from the coordinate data are presented in Table 3.

Table 3. Geometrical parameters of the blade profile based on the coordinate data.

Parameter	**Symbol**	**Value**
Initial aerodynamic profile	—	NACA 0021
Chord length	C	0.04 m
Chord length in coordinate data	Ccoord	400
Maximum upper-surface ordinate	ymax/C	0.1050
Maximum lower-surface ordinate	ymin/C	−0.1050
Maximum profile thickness	tmax/C	0.2100
Maximum profile thickness	tmax	0.0084 m
Position of maximum thickness	xt/C	0.3014
Leading-edge coordinate	x/C; y/C	0; 0
Trailing-edge coordinate	x/C; y/C	1; 0
Trailing-edge thickness	δTE/C	0
Number of coordinate points	Np	201

2.2 Basic Equations

Dimensionless aerodynamic parameters such as the power coefficient (Cp), torque coefficient (Cm), lift coefficient (Cl), and drag coefficient (Cd) are used to quantify the aerodynamic performance of a wind turbine. These coefficients allow one to determine the turbine's energy efficiency and compare the obtained calculation results. The actual power (P) extracted by the turbine from the flow is determined by the ratio of its theoretical maximum power (P_a), and the power coefficient is given by the following expression:

$$C_P = \frac{P}{\frac{1}{2}\rho A V^3} \quad (1)$$

where ρ – air density (kg/m³), A – rotor projection area (m²), and V – wind speed at the inlet (m/s).

The power generated by a turbine is determined by the product of torque (T) and angular velocity (ω):

$$P = T \cdot \omega \quad (2)$$

Using this relationship, the power factor can be expressed in terms of torque characteristics:

$$C_P = \frac{T \cdot \omega}{\frac{1}{2}\rho A V^3} \quad (3)$$

The torque coefficient (Cm) is determined by the following formula:

$$C_M = \frac{T}{\frac{1}{2}\rho A R V^3} \quad (4)$$

where R – rotor radius (m).

The relationship between Cp and Cm is defined as follows:

$$C_P = C_M \cdot \lambda \quad (5)$$

where $\lambda = \frac{\omega R}{V}$ – blade TSR.

The physical model of flow near a blade surface is based on the laws of conservation of mass, momentum, and energy. For incompressible and isothermal airflow, these processes are described by the Navier-Stokes equations:

$$\nabla \cdot u = 0 \quad (6)$$

$$\frac{\partial u}{\partial t} + (u \cdot \nabla)u = -\frac{1}{\rho}\nabla p + \nu \nabla^2 u + f \quad (7)$$

where u – flow velocity vector, p – pressure, ρ – air density, v – kinematic viscosity, f – mass forces. Here, f is the body force term. In this study, body forces were neglected due to their insignificant influence on the considered incompressible and isothermal airflow; therefore, f = 0 was used in the numerical simulations.

Because direct numerical modeling (DNS) is computationally expensive for high-Reynolds number flows, Reynolds-averaged Navier-Stokes (RANS) equations are used in engineering calculations. Averaging leads to turbulent Reynolds stresses, so a turbulence model must be introduced to describe the system. The averaged continuity equation is:

$$\frac{\partial \overline{u_i}}{\partial x_i} = 0 \quad (8)$$

The average momentum equation is:

$$\frac{\partial \overline{u_i}}{\partial t} + \overline{u_j}\frac{\partial \overline{u_j}}{\partial x_j} = -\frac{1}{\rho}\frac{\partial \overline{p}}{\partial x_i} + \nu \frac{\partial^2 \overline{u_i}}{\partial x_j^2} - \frac{\partial \tau_{ij}}{\partial x_j} \quad (9)$$

where $\overline{u_i}$ – average flow rate, $\tau_{ij} = \overline{u_i' u_j'}$ – Reynolds tensor of turbulent stresses.

To fully capture the system, the k-ω SST turbulence model, widely used in engineering aerodynamics, was chosen. This model allows for synergy with the k-ε model in the free-flow zone while maintaining accuracy in high-gradient regions. The model consists of two main auxiliary equations: the turbulent kinetic energy (k) and the specific dissipation rate (ω):

$$\frac{\partial(\rho k)}{\partial t} + \frac{\partial(\rho u_j k)}{\partial x_j} = P_k - \beta^* \rho \omega k + \frac{\partial}{\partial x_j}\left[(\mu + \sigma_k \mu_t)\frac{\partial k}{\partial x_j}\right] \quad (10)$$

$$\frac{\partial(\rho \omega)}{\partial t} + \frac{\partial(\rho u_j \omega)}{\partial x_j} = \gamma \frac{\omega}{k} P_k - \beta \rho \omega^2 + \frac{\partial}{\partial x_j}\left[(\mu + \sigma_\omega \mu_t)\frac{\partial \omega}{\partial x_j}\right] + 2(1 - F_1)\rho \sigma_{\omega 2}\frac{1}{\omega}\frac{\partial k}{\partial x_j}\frac{\partial \omega}{\partial x_j} \quad (11)$$

where ρ – density, k – turbulent kinetic energy, P_k – a source of turbulent energy caused by a change in velocity, β^*, γ, β – empirical constants, ω – specific dissipation rate, μ – dynamic viscosity, μ – turbulent viscosity, σ_k – diffusion coefficient for k.

The system of governing equations (6)–(11) was solved using the finite volume method. A transient pressure-based solver was applied to describe the unsteady aerodynamic interaction between the rotating blades and the airflow. Pressure–velocity coupling was performed using the SIMPLE algorithm. The pressure equation was discretized using a second-order scheme, while the convective terms in the momentum and turbulence equations were approximated by a second-order upwind scheme. The transient terms were discretized using a second-order implicit formulation. The gradients were calculated using the least-squares cell-based method. The convergence criterion for the residuals of the governing equations was set to 10^{-5}, and

the torque coefficient was additionally monitored until a periodic solution was obtained over several complete rotor revolutions.

The computational domain consisted of an inner rotating cylindrical region and an outer stationary rectangular region. The rotating region contained the three-bladed rotor, and its angular velocity was prescribed according to the selected TSR value. The outer region remained stationary and represented the far-field flow with specified inlet, outlet, and side boundary conditions. The RANS equations with the k–ω SST turbulence model were solved in both regions using the finite volume method. The interaction between the rotating and stationary domains was implemented through a sliding mesh interface, where pressure, velocity, and turbulence quantities were exchanged at each time step.

2.3 Mesh generation

In this study, a multi-layer hybrid mesh was used to accurately calculate the aerodynamic characteristics of a wind turbine. The mesh structure is designed to accurately represent the boundary layer near the blade, vortex shedding regions, and complex flow fields around the rotor. The images below illustrate the mesh features in various regions.

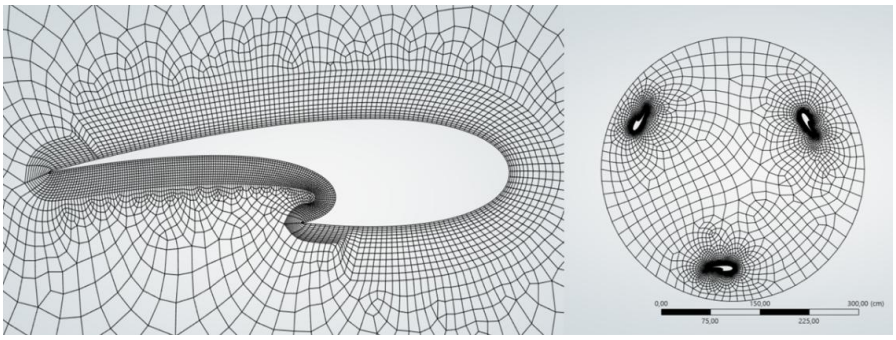

Fig.4. Mesh near the NACA0021 asymmetric blade

The mesh shown in Figure 4 is a multi-block hybrid structure designed to accurately discretize the flow region near a blade airfoil. In the region close to the blade surface, prismatic elements with 15–25 layers are used to accurately describe the boundary layer, ensuring the condition $y^+ \approx 1–5$, while the mesh is significantly denser to correctly account for sharp changes in pressure gradients at the leading and trailing edges. As the distance from the blade increases, the element sizes gradually increase in accordance with geometric patterns, improving the computational efficiency of the entire domain. While the structured regions of the mesh accurately capture the complex geometry of the airfoil, the free-form elements in the outer regions do not disrupt the natural flow distribution. Overall, this mesh enables highly accurate computation of turbulent flow–especially vortex structures at the blade tip and separation zones at the rear.

The mesh configuration in Figure 5 is designed to discretize the entire flow domain of a vertical-axis Darrieus wind turbine and accurately model aerodynamic phenomena around a rotor with complex geometry. The three-dimensional mesh of the rectangular computational domain (left figure) is formed using mesh densification near the rotor to accurately determine vortex structures, flow separation, and low-pressure zones in the rotor region.

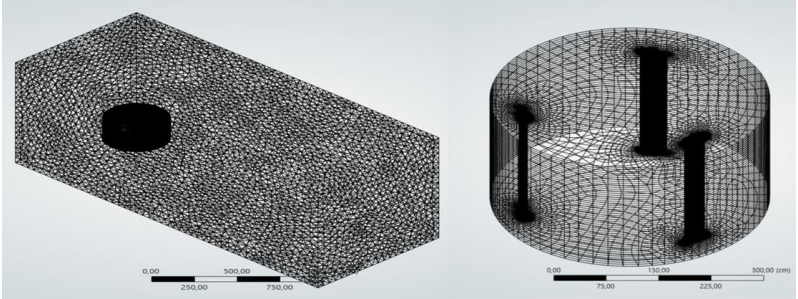

Fig.5. Grid of computational domains for an asymmetric three-bladed Darrieus wind turbine.

In distant regions, element sizes gradually increase, reducing the overall computational load. In regions close to the cylindrical rotor body located in the center, triangular-tetrahedral meshes ensure a natural flow distribution along the complex geometry. The mesh of the three-bladed rotor, located within the cylindrical region shown in the figure on the right, is based on a multi-block structured system. To accurately model the boundary layer near each blade, concentric layers are formed in the radial direction, and the mesh is particularly fine in the high-gradient regions near the blade tips. The cylindrical outer boundary ensures constant flow conditions at the outlet and inlet, while maintaining the geometric consistency of the mesh. Overall, the mesh quality enables highly accurate calculations of flow variations.

2.4 Grid and time-step independence analysis

To ensure the stability and reliability of the obtained numerical results, a convergence analysis of the numerical solution was carried out during the CFD simulations. During the calculations, the residuals of the governing equations were monitored, and the stabilization of the main aerodynamic parameters, including the torque coefficient (Cm), was analyzed over several complete rotor revolutions. In addition, a grid independence study was performed to evaluate the influence of mesh resolution on the calculated aerodynamic characteristics.

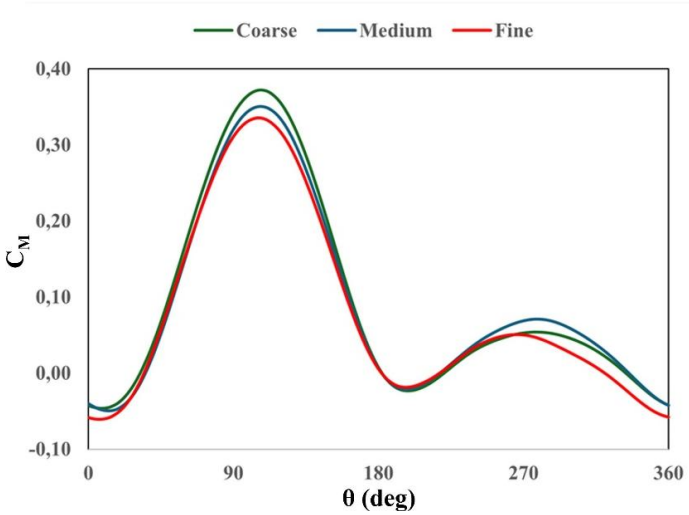

Fig.6. Mesh sensitivity analysis.

Three mesh levels, namely coarse, medium, and fine, were considered, as shown in Table 4. The comparison was performed for the representative operating condition TSR = 2.5, where the rotor demonstrates the highest positive torque coefficient and the maximum average useful torque. The average torque coefficient and power coefficient were selected as the main convergence criteria.

Table 4. Grid convergence analysis

Mesh type	Number of elements	Type of elements	First layer thickness	y^+
Coarse	486,325	Predominantly triangular elements	5×10^{-4} m	6.8
Medium	1,204,786	Hybrid mesh (quadrilateral + triangular elements)	10^{-5} m	0.85
Fine	2,148,532	Fine hybrid mesh with quadrilateral refinement	10^{-6} m	0.12

3. Results and discussion

As the rotor rotates, the blade's angle of attack constantly changes, which in turn directly affects the pressure distribution and the formation of flow lines on the blade surface. While pressure contours indicate the location of high and low pressure regions, flow lines visually describe the overall flow dynamics. The configuration and location of these regions constantly change as the rotor rotates, so it is important to analyze changes in the pressure field and flow structure at different rotation angles.

In this regard, the study comprehensively examined pressure changes and flow structure reorganization at various rotor azimuthal positions. This analysis allows us to determine the characteristics of airflow-blade interactions and assess the impact of the angle of attack on turbine aerodynamic performance. The results obtained provide the basis for a deeper understanding of time-dependent flow behavior during rotor operation and for analyzing the effectiveness of blade geometry.

3.1 Pressure contour

Figure 7 shows the numerical results of the pressure distribution for a three-bladed Darrieus rotor with a modified asymmetric profile. There are the static pressure contours for various TSR values for a three-blade Darrieus rotor with an asymmetric profile. At low TSR values (1.5–2.0), high-pressure zones are clearly visible on the leading edge of the blades, while low-pressure zones are visible on the trailing edge, indicating a high aerodynamic load on the rotor. As the TSR value increases (2.5–3.0), the pressure field somewhat equalizes, and the distribution of high- and low-pressure zones stabilizes. At high TSR values (3.5–5.0), the pressure gradient decreases, and a uniform flow distribution around the rotor is observed, indicating stabilization of aerodynamic interactions and a stable operating mode.

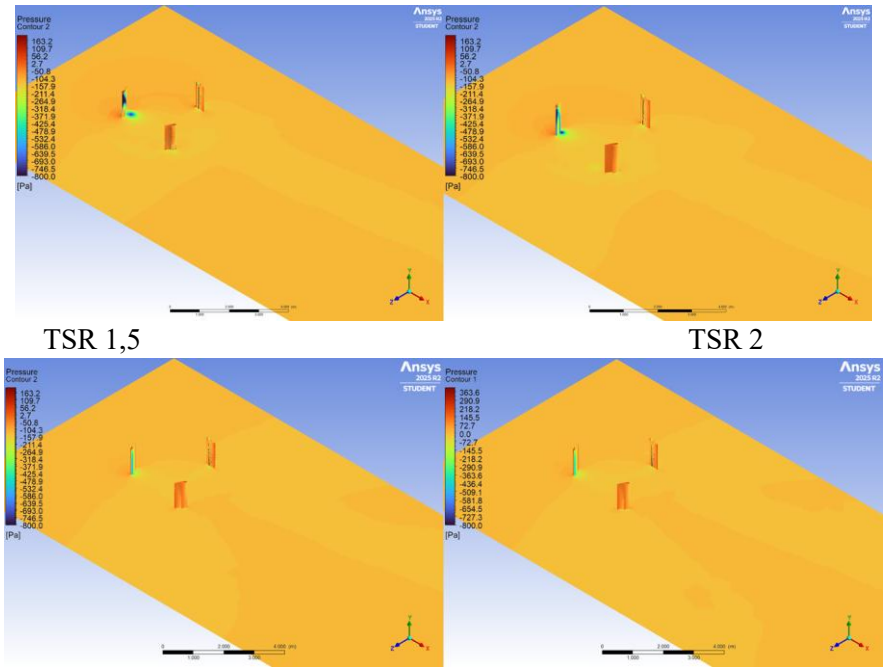

TSR 1,5 TSR 2

TSR 3,5 TSR 4

Fig.7. Contours of static pressure around an asymmetric 3-blade Darrieus rotor at different values of TSR.

3.2 Turbulent wake contour

Figure 8 shows the turbulent wake contours for a three-blade Darrieus rotor with an asymmetric airfoil at different TSR values. At low TSR values (1.5–2.0), distinct and irregular turbulent structures form behind the rotor, and a high level of vorticity is observed. As the TSR value increases (2.5–3.0), the turbulent wake lengthens, its structure becomes somewhat more regular, and energy losses are gradually distributed along the flow. At high TSR values (3.5–5.0), the turbulent wake intensity decreases, and the vortex amplitude decreases, indicating flow stabilization and improved rotor aerodynamic performance.

3.3 Change in torque coefficient at different TSR values per one complete revolution

Figure 9 shows a comparative dependence of the torque coefficient (Cm) on the azimuth angle (Θ) for a three-bladed Darrieus rotor with an asymmetric profile at TSR = 1.5–5.0. These results clearly illustrate the nature of the change in aerodynamic load and the differences in efficiency in different rotor operating modes.

At low and medium TSR values (TSR = 1.5–3.0), the Cm amplitude is significantly higher, and oscillations are clearly visible. Especially at TSR = 2.5, the highest positive torque coefficient values are recorded, and the influence of negative torque zones is weak. In this mode, the blade angle of attack is in the aerodynamically favorable range, and lift is generated efficiently. As a result, the average useful torque obtained from the rotor is maximum, characterizing the TSR = 2.5 mode as the most efficient operating zone.

Although positive Cm values predominate at TSR = 1.5 and TSR = 2.0, the presence of regions with oscillation amplitude and negative torque indicates a more frequent occurrence of flow separation. This situation reduces rotor stability and limits overall energy efficiency. In the high TSR region (TSR = 3.5–5.0), the Cm curves flatten out, and the oscillation amplitude decreases significantly.

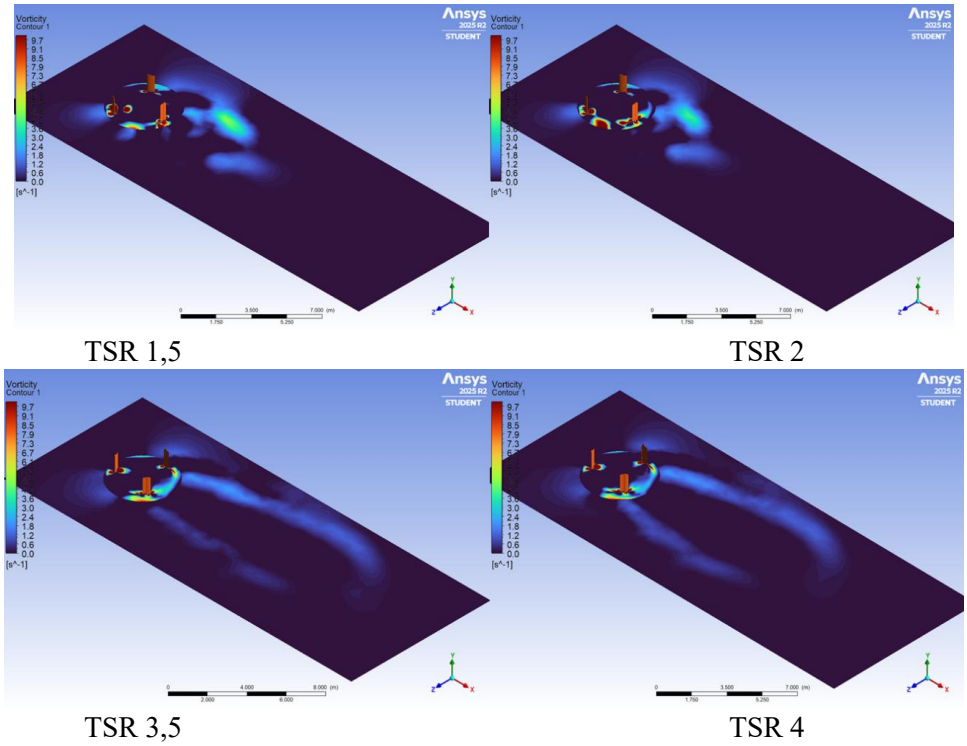

Fig.8. Turbulent wake contours generated by an asymmetric 3-blade Darrieus rotor at different TSR values.

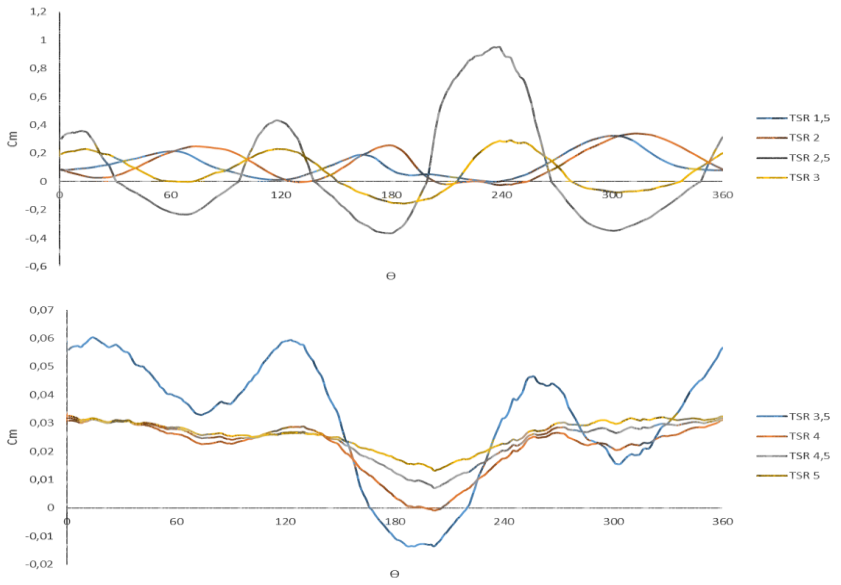

Fig.9. Variation of the torque coefficient Cm for asymmetric blades at full rotation at different values of TSR.

However, this stability is accompanied by a decrease in the average torque coefficient. At TSR = 3.5, a negative torque is observed in a certain azimuthal region (approximately 170–210°), indicating increased inertial and aerodynamic losses. In TSR = 4.0–5.0 regimes, although the negative torque regions weaken, the positive torque also remains low, which is explained by the inability of the blades to fully effectively extract energy from the flow.

A general comparative analysis revealed that the most favorable combination of torque coefficient and maximum average value is achieved in the TSR range of 2.5. This finding confirms the aerodynamic advantage of asymmetric blades in medium TSR modes and the limited optimal operating range for Darrieus-type vertical-axis wind turbines.

3.4 Power factor versus TSR

Figure 10 shows a comparison of the power factor Cp as a function of TSR for an asymmetric 3-blade wind turbine, where the experimental values are taken from the literature [25]. For the asymmetric blade (blue line), the power factor increases as TSR increases from 1.5 to the range of 2.0–2.2, reaching its maximum value around Cp ≈ 0.24–0.25. This range is the most efficient operating mode of the turbine. As TSR further increases (after 2.5), Cp gradually decreases. At TSR ≈ 4–5, the power factor decreases significantly, indicating an increase in aerodynamic losses. This phenomenon is explained by the flow disturbance in the blade, increased turbulence, and inefficiency of the rotation mode.

According to experimental data (red line), Cp starts at low values and steadily increases with increasing TSR. The maximum power factor is observed in the range of TSR ≈ 3.2–3.5, reaching Cp ≈ 0.28–0.29. This value indicates that the efficient operating mode is achieved at increasingly higher TSR values than the calculated maximum obtained for the asymmetric blade.

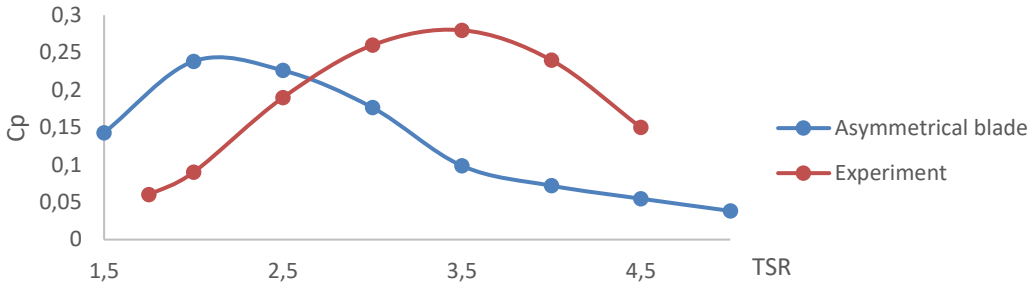

Fig.10. Power factor Cp versus TSR for an asymmetric 3-blade wind turbine.

It should be noted that the comparison between the experimental and numerical results is qualitative rather than a direct one-to-one validation, since the experimental data correspond to a turbine with a symmetric blade profile, whereas the present CFD results were obtained for a modified asymmetric blade. The discrepancy in the maximum Cp value and optimal TSR can be explained by differences in blade geometry, rotor scale, Reynolds number, three-dimensional flow effects, end losses, support elements, mechanical losses, and idealized CFD boundary conditions. Nevertheless, both curves show the same general trend: Cp increases with TSR up to an optimal range and then decreases due to aerodynamic losses, wake development, and flow separation. Therefore, the comparison confirms the physical consistency of the numerical results, while further experimental validation of the proposed asymmetric blade geometry is required.

4. Conclusion

This study, using numerical simulations and experimental data, conducted a comprehensive analysis of the aerodynamic and energy characteristics of a vertical-axis wind turbine with asymmetric blades. The results showed that the power factor (Cp) depends on the total speed ratio (TSR) and that blade geometry plays a decisive role in determining turbine efficiency.

An analysis of the power factor versus TSR curves showed that the highest efficiency of the asymmetric blade is observed at low and medium TSR values (approximately TSR ≈ 2.5). At this point, Cp reaches its maximum value, demonstrating the turbine's ability to efficiently generate power even at low rotational speeds. With further increases in TSR, Cp gradually decreases, which is associated with increased aerodynamic losses, flow disturbance zones, and turbulence levels at high rotational speeds.

According to experimental data, the maximum power factor is observed at higher TSR values (TSR ≈ 3–3.5), and the maximum Cp value is higher than that of the asymmetric computational model. This indicates the complexity of inertial effects, three-dimensional flow structures, and blade-flow interactions under real-world conditions. At the same time, this difference highlights the need to refine the computational model and the importance of adapting the turbine operating mode to real-world conditions.

An analysis of the flow velocity and pressure contours showed that the load is uniformly distributed across the asymmetric blade, and in the effective TSR region, high-velocity flows continuously form on the blade surface. In inefficient modes (at high TSR), the contours show an increase in turbulent zones, an increase in vortices, and a decrease in the pressure difference, which directly contributes to a reduction in the power factor. Overall, the obtained results demonstrate the effectiveness of a vertical wind turbine with asymmetric

blades in areas with low wind speeds and low relative drag coefficients. This design makes it promising for use in areas with light to moderate wind conditions. The study's findings can serve as a basis for optimizing wind turbine blade geometry, increasing their energy efficiency, and further improving their aerodynamic performance.

Conflict of interest statement

The authors declare that they have no conflict of interest in relation to this research, whether financial, personal, authorship or otherwise, that could affect the research and its results presented in this paper.

CRediT author statement

Manatbayev R.: data curation, validation; Kalasov N.: investigation, funding acquisition; Seydulla Z.: writing – review & editing; Isataev M.: visualization & methodology; Baizhuma Z.: supervision, conceptualization; Kuykabayeva A.: resources, formal analysis; Kozhash R.: writing original draft, modeling. The final manuscript was read and approved by all authors.

Statement on the use of Artificial Intelligence.

The authors declare that no artificial intelligence tools were used to generate scientific content, results, or conclusions of this article.

Data Availability Statement

The data are available upon reasonable request from the authors.

Funding

This research has been funded by the Science Committee of the Ministry of Science and Higher Education of the Republic of Kazakhstan (Grant No. BR28713563, «Hybrid wind-solar power system with intelligent control to improve energy efficiency in different climate conditions»).

References

1 Li, C., Zhu, S., Xu, Y.L., Xiao, Y. (2013). 2.5D large eddy simulation of vertical axis wind turbine in consideration of high angle of attack flow, Renew. *Energy*, 51, 317–330. https://doi.org/10.1016/j.renene.2012.09.011

2 Shukla, V., Kaviti, A. (2017). Performance evaluation of profile modifications on straight-bladed vertical axis wind turbine by energy and Spalart Allmaras models. *Energy*, 126, 766-95. https://doi.org/10.1016/j.energy.2017.03.071

3 Murata, J., Endo, M., Maeda, T. (2016). Experimental and numerical investigation of the effect of turbulent inflow on a Horizontal Axis Wind Turbine (part I: power performance). *Energy,* 113, 713–722. https://doi.org/10.1016/j.energy.2016.06.138

4 Hameed, M., Afaq, S.K. (2013). Design and analysis of a straight bladed vertical axis wind turbine blade using analytical and numerical techniques. *Ocean Eng*, 57, 248–55. https://doi.org/10.1016/j.oceaneng.2012.09.007

5 Liu, J., Lin, H., Zhang, J. (2019). Review on the technical perspectives and commercial viability of vertical axis wind turbines. *Ocean Eng.*, 15, 608–626. https://doi.org/10.1016/j.oceaneng.2019.04.086

6 Islam, M., Ting, D.K., Fartaj, A. (2008). Aerodynamic models for Darrieus-type straight-bladed vertical axis wind turbines. *Renew Sustain Energy Rev,* 12(4), 87–109. https://doi.org/10.1016/j.rser.2006.10.023

7 Gupta, A., Abderrahmane, H., Janajreh, I. (2024). Flow analysis and sensitivity study of vertical-axis wind turbine under variable pitching. *Appl Energy,* 358, 122648. https://doi.org/10.1016/j.apenergy.2024.122648

8 McKenna, R., Leye, P., Fichtner, W. (2016). Key challenges and prospects for large wind turbines. *Renew Sustain Energy Rev*, 53, 1212–1221. https://doi.org/10.1016/j.rser.2015.09.080

9 Jin, X., Zhao, G., Gao, K. (2015). Darrieus vertical axis wind turbine: basic research methods. *Renewable and Sustainable Energy Reviews*, 21(4(41)), 212-225 https://doi.org/10.1016/j.rser.2014.10.021

10 Rakesh, K., Kaamran, R., Alan, S. (2018). A critical review of vertical axis wind turbines for urban applications, *Renew. Sustain. Energy Rev*., 14(8(89), 281–291. https://doi.org/10.1016/j.rser.2018.03.033

11 Sebastian, B., Rosario L., Michele, M. (2014). Design of a vertical-axis wind turbine: how the aspect ratio affects the turbine's performance. *Int. J. Energy Environ. Eng.*, 11(4(37), 333–340. http://dx.doi.org/10.1007/s40095-014-0129-x

12 Wang, Q., Chen, J., Pang, X., Li, S., Guo, X. (2013). A new direct design method for the medium thickness wind turbine airfoil. *Journal of Fluids and Structures*, 19(3(37), 287–301. http://dx.doi.org/10.1016/j.jfluidstructs.2013.08.003

13 Mazarbhuiya, H., Biswas, A., Sharma, K. (2020). Low wind speed aerodynamics of asymmetric blade H-darrieus wind turbine-its desired blade pitch for performance improvement in the built environment, *Braz. Soc. Mech. Sci. Eng*., 42, 326, http://dx.doi.org/10.1007/s40430-020-02408-0.

14 Mohamed, M.H. (2012). Performance investigation of H-rotor Darrieus turbine with new airfoil shapes. *Energy* 47 (1), 522–530. https://doi.org/10.1016/j. energy.2012.08.044.

15 Baizhuma, Z., Kalassov, N., Manatbayev, R., Isataev, M., Seydulla. Z., Georgiev, A. (2026). Time- resolved CFD analysis of torque generation in an L-shaped vertical-axis wind turbine. *Energy,* 344. https://doi.org/10.1016/j.energy.2026.140149

16 Tanasheva, N., Sakipova, S., Minkov, L., Bakhtybekova, A., Shuyushbaeva, N., & Burkov, M. (2021). Study of aerodynamic characteristics of a cylindrical blade with deflector. *Eurasian phys. tech. j.*, 18(3(37), 48–52. https://doi.org/10.31489/2021No3/48-52

17 Tleubergenova, A., Dyusembayeva, A., Tanasheva, N., Bakhtybekova, A., Kutumova, Z., & Mukhamedrakhim, A. (2024). Experimental studies of the performance efficiency of a wind turbine with combined blades. *Eurasian phys. tech. j.*, 21(2(48), 31–37. https://doi.org/10.31489/2024No2/31-37

18 Shaimerdenova, K., Tleubergenova, A., Tanasheva, N., Dyusembaeva, A., Minkov, L., & Bakhtybekova, A. (2025). Aerodynamic improvement of a two-blade magnus wind turbine: numerical and experimental analysis of aerodynamics and pressure distribution. *Eurasian phys. tech. j.*, 22(2 (52)), 79–87. https://doi.org/10.31489/2025N2/79-87.

19 Kalassov, N., Baizhuma, Z., Manatbayev, R., Yershina, A., Isataev, M., Kalassova, A., Seidulla, Z., Bektibay, B., Amir, B. (2025). Integrated approach to aerodynamic optimization of darrieus wind turbine based on the taguchi method and computational fluid dynamics. *Applied Sciences*, 15(10), 5739. https://doi.org/10.3390/app15105739

20 Isataev, M., Manatbayev, R., Seydulla, Z., Bektibai, B., & Kalassov, N. (2024). Study of aerodynamic characteristics of asymmetrical blades and a wind-driven power plant with a vertical axis of rotation. *Applied Sciences*, 14(24), 11654. https://doi.org/10.3390/app142411654

21 Seydulla, Z., Kalassov, N., Isataev, M., Baizhuma, Z., Baizhumanov, K., Kuykabayeva, A., Gabitova, Z., & Satkynova, A. (2026). Performance enhancement of darrieus vawt using modified asymmetric blades: experimental and cfd validation. *Energies*, 19(3), 743. https://doi.org/10.3390/en19030743

22 Isataev, M., Manatbayev, R., Seydulla, Z., Kalassov, N., Yershina, A., & Baizhuma, Z. (2025). Experimental and computational study of the aerodynamic characteristics of a darrieus rotor with asymmetrical blades to increase turbine efficiency under low wind velocity conditions. *Applied System Innovation*, 8(2), 49. https://doi.org/10.3390/asi8020049

23 Baizhuma, Z., Kalassov, N., Isataev, M., Gabitova, Z., Baizhumanov, K., Kuykabaeva, A., Seydulla, Z., Auyezkhan, N. (2026). Investigation of the aerodynamic characteristics in twin-rotor carousel wind turbines. *Energy*, 351, 140833, https://doi.org/10.1016/j.energy.2026.140833

24 Baizhuma, Z., Kalassov, N., Manatbayev, R.K., Isataev, M., Seydulla, Z., Georgiev, A. (2026). Time-resolved CFD analysis of torque generation in an L-shaped vertical-axis wind turbine. *Energy*, 344, 140149. https://doi.org/10.1016/j.energy.2026.140149

25 Kjellin, J., Bülow, F., Eriksson, S., Deglaire, P., Leijon, M., Bernhoff, H. (2011). Power coefficient measurement on a 12 kW straight bladed vertical axis wind turbine. *Renew Energy,* 36, 11, 3050–3053. https://doi.org/10.1016/j.renene.2011.03.031

AUTHORS' INFORMATION

Manatbayev, Rustem – Associate Professor, Al-Farabi Kazakh National University, Department of Thermophysics and Technical Physics, Faculty of Physics and Technology, Almaty, Scopus ID: 55848346700, https://orcid.org/0000-0003-2151-2606, rustemmanatbayev@gmail.com

Kalassov, Nurdaulet – PhD, Al-Farabi Kazakh National University, Department of Thermophysics and Technical Physics, Faculty of Physics and Technology, Almaty, Scopus Author ID: 57222177960, https://orcid.org/0000-0003-3709-5544, kalasov.nurdaulet@gmail.com

Seydulla, Zhanibek – PhD, Al-Farabi Kazakh National University, Department of Thermophysics and Technical Physics, Faculty of Physics and Technology, Almaty, Scopus Author ID: 57202515147, https://orcid.org/0000-0003-0413-6557, seidulla.zhanibek@kaznu.edu.kz

Isataev, Muhtar – Candidate of Physical and Mathematical Sciences, Al-Farabi Kazakh National University, Department of Thermophysics and Technical Physics, Faculty of Physics and Technology, Almaty, Scopus ID: 56943370900, https://orcid.org/0000-0001-8248-670X , muhtar.isataev@kaznu.kz

Baizhuma, Zhandos – PhD, Al-Farabi Kazakh National University, Department of Thermophysics and Technical Physics, Faculty of Physics and Technology, Almaty, Scopus Author ID: 57205433240, https://orcid.org/0000-0002-1226-7736, zhandos.baizhuma@kaznu.kz

Kuykabayeva, Aizhan – PhD, Al-Farabi Kazakh National University, Department of Thermophysics and Technical Physics, Faculty of Physics and Technology, Almaty, Scopus Author ID: 34968215400, https://orcid.org/0000-0002-0905-4422, a.kuikabaeva1@gmail.com

Kozhash, Rasul – Bachelor's student, Al-Farabi Kazakh National University, Department of Thermophysics and Technical Physics, Faculty of Physics and Technology, Almaty, https://orcid.org/0009-0005-3583-0850 , kozhash@list.ru

EURASIAN PHYSICAL TECHNICAL JOURNAL

2026, Volume 23, No. 2 (56)

https://doi.org/10.31489/2026N2/47-56

Received: 09/12/2025 Revised: 31/052026 Accepted: 26/06/2026 Published online: 30/06/2026

Original Research Article

UDC 536.7

COMPARATIVE ANALYSIS OF MIXING REGIMES IN BIOGAS PLANTS FOR OPTIMIZATION OF THE STIRRING PROCESS

Yessenzhol D.K.[1]*., Sakipov K.Ye.[1], Imomov Sh.J.[2], Sharipov M.Z.[3],

Majitov J.A.[4], Akhmetov S.K.[1]

[1] L.N. Gumilyov Eurasian National University, Astana, Kazakhstan

[2] National Research University "Tashkent Institute of Irrigation and Agricultural Mechanization Engineers", Tashkent, Uzbekistan

[3] Bukhara State University, Bukhara, Uzbekistan

[4] Bukhara State Technical University, Bukhara, Uzbekistan

*Corresponding author: esenzhold@mail.ru

Abstract. *Effective mixing in anaerobic bioreactors plays a crucial role in ensuring uniform temperature and substrate distribution, which directly affects the efficiency of organic matter degradation and biogas yield. This study investigates the influence of mixing intensity and regime on gas transfer, heat transfer, and substrate degradation during anaerobic digestion. Special attention was given to the experimental data obtained from the pilot solar-powered biogas plant. The results demonstrated that intermittent mixing (e.g., 5 minutes per hour) provided the same biogas yield as continuous mixing, but with substantially lower energy consumption. Continuous mixing did not result in a significant increase in methane yield compared to intermittent operation, while it was associated with markedly higher energy demand. In contrast, the absence of mixing impaired reactor performance—the volume of gas produced decreased, and temperature stratification was observed, indicating uneven heating of the medium and incomplete substrate degradation. In this work, international studies (2019–2024), including experimental investigations and CFD models, were analyzed to assess the effects of mixing regimes on decomposition kinetics, temperature uniformity, and methane yield, and to compare them with our results. For quantitative evaluation, energy balance equations (e.g., the Lindorfer model) and stoichiometric formulas were applied. The findings indicate that intermittent mixing is the optimal strategy, as it ensures a high degree of organic matter degradation and biogas yield while requiring significantly less energy than continuous mixing.*

Keywords: anaerobic digestion, mixing efficiency, gas and heat transfer, substrate degradation, biogas yield

1. Introduction

Anaerobic digestion (AD) is widely used worldwide for the treatment of organic waste and the production of biogas [1]. Kazakhstan is currently paying increasing attention to the development of renewable energy sources and carbon neutrality strategies. According to national energy policy, the share of renewable energy in electricity generation is expected to increase significantly by 2030. In this context, biogas technologies are considered a promising solution for the utilization of agricultural waste and renewable energy production [2]. By converting organic substrates into methane and carbon dioxide, AD reduces greenhouse gas emissions and generates a renewable form of fuel [1,3]. In particular, CFD-based kinetic models of gas–liquid mixture formation in anaerobic digesters typically integrate hydrodynamic simulation (Euler–Euler multiphase flow with k–ε turbulence closure) with biochemical reaction kinetics (ADM1-based substrate degradation and

methane production models), allowing prediction of mixing efficiency and methane yield under different operational regimes. The efficiency of AD systems is determined by both biochemical processes and physical exchanges within the reactor [4,5]. In particular, mixing strongly influences gas transfer and heat transfer: active agitation ensures uniform distribution of heat and substrate, whereas insufficient mixing leads to temperature stratification and stagnant zones [3,5]. Approximately 44% of large-scale biogas plants report sedimentation problems due to improper mixing [4]. A significant proportion of livestock in Kazakhstan is concentrated in small-scale farms with relatively low numbers of cattle. Therefore, compact and energy-efficient biogas plants with simple mixing systems are particularly important for decentralized agricultural applications [6].

The analysis of energy costs for maintaining the optimal mixing mode of organic waste in the installation allows us to conclude that the mixing method is most acceptable by means of multilevel reciprocating movement of biomass. Most authors believe [7] that the mixed biomass in the reactor should have a limited velocity (up to 0,5 m/s), since a high velocity of the substrate is unprofitable from a microbiological point of view. In addition, although it leads to an increase in the intensity of heat transfer, it also increases the energy consumption for mixing. It is easy to verify this by analyzing the known equations of heat transfer and hydraulic resistances during turbulent fluid movement in a tube heat transfer [7].

$$\mathrm{N}_u = 0{,}021 R_e^{0.8} \times P_z^{0.43} \tag{1}$$

$$\Delta P = \frac{\xi_{mp} \ell}{d} + \frac{\sum \xi_м \rho \omega^2}{2}, \tag{2}$$

where Nu is the Nusselt number, Re is the Reynold's number, P_z is the Prandtl number, ΔP is the hydraulic resistance of the heat exchanger on the side of the given working medium, ω is the speed of the working environment, ρ is the density of the medium, ℓ is the channel length, d is the channel diameter, ξ is the coefficient of friction and $\sum \xi_м$ is the sum of the local resistance coefficient. From (1) and (2) are

$$\alpha = \mathrm{A1}\, \omega\, 0{,}8, \tag{3}$$

$$\Delta \rho = \mathrm{A2}\, \omega\, 1{,}75, \tag{4}$$

where A1and A2 are the coefficients of proportionality.

From the obtained ratios, it can be seen that a doubling of the flow velocity provides a 1.75-fold increase in heat transfer, and in this case, the increase in hydraulic resistance occurs up to 3.4 times.

From the above considerations, it follows that the intensification of the process cannot be considered in isolation from the energy costs involved. Mixing also affects substrate degradation, i.e., the efficiency of organic solids breakdown. Sufficient mixing intensity enhances contact between fresh substrate and active sludge (inoculum), thereby improving mass transfer of enzymes and nutrients, which accelerates hydrolysis and subsequent degradation stages. In recent years, a considerable number of studies have been devoted to optimizing mixing strategies in anaerobic digestion in order to improve its efficiency. Within the framework of this study, a review was carried out covering scientific publications from 2019 to 2024, including both experimental investigations and computational fluid dynamics (CFD) modeling of hydrodynamics in anaerobic reactors. The CFD approaches considered in the reviewed studies are mainly based on multiphase Euler–Euler flow modeling combined with the k–ε turbulence model, often coupled with biochemical kinetic sub-models such as ADM1 and first-order hydrolysis kinetics to describe gas–liquid mixing, mass transfer, and methane formation processes. Li et al. (2022) emphasized that mixing “significantly influences methane production in AD” and concluded that periodic mixing is preferable for maximizing biogas yield [8].

Singh et al. (2022) noted that mixing improves substrate–microbe contact and enhances thermal homogeneity, thereby reducing volatile fatty acid (VFA) concentrations and increasing organic removal efficiency [4]. Conversely, mechanical agitation may cause microbial floc disruption and suppression of syntrophic bacteria, as observed in several experiments [4]. Indeed, excessively high mixing intensity can increase the availability of soluble substrates but may also disrupt biomass structure, sometimes resulting in a reduction of overall methane yield [4]. Most studies indicate that intermittent mixing often provides the best

balance. For instance, Kowalczyk et al. (2013) demonstrated that reducing daily mixing time from 7 hours to 2 hours resulted in 12–29% energy savings without compromising methane yield [9].

For example, Bose et al. (2021) added granular activated carbon into a CSTR and reported that the methane yield in the non-mixed case reached 318 mL CH_4/g COD (chemical oxygen demand), compared to ~290 mL/g in mixed conditions [10]. This suggests that specific factors such as substrate type, additives, and reactor design can modify the impact of mixing on microbial performance.

The literature also highlights the physical consequences of mixing. Mixing enhances mass transfer by reducing boundary layers around biomass and redistributing the substrate [5]. Hu et al. (2021) visualized mixing using LIF and PIV techniques and showed that poor mixing leads to substrate accumulation zones and dead zones in reactors with high solid content [11]. Mixing also contributes to temperature homogenization: in unmixed reactors, thermal stratification due to buoyancy often occurs [3], potentially creating "cold zones" that slow hydrolysis. El Ibrahimi et al. (2021) measured unmixed reactors and found significant vertical temperature gradients. Their CFD simulations indicated that double-wall heating could eliminate this effect, linking thermal homogeneity directly to methane yield [3]. These findings underline that the role of mixing in heat transfer is as crucial as in mass transfer [3,5]. Experimental data and mathematical modeling are used for quantitative assessment. For example, Lindorfer (2007) developed a dynamic model of the energy balance of a bioreactor, in which the net power output is expressed by the equation [12]:

$$\frac{dP_{net}}{dt} = P_{prod,e} - \left(P_{loss,pump} + P_{loss,stir} + P_{loss,rad} + P_{loss,sub}\right) + P_{loss,term} + P_{loss,mic} \quad (5)$$

where $P_{prod,e} = Q_G \cdot P_{CH4} \cdot HC \cdot \eta_e$ and $P_{prod,therm} = Q_G \cdot P_{CH4} \cdot HC \cdot \eta_t$ – electric and thermal power outputs of biogas, $Ploss_{,terms}$ and others – the cost of pumping, mixing, heating the substrate, radiation, etc.

Using such formulas, it is possible to estimate the yield of clean energy under various mixing modes. For substrate decomposition, classical stoichiometry (Buswell's equation) predicts the yields of Ch_4/co_2 from the composition of C:H:O:N [13], and kinetic models (for example, first-order or ADM1) describe the rate constants. In practice, mixing affects both the effective rate of decomposition (preventing deposition of the substrate) [4,5] and the proportion of the substrate converted to gas (by reducing pH or inhibiting PLA [4]). Thus, world practice shows that the mixing mode has a profound effect on the productivity of the AD. Continuous mixing ensures uniformity, but requires a lot of energy [4,12]. Intermittent mixing has become the optimal option [4,8]. The absence of mixing minimizes energy consumption, but creates a risk of stratification and reduced conversion [3,4].

This study investigates the effect of three mixing regimes (continuous, intermittent, and no mixing) on the performance of AD. Using experimental data from a biogas plant, we evaluate how each regime influences heat and mass transfer, substrate degradation rate, and methane yield. These results are compared with an extensive literature review covering international studies from 2019–2024, including experimental research [5,8]. Quantitative models are also applied, such as the energy balance equation, to interpret the obtained results [12]. The main objective is to determine the optimal mixing regime in anaerobic bioreactors that ensures maximum methane productivity while minimizing energy consumption for mixing and maintaining thermal stability.

2. Materials and methods

2.1. Materials

The object of the study was the operating regimes of anaerobic digestion (no mixing, intermittent mixing, and continuous mixing) evaluated in a solar-assisted biogas reactor under mesophilic conditions.

The experimental system consisted of a solar-assisted vertical biogas reactor designed for anaerobic digestion of cattle manure. The reactor had a cylindrical body with a conical bottom and was equipped with a water jacket connected to a solar thermal collector to maintain stable operating temperatures. A two-blade mechanical stirrer was installed inside the reactor to provide controlled mixing of the substrate. The digester was mounted on a supporting frame to ensure structural stability during operation [14,15]. The main research object was the determination of the optimal mixing regime that maximizes methane production while minimizing energy consumption in a solar-assisted biogas reactor.

The substrate used in the experiments was a mixture of cattle manure and water with an initial carbon-to-nitrogen ratio (C/N) of approximately 25 and a total solids (TS) content of about 8%. The reactor was operated under mesophilic conditions at a target temperature of 37 ± 1 °C.

The operational parameters were maintained as follows:

– Organic Loading Rate (OLR): 2 kg VS m^{-3} d^{-1};
– Hydraulic Retention Time (HRT): 20 days;
– Daily substrate feeding;
– Reactor operation under stable mesophilic conditions.

Three mixing regimes were investigated:

1. No mixing (NM): the stirrer remained switched off during the entire digestion process.
2. Intermittent mixing (IM): the stirrer operated for 5 min every hour (5 min h^{-1}).
3. Continuous mixing (CM): the stirrer operated continuously at 60 rpm throughout the day.

The comparison of these operating modes enabled the evaluation of their influence on heat transfer, gas transfer, substrate degradation, methane production, and overall energy efficiency.

Figure 1 shows the external appearance of the digester, equipped with a solar heating system using support frame. The configuration of this biogas plant includes a water jacket and a two-blade mechanical stirrer.

Fig.1. Experimental solar-assisted vertical biogas plant/

2.2 Research methods

The reactor performance was monitored using calibrated measuring instruments to ensure reliable and repeatable experimental results.

The following parameters were measured during the experiments:

– Temperature: digital immersion thermometers with an accuracy of ±0.5 °C installed at the middle section of the reactor. Measurements were recorded every 2 h.

– pH: determined using colorimetric indicator strips and periodically verified by a portable electrochemical pH meter equipped with automatic temperature compensation. Measurements were performed every 4 h.

– Biogas composition (CH_4 and CO_2): measured using a portable nondispersive infrared (NDIR) gas analyzer with a measurement range of 0–100% and an accuracy of ±1%.

– Pressure: measured using a diaphragm pressure gauge (0–200 kPa, accuracy ±0.25%).

– Biogas volume: continuously recorded using a wet-type diaphragm gas meter with an accuracy of ±1%.

– Substrate level: monitored by an ultrasonic distance sensor mounted at the top of the reactor.

Digestate samples were periodically collected from the upper, middle, and lower sections of the reactor for laboratory analysis.

The determination of volatile solids (VS), chemical oxygen demand (COD), and volatile fatty acids (VFA) was carried out according to internationally recognized analytical procedures. COD analysis was performed following APHA Standard Methods for the Examination of Water and Wastewater. The determination of bio-based carbon content was conducted in accordance with EN 16640:2017 “Bio-based products – Bio-based carbon content – Determination of the bio-based carbon content using the radiocarbon

method". Methane concentration was determined by gas chromatography. The obtained experimental data were used to evaluate substrate degradation, methane productivity, and reactor energy efficiency.

2.3. Analytical Calculations

The chemical oxygen demand (COD) was calculated as:

$$COD = \frac{(A-B)\cdot N\cdot 8000}{V}, \text{ mg/L} \quad (6)$$

where A is the volume of titrant in the blank experiment (ml), B is the volume in the sample (ml), N is normality, and V is the volume of the sample (ml).

The concentration of volatile fatty acids (VFA) was calculated using:

$$VFA = \frac{V_{NaOH}\cdot N\cdot 60\cdot 1000}{V_{sample}}, \text{ mg/L} \quad (7)$$

where V_{NaOH} is the volume of NaOH (ml), N is normality, 60 is m.m.CH_3COOH, Vs_{ample} is the volume of the sample (ml).

The removal coefficient (%) was calculated from incoming and outgoing solid particles:

$$VS_{removal} = \frac{VS_{in}\cdot VS_{out}}{VS_{in}} \times 100\% \quad (8)$$

where VS_{in} is VS in the input substratum, VSout is in the digest.

The methane yield was expressed in terms of g of consumed methane and m^3 of reactor volume.

$$Y_{CH_4VS} = \frac{V_{CH_4}}{m_{VSdestroyed}} \quad (9)$$

where V_{CH_4} is the volume of methane, $m_{VSdestroyed}$-is the mass of destroyed VS, g.

$$Y_{CH_4vol} = \frac{V_{CH_4}}{V_{reactor}} \quad (10)$$

where V_{CH_4} is the volume of methane, V_{reactor} is the volume of the reactor (m^3).

2.4. Energy Balance Analysis

The Lindorfer model was used: electric energy P_{elect}^{prod} and thermal energy P_{therm}^{prod} from biogas were calculated using the formula [11]:

$$P_{elect}^{prod} = Q_G \cdot P_{CH_4} \cdot H_{c\eta_{elect}} \ (kWhd^{-1}) \quad (11)$$

$$P_{therm}^{prod} = Q_G \cdot P_{CH_4} \cdot H_{c\eta_{therm}} \ (kWhd^{-1}) \quad (12)$$

where Q_G is the biogas production (m^3d^{-1}), P_{CH4} is the methane content (%), H_C is the calorific value of methane (kWh Nm^{-3}), η_{elect} is the electrical degree of efficiency (-) and η_{therm} is the thermal degree of efficiency (-) [11].

Stirrer losses according to the equation:

$$P_{stir}^{loss} = V_{liq} \cdot St_s \ (kWhd^{-1}) \quad (13)$$

where V_{liq} is the liquid volume (m^3), S is the specific power of the stirrer (kWm^{-3}) and t_s is the time for stirring (hd^{-1}).

Pump losses according to the equation:

$$P_{pump}^{loss} = Q_{in} \cdot H_{\rho g t_p} \frac{1}{\eta_{ecc\_warm}} \ (kWhd^{-1}) \quad (14)$$

where Q_{in} is the inflow rate (kgs^{-1}), H is the conveyor height (m), ρ is the density of the pumped media (kgm^3), g is the acceleration of gravity (ms^{-2}), tp is the time for pumping (hd^{-1}) and η_{ecc_warm} is the degree of efficiency (-)

Radiation losses according to the equation:

$$P_{rad}^{loss} = K_{heat\_trans}\left[(T_{liq} - T_{ambient})V_{liq} + (T_{gas} - T_{ambient}) \times (V_{tot} - V_{liq})\right] \cdot \frac{2}{r} \cdot \frac{24}{1000} (kWhd^{-1}) \quad (15)$$

where K_{heat_trans} is the heat transfer coefficient ($Whm^{-2}h^{-1}\ K^{-1}$), T_{liq} is the temperature of the substrate within the digester (K), $T_{ambient\ is}$ the ambient temperature, V_{liq} is the liquid volume (m^3), T_{gas} is the gas temperature (K), V_{tot} is the total digester volume (m^3) and r is the radius of the digester (m).

Heat transfer losses according to the equation:

$$P_{sub\_heat}^{loss} = Q_{in} c (T_{digester} - T_{substrate}) \frac{1}{3{,}6} \ (kWhd^{-1}) \quad (16)$$

where Q_{in} is the reactor inflow (m^3d^{-1}), c is the heat capacity of the substrate ($kjkg^{-1}K^{-1}$), $T_{digester}$ is the temperature of the digester (K) and $T_{substrate}$ is the temperature of the stored substrate (K).

The calculated energy indicators were used to compare the effectiveness of the investigated mixing regimes and to determine the optimal operating mode for methane production and energy utilization. In addition to experimental analysis, CFD-informed kinetic interpretation was used, where multiphase flow behavior and substrate conversion were analyzed using Euler–Euler hydrodynamic assumptions coupled with ADM1-based biochemical kinetics.

3. Results and discussion

The experiments revealed clear trends in the production of biogas and methane in three modes. Table 1 contains average data on biogas production, methane content, VS removal, and mixing costs for each regime.

Table 1. AD productivity in an experimental biogas plant under various mixing modes (OLR = 2 kg/m³·day, 37°C, HRT = 20 days).

Mixing model	Biogas production (l m³·/day)	CH_4 (%)	Removing VS (%)	Mixing energy (kWh/day)
Without stirrer	0.65	58	48	0.00
Intermittent (5 min/h)	0.78	61	53	1.5
Continuous (60 rpm)	0.75	60	56	4.8

Figure 2 presents the effect of different mixing regimes on anaerobic digestion performance. Figure 2(a) illustrates methane yield and VS removal efficiency under no-mixing, intermittent, and continuous mixing conditions, while Figure 2(b) shows the corresponding temperature gradients within the reactor. The results indicate that intermittent mixing achieved the highest methane concentration (61% CH_4), slightly exceeding that of continuous mixing (60%). Continuous stirring provided the greatest VS removal efficiency, approximately 5% higher than that observed in the non-mixed reactor. However, continuous mixing required about three times more energy (4.8 versus 1.5 kWh per day) than intermittent mixing. In contrast, the reactor without stirring consumed no mechanical energy, but its methane production was about 15% lower than in the intermittent stirring mode, which is consistent with reports that the absence of stirring reduces the overall gas output [4]. It is noteworthy that the pH and VFA values indicate a slight accumulation of VFA in the static reactor, while the content of acetate and propionate remains at the lowest level during periodic stirring. These trends are consistent with previous findings that periodic stirring stabilizes the chemical composition of the reactor more effectively than without stirring [4].

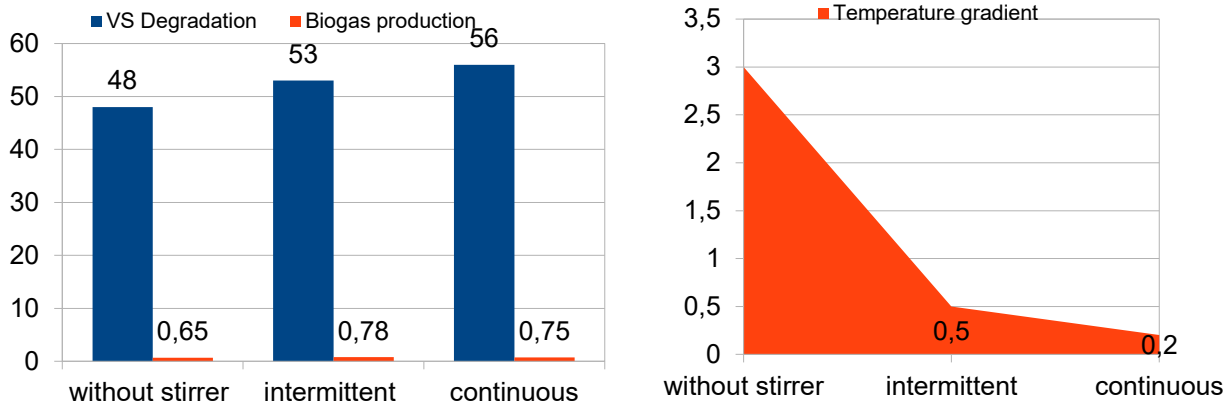

Fig.2. Effect of mixing regimes on anaerobic digestion performance: (a) methane yield and VS removal efficiency; (b) temperature gradient inside the reactor.

The results demonstrate a trade-off between mixing regimes. Continuous mixing ensured the most uniform substrate distribution and enhanced degradation (see Table 2), as predicted by mixing models [12]. It prevented solid settling and increased organic matter conversion; however, the associated energy demand was very high [4,12]. Intermittent mixing achieved nearly the same level of VS removal with considerably lower energy consumption. This is consistent with the literature: Singh et al. and others reported that short mixing pulses provide almost the same gas yield as continuous mixing, while using electricity more efficiently [4]. In our experiments, a 5 min/h pulse proved effective, although the optimal intervals may vary for other scales and substrates. From a mechanistic perspective, intermittent mixing combines several advantages: short bursts distribute fresh substrate, while pauses allow microbes to operate without strong shear stress. This typically promotes acetolactic methanogens and prevents the accumulation of volatile fatty acids (VFAs) [4]. In our reactor, VFA concentrations stabilized at lower levels under the intermittent regime. As noted by Caillet et al., improved mixing enhances the mass transfer coefficient and eliminates thermal gradients [5].

The energy balance highlights the advantages of the intermittent regime: according to the Lindorfer model [12], continuous mixing requires ~0.14 kWh/m³·d solely for the agitator, whereas intermittent mixing needs only ~0.04. At the same time, the thermal and electrical energy recovered from biogas (≈6.5 kWh/m³·d) shows a smaller reduction under intermittent operation. The resulting net power (~6.3 kWh/m³·d) was higher than under continuous mixing (~6.1). This is consistent with the findings of El Ibrahimi et al. (2025), who reported that combining mixing with heating can reduce energy consumption by more than 75% [16]. Our results also support the observations of Kowalczyk et al., who reported a 29% reduction in energy demand when mixing time was shortened, as well as the conclusion of Semen et al. that longer pauses lead to higher yields.

It should be noted that the specific methane yield (per g VS) was the lowest in the non-stirred reactor, which is consistent with the reports of Bose et al. on efficiency losses in the absence of mechanical agitation [4]. Nevertheless, some self-induced convective flows still occurred without a stirrer. Our measurements revealed a vertical temperature gradient of ~3 °C, confirming the CFD modeling of El Ibrahimi, which showed stratification in the absence of mixing [3]. This likely slowed down hydrolysis in the cooler upper zone, further highlighting the benefits of short mixing periods in ensuring uniform heating and mixing.

An additional comparative analysis was conducted between the experimental results and the predictions of mathematical models based on differential equations (Table 3, Fig. 3), as reported in the studies of Li et al. [8], Singh et al. [4], El Ibrahimi et al. [3], Lindorfer [12], and other researchers.

Table 3. Data from mathematical models based on differential equations

Mixing model	CH_4 (%)	Removing VS (%)	Temperature gradient (°C)	Clean energy (kWh/m³ day)
Without stirrer	57	47	3,2	5,4
Intermittent(5 min/h)	62	52	0,4	6,35
Continuous (60 rpm)	60	55	0,1	6,05

Figure 3 presents a comparison between the obtained experimental data and the model predictions. Figure 3(a) shows the methane concentration (CH_4, %), Figure 3(b) presents the volatile solids removal efficiency (VS removal, %), Figure 3(c) illustrates the temperature gradient within the reactor (°C), and Figure 3(d) depicts the net energy production (kWh m^{-3} day^{-1}).

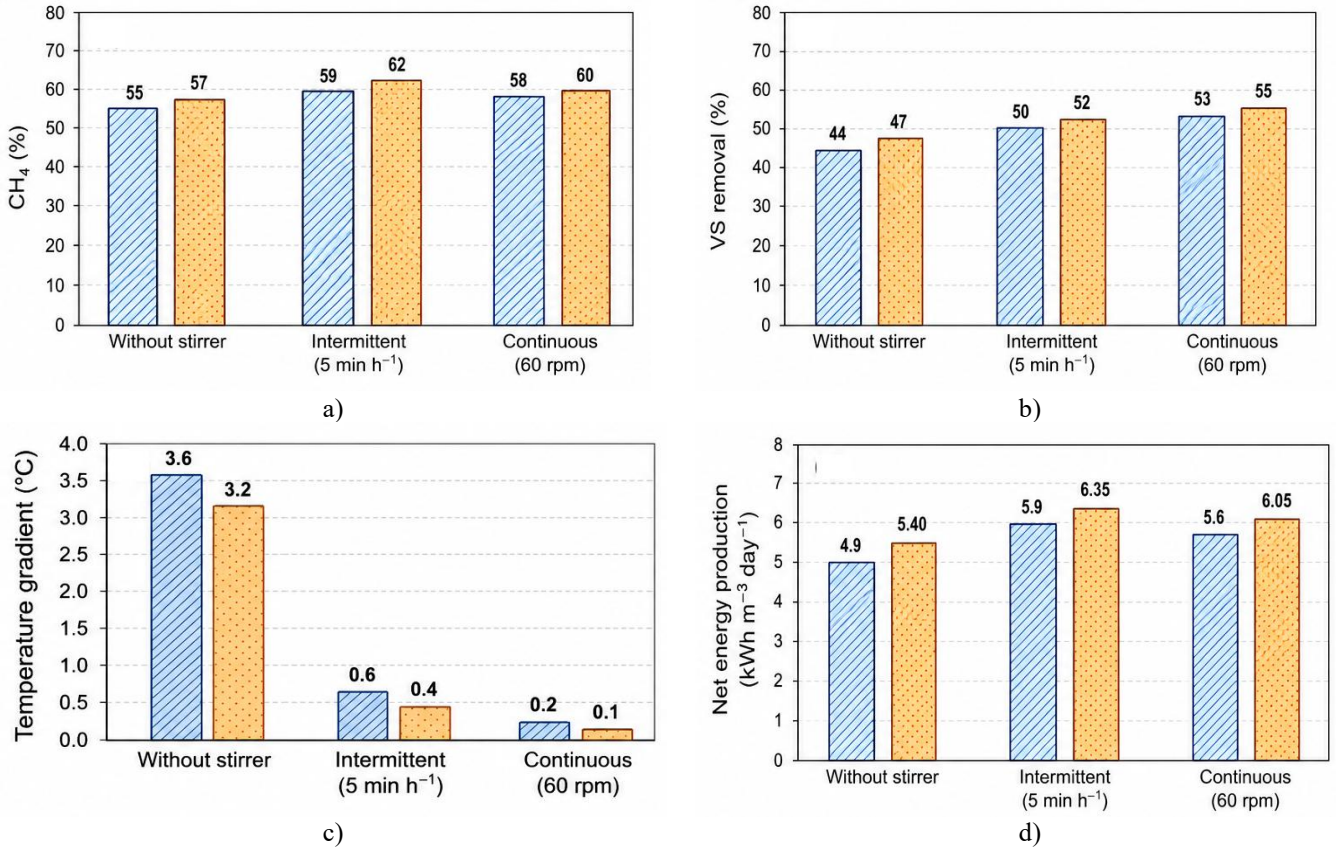

Fig.3. Comparison between experimental data and model predictions: (a) methane concentration, CH_4 (%); (b) volatile solids removal, VS (%); (c) temperature gradient (°C); (d) net energy production (kWh m^{-3} day^{-1}).

The following computational models were used:

- a first-order kinetic model for hydrolysis;
- the structured ADM1 model describing the dynamics of VFAs, pH, and methanogenesis;
- the Lindorfer energy model accounting for power balance.

Thus, both experimental data and literature sources converge on the conclusion that an intermediate regime between the extremes is optimal [4,12]. Continuous mixing does not provide a significant gain in yield compared to intermittent operation but consumes considerable energy. The complete absence of mixing saves energy but reduces biogas yield and causes stratification. Intermittent mixing enables nearly maximal yield at substantially lower costs [4]. Our data show that short mixing pulses are sufficient to sustain microbial activity and prevent inhibition (with VFAs remaining at low levels). In line with global studies, we recommend periodic mixing (e.g., 5–15 min every 1–4 h) at moderate speed to break the surface crust and keep particles in suspension without creating excessive shear stress [4,8].

4. Conclusion

The study clearly demonstrates that the mixing regime has a profound impact on the efficiency of anaerobic digestion. Based on experiments and an extensive literature review, we conclude that intermittent mixing is the optimal strategy, as it maintains high methane yield and degradation efficiency at substantially lower energy costs than continuous mixing. In particular, short mixing pulses (5–10 min every 1–2 h) resulted in nearly the same biogas yield as continuous mixing but required three times less electricity, consistent with

the findings of other authors. Continuous mixing did not improve yield compared to intermittent operation but significantly increased energy demand. The non-mixed regime provided the lowest yield and showed temperature stratification, although it required minimal energy input.

Therefore, the analysis of energy expenditures in anaerobic digestion systems indicates that efforts to reduce the overall energy intensity should primarily focus on heat recovery from digested organic residues and on the optimization of biomass mixing within bioreactors. Considering the intensive treatment of biomass under thermophilic conditions, the application of high-efficiency heat exchangers appears most appropriate. Furthermore, the selected equipment must comply with the operational requirements of systems handling non-Newtonian fluids, a characteristic property of biomass.

In practice, it is recommended to design AD plants with programmable intermittent mixing. For instance, mixer operation can be synchronized with heating periods. The reactor geometry (height-to-diameter ratio) should promote natural circulation during idle phases. Operators should monitor biogas yield and temperature profiles to detect potential stratification. These recommendations are consistent with global trends in optimizing the energy efficiency of AD systems.

In the future, it will be reasonable to refine CFD-kinetic models for specific operating conditions and substrates. Overall, the experimental results combined with the analysis of international studies demonstrate that intermittent mixing is the optimal regime for anaerobic bioreactors. It ensures effective heat and mass transfer, a high degree of substrate degradation, and maximum biogas yield at minimal energy input.

Conflict of interest statement

The authors declare that they have no conflict of interest in relation to this research, whether financial, personal, authorship or otherwise, that could affect the research and its results presented in this paper.

CRediT author statement

Yessenzhol D.K.: investigation, visualization, writing—original draft; **Sakipov K.Ye.**: supervision, Writing – review & editing; **Imomov Sh.J.:** project administration, conceptualization; **Sharipov M.Z.:** methodology, formal analysis, **Majitov J.A.:** data curation, validation; **Akhmetov S.K.:** data curation. The final manuscript was read and approved by all authors.

Statement on the use of Artificial Intelligence

During the preparation of this manuscript, artificial intelligence tools were used solely for language editing and grammatical improvement. No AI tools were used to generate scientific content, analysis, results, or conclusions.

Data Availability Statement

The data are available upon reasonable request from the authors.

Acknowledgements

The authors would like to express their gratitude to Bukhara State Engineering Technological Institute for providing the experimental setup and for the support in conducting the research.

References

1 Global Methane Initiative. (2014). *A global perspective of anaerobic digestion policies and incentives*. https://www.globalmethane.org/documents/tools/A-Global-Perspective-of-AD-Policies-Incentives.pdf

2 Yessenzhol, D., Bakhtiyar, B., Sakipov, K., & Olzhabayeva, K. (2024). Classification and improvement bioenergy plants. KazATC Bulletin, 135(6), 458–465. https://doi.org/10.52167/1609-1817-2024-135-6-458-465

3 El Ibrahimi, M., Khay, I., El Maakoul, A., & Bakhouya, M. (2021). Energy performance of an unmixed anaerobic digester with submerged solid waste: Effects of temperature distribution. *Energy, 231*(C). https://doi.org/10.1016/j.energy.2021.120926

4 Singh, B., Kovács, K.L., Bagi, Z., Petrik, M., Szepesi, G. L., Siménfalvi, Z., Szamosi, Z. (2022). Significance of intermittent mixing in mesophilic anaerobic digester. *Fermentation, 8*, 518. https://doi.org/10.3390/fermentation8100518

5 Caillet, H., Bastide, A., & Adelard, L. (2023). Advances in computational fluid dynamics modeling of anaerobic digestion process for renewable energy production: A review. *Cleaner Waste Systems, 6*, 100124. https://doi.org/10.1016/j.clwas.2023.100124

6 Ward, A.J., Hobbs, P.J., Holliman, P.J., & Jones, D.L. (2008). Optimisation of the anaerobic digestion of agricultural resources. *Bioresource Technology*, 99(17), 7928–7940. https://doi.org/10.1016/j.biortech.2008.02.044

7 Salimov, O. U., Imomov, Sh. J., Shodiyev, E. B., Juraev, T. Kh., & Sabirov, K. N. (2021). Physical-mechanical properties of organic waste reduced to bioreactor. *IOP Conf. Series: Earth and Environmental Science, 868*(1), 012088. https://doi.org/10.1088/1755-1315/868/1/012088

8 Li, L., Wang, K., Zhao, Q., Gao, Q., Zhou, H., Jiang, J., Mei, W. (2022). A critical review of experimental and CFD techniques to characterize the mixing performance of anaerobic digesters for biogas production. *Reviews in Environmental Science and Biotechnology, 21*, 665–689. https://doi.org/10.1007/s11157-022-09626-z

9 Kowalczyk, A., Szewczyk, P., & Głowacka, A. (2013). Different mixing modes for biogas plants using energy crops. *Applied Energy, 112*, 465–472. https://doi.org/10.1016/j.apenergy.2013.03.065

10 Bose, R. S., Chowdhury, B., Zakaria, B. S., Tiwari, M. K., & Dhar, B. R. (2021). Significance of different mixing conditions on performance and microbial communities in anaerobic digester amended with granular and powdered activated carbon. *Bioresource Technology, 341*, 125768. https://doi.org/10.1016/j.biortech.2021.125768

11 Hu, Y., Zhan, S., Wang, X., Peng, X., Hu, F., Wang, C., Li, H. Z. (2021). Visualization of mass transfer in mixing processes in high solid anaerobic digestion using Laser Induced Fluorescence (LIF) technique. *Waste Management, 127*, 121–129. https://doi.org/10.1016/j.wasman.2021.04.038

12 Lübken, M., Wichern, M., Schlattmann, M., Gronauer, A., & Horn, H. (2007). Modelling the energy balance of an anaerobic digester fed with cattle manure and renewable energy crops. *Water Research, 41*(18), 4085–4096. https://doi.org/10.1016/j.watres.2007.05.061

13 Farid, M. U., Olbert, I. A., Bück, A., Ghafoo, A., & Wu, G. (2025). CFD modelling and simulation of anaerobic digestion reactors for energy generation from organic wastes: A comprehensive review. *Heliyon, 11*(2), e41911. https://doi.org/10.1016/j.heliyon.2025.e41911

14 Majitov, J.A., Kamilov, O.S., Yuliyev, O.O. (2024). Solar biogas plant. Utility model patent No. FAP 2440. Published 19.03.2024. [in Uzbek] https://im.adliya.uz/document/check/e00d4d85-4e28-4988-917b-eb8f60e58fb711

15 Sharipov, M., Majitov, J., Imomov, S., Kovalev, I., Narzullayev, M., B., N., & Ziyoyev, D. (2026). Optimization of thermal processes in solar biogas plant. *Eurasian Physical Technical Journal*, 23(1 (55), 48–59. https://doi.org/10.31489/2025N2/48-59

16 El Ibrahimi, M., Khay, I., El Maakoul, A., & Bakhouya, M. (2025). A novel coupled mixing and heating strategy for improving the energy efficiency of anaerobic digesters with submerged waste: An integrated experimental and numerical study. *Chemical Engineering Journal, 513*, 162610. https://doi.org/10.1016/j.cej.2025.162610

AUTHORS' INFORMATION

Yessenzhol, Dina Kanashkyzy – PhD student, Faculty of Transport and Energy, L.N. Gumilyov Eurasian National University, Astana, Kazakhstan; https://orcid.org/0009-0002-9951-9699, esenzhold@mail.ru

Sakipov, Kamalkhan Yerkeshevich – Candidate of technical sciences, Associate Professor, Department of Heat Power Engineering, L.N. Gumilyov Eurasian National University, Astana, Kazakhstan; Scopus ID: 57197722422, https://orcid.org/0000-0003-2477-3879; sakipov_kye@enu.kz

Imomov, Shavkat Jahonovich – Doctor of technical sciences, Professor, National Research University, Tashkent Institute of Irrigation and Agricultural Mechanization Engineers, Tashkent, Uzbekistan; Scopus ID: 59619616500, https://orcid.org/0009-0001-0191-7430

Sharipov, Mirzo Z. – Doctor of Physical and Mathematical Sciences, Professor, Head of Department, Bukhara State University, Bukhara, Uzbekistan; SCOPUS ID: 24177719300, https://orcid.org/0000-0003-0370-8066; m.z.sharipov@buxdu.uz

Majitov, Jurabek – Doctor PhD (Eng), Associate professor, Physics Department, Bukhara State Technical University, Bukhara, Uzbekistan; SCOPUS ID: 57221226030; https://orcid.org/0009-0005-9453-279X; majitov@mail.ru

Akhmetov, Sanat Karimkhanovich – PhD student, Faculty of Transport and Energy, L.N. Gumilyov Eurasian National University, Astana, Kazakhstan; https://orcid.org/0009-0008-7708-8801, sanat_95_01@mail.ru

EURASIAN PHYSICAL TECHNICAL JOURNAL

2026, Volume 23, No. 2 (56)

https://doi.org/10.31489/2026N2/57-66

Received: 21/01/2026 Revised: 26/05/2026 Accepted: 26/06/2026 Published online: 30/06/2026

Original Research Article

UDC 53.538.9; 629.7.064.56

MODELING OUTPUT PERFORMANCE OF BIFACIAL SOLAR CELLS BASED ON SINGLE DIODE MODEL

Rustemov A., Ibraimov M., Almen D.*, Svanbayev Ye., Saymbetov A., Nurgaliyev M., Kapparova A., Orynbassar S.

Al-Farabi Kazakh National University, Almaty, Kazakhstan
*Corresponding author: dinara.almen@gmail.com

Abstract. *Bifacial photovoltaic cells represent a promising solution for increasing the energy efficiency of solar modules by utilizing the rear surface. In this study, the bifacial solar cell was modeled based on the single-diode model. Current-voltage (I-V) and power-voltage (P-V) characteristics were constructed for various bifacial factor values, allowing us to consider both typical operating conditions and configurations with increased reflectivity of the rear surface. Calculations showed that a 36-cell module provides a 3.5% increase in efficiency compared to a monofacial module. The annual energy output of the bifacial module was 910 Wh versus 517 Wh for the monofacial module, representing a 76% increase. Daily and monthly energy production profiles confirmed the significant contribution of the rear side and the consideration of seasonal fluctuations in solar radiation. These results demonstrate the high potential of bifacial modules to improve power generation and overall energy efficiency of photovoltaic systems.*

Keywords: Bifacial photovoltaic cells, Monofacial photovoltaic cells, Single-diode model, Bifacial factor, Bifacial energy effect.

1. Introduction

With the increasing demand for renewable energy sources, the cost-effective and efficient fabrication of photovoltaic (PV) cells has been developing in recent decades. One of the most promising technologies in the PV field in recent years is bifacial solar cells (BSC). Bifacial solar cells are already accounting for a significant portion of the PV market and demand for these cells is increasing. Solar cell manufacturers such as Panasonic, Prism Solar, LG, Solar World, Centrotherm are increasing their share of BSC production.

BSC panels have been produced and experimentally investigated since the 1980s and they were found to be able to generate up to 50% more energy than flat monofacial solar cells (MSCs) [1]. Currently, new BSC technologies such as PERC, PERT, and HIT are rapidly developing, and the price of such solar cells is becoming cheaper every year. The use of BSC technology reduces the levelized cost of energy (LCOE), because it collects light from both sides and expands the energy yield. Accordingly, costs such as land, cabling, and installation structure are reduced than MSCs [2]. That is, BSC modules capture sunlight from both the front and rear sides, thereby increasing the output power. This advantage not only increases energy efficiency, but also reduces the area occupied by the module, thereby increasing the power density. MSC albedo radiation utilization does not exceed 2%, while BSC has a much higher figure. Thus, this system is also more economical as the presence of both front and rear sides allows for a greater amount of electricity to be captured from the same area than MSC [3].

The disadvantage of BSC over MSC is its higher cost because the material is bifacial and requires more expenses. However, the advantage of BSC is that the warping effect is reduced due to the small difference in the thermal expansion coefficients of silicon and aluminum, and this reduces electrical losses. BSC also has a lower operating temperature and a better temperature coefficient [4].

Vertically mounted BSCs have higher yields at noon because they receive light from both sides. Another advantage of this configuration is that snow and dust do not accumulate on the surface of the solar cell, which reduces soiling. Currently, issues such as optimal installation of BSCs, installation at a certain angle or on sun trackers are being addressed. In the work [5], three configurations of south-facing monofacial, south-facing tilted bifacial, and ground-sculpted vertical bifacial modules were compared, and the south-facing tilted bifacial configuration was 73.3% better than the vertically mounted bifacial panel. And the south-facing tilted BSCs yield 21.3% better than the south-facing tilted MSC.

To extract maximum energy from BSCs panels, the problem is to maximize the light incident on both sides. One solution to this problem is to study the bifacial irradiance using a BSC model. For this, a precise model of BSCs is required. A precise model of BSCs also solves the problem of predicting its output energy under different environmental conditions [6]. Since the element has two sides, the illumination incident on it varies nonlinearly depending on the efficiency of the front and rear solar cells. Therefore, it is important to accurately characterize the total BSC current-voltage (I-V) and its parameters, taking into account the received irradiance of both sides [7]. The electrical characteristics of BSCs are more complex than those of MSCs, and traditional models may not fully describe the bifacial properties of the solar cell.

Typically, two methods are used to describe the electrical characteristics of BSCs: the single-diode model and the double-diode model [8]. The single-diode model is simple and easy to use, has low computational cost, and consists of five parameters. However, it cannot fully describe the recombination under low illumination and different temperatures [9]. For this reason, the double-diode model is used and consists of seven parameters. Although the double-diode model can describe solar cells more accurately, it is considered more complex, especially for BSC cells, because the two-sided asymmetric irradiance distribution makes the model even more complicated. In the work [10], a method for characterizing the electrical characteristics of BSCs was proposed, and this method was based on the standard MSC model of BSCs. By studying the two sides of the solar cell separately, new bifacial parameters of BPV, such as short-circuit current, open-circuit voltage, fill factor and efficiency, were introduced for the one-diode model of PV. Thus, the BSC characteristics for different illumination conditions were compared with the experimental results and found a deviation of 1%. In addition, many works have tried to describe the BSC more precisely. For example, in the work [11], a dataset-based five-parameter analytical model of the MSC was developed based on the single-diode model, and it was tested with commercial panels under different irradiance and temperature conditions, and it showed good performance.

In the study [12], the generalized MSC model for BSC was able to describe the effect of the back side of the solar cell by adding an additional parameter. The next work [13] described the BSC using a single double-diode model by including alpha and beta parameters. Here, α refers to the error and precision of the measurements, and β is a parameter that describes the interaction of the illumination of the rear and front parts. The authors of [14] proposed a method for characterizing BSC and tested their model under standard test conditions (STC). The proposed model considers the radiation from the rear and front surfaces simultaneously, rather than separately. Two new parameters are introduced: the bifacial effective efficiency and the gain-efficiency product. The article [15] is also based on the single-diode model, but they consider each parameter as a function of the individual side's parameter. The next study [16] proposed a method for reducing the error of the single-diode model for BSC by accurately determining the saturation current. The work [12] also proposes a new parameter to adjust the series resistance of BSC using traditional MSC and compared with conventional single-diode and double-diode models, the proposed method can provide an accurate model for the whole operating range of BSC. Another work [17] also models the BSC using a single-diode model and describes the series resistance and shunt resistance values using two physical equations. The study [18] evaluated the performance of the BSC using the single-side illumination method instead of double-side illumination and showed that the short-circuit current and the open-circuit voltage parameters were not significantly different from those when double-side illumination was considered. Most of the parameter extraction methods are based on numerical optimization and provide limited insight into the mathematical role and sensitivity, so the work [19] proposed a new method that combines analytical formulation, hybrid optimization, and parametric sensitivity analysis and does not require single-diode modification. As a result, the model was tested for different environments and showed an error of 1.1%. Obtaining an accurate model of

BSC and extracting its parameters is very important and fundamental. The work [20] demonstrated a method for estimating the output power of vertically mounted bifacial solar panels using an optical and electrical model.

Thus, an accurate BSC description allows for a more accurate prediction of the energy production of the panel under different environmental conditions. This plays an important role in assessing the panel performance in advance when installing BSC panels in different locations. This is because the data in the datasheets of bifacial solar panels is often measured under standard test conditions (STC) and is not sufficient for accurate analysis and planning of the installation, since it is exposed to different environmental conditions in real-world applications. An accurate model of the panel can not only increase the efficiency of its installation but also reduce economic costs. In addition, a model that describes its operation is also needed to obtain the maximum output power from the panel during operation [21].

Many works proposed methods to accurately describe the BSC behavior and the problem of improving these models and using them correctly in energy forecasting is still a problem [12, 22]. Many works have validated their models with experimental results or performed simulations, but there is still a lack of work that has performed an in-depth analysis of the IV curve. In-depth analysis of the IV curve and each parameter is needed. In particular, since the combination of the rear-side irradiance and the front-side irradiance increases the nonlinearity of the BSC, it is important to accurately describe the bifacial illumination. In real-world conditions, part of the other side of the BSC may be shaded and the nonlinearity of the model increases. At this point, simple single-diode and double-diode models reduce accuracy. Therefore, the nonlinearity characteristics of the BSC should be considered and the different combinations of the front- and rear-side illuminations should be considered when performing their models.

In this paper, a method for obtaining a bifacial silicon solar cell model, taking into account the two-sided illumination parameter, is presented using a five-parameter single-diode equivalent model. The output power of the bifacial solar module at different coefficients x is determined. The obtained bifacial solar module output power is compared with that of the monofacial solar module. As a result of the proposed modeling, it is found that the bifacial solar module produces more energy in the same area than the monofacial solar module.

2. Methodology

In this study, a single-diode equivalent model, which is widely used to analyze the current-voltage characteristics of solar cells, is used to describe the electrical characteristics of a bifacial silicon solar cell. This model accounts for the key physical processes that determine cell operation, including photogeneration of charge carriers, recombination losses, and the influence of internal resistances:

$$I = I_{ph} - I_0 \left[exp\left(\frac{q(V+R_s I)}{nkT}\right) - 1 \right] - \frac{V+R_s I}{R_{sh}}, \quad (1)$$

where I denotes the output current of the solar cell, V is the terminal voltage, k represents the Boltzmann constant, and T is the absolute temperature.

The five-parameter solar cell model is formulated based on the open-circuit voltage V_{OC}, the voltage at the maximum power point V_{mp}, the short-circuit current I_{sc}, and the current at the maximum power point I_{mp}. These parameters are either specified by the manufacturer or obtained through experimental measurements. The remaining solar cell model parameters are subsequently evaluated using Equations (2)-(6) [23].

$$I_0 = \left(I_{sc} - \frac{V_{oc}}{R_{sh}}\right) exp\left(-\frac{qV_{oc}}{nkT}\right) \quad (2)$$

$$I_{ph} = I_{sc}\left(1 + \frac{R_s}{R_{sh}}\right) + I_0 \left[exp\left(1 + \frac{qI_{sc}R_s}{nkT}\right) - 1 \right] \quad (3)$$

$$R_s = R_{s0} - \left[\frac{nkT}{qI_0} exp\left(-\frac{qV_{oc}}{nkT}\right) \right] \quad (4)$$

$$R_{sh} = R_{sh0} \quad (5)$$

$$n = \frac{V_m + I_{mpp}R_{OC} - V_{OC}}{[\ln(I_{sc} - I_{mpp}) - \ln(I_{sc})]V_T}, \quad (6)$$

where R_{sc} and R_{oc} denote the short-circuit and open-circuit resistances, respectively.

The parameters I_{sc} and V_{oc} correspond to the short-circuit current and open-circuit voltage, while I_{mpp} and V_m represent the current and voltage at the maximum power point. The thermal voltage is defined as $V_T = kT$, where k is the Boltzmann constant and T is the absolute temperature. Below is the equivalent circuit diagram of a bifacial solar cell, in which the total output current is defined as the algebraic sum of the currents generated by the front and rear sides of the cell [24]. This model allows for the contribution of radiation incident on both sides of the cell, as well as the influence of internal electrical parameters described within the single-diode approximation (Figure 1).

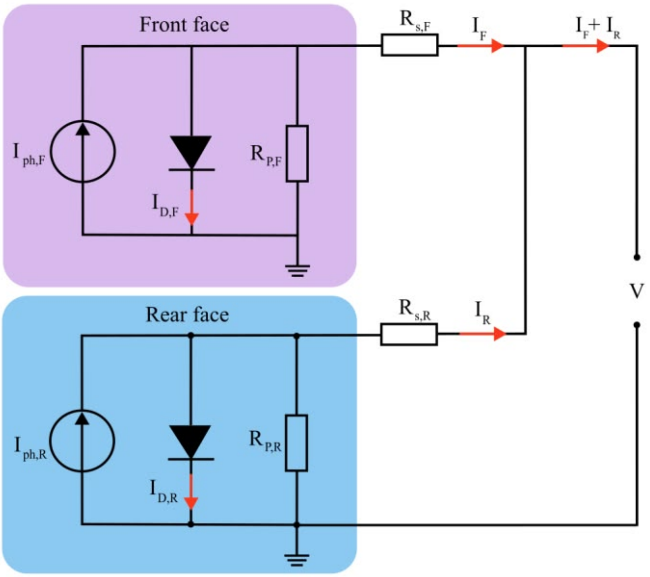

Fig.1. Equivalent circuit for a bifacial solar cell.

When determining the energy performance of bifacial photovoltaic cells, it's important to consider the characteristics of incident solar radiation, as the output power is directly determined by the irradiance of the active surface. Unlike monofacial photovoltaic cells, bifacial cells receive solar radiation from both the front and rear sides (Figure 2).

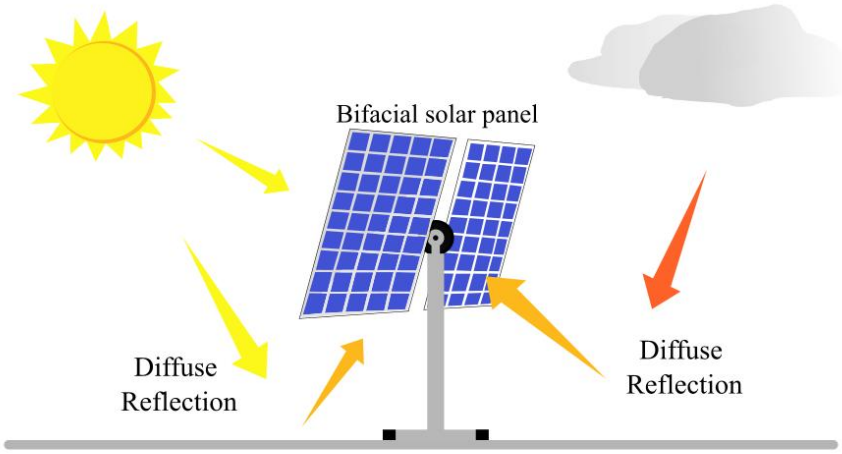

Fig. 2. Bifacial solar panel.

To quantify the contribution of insolation from the rear side, a dimensionless coefficient x is introduced, called the bifacial impact factor. This coefficient is defined as the ratio of the radiation incident on the rear surface of the cell to the radiation incident on its front surface:

$$x = \frac{G_r}{G_f} \tag{7}$$

where G_f is the solar radiation falling on the front side of the module (W/m²), G_r is the solar radiation arriving on the rear side (W/m²) [14].

The value of the coefficient x is determined depending on the reflectivity of the lower surface, the installation geometry and the operating conditions. This allows one to determine the energy of a bifacial solar cell taking into account the additional contribution of radiation from the rear side. Typically, the x-factor ranges from 0.05 to 0.5 for simple practical installations and can reach 0.8 in optimized or experimental configurations with surrounding highly reflective surfaces [25].

The efficiency of converting solar energy into electrical energy is characterized by the efficiency factor, which is defined as the ratio of the maximum output electrical power of a photovoltaic cell to the total power of solar radiation incident on it. For a bifacial solar cell, the efficiency is written as:

$$\eta = \frac{P_{max}}{A(G_f+G_r)}, \tag{9}$$

where A is the active area of the bifacial solar cell (m²), P_{max} is the maximum output electrical power of the solar cell (W).

The active area is determined by the geometric dimensions of the bifacial cell and is independent of the cell's operating mode. The contribution of the rear side is taken into account solely through the magnitude of incident radiation, not through changes in area. Therefore, when comparing monofacial and bifacial photovoltaic cells, the active area is assumed to be the same [8]:

$$A = A_{mono} = A_{bif}. \tag{10}$$

Taking into account the introduced coefficient x, the expression for the output power of a bifacial photovoltaic cell can be represented as follows:

$$P_{out} = \eta(1 + x)GA. \tag{11}$$

This allows one to clearly see the effect of rear insulation on increasing output power at a constant active area and front illumination.

To estimate the daily energy output of a photovoltaic cell, the instantaneous output power is integrated over time. Daily electrical energy output is determined by the expression:

$$E = \int_{t_{sr}}^{t_{ss}} P(t)dt, \tag{12}$$

where t_{sr} is the sunrise time, t_{ss} is the sunset time.

To determine the temporal dependence of solar radiation during daylight hours, a sinusoidal model is used, approximating the characteristic distribution of solar radiation depending on the time of day. This model is widely used in modeling insolation and hourly radiation distribution:

$$G(t) = G_{max} \cdot \sin\left(\frac{\pi(t-t_{sr})}{t_{ss}-t_{sr}}\right), \quad t_{sr} \le t \le t_{ss}, \tag{13}$$

where G_{max} is the peak value of solar radiation corresponding to midday and the maximum angle of incidence of solar rays.

When performing calculations over long periods of time, such as a month or a year, using peak solar radiation does not accurately account for temporal variability in insolation. Annual energy calculations use the average daily solar radiation value G_{avg}, which is determined by integrating the daily radiation profile over time. Using this value allows for seasonal fluctuations in insolation to be taken into account.

The energy efficiency of a bifacial module is the difference in energy production between bifacial and monofacial systems with the same active area:

$$\Delta E = \frac{E_{bif} - E_{mono}}{E_{mono}}, \quad (14)$$

where E_{bif} is the energy generated by a bifacial solar cell, E_{mono} is the energy generated by a monofacial solar cell.

3. Results and discussion

To construct the current-voltage characteristic of a bifacial photovoltaic cell, the current equation according to formula (1), which is used to describe monofacial solar cells, was used. This approach is based on the equivalent electrical circuit of a bifacial solar cell, shown in Figure 1. To analyze the effect of different illumination levels on the electrical characteristics of the module, several values of the coefficient *x*, listed in Table 1, were considered.

Table 1. Calculated characteristics of a bifacial solar cell.

№	Coefficient *x*	G_f, W/m²	G_r, W/m²	P_{max}, W
1.	0.5	600	300	0.27
2.	0.66	600	400	0.28
3.	0.75	800	600	0.37
4.	0.4	1000	400	0.35
5.	0.6	1000	600	0.39
6.	0.8	1000	800	0.44

As the table shows, this allows us to cover both typical practical operating conditions for bifacial modules and configurations that optimize the reflectivity of the lower surface.

The I-V and P-V characteristics are shown in Figure 3, a and b. The curve designations in the graphs correspond to the numbering of the variants in Table 1, and each characteristic is plotted based on the corresponding solar radiation values.

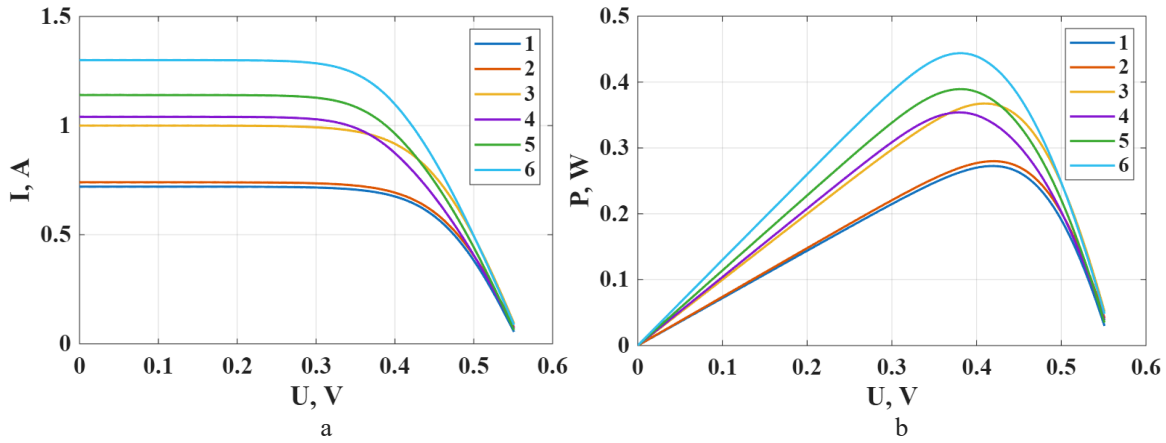

Fig. 3. I-V and P-V characteristics of a bifacial photovoltaic cell.

As can be seen from the obtained results, with an increase in the coefficient *x* and an increase in solar radiation on the surface, the corresponding current-voltage characteristics show an expected increase in the output current and power. After constructing the current-voltage and power-voltage characteristics of the bifacial PV cells, the efficiency of a module consisting of 36 bifacial cells was calculated based on the obtained results.

Based on this simulation, the efficiency values for monofacial and bifacial cells were determined using the standard formula and formula (9), respectively. The calculation results showed that the bifacial module provides a 3.5% efficiency increase compared to a monofacial module with the same active area and the same lighting conditions. This result indicates a positive impact of the rear side on the energy efficiency of the bifacial PV cell. To determine the module's daily output power, the solar radiation-time dependence G(t) was used using formula 13 described above (Figure 4, a). Based on this data and the corresponding formula for

calculating output power with formula (11), a graph of the module's power change over the course of the day was constructed, reflecting the dynamics of energy production (Figure 4, b).

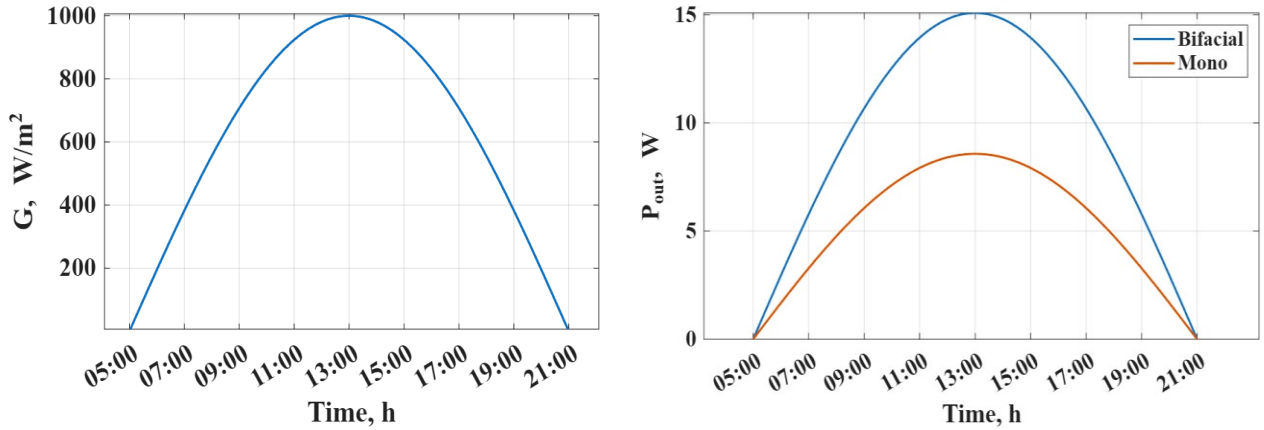

a) b)

Fig.4. Time-dependent solar irradiance and output power

Using formula (14), the increase in energy generated by a bifacial solar cell compared to a monofacial one was calculated to be 76%, demonstrating a significant increase in energy efficiency when using the rear side of the module. Figure 5 shows a histogram of monthly energy production for a monofacial and bifacial PV module. The calculations were based on average solar radiation values G_{avg} for each month, accounting for seasonal variations in solar radiation.

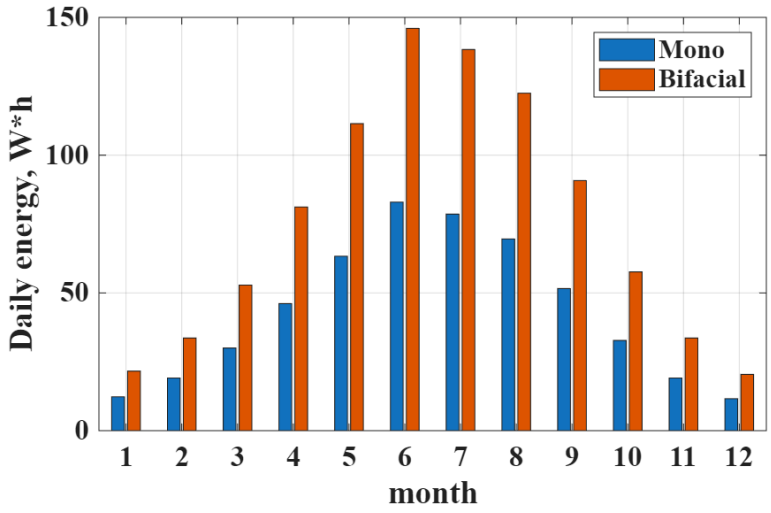

Fig.5. Monthly distribution of energy production

As the histogram shows, the bifacial cell exhibits higher energy yield than the monofacial module in all months of the year. Annual energy yield was 517.0 Wh for the monofacial module and 910.0 Wh for the bifacial module, confirming the significant contribution of the rear side to the overall energy output of the module. The maximum increase is observed during periods of high insolation. These results allow us not only to estimate the annual energy efficiency but also to determine the efficiency of bifacial cells compared to monofacial cells.

4. Conclusion

The conducted modeling of bifacial photovoltaic cells was based on a single-diode model previously used for monofacial cells. This allowed for a comprehensive assessment of their electrical efficiency and comparison with single-sided cells. The constructed current-voltage and power-voltage characteristics for

various values of the bifacial factor demonstrated that using the rear side of the module significantly increases output current and power. Based on the characteristics of individual cells, the efficiency of a 36-cell module was calculated: the bifacial module demonstrated a 3.5% efficiency increase compared to the monofacial module under the same area and illumination conditions. Daily power calculations confirmed the positive impact of the rear side on energy production dynamics throughout the day, and the monthly and annual integrated values showed a significant increase in total energy: 910 Wh versus 517 Wh, corresponding to an increase of 76%. An analysis of monthly generation profiles also allowed us to account for seasonal fluctuations in solar radiation and determine the periods of peak performance for bifacial modules. Overall, the study's results demonstrate that the use of bifacial modules significantly improves the energy efficiency of photovoltaic systems, which is particularly important for optimizing solar power plant operation in various climatic and operating conditions.

Conflict of interest statement

The authors declare that they have no conflict of interest in relation to this research, whether financial, personal, authorship or otherwise, that could affect the research and its results presented in this paper.

CRediT author statement

Rustemov A.: Investigation, Writing – original draft; **Ibraimov M.**: Conceptualization, Methodology; **Almen D.**: Data curation, Writing – review & editing; **Svanbayev Ye.**: Methodology, Supervision; **Saymbetov A.**: Funding acquisition, Project administration; **Nurgaliyev M.:** Validation, Funding acquisition; **Kapparova A.**: Formal analysis, Writing – review & editing; **Orynbassar S.**: Visualization, Writing – original draft. The final manuscript was read and approved by all authors.

Statement on the use of Artificial Intelligence.

The authors declare that no artificial intelligence tools were used to generate scientific content, results, or conclusions of this article.

Data Availability Statement

The data are available upon reasonable request from the authors.

Funding

This work has received funding from the research project AP26197983 of Committee of Science of the Ministry of Science and Higher Education of the Republic of Kazakhstan.

References

1 Diao, A., Thiaw, B., Boiro, M., Mbodji, S., Sissoko, G. (2021). A junction electric field determination of a bifacial silicon solar cell under a constant magnetic field effect by using the photoconductivity method. *Journal of Modern Physics*, 12(5), 635-645. https://doi.org/10.4236/jmp.2021.125041

2 Patel, M. T., Khan, M. R., Sun, X., & Alam, M. A. (2019). A worldwide cost-based design and optimization of tilted bifacial solar farms. *Applied Energy*, 247, 467 – 479. https://doi.org/10.1016/j.apenergy.2019.03.150

3 Matarneh, G. A., Al-Rawajfeh, M. A., & Gomaa, M. R. (2022). Comparison review between monofacial and bifacial solar modules. *Technology audit and production reserves*, 6(1/68), 24 – 29. https://doi.org/10.15587/2706-5448.2022.268955

4 Guerrero-Lemus, R., Vega, R., Kim, T., Kimm, A., & Shephard, L. E. (2016). Bifacial solar photovoltaics–A technology review. *Renewable and sustainable energy reviews*, 60, 1533-1549. https://doi.org/10.1016/j.rser.2016.03.041

5 Jahangir, J. B., Al-Mahmud, M., Shakir, M. S. S., Haque, A., Alam, M. A., & Khan, M. R. (2022). A critical analysis of bifacial solar farm configurations: Theory and experiments. *IEEE Access*, 10, 47726-47740. https://doi.org/10.1109/ACCESS.2022.3170044

6 Joseph, K. V., Rosana, N. M., Kumar, J. A., & Samrot, A. V. (2025). Commercial bifacial silicon solar cells-Characteristics, module topology and passivation techniques for high electrical output: An overview. *Results in Engineering,* 26, 104971. https://doi.org/10.1016/j.rineng.2025.104971

7 Ohtsuka, H., Sakamoto, M., Koyama, M., Tsutsui, K., Uematsu, T., & Yazawa, Y. (2001). Characteristics of bifacial solar cells under bifacial illumination with various intensity levels. *Progress in Photovoltaics: Research and Applications*, 9(1), 1-13. https://doi.org/10.1002/pip.336

8 Silvestre, S., Boronat, A., & Chouder, A. (2009). Study of bypass diodes configuration on PV modules. *Applied energy*, 86(9), 1632-1640. https://doi.org/10.1016/j.apenergy.2009.01.020

9 Ko, S. W., Ju, Y. C., Hwang, H. M., So, J. H., Jung, Y. S., Song, H. J., & Kang, G. H. (2017). Electric and thermal characteristics of photovoltaic modules under partial shading and with a damaged bypass diode. *Energy,* 128, 232-243. https://doi.org/10.1016/j.energy.2017.04.030

10 Singh, J. P., Aberle, A. G., & Walsh, T. M. (2014). Electrical characterization method for bifacial photovoltaic modules. *Solar energy materials and solar cells*, 127, 136-142. https://doi.org/10.1016/j.solmat.2014.04.017

11 Brano, V. L., & Ciulla, G. (2013). An efficient analytical approach for obtaining a five parameters model of photovoltaic modules using only reference data. *Applied Energy*, 111, 894-903. https://doi.org/10.1016/j.apenergy.2013.06.046

12 Ahmed, E. M., Aly, M., Mostafa, M., Rezk, H., Alnuman, H., & Alhosaini, W. (2022). An accurate model for bifacial photovoltaic panels. *Sustainability*, 15(1), 509. https://doi.org/10.3390/su15010509

13 Hong, D., Ma, J., Man, K. L., Wen, H., & Wong, P. (2022). Prediction of IV characteristics for Bifacial PV Modules via an alpha-beta single double-diode model. In *2022 IEEE Energy Conversion Congress and Exposition (ECCE),* 1-5. IEEE. https://doi.org/10.1109/ECCE50734.2022.9948042

14 Singh, J. P., Walsh, T. M., & Aberle, A. G. (2014). A new method to characterize bifacial solar cells. *Progress in Photovoltaics: Research and Applications*, 22(8), 903-909. https://doi.org/10.1002/pip.2341

15 Sahu, P. K., Batzelis, E. I., Chakraborty, C., & Roy, J. N. (2024). Electrical modeling of bifacial PV modules. *IEEE Journal of Photovoltaics*. https://doi.org/10.1109/JPHOTOV.2024.3501403

16 Becerra, V. G., Valdivia-Lefort, P., Barraza, R., & García, J. G. (2024). Electrical model analysis for bifacial PV modules using real performance data in laboratory. *Energies*, 17(23), 5868. https://doi.org/10.3390/en17235868

17 Raya-Armenta, J. M., Ortega, P. R., Bazmohammadi, N., Spataru, S. V., Vasquez, J. C., & Guerrero, J. M. (2021). An accurate physical model for PV modules with improved approximations of series-shunt resistances. *IEEE Journal of Photovoltaics*, 11(3), 699-707. https://doi.org/10.1109/JPHOTOV.2021.3056668

18 Zhang, Y., Yu, Y., Meng, F., & Liu, Z. (2019). Experimental investigation of the shading and mismatch effects on the performance of bifacial photovoltaic modules. *IEEE Journal of Photovoltaics*, 10(1), 296-305. https://doi.org/10.1109/JPHOTOV.2019.2949766

19 Shahverdian, M. H., Sayyaadi, H., & Sohani, A. (2026). Integrated mathematical and hybrid optimization framework for parametric analysis of single diode bifacial photovoltaic panels. *Energy Conversion and Management*. X, 101516. https://doi.org/10.1016/j.ecmx.2025.101516

20 Becchi, L., Belloni, E., Bindi, M., Intravaia, M., Lozito, G. M., & Laudani, A. (2024). Optical and electrical model for vertical-mounted bifacial solar panels. In 2024 IEEE International Symposium on Systems Engineering (ISSE), 1-6. https://doi.org/10.1109/ISSE63315.2024.10741094

21 Nussbaumer, H., Klenk, M., Morf, M., & Keller, N. (2019). Energy yield prediction of a bifacial PV system with a miniaturized test array. *Solar Energy*, 179, 316-325. https://doi.org/10.1016/j.solener.2018.12.042

22 Bouchakour, S., Valencia-Caballero, D., Luna, A., Roman, E., Boudjelthia, E. A. K., & Rodríguez, P. (2021). Modelling and simulation of bifacial PV production using monofacial electrical models. *Energies*, 14(14), 4224. https://doi.org/10.3390/en14144224

23 Dosymbetova, G., Mekhilef, S., Saymbetov, A., Nurgaliyev, M., Kapparova, A., Manakov, S., & Koshkarbay, N. (2022). Modeling and simulation of silicon solar cells under low concentration conditions. *Energies*, 15(24), 9404. https://doi.org/10.3390/en15249404

24 Salilih, E. M., Leon-Salas, W. D., Gonzalez, L. G. R., Larico, P. F., Cornejo, M. V., Postigo-Málaga, M., & Gonzales, J. M. J. (2025). Energy output assessment and tilt angle optimization of north/south configured bifacial PV module using single diode model in mountainous region. *Energy Conversion and Management*: X, 101302. https://doi.org/10.1016/j.ecmx.2025.101302

25 Ghafiri, S., Darnon, M., Davigny, A., Trovão, J.P.F., & Abbes, D. (2024). A comprehensive performance evaluation of bifacial photovoltaic modules: insights from a year-long experimental study conducted in the Canadian climate. *EPJ Photovoltaics*, 15, 28. https://doi.org/10.1051/epjpv/2024025

AUTHORS' INFORMATION

Rustemov, Almas – PhD student, Department of Physics and Technology, Al-Farabi Kazakh National University, Almaty, Kazakhstan; https://orcid.org/0009-0009-6970-0746 rustemov_almas3@kaznu.edu.kz

Ibraimov, Margulan – PhD, Acting Professor, Department of Physics and Technology, Al-Farabi Kazakh National University, Almaty, Kazakhstan; Scopus ID: 57189617696, https://orcid.org/0000-0002-8049-3911, Margulan.Ibraimov@kaznu.edu.kz

Almen, Dinara – PhD, Department of Physics and Technology, Al-Farabi Kazakh National University, Almaty, Kazakhstan; Scopus ID: 58837948600, https://orcid.org/0009-0000-8527-4921; dinara.almen@gmail.com

Svanbayev, Yeldos – Candidate of Physical and Mathematical Sciences, Associate professor, Department of Physics and Technology, Al-Farabi Kazakh National University, Almaty, Kazakhstan; Scopus ID: 54906220800, https://orcid.org/0000-0002-0093-7958, yeldos.svanbayev@kaznu.edu.kz

Saymbetov, Ahmet – PhD, Professor, Department of Physics and Technology, Al-Farabi Kazakh National University, Almaty, Kazakhstan; Scopus ID:58529450500, https://orcid.org/0000-0003-3442-8550, Ahmet.Saymbetov@kaznu.edu.kz

Nurgaliyev, Madiyar – PhD, Associate Professor, Department of Physics and Technology, Al-Farabi Kazakh National University, Almaty, Kazakhstan; Scopus ID: 57202335235, https://orcid.org/0000-0002-6795-5384, Madiyar.Nurgaliyev@kaznu.edu.kz

Kapparova, Ainur – PhD student, Department of Physics and Technology, Al-Farabi Kazakh National University, Almaty, Kazakhstan; Scopus ID: 58028607300, https://orcid.org/0009-0008-8348-902X, Ainur.Kapparova@kaznu.edu.kz

Orynbassar, Sayat – PhD student, Department of Physics and Technology, Al-Farabi Kazakh National University, Almaty, Kazakhstan; Scopus ID: 58028274600, https://orcid.org/0009-0001-9124-2560, Sayat.Orynbassar@kaznu.edu.kz

EURASIAN PHYSICAL TECHNICAL JOURNAL

2026, Volume 23, No. 2(56)

https://doi.org/10.31489/2026N2/67-77

Received: 04/11/2025 Revised: 29/01/2026 Accepted: 26/06/2026 Published online: 30/06/2026

Research Article

UDC 539.5; 62-144; 62-762.63

INVESTIGATION OF THE DURABILITY PARAMETERS AND JUSTIFICATION OF THE EFFECTIVENESS OF THE NEW MODEL OF THE VALVE ASSEMBLY OF THE ROD DEPTH PUMP

Ivanova O.V.*, Savinkin V.V.

M. Kozybayev North Kazakhstan University, Petropavlovsk, Kazakhstan
*Corresponding author: itf.nkzu@mail.ru

Abstract. *The scientific article is devoted to the study of the criterion parameters of the durability of the rod depth pump and the determination of the dependencies of the effective operation of the valve on the structural and material characteristics of the ball-saddle pair. The purpose of the study is to substantiate the possibility of using modern structural materials, new structures with elastic-damping properties of the valve while increasing its tightness. To solve the problems of valve wear and increase the maintenance period, the choice of a synthetic polymer for the outer surface of the locking device from the group of organic synthetic polymers (7B-14MA TS 38-105-1082-86) with a ceramic filler made of zirconium dioxide (ZrO_2) is justified. This development will provide damping and an increase in the width of the contact belt of the conditional meridian of the ball for effective redistribution of the shock load. The proposed ceramic filler made of zirconium dioxide will reduce the wear on the surface of the locking device. Mathematical simulation and bench tests have confirmed the validity of the choice of method and materials for the developed combined ball design, which consists of a steel core gummed with a rubber compound with a zirconium dioxide filler. The use of a combined rubberized ball with filler increases the fatigue strength of the valve seat by more than 30%.*

Keywords: rod depth pump, valve pair, wear, resource durability, combined materials.

1. Introduction

The oil and gas industry plays an important role in the development of the economy of any dynamically developing country. According to experts, the stock of wells at a late stage of development (with a flow rate of less than 40 m^3/day) currently accounts for more than 50% of the total number of operating wells. This is due to a decrease in light oil reserves due to its intensive production and depletion of existing fields [1-2].

As oil fields are developed, the operating conditions of pumping complexes deteriorate, and accordingly, the requirements for their reliability and durability become stricter. Consequently, companies face the challenge of developing and applying modern energy-efficient extractive pumping systems with increased durability. Today, approximately 70% of existing oil wells in the world are operated by downhole rod pumps (DRP). Despite the high failure rate of rod installations, the massive scale of their operation and extensive functionality confirm the relevance of research and development work on the development of new structural and technological solutions in order to increase the service life of rod depth pumps [3-5].

The scientific and technical problem lies in the fact that the pumping unit is put into operation at the set factory (ideal) parameters. Since the beginning of operation of oil-producing pumps, their technical characteristics change and over time do not correspond to the nominal values of the manufacturer. The wear

of the main pump parts, as a result of the aggressive action of the medium and dynamic loads, generally reduces the service life of mining plants. Preliminary studies have allowed us to form a group of parts operating with a high degree of loading (plunger-cylinder) and increased intensity of cyclic operation (valve assembly). As a result, there is a need to develop fundamentally new design and technological solutions to improve performance and resource durability. To solve the tasks set, a systematic research approach and digital methods (CAD/CAM/CAE) should be used to substantiate the optimal pump characteristics with a high confidence probability.

2. Materials and Methods

The analysis of the factors and causes of the failure of rod depth pumps for 2017-2024 under various operating conditions allowed us to form the main types of defects of the RDP (Figure 1) [6-12]. It can be seen from the diagram (Figure 1) that the main factors reducing the durability and reliability of RDP are the presence of mechanical impurities, asphalt-resin-paraffin deposits (ARPD) and corrosive environments in the extracted petroleum products. These figures are 27, 24 and 19%, respectively.

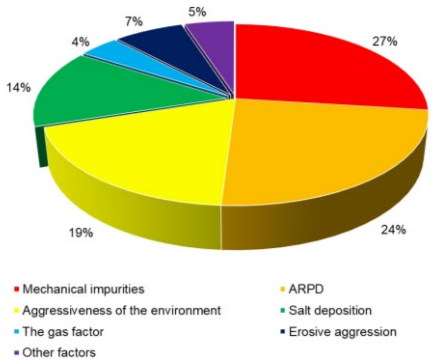

Fig.1. Factors determining the causes of wear of elements of rod depth pumps

It has been established that the main components of the RDP, which are subject to intense wear, include a fixed cylinder, a plunger, a rod, a valve assembly (suction and discharge) and a locking support (for plug-in pumps). The increased intensity (Figure 1) of abrasive-mechanical and corrosive wear of the coupled pump elements leads to a change in the design geometry, a decrease in the physical and mechanical properties of the working surface and a deviation from the design trajectory of the axis of movement of the rod and plunger of the pump. The combination of these parameters leads to an increase in the cyclically changing dynamic shock load, which causes failures (stopping and jamming) of the extraction pumps. The dynamics of the distribution of failures across the structural elements of the RDP is shown in the diagram (Figure 2) [5, 12-14].

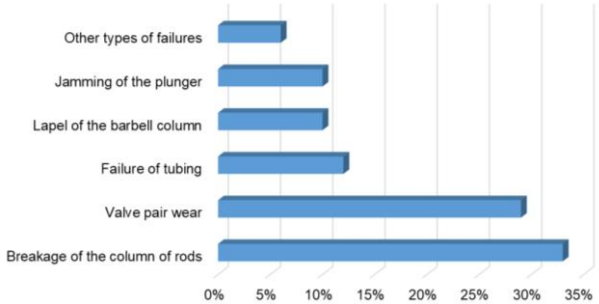

Fig.2. Distribution of the failure rate by the structural elements of the RDP

Valve sticking and ulcerative corrosion of the ball due to the presence of carbon dioxide in the extracted liquid significantly reduce the tightness and performance of the pump. In addition, the wear of the saddle in the ball-saddle pair (about 25%) is also a critical factor, since even minor damage leads to leaks and inefficient operation of the equipment. To solve the scientific and practical problem of determining the dependencies of RDP failures on changes in its dynamometric cyclogram during the wear of highly loaded couplings, an in-depth study of the nodes using 3D modeling is required. It is possible to increase the durability of the valve pair by using new manufacturing technologies and a multicomponent material with damping properties. To

date, insufficient attention has been paid to the technical and operational significance of the valve mechanism. Operating under large alternating loads and fluid pressure, the valve mechanism (Figure 3) generates the volume of the intake oil column, and the condition and performance characteristics of the valve affect the volume of leaks between the coupled elements.

The valve assembly is being investigated as a single ball-seat system. Due to the extreme operating conditions of the ball-saddle system, strict requirements are placed on its reliability and durability. Quartz sand is known to be the main component of mechanical impurities. On the Mohs scale, the hardness of quartz sand particles corresponds to 7 degrees out of 10, which on the Rockwell scale is 60÷70 HRC [15]. Mechanical impurities during the operation of pumping equipment enter the contact zone of the ball and the valve seat, which leads to premature wear and destruction of the hardened surface of the structural elements. The presence of ARPD in the extracted liquid contributes to the build-up, pressing and coking of deposits, reducing the nominal diameter of the bore and the technological gap δ. The effect of alternating loads, cyclically repeated impacts of the ball on the seat contributes to the formation of microcracks and depressurization of the ball seat. Also, complicated operating conditions lead to additional sliding resistance forces of the mating surfaces, giving a singularity to the wear process. All of the above factors lead to rapid wear of the valve assembly, and as a result, to a decrease in the maintenance period and, subsequently, to the failure of the RDP [4]. Based on the research results of domestic and foreign scientists, an understanding of the process of ball deformation and seat discoloration due to friction and internal stresses during shock loads of the ball and seat has been formed.

Due to the configuration of the working surfaces of the ball and the seat, when examining wear, the mating surfaces should include a part of the edge (small area) of the seat with the conditional meridian of the contacting surface of the ball. A sphere inscribed in a cone forms a conditional meridian along the tangent line (Figure 4). With linear sealing, any discrepancy with the projected geometric shapes increases the size of the gap between the contacting elements, which leads to increased leaks of the pumped reservoir fluid [5, 15, 16]. Thus, the distribution of the current cyclic loads is concentrated on a small unit of contact area per unit time.

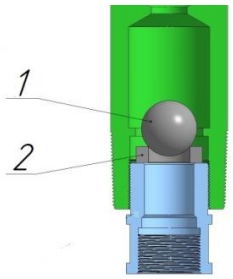

Fig.3. 3D modeling of the valve assembly: 1 – ball, 2 – valve seat

Fig.4. The contact field of the ball-seat valve pair elements

Dolov T.R., Ivanovsky V.N. and other researchers based on a mathematical model and bench tests proved that the ratio of hardness of the ball and the valve seat should be in the range of 1.01÷1.05 [5]. Thus, researchers prioritize the hardness of the ball-seat surfaces, which does not fully describe the effectiveness of the valve opening and closing process. According to GOST 31835-2012, the ball-seat valve pair of the pump is manufactured in two versions (Figure 5). The optimal value of the ratio of the diameter of the seat hole d_h to the diameter of the ball d_b is 0.865. This ratio plays an important role in optimizing the operation of the valve assembly, ensuring effective interaction between the seat and the ball, minimal hydraulic resistance of the fluid and increasing its operability [5, 17].

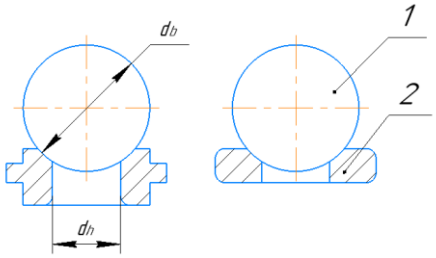

a) b)

Fig.5. Ball-seat valve pair: 1 – ball; 2 – seat; a – valve with a collar (VC); b –valve with a cylindrical seat (V)

The main materials used to make the valve pair are: for the ball – 95Cr18 steel (high carbon stainless steel with a hardness of 65 HRC) and for the seat – 30Cr13 and 95Cr18 (stainless steel with a hardness of 45 HRC). A selection of hard alloys such as tungsten carbide, titanium carbide and cobalt alloys provides high wear resistance. The use of stellites – alloys of cobalt, nickel and chromium, ceramets improve the performance and reliability of valves. These innovations help to reduce leaks and extend the service life of pumps [17, 18].

The problems of improving the efficiency of RDP were solved by domestic and foreign scientists. The main disadvantages of the known designs are an increase in the cost of the pumping unit due to the inclusion of additional elements in the design, for example, spring mechanisms, and a decrease in the reliability of equipment due to an increase in the number of parts, especially small ones.

It is proposed to increase the efficiency and service life of the RDP by increasing the wear resistance of the contacting elements of the parts, without changing the integrity of its structure. The operability of the valve assembly design, based on standard requirements, depends on maintaining the criteria parameters [5, 15, 18]:

- the mass of the ball should be less than the mass of the saddle (reducing the weight of the ball by reducing the diameter or replacing the material);
- the strength characteristics of the saddle must exceed the parameters of the ball to prevent the saddle from crumpling from the action of cyclic impacts of the ball;
- the hardness of the ball must be higher than the hardness of the saddle in order for the ball to retain its original shape and condition.

Therefore, the main focus of reducing operating costs is the introduction of innovative ways to reduce wear on the valve assembly. Since the operability of the valve assembly during operation is affected not only by the physico-mechanical properties of the mating surfaces, but also by the kinematic features (moment, forces, mass and velocity, gap overlap) of the locking element, it is theoretically assumed that in order to ensure high durability of the valve mechanism, it is necessary to ensure uniform redistribution in conditions of small contact areas a cyclically varying shock load at the moment the valve is closed.

The scientific and technical problem is proposed to be solved by creating an elastic valve closure effect through the use of materials with damping properties. To reduce valve wear and increase the maintenance period, it is proposed to use a coating of a material from a group of organic synthetic polymers with a ceramic filler made of zirconium dioxide (ZrO_2) for the outer surface of the locking device [19-21]. A reasonable choice of synthetic material applied to the valve ball will solve the problem of damping and increasing the width of the contact belt of the conditional meridian of the ball to effectively redistribute the shock load, and the use of a ceramic filler made of zirconium dioxide will increase the wear of the surface of the locking device.

The analysis of defective certificates and repair works of Mangystaumunaigas JSC (Kazakhstan) shows that the main wear is observed on the valve seat, where a harder ball creates an annular spot, which gradually increases due to deepening. The valve seat is made of 40Cr steel (GOST 4543-71) with normalization up to 45÷53 HRC. The locking ball is made of high-strength specialized steel type BCr15 (bearing structural steel) (GOST 801-2022) with a hardness of 60÷65 HRC. Therefore, it is necessary to conduct a theoretical study to substantiate the optimal kinematic parameters of a valve with different materials of the shut-off ball.

To evaluate the stress-strain state (SSS) of the valve pair elements during the seating of the closure member and to predict its operational durability, numerical modeling was performed using the Finite Element Method (FEM). The calculations were carried out in the COMPASS 3D computer-aided design environment using the integrated structural and fatigue analysis module APM FEM (Research and Development Center "APM"). The problem was solved in a three-dimensional quasi-static formulation (linear static analysis), where dynamic factors were converted into equivalent static loads. The structural configuration and boundary conditions of the numerical model were defined as follows:

– Seat Constraints: The lower and external cylindrical faces of the valve seat were rigidly fixed in all directions (full displacement constraint: $U_x = U_y = U_z = 0$), simulating its press-fit installation into the pump housing.

– Ball Degrees of Freedom: To ensure numerical stability of the contact interface and eliminate any unconstrained rigid-body motion (loss of stability), the ball was restricted from moving along the horizontal axes X and Y ($U_x = U_y$). Displacement along the vertical working axis Z (the valve's axis of symmetry) was left free to absorb operational loads.

– Contact Interaction: A non-linear, one-way "Sliding" interaction type was specified at the mating surfaces between the ball sphere and the seat cone. This contact condition allows mutual sliding and micro-

displacements of the surfaces without structural penetration of the bodies, thereby capturing the true distribution of contact pressure.

A combination of external forces simulating the final phase of valve closure was simultaneously applied to the numerical model:

1 Resultant differential pressure (ΔP = 7.6 MPa): Applied normally to the upper geometric segment of the ball bounded by the actual circular seating contact line located below the equator. This consolidated parameter accounts for the combination of downhole and operational factors acting at the moment of valve closure: the wellhead discharge pressure, the hydrostatic pressure of the fluid column at the pump setting depth, the hydrodynamic water hammer pressure generated by the instantaneous stoppage of the flow upon valve closure, and the static reservoir pressure. Simultaneously, the structural elements of the valve seat were subjected to their respective downhole pressures: the upper face of the seat was exposed to the combined downward pressure of 20.78 MPa, while the inner cylindrical surface of the orifice (d_h=35 mm) experienced the outward radial reservoir pressure of 14.04 MPa.

2 Total equivalent vertical force (F_{tot}): Applied as a body force to the center of mass of the closure member, directed vertically downward along the valve axis of symmetry. This parameter combines the dead weight of the component and the dynamic inertial force generated during its seating deceleration. Depending on the design variant and material density, the total force is set to 6.03 N for the solid steel ball and 3.55 N for the rubberized ball with filler.

To assess the operational reliability of the ball-seat pair under cyclic loading, a fatigue life calculation was conducted within the APM FEM module:

– Loading Regime: An asymmetric loading cycle was defined to match the pulsating nature of the oil pump's operation (stress ratio R=0, where the lower limit of the cycle corresponds to the open valve state and the upper limit corresponds to the moment of hard seating under pressure).

– Fatigue Base: The calculation was performed for a standard base number of loading cycles N = 2.5 · 10^6, which defines the limit of finite life for heavily loaded components operating under contact and crushing stresses.

– Fatigue Strength Parameters: The physical and mechanical parameters of the fatigue curves (including the endurance limits under symmetrical bending σ_{-1} and torsion τ_{-1}) for the investigated steel grades (Steel BCr15, Steel 40Cr and Steel 20) were retrieved automatically from the integrated standard reference database of the APM FEM software. This eliminated subjective interpolation errors associated with experimental Wöhler curves.

The physical and mechanical properties of the materials used are shown in Table 1.

Table 1. Physical and Mechanical Properties of Materials

Structural Element	Material / Regulatory Document	Elastic Modulus E, MPa	Poisson's Ratio, ν	Density ρ, kg/m³	Yield Strength, σ_y, MPa	Ultimate Tensile Strength, σ_{UTS}, MPa
Seat	Steel 40Cr / GOST 4543-71	$2.0 \cdot 10^5$	0.30	7820	~800	~1000
Metal ball	Steel BCr15 / GOST 801-2022	$2.1 \cdot 10^5$	0.30	7812	1100 – 1200	1400
Core	Steel 20 / GOST 1050-2013	$2.1 \cdot 10^5$	0.29	7860	250	410
Coating 1	Combined material: rubber compound 7B-14MA and PCRK-3 (20%) / TS 38-105-1082-86 and GOST 21907-76	30 ÷ 50*	0.45	~1621	–	10 ÷ 15*
Coating 2	Combined material: polyurethane brands Adiprene L167 and PCRK-3 (10%) / TS 38.103-137-78 and GOST 21907-76	500 ÷ 2000*	0.45	~1368	~10 – 40	~15 – 55*

** Note to Table 1: Values for the rubber compound are specified conditionally within a linear-elastic framework. The actual values of the elastic modulus E and ultimate tensile strength σ_{UTS} are subject to verification against the physical testing certificate of the specific rubber batch.*

The geometry was discretized using an adaptive method with a mesh composed of four-node rigid tetrahedral elements:

– the baseline mesh size for both the ball and the seat bodies was set to 2.0 mm;

– local mesh refinement (densification) was implemented in the immediate area of mechanical contact (on the conical chamfer of the seat and the mating zone of the sphere). The finite element size in the contact zone was reduced to 1.0 mm to ensure accurate approximation of the Hertzian contact stress gradient.

When interpreting the results of the numerical experiment, the fundamental limitations of the built-in APM FEM solver were taken into account:

– Linear Elasticity of Media: Material behavior is described by Hooke's generalized law. The module does not account for physical non-linearity (plastic deformation of metals during local crushing) or the hyperelastic behavior of elastomers (models of Mooney-Rivlin, Ogden and others). Stresses exceeding the yield strength σ_y are treated as potential initiation zones for plastic deformation.

– Quasi-Static Load Application: Transient dynamic wave processes occurring in the metal during the microsecond duration of the impact were not modeled. The load was applied instantaneously as a steady-state static system of forces.

– Absence of Lubrication Film: The calculation assumes dry contact conditions between the surfaces. The damping and hydrodynamic effects of the fluid film (crude oil) directly within the contact gap were omitted, which provides a safety margin for structural strength.

3. Results and discussion

To maintain the lowest possible level of liquid leakage through the valve pair, it is necessary to ensure that the shut-off element fits on the valve seat in a timely manner. In the works of Pirverdyan A.M. and Greifer V.I., the dependence of the landing speed of the locking element on the valve seat was established. At the same time, the landing speed of the locking element must be at least 0.1 m/s. This dependency has the following form [15, 22]:

$$v = \frac{V_{l.e.} \cdot g \cdot (\rho_{l.e.} - \rho_l)}{6\pi \cdot r \cdot \mu}, \tag{1}$$

where v – the landing speed of the locking element on the valve seat, m/s; $V_{l.e.}$ – volume of the locking element, m^3; g – acceleration of free fall, g=9.81 m/s^2; $\rho_{l.e.}$ – material density of the locking element, kg/m^3; ρ_l – the density of the pumped liquid, kg/m^3; r – radius of the locking element, m; μ – dynamic viscosity of the liquid, mPa·s.

Substituting the expression for the volume of the ball into formula (1), we obtain:

$$v = \frac{2r^2 g \cdot (\rho_{l.e.} - \rho_l)}{9\mu}. \tag{2}$$

We accept oil with a density of 904 kg/m^3 and a dynamic viscosity of 39.4 mPa·s as a working medium (Kalamkas field, RK). The landing speed of the locking element in the form of a metal ball (Steel BCr15 GOST 801-2022, density 7812 kg/m^3) will be v_{st} = 0.24 m/s. When replacing the ball material, in order to ensure the optimal landing speed, it is necessary to change the mass of the locking element as little as possible (m_{st} = 0.511 kg). To achieve this goal, a multicomponent structure was developed, which is a spherical steel core, gummed with a combined shell. Taking into account the imposed restriction on the landing speed of the locking element, a dependence is obtained for calculating the minimum radius of the core r_c (3):

$$r_c > r \cdot \sqrt[3]{\frac{\frac{0{,}9\mu}{2r^2 g} + \rho_l - \rho_{sh}}{\rho_c - \rho_{sh}}}, \tag{3}$$

where ρ_c – core density (steel), kg/m^3; ρ_{sh} – shell density (rubber compound, polyurethane), kg/m^3.

Taking Steel 20 GOST 1050-2013 with a density of ρ_c=7860 kg/m^3 as the material for the ball core, for a shell made of a rubber compound, $\rho_{sh.rub}$=1370 kg/m^3 and for a shell made of polyurethane, $\rho_{sh.pol}$=1259 kg/m^3, we obtain the minimum radius of a core gummed with a rubber compound $r_{st.rub}$=0.0180 m and polyurethane $r_{st.pol}$=0.0182 m. To approximate the mass of a gummed ball to the mass of a solid ball, we take the core diameter to be 38 mm. Then, for a rubberized ball, the average density will be $\rho_{st.rub}$=4219 kg/m^3 ($m_{st.rub}$=0.276 kg), and for a ball with a polyurethane shell $\rho_{st.pol}$=4157 kg/m^3 ($m_{st.pol}$=0.272 kg), and, accordingly, the landing velocity of the locking element will be $\nu_{st.rub}$=0.115 m/s and $\nu_{st.pol}$=0.113 m/s. The obtained values of the landing

velocity of rubberized and polyurethane balls with a metal core are slightly higher than the critical value (v>0.1 m/s). There are two possible solutions to increase the mass of the locking element. The first is to reduce the thickness of the gummed shell, which will lead to a decrease in the resource life of the coating. The second option is the introduction of strengthening additives into the elastomeric matrix, which will lead to an increase in density and an improvement in the strength characteristics of the shell.

A reasonable choice of a gumming compound consisting of a base (rubber compound or polyurethane) and a synthetic material with a zirconium dioxide filler applied to the metal core of the valve ball provides damping and an increase in the width of the contact belt of the conditional meridian of the ball for effective redistribution of shock load. The experiment used a rubber compound grade 7B-14MA according to Technical Specification TS 38-105-1082-86. To achieve maximum mechanical strength, aging resistance, and heat resistance, the maximum allowable mass fraction of the zirconium dioxide filler should not exceed 25 phr (parts per hundred rubber), i.e., no more than 20% (ρ_{ZrO_2}=6080 kg/m^3). Exceeding this threshold often leads to particle agglomeration (the filler clumping together) and deterioration of the physical and mechanical properties of the product. For polyurethane, this value should not exceed 10–15%.

Then the parameters of the studied samples of the locking elements will be as follows:

- for a rubberized ball with filler: the maximum permissible mass fraction of the filler with zirconium dioxide is 20%; the average density of $\rho_{st.rub.fil}$=4355 kg/m^3, the mass of the ball is $m_{st.rub.fil}$=0.285 kg;
- for a polyurethane ball with filler: the maximum permissible mass fraction of a filler with zirconium dioxide is 10%; the average density of $\rho_{st.pol.fil}$=4218 kg/m^3, the mass of the ball $m_{st.pol.fil}$=0.276 kg.

The average density of the shell of the ball for different variants is calculated according to the following dependence (4):

$$\frac{1}{\rho_{sh}} = \frac{\omega_{base}}{\rho_{base}} + \frac{\omega_{ZrO_2}}{\rho_{ZrO_2}}, \tag{4}$$

where ρ_{sh} – the density of the shell with filler, kg/m^3; ρ_{base} – the density of the base material, kg/m^3; ρ_{ZrO_2} – the density of zirconium dioxide, kg/m^3; ω_{base} – mass fraction of the base material in the shell; ω_{ZrO_2} – the mass fraction of zirconium dioxide in the shell material.

The total density of the ball and its mass are determined by well-known mathematical relationships.

The landing speeds of the locking elements will be $v_{st.rub.fil}$=0.135 m/s and $v_{st.pol.fil}$=0.123 m/s, respectively. The obtained value of the landing velocity of the locking element made of a combined rubberized ball with filler more fully satisfies the condition v>0.1 m/s.

To calculate the hydraulic losses in the valve assembly connections, it is necessary to determine the pressure loss in the valve assembly during suction (Δp, Pa) [22]:

$$\Delta p = \frac{v_{\max}^2 \cdot \rho_{ld}}{2 \cdot \xi_{val}^2}, \tag{5}$$

where v_{max} – the maximum speed of product movement in the valve seat opening, m/s; ρ_{ld} – the density of the degassed liquid, kg/m^3; ξ_{val} – the valve flow rate, determined by special graphs (Figure 6) depending on the Reynolds number in the valve (in the seat opening).

Maximum speed of product movement in the valve:

$$v_{\max} = \frac{4 \cdot q_{val}}{d_{val}^2}, \tag{6}$$

where q_{val} – product consumption through the valve, m^3/s; d_{val} – valve seat hole diameter, m.

The Reynolds number in the valve seat opening is determined by the following relationship:

$$Re_{val} = \frac{v_{\max} \cdot d_{val}}{v_l}, \tag{7}$$

where v_l – kinematic viscosity of a liquid, m^2/s.

To perform the calculations, we take the following initial data: valve seat hole diameter d_h=35 mm; maximum pump pressure p_{exit} =6.3 MPa; volumetric pump flow q_{val}=20.9 m^3/day, q_{val}=2.42·10^{-4} m^3/s; kinematic viscosity of oil v_l=4.36·10^{-5} m^2/s; oil density ρ_l=904 kg/m^3.

The maximum velocity of the working fluid in the pump is calculated by formula (6) – $v_{\max}$=0.79 m/s. We determine the Reynolds number by the formula (7) – Re_{val}=634.17. The resulting value of the Reynolds number is less than the critical value (Re_{cr}≈ 2100÷2300). The value of the Reynolds number depends on the

specific type of flow through the cross-section of the passage channel when the ball is flowing. Small values of the Reynolds number correspond to a situation where the viscosity forces (v_l=4.36·10^{-5} m^2/s) dampen turbulence, making the flow laminar. The flow coefficient of the valve ξ_{val} with a value of the Reynolds number in the range 600<Re< 3·10^4 will be equal to ξ_{val}=0.4 (Figure 6, curve 1) [22].

Using formula (5), we calculate the pressure loss in the valve Δp=0.002 MPa during suction, taking into account that the density of the degassed liquid ρ_{ld}=990.4 kg/m^3. Then the maximum pressure in the pump cylinder will be: $p = p_{exit} + \Delta p$. Then p=6.302 MPa.

The coefficient of hydraulic resistance λ along the length of the flow, which takes into account the hydraulic conditions of the fluid flow, the viscosity of the fluid and the relative roughness Δ/d of the walls (Δ is the absolute roughness) is a function of these parameters, that is, $\lambda = f$ (Re, Δ/d).

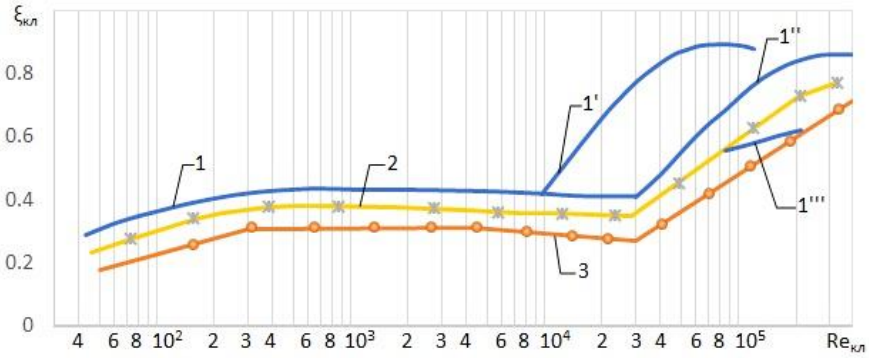

Fig.6. Dependence of the valve flow rate on the Reynolds number: 1 – with one ball and with windows: 1' – d_{val}=14 mm; 1'' – d_{val}=5 mm; 1''' – d_{val}=30 mm; 2 – with one ball and a stack; 3 – with two balls

For the studied operating conditions of the valve pair in laminar operation (Re=634.17), the hydraulic resistance coefficient λ along the flow length is a function of the Reynolds number – $\lambda = f$ (Re) and, according to the method of T.M. Bashta, it is proposed to determine the dependence (8):

$$\lambda = \frac{75}{\mathrm{Re}}. \tag{8}$$

Then, at Re < 2320, the coefficient of hydraulic resistance will be equal to λ=0.118.

Provided that the initial velocity of the shut-off element is v_0=0 m/s and the movement is considered to be equidistant, the opening time of the valve t_x (s) will determine the dependence (9):

$$t_x = \sqrt{\frac{2m_P \cdot h_{\max}}{\Delta p \cdot F_{sav}}}, \tag{9}$$

where m_P – weight of the locking element with attached parts, kg; h_{max} – maximum stroke of the closing element, m; F_{sav} – cross-sectional area of the valve passage, m^2.

From the valve design, the maximum stroke of the closing element is 23 mm. For a steel ball, the opening time t_{st} and acceleration a_{st} of the valve movement is t_{st}=0.12 s and a_{st}=2 m/s^2. Accordingly, for a rubberized ball with filler, the opening time and acceleration of the valve movement are $t_{st.rub.fil}$=0.09 s and $a_{st.rub.fil}$ =1.5 m/s^2. According to a theoretical study, it is advisable to replace the steel shut-off element of the valve with a new ball design, which is a metal ball gummed with a composite rubber compound with a zirconium dioxide filler. The effectiveness of the combined valve must be checked by simulation. The simulation problem was solved using the numerical method in the APM FEM software module. This software module is an APM Studio module adapted for COMPASS 3D from APM WinMachine. The geometric 3D model was created in the COMPASS-3D environment, where materials and their properties were also specified (Figure 7a). The finite element model is based on 10-node tetrahedra and contains 86077 nodes and 50112 finite elements. To simulate the stress-strain state of the valve pair and perform calculations, a computational model was built (Figure 7b).

a) b)

Fig.7. Valve pair: a) a model of a pump valve pair made in the Compass 3D software environment; b) calculated CAM of the valve assembly in the APM FEM environment

The APM FEM software module performs calculations for strength and fatigue at $2.5 \cdot 10^6$ loading cycles. The simulation was carried out for two cases: the first, the interaction of the valve seat with a steel ball, and the second, the interaction of the seat and a combined rubberized locking element with a zirconium dioxide filler. The parameter to be determined in the study of the strength characteristics of the working elements of the pump structure is equivalent stresses (σ_e), determined by the fourth theory of strength in dynamic calculation. Based on the simulation results, maps of the equivalent stress distribution according to Mises (Figure 8), yield strength reserve coefficients (Figure 9) and fatigue strength reserve coefficients (Figure 10) were obtained.

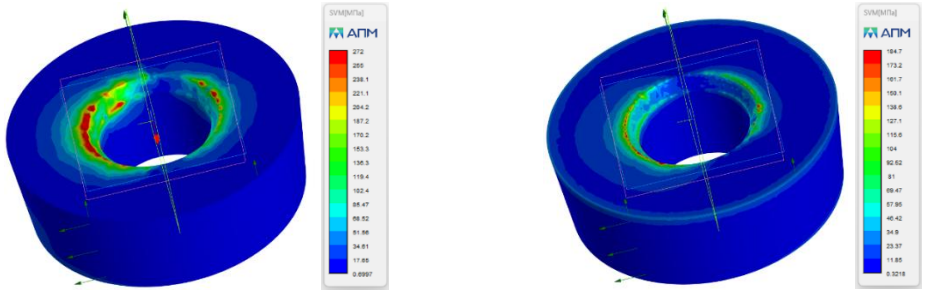

a) b)

Fig.8. Distribution of equivalent Mises stresses in the valve seat: a – when interacting with a steel ball (σ_{max}=272 MPa); b – when interacting with a rubberized ball with filler (σ_{max}=185 MPa)

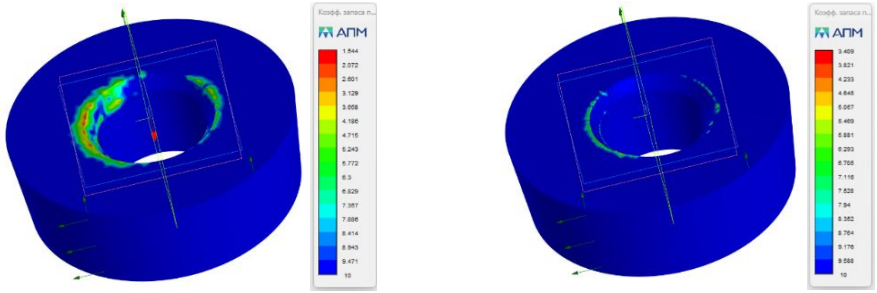

a) b)

Fig.9. Distribution of the reserve coefficient according to the yield strength of the valve seat: a – when interacting with a steel ball (n_{min}=1.55); b – when interacting with a rubberized ball with filler (n_{min}=3.41)

The calculations were performed for a shut-off element lined with a combined rubber compound containing a ceramic filler of zirconium dioxide (the mass fraction of the filler is 20%).

An analysis of the results obtained from a study of the design of a ball gummed with a combined rubber compound with a ceramic filler made of zirconium dioxide shows a 30% reduction in stresses in the valve seat and an increase in the coefficient of reserve for the fatigue strength of the valve seat surface in the most stressed areas from n_{min}=1.43 to n_{min}=1.9.

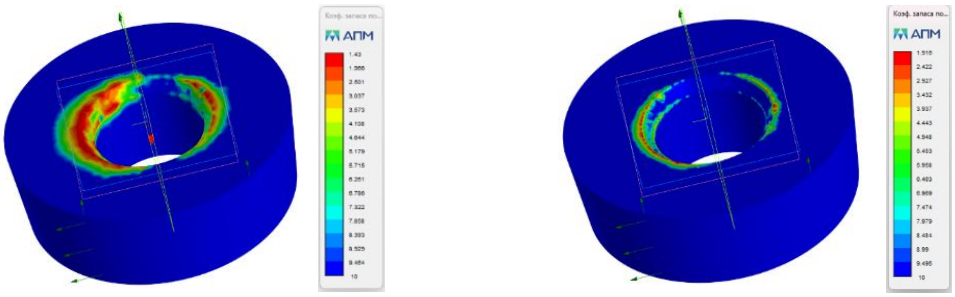

a) b)

Fig.10. Distribution of the reserve coefficient for the fatigue strength of the valve seat: a – when interacting with a steel ball (n_{min}=1.43); b – when interacting with a rubberized ball with filler (n_{min}=1.9)

4. Conclusion

Reducing the rate of change in the regulatory clearance value and reducing the leakage rate during pump operation is achieved by using an effective method to increase the wear resistance of the contacting surfaces of the ball-seat valve pair, which ensures uniform redistribution of the cyclically varying shock load per unit time of valve closure. To meet the speed requirement (v>0.1 m/s) for the landing of the locking element, a composite ball structure consisting of a steel core and a combined rubber shell on the outside has been developed. A ceramic material based on zirconium dioxide (ZrO_2) was chosen as the filler for the rubber compound. The elastic effect of closing the valve is also created through the use of materials (combined rubber compound) with damping properties. The additive material was determined – PCRK-3 powder with a content of 2.5-5% ZrO_2 (72 HRC) –15Cr17Ni12V3F35ZrO_2.

The validity of the choice of the valve assembly improvement method is confirmed by the method of 3D simulation modeling. The use of a combined ball with a filler based on a rubber compound and zirconium dioxide increases the fatigue strength of the valve seat by more than 20%, which leads to an increase in the life of the valve assembly with the same number of loading cycles.

Conflict of interest statement

The authors declare that they have no conflict of interest in relation to this research, whether financial, personal, authorship or otherwise, that could affect the research and its results presented in this paper.

CRediT author statement

Ivanova O.V.: Conceptualization, Methodology, Validation, Investigation, Software, Data Curation, Writing - Review & Editing; **Savinkin V.V.**: Methodology, Validation, Investigation, Data Curation, Writing Review & Editing, Writing - Original Draft. The final manuscript was read and approved by all authors.

Statement on the use of Artificial Intelligence.

During the preparation of this manuscript, artificial intelligence tools were used solely for language editing and grammatical improvement. No AI tools were used to generate scientific content, analysis, results, or conclusions.

Data Availability Statement

The data are available upon reasonable request from the authors.

References

1 Kurmanbekov, A., Kabzhalyalova, M., Kaldarov, S., Kamedenova, G. (2024). *An overview of the oil sector for 2023*. Analytical Center of Halyk Finance JSC, 17. https://halykfinance.kz/download/files/analytics/HF.pdf [in Russain]

2 Kurmanbekov, A., Kabzhalyalova, M., Kaldarov, S., Kamedenova, G. (2024). *Problems of development of mature deposits*. Analytical Center of Halyk Finance JSC, 4. https://halykfinance.kz/download/files/analytics/HF_Problemy_razrabotki_zrelyh_mestorozhdeniy.pdf [in Russain]

3 Ivanova, O.V. (2022). Analysis of ways to increase the efficiency of low-flow wells. *Proceedings of the 6th International Scientific and practical conference of students, postgraduates and young scientists "Fundamental and applied research of young scientists"*, Omsk, Russia, 61-64. https://is.ku.edu.kz/publishings/%7BE71C0870-2993-4B36-BF3E-5144D6382FD9%7D.pdf [in Russain]

4 Ivanova, O.V., Ratushnaya, T.Yu., Ivanov, E.A. (2022). Analysis of modern technologies for increasing the durability of the valve assembly of an oil-producing rod depth pump. *Proceedings of the international scientific and practical conference "Trends in the development of natural and technical sciences in the modern world"*, Petropavlovsk, 572-579. https://is.ku.edu.kz/publishings/%7B8C458654-BF47-4A4F-A039-A00724BADECD%7D.pdf [in Russain]

5 Dolov, T.R., Ivanovskiy, V.N., Merkushev, S.V., Zhulanov, A.V., Krasnoborov, D.N. (2018). Bases of the Choice of Valvate Knots Borehole of Pump Installations. *Territorija «NEFTEGAS» Oil and Gas Territory*, 6, 66-70. https://cyberleninka.ru/article/n/osnovy-vybora-klapannyh-uzlov-skvazhinnyh-shtangovyh-nasosnyh-ustanovok [in Russain]

6 Serebrennikov, A.V., Petrikevich, P.A., Torop, O.V., Frolov, V.V. (2017). Operation of a mechanized well stock in complicated conditions. *Business Magazine "Neftegaz.RU"*, 7(67), 86-97. https://magazine.neftegaz.ru/articles/dobycha/543654-ekspluatatsiya-mekhanizirovannogo-fonda-skvazhin-v-oslozhnennykh [in Russain]

7 Valiakhmetov, R. (2017). Everything has its place. The use of RDP remains effective under certain conditions. *Oil and Gas Vertical Magazine,* 9, 78-79. http://pump-sovet.com/files/%D0%92%D0%B0%D0%BB% D0%B8%D.pdf

8 Sakhnov R.V. (2015) An integrated approach to the operation of a complicated well stock as a tool to achieve the goal. The concept. *Russian Oil and Gas journal of technologies and equipment "Engineering Practice"*, 12. https://glavteh.ru/ [in Russain]

9 Ivanova, T.N., Novokshonov, D.N., Galeyeva, O.A., Bartoshova, A. (2020). Analysis of the effectiveness of the used rod installations deep-water pumps in high-viscosity oil production conditions. *Bulatov readings,* 2, 218-224. https://elibrary.ru/item.asp [in Russain]

10 Ivanova, L.V., Burov, E.A., Koshelev, V.N. (2011). Asphaltene-resin-paraffin deposits in the processes of oil production, transportation and storage. *Electronic scientific journal "Oil and Gas business"*, 1, 268-284. https://ogbus.ru/files/ogbus/authors/IvanovaLV/IvanovaLV_1.pdf [in Russian]

11 Savinkin, V.V., Dmitriev, F.S., Ivanova, O.V., Netesova, E.A. (2017). Problems of efficient operation of downhole deep rod pumps and promising ways to solve technological problems in the production of hydrocarbons. *Bulletin of M. Kozybaev NKSU*, 3(36), 50-55. https://is.ku.edu.kz/Publishings/%7BBB4882F3-793B-41.pdf [in Russain]

12 Shishkina, L.V., Savinov, S.A. (2013). Statistical studies of the causes of failures of deep rod pumps. *Intelligent systems in production*. *Mechanical engineering*, 1, 113-115. [in Russain]

13 Pyalchenkov, D.V. (2016). Investigation of the influence of parameters of producing wells on failures of rod pumping units. *Online magazine "naukovedenie"*, 8, 2, 1-10. https://doi.org/10.15862/140TVN216 [in Russain]

14 Urazakov, K.R., Bogomolny, E.I., Seitpagambetov, Zh.S., Gazarov, A.G. (2003). *Pump Extraction of Highly Viscous Oil from Slant and Drowned Wells*. Nedra-Businesscenter Publishing House LLC, Moscow, Russia, 303. https://www.geokniga.org/bookfiles/geokniga-nasosnayadobychavysokov.pdf [in Russain]

15 Dolov, T.R. *Investigation of the operation of valve assemblies of borehole rod pumping units*. Ph.D. dissertation, Ukhta State Technical University, Ukhta, Russia, 2017. https://www.dissercat.com/content/issledovanie-raboty-klapannykh-uzlov-skvazhinnykh-shtangovykh-nasosnykh-ustanovok [in Russian]

16 Zaurbekov, S.A., Akanova, G.K., Balgayev, D.Y., Zaurbekov, K.S. (2021). Extension of operational life of ball valves in piston and plunger pumps. *MIAB. Mining Inf. Anal. Bull*, 7, 165-175. https://doi.org/10.25018/0236_1493_2021_7_0_165

17 GOST 31835–2012. Well sucker-rod pumps. General technical requirements. Interstate Standard, Moscow, Russia: Standardinform, 2019. https://meganorm.ru/Index/53/53731.htm

18 Yakimov, S., Podkorytov, S. (2013). The quality of RDP valve pairs. TOC is switching to import. *Oil and Gas Vertical Magazine,* 2, 74-77. https://www.ngv.ru/upload/iblock/c62/c625c7a325ae6a34fd9f25def7f368bb.pdf

19 Savinkin, V.V., Ivanova, O.V., Zhumekenova, Z.Z., Sandu, A.V., Vizureanu, P. (2023). Effect of New Design of the Laser Installation and Spraying Method on the Physical and Mechanical Properties the Inner Surface a Small Diameter Coated with 15Cr17Ni12V3F35ZrO_2. *Coatings*, 13(3), 514. https://doi.org/10.3390/coatings13030514

20 Savinkin, V.V., Ivanova, O.V., Kolisnichenko, S.N., Sandu, A.V. (2023). Ensuring the Durability of Oil Producing Pumps Through the Use of Laser Spraying Technology. *Monograph*, *Published by Materials Research Forum LLC*, Millersville, USA, 120. https://www.mrforum.com/product/ensuring-the-durability-of-oil-producing-pumps/

21 Ivanova, O.V., Savinkin, V.V., Sandu, A.V. (2023). Study of Structural Materials 95X18SH in Conjunction with a Rubber Mixture of Group VI and Polyurethane Grade PU SKU-PFL-100 with Damping Properties. *Proceeding of the Intern. Conf. Innovative Research «EUROINVENT ICIR 2023»*, Iasi, Romania, 98. http://www.euroinvent.org/cat/ICIR_2023.pdf

22 Morgunov, K.P. (2014). *Hydraulics: Textbook*. Lan Publishing House, St. Petersburg, Russia, 288. https://techlibrary.ru/b1/2u1p1r1d1u1o1p1c_2s.2x._2k1j1e1r1a1c1m1j1l1a._2014.pdf [in Russian]

AUTHORS' INFORMATION

Ivanova, Olga Vladimirovna – Master, Senior Lecturecity, Department of Transport and Mechanical Engineering, M.Kozybayev North Kazakhstan University, Petropavlovsk, Kazakhstan; SCOPUS Author ID: 57210389962; https://orcid.org/0000-0002-3702-882X; itf.nkzu@mail.ru

Savinkin, Vitaliy Vladimirovich – Doctor of Technical Sciences, Associate Professor, Department of Transport and Mechanical Engineering, M.Kozybayev North Kazakhstan University, Petropavlovsk, Kazakhstan; SCOPUS Author ID: 57195726895; https://orcid.org/0000-0002-7748-3720; cavinkin7@mail.ru

EURASIAN PHYSICAL TECHNICAL JOURNAL

2026, Volume 23, No. 2 (56)

https://doi.org/10.31489/2026N2/78-90

Received: 09/12/2026 Revised: 20/05/2026 Accepted: 26/06/2026 Published online: 30/06/2026

Original Research Article

UDC 532.5

ENHANCEMENT OF DYNAMICS AND DEVELOPMENT OF CONTROL METHODS FOR IMPULSE HYDRAULIC SHOCK MECHANISMS

Smakova N.[1]*, Pankov S.[2], Baisadykov B.[2], Zelenkov V.[2], Toibazarov D.[2], Karypov A.A.[3]

[1] Kazakh University of Technology and Business named after K. Kulazhanov, Astana, Kazakhstan

[2] National Defense University of the Republic of Kazakhstan, Astana, Kazakhstan

[3] LLP "Scientific and Technical Center Almaty Special Design Bureau «Alatau», Almaty, Kazakhstan

Corresponding author: nuri_5@mail.ru

Abstract. *This study examines the dynamic characteristics and improvement of control methods for impulse hydraulic shock mechanisms used in high-performance hydraulic systems. The work focuses on eliminating the common discrepancy between theoretical and actual output parameters caused by inefficient processing of control signals. A mathematical model has been developed that describes the displacement, velocity, and acceleration of the actuator, taking into account nonlinear fluid dynamics and changes in external load. Based on this model, improved control methods are proposed, aimed at increasing system stability, reducing response errors, and improving the energy efficiency of the impact action. Numerical simulation has shown that adaptive input signal shaping significantly improves the system's performance. Under identical modeling conditions, the proposed logic-based control method reduced the normalized force deviation by approximately 15–20% compared with the conventional control scheme. A logical structure for generating the input signal X(t) has been developed, ensuring more precise synchronization of dynamic processes. The results obtained contribute to the development of control methods for hydraulic shock mechanisms and propose improved algorithms applicable in engineering systems where high accuracy and reliability are required. Future plans include experimental verification of the proposed solutions on physical prototypes, as well as refinement of the mathematical models to account for the compressibility of the working fluid and real-time load changes.*

Keywords: Impulse hydraulic shock mechanisms; mining machinery; control systems; actuator dynamics; mathematical modeling; input signal generation; logic circuits; numerical simulation; energy efficiency

1. Introduction

Hydraulic impact systems are used in mining equipment where short-time high-energy pulses are required for breaking, excavation, and related technological operations. Although such systems are well known in engineering practice, their actual operating parameters do not always coincide with the values predicted at the design stage. One of the reasons for this mismatch is the limited accuracy of control actions during different phases of the operating cycle, especially when the motion of the striker changes under load [1-3]. The performance of an impulse hydraulic mechanism depends not only on the hydraulic circuit itself, but also on how accurately the control signal is coordinated with the current kinematic state of the main actuating element. In cyclic operation, even small errors in signal formation may affect the displacement law, the stability of the return and working stroke phases, and the resulting impact characteristics. For this reason, the improvement of control methods remains an important task in the development of hydraulic shock systems [5-7].

A promising way to solve this problem is to construct the control action on the basis of motion parameters of the actuator. In this study, particular attention is paid to displacement, velocity, acceleration, and the third derivative of displacement as informative variables for control. Such an approach makes it possible to describe the dynamic state of the system more fully and to relate the generated signal to the actual motion of the striker during the full working cycle.

Based on the principles of control theory and mathematical logic, this paper develops logic schemes for signal formation in the return and working stroke phases of an impulse hydraulic shock mechanism. The proposed approach uses converters, integrators, and summing elements to decompose and transform the kinematic signals into the corresponding control action. The obtained schemes are intended to improve synchronization of dynamic processes and to reduce the discrepancy between calculated and actual operating parameters under practical conditions [7,8]. The purpose of the study is to improve the dynamic performance of impulse hydraulic shock mechanisms by developing control methods based on the kinematic parameters of the main actuating element. Special attention is given to the formation of logic-based control signals and to the use of acceleration and the third derivative of displacement as governing parameters for more accurate motion control.

The novelty of this study lies in the development of logic-based control methods for impulse hydraulic shock mechanisms in which the control action is formed from the kinematic parameters of the main actuating element, including displacement, velocity, acceleration, and the third derivative of displacement. Unlike our previous work, which focused on dynamic modeling and surface integrity optimization of low-frequency hydraulic impulse systems, the present study is aimed at improving the coordination of control signals.

2 Literature review and problem statement

Hydraulic shock and impulse systems have been studied for many years in connection with mining machines, hydraulic drives, and impact devices operating under cyclic loading. Earlier works mainly described the general theory of hydraulic impulse systems, the design principles of impact machines, and the motion laws of the main actuating element under different operating conditions. These studies created the theoretical basis for analyzing pressure changes, striker motion, and impact energy generation in hydraulic systems [9,10]. At the same time, practical operation of such systems shows that their efficiency depends not only on the hydraulic layout, but also on the quality of control during the full operating cycle. In real machines, deviations between calculated and actual output parameters often appear because the control signal is not sufficiently coordinated with the instantaneous dynamic state of the striker. This reduces motion accuracy, affects the stability of the return and working stroke phases, and may lead to a decrease in impact efficiency [11].

A number of researchers have considered continuous control methods for hydraulic systems, where the state of the main actuating element is monitored throughout the entire cycle. This approach is especially relevant for hydraulic machines operating at relatively low frequencies and under considerable force loading. Previous studies have also shown that the use of displacement, velocity, and acceleration as control-related variables can improve the precision of actuator motion. However, the use of the third derivative of displacement as a basis for forming the control action remains insufficiently developed for impulse hydraulic shock mechanisms. In oscillation theory, the third derivative of the motion law is known as sharpness and characterizes the rate of change of acceleration in time. From the viewpoint of control, this parameter is important because it reflects the dynamic intensity of the driving action and may provide a more sensitive basis for synchronizing the control signal with the actual motion of the striker. Although this concept has been mentioned in the literature on optimal hydraulic drive control, its application to logic-based signal formation in hydraulic shock systems has not yet been fully formalized.

Therefore, the main problem considered in this paper is the insufficient coordination between the control action and the actual motion of the main actuating element during the return and working stroke phases, particularly under resistance conditions. Conventional control approaches do not always ensure the required synchronization of dynamic processes, which leads to force deviation, reduced stability of the operating cycle, and lower agreement between design and real operating parameters [11,12]. The present study addresses this problem by developing logic-based methods for forming control signals from the kinematic parameters of the main actuating element, including displacement, velocity, acceleration, and the third derivative of displacement. In contrast to studies focused on surface integrity, machining effects, or digital monitoring, this work concentrates on improving the dynamic coordination of control actions during the full operating cycle of an impulse hydraulic shock mechanism [13].

3 Methodology

The methodological basis of this study combines elements of control theory, hydraulic drive analysis, and logic-based signal synthesis for cyclic impact systems. The research is aimed at improving the control of an impulse hydraulic shock mechanism by coordinating the generated control action with the kinematic state of the main actuating element during the full working cycle. Particular attention is given to the return and working stroke phases, since the dynamic behavior of the system in these intervals determines the accuracy of motion, the stability of the cycle, and the efficiency of impact energy transfer. At the first stage, the operating features of hydraulic shock systems used in mining machines were analyzed. These systems function under significant force loading and relatively low operating frequency, which makes continuous control methods more suitable than discrete approaches. Continuous control allows the state of the striker to be tracked throughout the whole cycle and makes it possible to influence the law of motion at any moment of time. On this basis, the study adopts the assumption that the change in control action can be described most completely through the higher-order kinematic characteristics of motion, including acceleration and the third derivative of displacement.

The next stage involved the construction of a mathematical description of the main actuating element motion. The model is based on the classical relation between the resultant force and acceleration and considers the motion of the striker along its axis. From this basis, analytical relations were used to describe the displacement, velocity, acceleration, and the variation of the control action in time. For simplification of the obtained expressions, dimensionless or reduced coefficients were introduced to reflect the connection between the input parameters of the hydraulic shock system and its output characteristics under given technical and operating conditions.

A separate part of the methodology concerns the formation of control signals for different motion phases. The return phase and the working stroke phase were considered separately, since the structure of the kinematic relations and the role of the control action differ in these two parts of the cycle. Based on the derived expressions, logic schemes were developed to generate the input signal and the corresponding control action. These schemes were built using converters, integrators, phase-shifting elements, multipliers, and summing units. Such a structure makes it possible to decompose the kinematic signal into components, transform them using the required coefficients, and combine them into the final control function. Special attention was paid to the use of acceleration and the third derivative of displacement as governing parameters. In the adopted approach, the third derivative characterizes the rate of change of acceleration and is treated as an informative quantity for continuous control of the striker motion. This makes it possible to form a control signal that is more sensitive to transient changes in the operating state of the mechanism and to improve synchronization between the hydraulic and mechanical processes during the cycle.

The methodology also includes analysis of system behavior under constant resistance. In this case, the control action was formed with allowance for the drag-related terms affecting the striker motion. The comparison of signal structures under resistance and no-resistance conditions was used to reveal how the amplitudes and durations of control impulses change depending on the operating environment. This comparison provides the basis for evaluating the adaptability of the proposed control schemes and their suitability for practical hydraulic shock systems working under load. At the final stage, the developed logic schemes and analytical relations were used for numerical analysis of the control process. The purpose of this stage was to assess the qualitative behavior of the generated control actions, to compare conventional and improved signal formation principles, and to identify the control variables that provide the most accurate coordination of dynamic processes. The methodology therefore combines analytical derivation, phase-based signal synthesis, and comparative dynamic analysis, which together form the basis for improving the control of impulse hydraulic shock mechanisms.

4 Formation of control signals

The formation of control actions in the impulse hydraulic shock mechanism is based on the kinematic parameters of the main actuating element during the full operating cycle. In the adopted approach, displacement, velocity, acceleration, and the third derivative of displacement are treated as informative variables that reflect the current dynamic state of the striker. The purpose of the control scheme is to transform these variables into a coordinated control action that ensures stable motion in both the return phase and the working stroke phase.

From the control standpoint, the return phase and the working stroke phase must be considered separately. Although both phases belong to the same cycle, the structure of motion and the role of the control action are different in each of them. For this reason, the signal formation process was developed not as a single universal transformation, but as a phase-dependent logic procedure that takes into account the specific form of the kinematic relations in each interval.

At the analytical level, the control action is related to the law of motion of the main actuating element and to its derivatives. The starting point of the signal synthesis is the set of kinematic expressions describing the striker motion. In order to simplify their practical use, coefficients were introduced to connect the motion parameters with the operating and design conditions of the hydraulic shock system. These coefficients make it possible to adapt the control signal to a particular machine configuration and to the expected resistance conditions.

In the present study, the mathematical model is used to describe the phase-dependent motion of the main actuating element and to determine the corresponding control action. The return phase and the working stroke phase are considered separately because the direction of motion, the influence of resistance, and the required control signal differ in these two parts of the operating cycle. Therefore, the analytical expressions are written in a reduced form using coefficients that combine the design and operating parameters of the hydraulic shock system.

As a working hypothesis, the assumption that the third time derivative of its law of motion characterizes the change of the control action on the main actuating element in time to the fullest extent is used. Indeed, if we have in mind the classical expression

$$m\bar{a} = \bar{F},$$

where m – reduced mass of the main actuating element; $\bar{F}$ - the resultant of all forces acting on it; $\bar{a} = \ddot{x}$ - acceleration; $x(t)$ - law of motion, then after some transformations we obtain:

$$\ddot{x}(t) = \frac{1}{m}\bar{F}.$$

If we take into account that the motion of the main actuating element is carried out along its axis, then

$$\ddot{x}(t) = \frac{1}{m}F;\ \dddot{x}(t) = \frac{1}{m}\frac{dF}{dt} = \frac{1}{m}U(t),$$

where $U(t)$ – change in control action.

It should also be noted that the classical literature devoted to the theory of oscillations [8] uses the third time derivative of the law of motion, which is called sharpness. In physical terms, it is the intensity of change of acceleration in time. Practical realization of sharpness in control theory has found application in the study of the speed-optimal hydraulic drive, in particular, in [9]. Here it is convincingly proved, this approach allows "to provide the movement of the actuator actuator with minimum deviations from the required". Thus, sharpness is accepted as a setting influence for continuous methods of forming the control action [8]. The adopted method of forming the control action determines the stages of creating the automatic control body of the hydraulic shock system, different from the previously mentioned. The difference lies in the fact that before the structural synthesis of the control body, the establishment of the law of motion of the main actuating element of the system is made on the basis of operational requirements and limitations imposed on the system as a whole, as well as assumptions adopted in the study of the motion of the main actuating element. The found law of motion is a starting point for establishing the law of change of the control action in analytical form using the third time derivative.

The construction of the control action for this case is based on the laws of motion of the main actuating element obtained in Section 2.3. To simplify the equations defining the kinematic parameters of the main actuating element, we introduce coefficients expressing the relationship between the parameters and output parameters of the hydraulic shock system:

$$A^{(c)} = \frac{lp\left[1-(k_P-k_c)\varepsilon\right]}{(\varepsilon-1)};\ B^{(c)} = \frac{lp(\varepsilon+1)}{(\varepsilon-1)}\left(\alpha - \frac{C_o}{1+C_o}\right)\times\sqrt{\frac{(\varepsilon-1)(1+\mu_{uc})\left[U(\varepsilon+1)-1\right]}{(1+C_o)\left[1+\varepsilon(1-2k_c)\right]}};$$

$$C^{(c)} = \frac{\left[(k_p-k_c)\varepsilon+1\right]}{(1+C_o)(\varepsilon-1)};\ E^{(c)} = \frac{lp(1-k_c)}{(\varepsilon-1)}.$$

If necessary, these coefficients can be expressed through the input design and operating parameters of the hydraulic shock system.

Taking into account the introduced coefficients, the kinematic indices of the main actuating element of the system have dependencies:

in the reverse phase:

$$X = A^{(c)} \cos k_2 t + B^{(c)} \sin k_2 t + (C^{(c)} + D^{(0)} t; \quad (4.1)$$

$$\dot{X} = -A^{(c)} k_2 \sin k_2 t + B^{(c)} k_2 \cos k_2 t + D^{(0)}; \quad (4.2)$$

$$\ddot{X} = -A^{(c)} k_2^2 \cos k_2 t - B^{(c)} k_2^2 \sin k_2 t; \quad (4.3)$$

$$\dddot{X} = A^{(c)} k_2^3 \sin k_2 t - B^{(c)} k_2^3 \cos k_2 t; \quad (4.4)$$

in the travel phase:

$$X_1 = E^{(c)} (1 - \cos k_3 t); \quad (4.5)$$

$$\dot{X}_1 = E^{(c)} k_3 \sin k_3 t; \quad (4.6)$$

$$\ddot{X}_1 = E^{(c)} k_3^2 \cos k_3 t; \quad (4.7)$$

$$\dddot{X}_1 = -E^{(c)} k_3^3 \sin k_3 t. \quad (4.8)$$

In Equations (4.1)–(4.8), the motion of the main actuating element is described through displacement, velocity, acceleration, and the third derivative of displacement. The displacement characterizes the position of the striker along its working axis, the velocity describes the rate of this displacement, and the acceleration reflects the intensity of force interaction during the return and working stroke phases. The third derivative of displacement, referred to in this study as sharpness, characterizes the rate of change of acceleration over time and is used as an informative parameter for forming the control action.

The reduced coefficients used in these equations are introduced to simplify the analytical representation of the motion law. They combine the influence of the reduced mass of the actuating element, the parameters of the hydraulic drive, the phase of motion, and the resistance conditions. These coefficients are not independent empirical variables; they are used to present the return and working stroke equations in a compact form and to relate the mathematical model to the physical operating conditions of the hydraulic shock mechanism.

In terms of construction, the obtained expressions are similar to the dependences obtained in the study of the mode without resistance. As a consequence, the order of formation of signals determining the kinematic parameters of the main actuating element remains similar to that considered earlier [14,15].

The logic diagrams in Figures 1–6 show the sequence of signal-conditioning operations used to obtain the control action. In these diagrams, the input kinematic functions are decomposed into separate components. Each component is then transformed by multiplication with the corresponding coefficient, and the transformed components are combined in summing units. Multipliers represent coefficient-based scaling operations, while summing blocks represent the formation of the final control signal from several transformed components. Phase-shifting elements are used when the control signal requires temporal or phase correction during the working stroke.

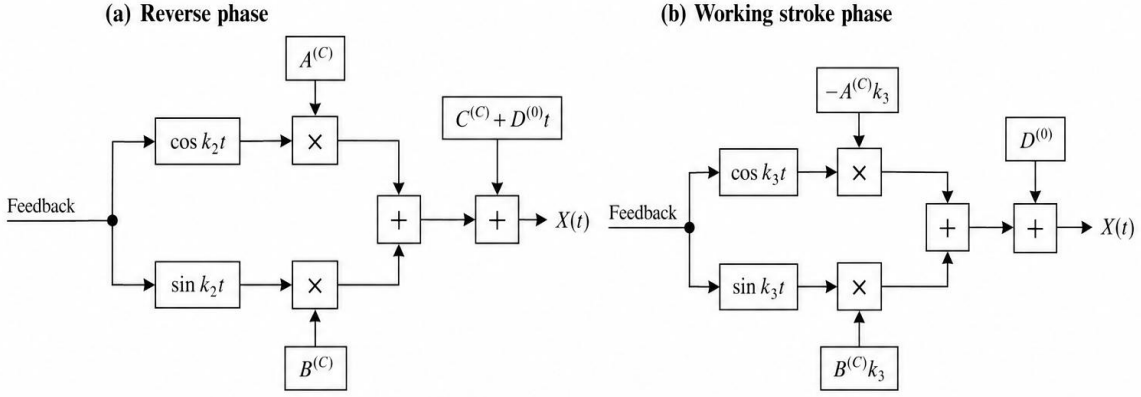

a and *b* - in reverse and working stroke phases, respectively

Fig. 1. Logical diagram of X(t) signal formation

The signal formation procedure is illustrated by the circuit shown in Figure 1. During the return phase, the input kinematic functions are generated and then multiplied by the corresponding coefficients. The transformed components are combined with the constant term to form the required signal for this phase.

During the working stroke phase, the generated signal component is multiplied by the corresponding coefficient to obtain the control signal for the forward motion. This procedure provides a phase-dependent transformation of the input signal and makes it possible to adapt the control action to the operating conditions of the hydraulic shock mechanism [14].

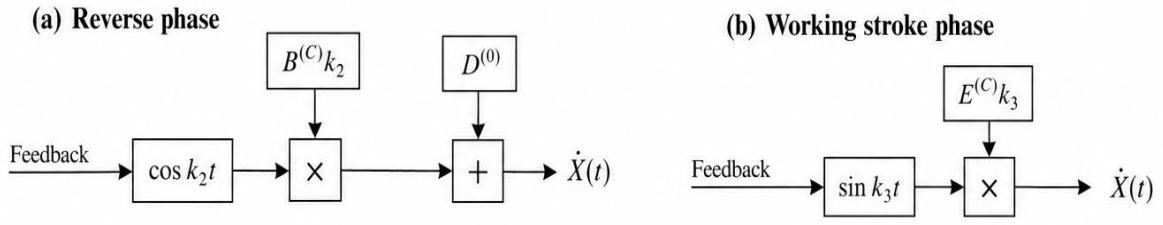

a and *b* - in reverse and working stroke phases, respectively

Fig. 2. Sequence of signal conditioning operations

In the backward phase (Figure 2a), the generated functions f_1 and f_2 are simultaneously multiplied by the corresponding coefficients k_1 and k_2. The resulting transformed signals are then summed together. In the working stroke phase (Figure 2b), the function generated in this mode must be multiplied by the coefficient k_3. This is the easiest way to generate a signal $\ddot{X}(t)$. Comparison of expressions determining the change of kinematic parameters of motion of the main actuating element during the working cycle makes it possible to construct a control action *U(t)*.

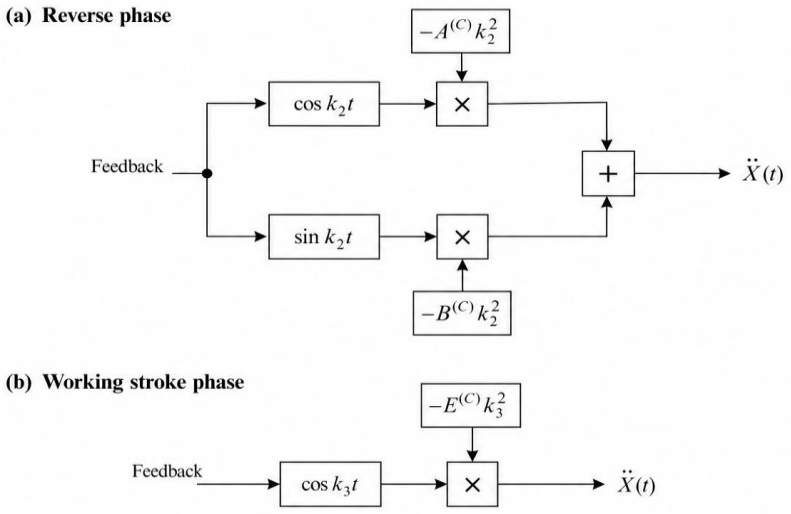

a and *b* - in reverse and working stroke phases, respectively

Fig. 3. Logic circuit of signal formation

The logic scheme for forming the control action using the displacement signal $X(t)$is shown in Figure 3. During the return phase, the displacement signal is decomposed into several components. The required components are multiplied by the corresponding coefficients and then summed to obtain the control action $U(t)$. The remaining component obtained after signal decomposition does not contribute to the resulting control function in this phase. During the working stroke phase, the corresponding signal component is transformed by phase correction and coefficient scaling. This makes it possible to obtain a control function that corresponds to the required motion phase [15-17].

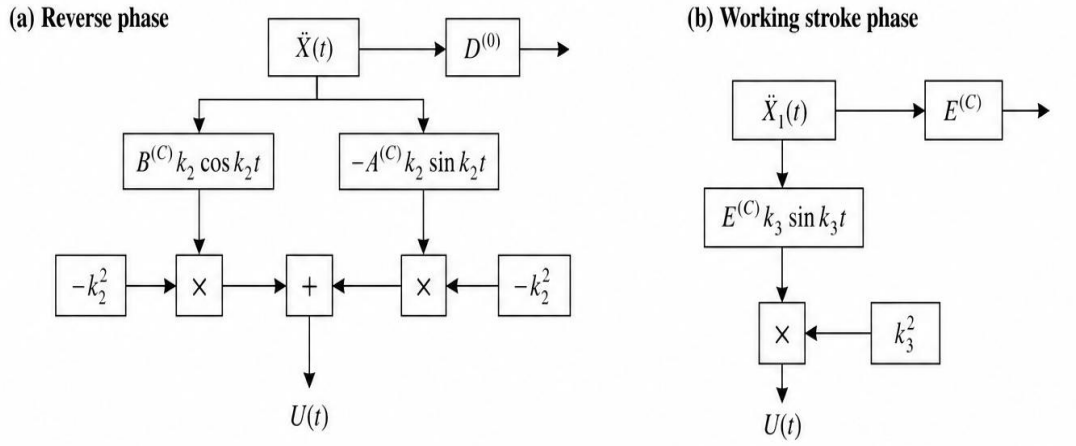

a and *b* - in reverse and working stroke phases, respectively
Fig. 4. Logic scheme of control action formation U(t) Displacement

Constructing the control action using the velocity v(t) and functions f_i is performed in accordance with the logic diagram shown in Figure 4. In the reverse phase (Figure 4a), the signal v(t) is decomposed into the components f_1, f_2, and f_3. The last two components are simultaneously multiplied by the corresponding coefficients, after which the transformed signals are summed. The remaining component obtained after decomposition does not contribute to the formation of the resulting control function.

In the working stroke phase (Figure 4b), the component that fully defines the control signal is multiplied by its corresponding coefficient.

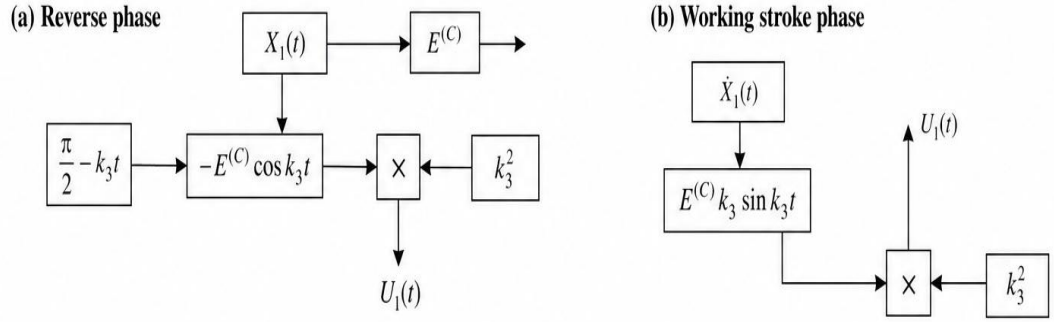

a and *b* - in reverse and working stroke phases, respectively
Fig. 5. Logic scheme of control action formation using the acceleration signal

The control action based on the acceleration signal is formed according to the logic scheme shown in Figure 5. During the return phase, the acceleration-related signal is decomposed into two components. These components are multiplied by the corresponding coefficients and then summed to form the resulting control action for this phase.

During the working stroke phase, the corresponding signal component is transformed by applying the required phase shift and coefficient scaling. This operation allows the control action to be synchronized with the dynamic state of the main actuating element.

Thus, under constant resistance conditions, the general logic of control signal formation remains similar to the no-resistance case. The main difference is quantitative: the coefficients applied to the signal components change because the control action must compensate for external resistance.

The variation of the control action for the considered case is determined by the expressions describing the motion of the main actuating element during the operating cycle. After transformation of these expressions in accordance with the developed logic schemes, the resulting control-action diagram for motion under constant resistance takes the form shown in Fig. 7. Its characteristic points are o, a', b', c', d', and e'. The values of the control action at the beginning and at the end of the cycle phases are defined by the corresponding segments of the diagram.

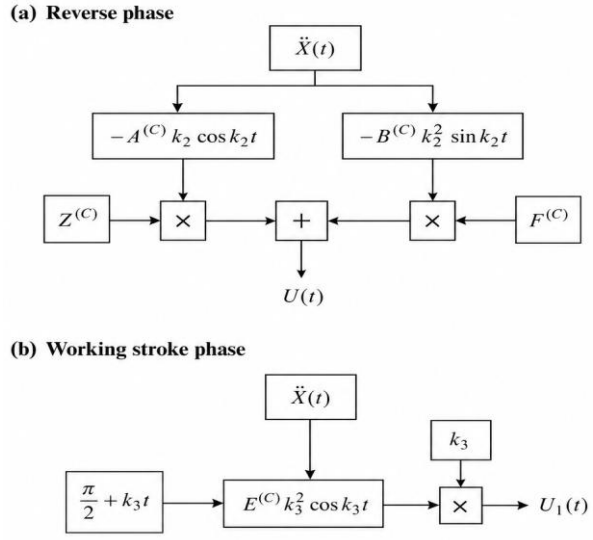

a and *b* - in reverse and working stroke phases, respectively

Fig. 6. Logic scheme of control action formation U(t) using acceleration

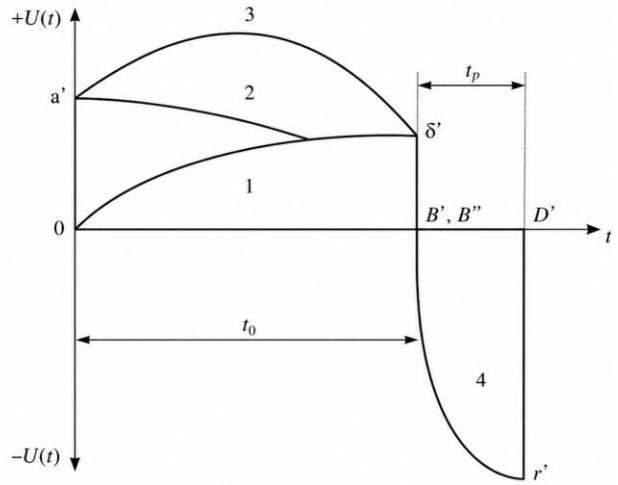

1 - $A^{(C)}k_2^3\sin k_2t$; 2 - $-B^{(C)}k_2^3\cos k_2t$; 3 – U(t); 4 – $U_1(t)$

1 – kinematic parameter curve; 2 – auxiliary dynamic curve; 3 – U(t); 4 – $U_1(t)$

Fig. 7. Dynamic diagram of motion parameters and control actions of the hydro-impact system

In comparison with the no-resistance case, these segments become larger due to the influence of the drag force coefficient K_c and the related changes in the governing coefficients. Thus, the obtained diagram reflects the effect of resistance on the amplitude and duration of the control action during the operating cycle.

The coefficient K_c is used as a normalized resistance coefficient. It characterizes the influence of external resistance on the motion of the main actuating element. The case $K_c = 0$corresponds to motion without resistance, whereas $K_c > 0$corresponds to motion under resistance conditions. An increase in K_c changes the required control action and leads to longer and more intensive control impulses during the working stroke.

When K_c approaches to zero, the control-action diagram approaches the no-resistance case. This confirms that resistance mainly affects the amplitude and duration of the control action, while the general structure of the signal formation process remains unchanged.

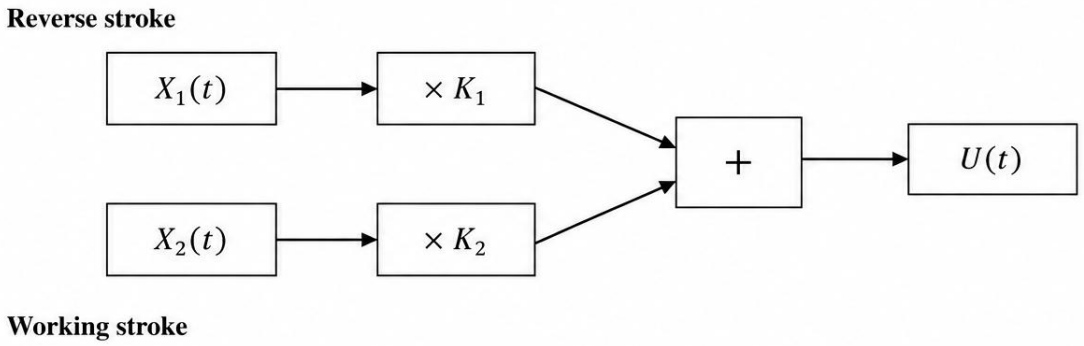

Fig. 8. Logical scheme of the signal formation process

The signal X(t) is generated by multiplying input functions $X_1(t)$ and $X_2(t)$ by constants K_1 and K_2, and summing the results to form the control action U(t).

Figures 8 and 9 summarize the auxiliary signal formation process. The input signals are scaled by the corresponding coefficients and then combined with the constant term to obtain the auxiliary control signal. This structure allows the control action to be adapted to the resistance conditions and to the selected phase of the operating cycle.

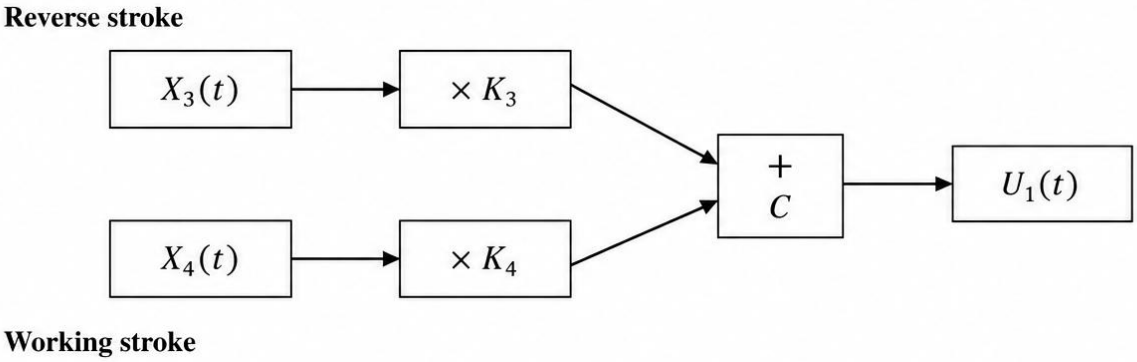

Fig. 9. Logic structure for generating the auxiliary control signal U1(t)

Input signals $X^3(t)$ and $X_4(t)$ are scaled by coefficients K_3 and K_4, then added with a constant C to generate the output control signal $U_1(t)$.

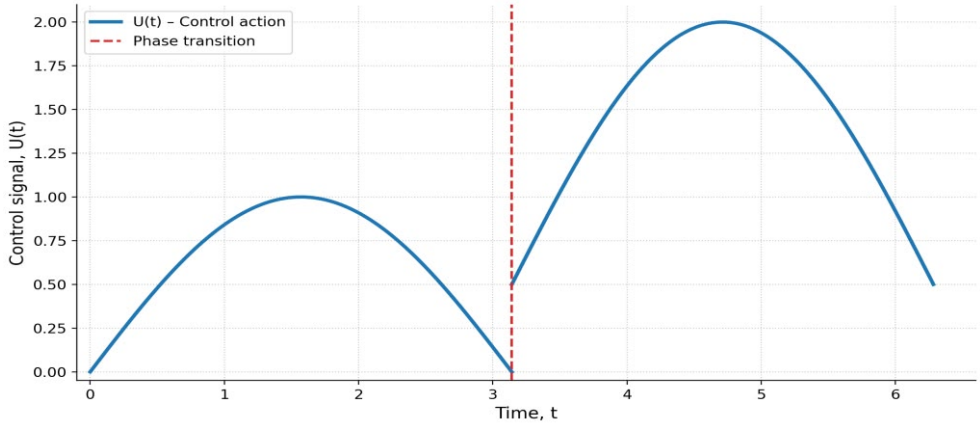

Fig. 10. Control action diagram under resistance conditions

The signal becomes more intense and prolonged during the working stroke to compensate for external resistance. This ensures accurate actuator motion and minimizes energy losses.

For each phase, the control signal U(t) is formed through a logic scheme consisting of:

– Signal decomposition: Splitting the motion law into components (e.g., $X_1(t)$, $X_2(t)$)

– Coefficient adjustment: Each component is multiplied by a system-specific constant based on design parameters and operating conditions

– Summation: Resulting signals are combined into a unified control function

To validate the proposed control strategy based on displacement, velocity, acceleration, and sharpness, a mathematical simulation of the actuator's motion was carried out. The actuator's displacement is modeled as a sinusoidal function over time.

Mathematical Model

Displacement function:

$X(t) = A \cdot sin(\omega t)$, where $A = 0.1m$, $\omega = 2\pi f$, and $f = 2Hz$

First derivative (velocity):

$V(t) = A\omega \cdot cos(\omega t)$

Second derivative (acceleration):

$A(t) = -A\omega^2 \cdot sin(\omega t)$

Third derivative (sharpness):

$S(t) = -A\omega^3 \cdot cos(\omega t)$

In this simulation, the sinusoidal displacement law was used as a simplified test function for evaluating the behavior of the control variables. The purpose of this model is not to reproduce all nonlinear hydraulic effects experimentally, but to compare how different kinematic quantities change over time and how they can be used for control signal formation. Velocity, acceleration, and sharpness were obtained by differentiating the displacement function with respect to time.

Simulation Results

The figure below illustrates the time-dependent behavior of four key motion parameters: displacement $X(t)$, velocity $V(t)$, acceleration $A(t)$, and sharpness $S(t)$.

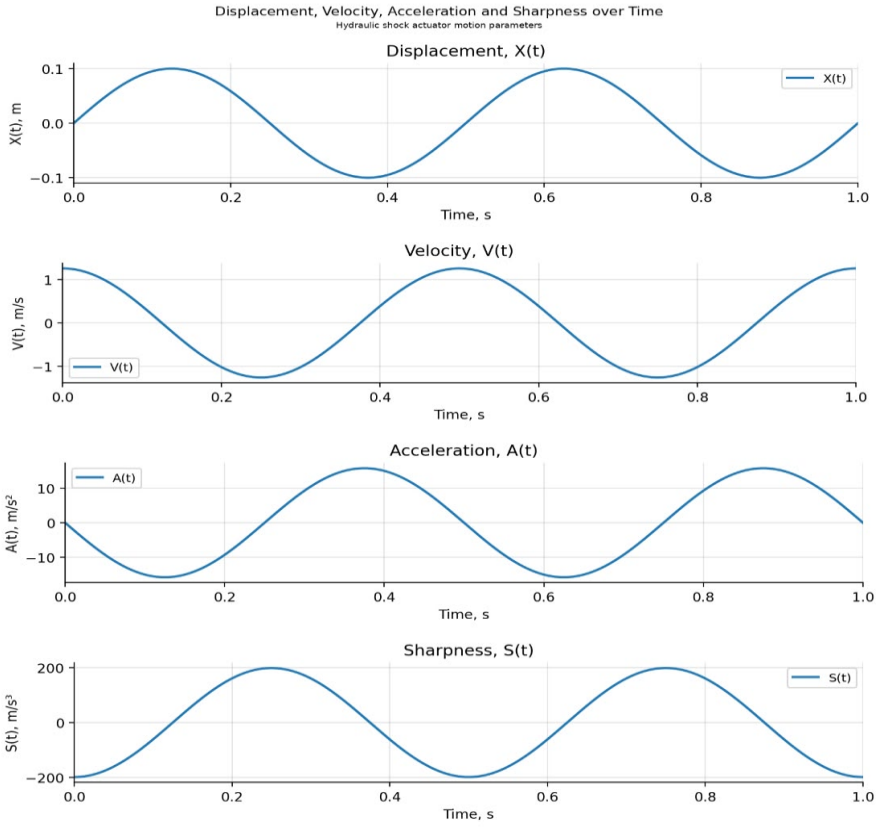

Fig. 11. The time-dependent behavior of four key motion parameters

The displacement follows a smooth sinusoidal profile. Velocity peaks at zero-crossings of displacement, while acceleration reaches maximum values at displacement extremes. Sharpness, being the third derivative,

shows the most rapid oscillations and highlights the responsiveness of the actuator's dynamics. This confirms the suitability of using sharpness as a control input in hydraulic impact systems.

When resistance is present, additional terms are introduced to offset the drag force coefficient K_c. This leads to stronger and longer control impulses during the working phase. The influence of resistance is visualized in comparative signal diagrams, where segments of the control function are visibly altered.

5 Results and Discussion

The proposed control strategies for hydraulic impact mechanisms were evaluated by means of mathematical modeling and numerical simulation. The analysis was performed using the main kinematic parameters of the actuating element, including displacement, velocity, acceleration, and sharpness, in order to assess the efficiency and accuracy of the developed control schemes. The obtained results showed that control based on acceleration and the third derivative of displacement provides more accurate tracking of the prescribed motion law than conventional approaches. In particular, the striker motion follows the required trajectory more closely during transitions between the return and working stroke phases, while overshoot and delay are reduced.

The improved synchronization between the generated control impulses and the mechanical response of the system also leads to better energy utilization. Under resistance conditions, the sharpness-based control method adjusts the control action more precisely in accordance with the current dynamic state of the actuating element. As a result, unnecessary energy expenditure is reduced and the operating cycle becomes more stable. The developed logic schemes also demonstrate adaptability to changing operating conditions, including variations in resistance force and the dynamic characteristics of the working element. Owing to the modular structure of the control diagrams, the coefficients of the governing relations can be adjusted according to the required operating mode.

A comparison of conventional and proposed control methods is presented in Table 1. The results indicate that the logic-based control scheme provides improved phase coordination, lower force deviation, and higher stability under load.

The reported 15–20% reduction in force deviation should be interpreted as a simulation-based comparative estimate. It was obtained by comparing the normalized deviation amplitudes of the conventional and proposed control schemes under identical modeling conditions. The relative reduction was calculated as

$$\eta = \frac{\Delta F_{conv} - \Delta F_{prop}}{\Delta F_{conv}} \times 100\%,$$

where $\Delta F_{conv}$is the normalized force deviation for the conventional control scheme and $\Delta F_{prop}$is the normalized force deviation for the proposed logic-based control scheme. This value is not presented as a full-scale experimental result. Experimental validation of the proposed control scheme is considered as the next stage of the research.

Table 1. Comparative assessment of conventional and proposed control methods

Performance criterion	**Conventional control scheme**	**Proposed logic-based control scheme**	**Improvement achieved**
Phase coordination	Incomplete synchronization between return and working stroke phases	Improved synchronization based on kinematic signal formation	Better coordination of operating phases
Force deviation	Baseline normalized deviation, ΔF_{conv}	Reduced normalized deviation, ΔF_{prop}	Approximately 15–20% reduction based on numerical simulation
Stability of operating cycle	Sensitive to resistance effects	More stable under resistance conditions	Increased cycle stability under load
Motion tracking accuracy	Moderate correspondence with the prescribed motion law	Improved correspondence with the prescribed motion law	Higher tracking accuracy
Adaptation to resistance effects	Limited compensation of resistance	Resistance coefficient K_c included in signal formation	Better compensation of external resistance
Energy utilization	Higher control losses	Reduced unnecessary control action under load	Improved energy utilization

The most direct quantitative improvement is related to the normalized force deviation. Under the same simulation conditions, the proposed logic-based control scheme reduced the normalized deviation amplitude by approximately 15–20% compared with the conventional scheme. The remaining criteria in Table 1 are presented as comparative engineering indicators because the present work is based on numerical modeling and logic-based signal synthesis. These criteria describe the observed improvement in phase coordination, resistance adaptation, and motion tracking behavior during the simulated operating cycle.

As shown in Table 1, the proposed logic-based control scheme demonstrates clear advantages over the conventional approach. The improved method provides more accurate phase coordination, lower force deviation, and greater stability under resistance conditions. In addition, the use of acceleration and the third derivative of displacement as governing parameters improves motion tracking accuracy and enhances the overall energy efficiency of the hydraulic shock mechanism.

6 Conclusions

This study examined the dynamic behavior of impulse hydraulic shock mechanisms and proposed improved control methods based on the kinematic parameters of the main actuating element. Particular attention was given to the formation of control signals from displacement, velocity, acceleration, and the third derivative of displacement in order to improve coordination between the generated control action and the actual motion of the striker during the operating cycle.

The developed logic-based approach makes it possible to form phase-dependent control signals for the return and working stroke phases and to adapt the control action to resistance conditions. The numerical simulation results indicate that the proposed method can reduce the normalized force deviation by approximately 15–20% compared with the conventional control scheme under the same modeling conditions.

The study also demonstrated that acceleration and sharpness can be used as informative governing parameters for hydraulic shock control, since they reflect transient changes in the dynamic state of the actuating element more sensitively than displacement alone. This provides a more accurate basis for signal generation and improves the correspondence between calculated and actual operating parameters.

Thus, the proposed control methods and logic schemes can be considered as a useful basis for improving the accuracy, reliability, and energy efficiency of impulse hydraulic shock mechanisms used in engineering applications. Further research will be aimed at experimental validation of the proposed solutions and refinement of the mathematical model with allowance for fluid compressibility, valve dynamics, and variable real-time loading conditions.

Conflict of interest statement

The authors declare that they have no conflict of interest in relation to this research, whether financial, personal, authorship or otherwise, that could affect the research and its results presented in this paper.

CRediT author statement

Smakova N.: Conceptualization, Methodology, Writing – original draft, Supervision; **Pankov S.:** Investigation, Data curation; **Baisadykov B.:** Experimental validation; **Zelenkov V.:** Software, Modeling; **Toibazarov D.:** Visualization, Data analysis; **Karypov A.:** Resources, Technical support. The final manuscript was read and approved by all authors.

Statement on the use of Artificial Intelligence

The authors declare that no artificial intelligence tools were used to generate scientific content, analysis, results, or conclusions of this article.

Data Availability Statement

The data used in this study are available from the corresponding author upon reasonable request.

Funding:

This research was carried out within the framework of the scientific project IRN AR196079/0222 "Prospective appearance of the troop control system considering the creation of mobile command posts in accordance with the paradigm of network-centric warfare." The work was funded by the Science Committee of the Ministry of Science and Higher Education of the Republic of Kazakhstan.

References

1 Smirnov, Y.M., Uraimov, M., & Smakova, N.S. (2019). Mathematical model of hydraulic manipulators of impulse machines. *Trudy Universiteta*, (1), 18–22 Available at: http://tu.kstu.kz/archive/issue/11

2 Glotov, B.N., Kokenova, A.T., & Smagina, V.S. (2015). Classification of hydraulic hand hammers. Applied Research Journal, (5), 385–388. Available at: https://s.applied-research.ru/pdf/2015/2015_05_3.pdf

3 Saruev, L.A., Ziyakaev, G.R., & Pashkov, E.N. (2011). Mathematical modeling of the hydro-impulse mechanism of drilling machines. *Mining Informational and Analytical Bulletin*. Available at: https://cyberleninka.ru/article/n/matematicheskoe-modelirovanie-gidroimpulsnogo-mehanizma-burilnyh-mashin

4 Gorodilov, L.V. (2013). Analysis of the dynamics of two-way hydropercussion systems. Part II: Influence of design factors and their interaction with rocks. *Journal of Mining Science*, 49(3), 465–474. https://doi.org/10.1134/S1062739149030143

5 Smakova, N.S., Smirnov, Y.M., Kenjin, B.M., & Zhurunova, M.A. (2020). Optimal control of operating modes of hydraulic impact actuators of mining machines. *Mining Informational and Analytical Bulletin (MIAB),* (6), 95–104. https://doi.org/10.25018/0236-1493-2020-6-0-95-104

6 Smakova, N., Pankov, S., Baisadykov, B., Zelenkov, V., Toibazarov, D., & Karypov, A.A. (2026). Dynamic modeling and surface integrity optimization of low-frequency hydraulic impulse systems. *Eurasian Physical Technical Journal*, 23(1(55)), 113–120. https://doi.org/10.31489/2026N1/113-120

7 Zhang, Y., Zhou, D., Li, Z. (2023). Adaptive control of nonlinear hydraulic actuators using neural networks. *ISA Transactions*, 129, 362–375.https://doi.org/10.1016/j.isatra.2022.08.045

8 Wang, X., Li, Q., Chen, L. (2023). Optimization of hydraulic impulse systems based on machine learning algorithms. *Mechanical Systems and Signal Processing*, 198. https://doi.org/10.1016/j.ymssp.2023.110520

9 Zhang, H., Liu, Y., Sun, C. (2023). Simulation and experimental study of hydraulic impulse energy conversion. *Journal of Mechanical Science and Technology*, 37, 2, 891–903. https://doi.org/10.1007/s12206-023-0142-2

10 Zhao, W., Chen, J., Hu, Y. (2023). Hybrid modeling and prediction of hydraulic cylinder performance using digital twin framework. *Applied Sciences*, 13, 4. https://doi.org/10.3390/app13042586

11 Li, H., Yu, X., Ren, J. (2023). Research on energy-saving control of hydraulic systems based on digital twin technology. *Sensors*, 23, 1. https://doi.org/10.3390/s23010345

12 Liu, P., Xie, X., Zhang, C. (2022). Machine learning-based optimization for hydraulic pump efficiency. *Energies*, 15, 19. https://doi.org/10.3390/en15197221

13 Xu, H., Tian, L., Sun, W. (2023). Modeling and optimization of hydraulic impulse systems using MATLAB/Simulink. *Intern. J. of Dynamics and Control*, 11, 1152–1164. https://doi.org/10.1007/s40435-023-01231-8

14 Chen, R., Gao, D., Wu, Z. (2023). Deep learning for fault prediction in hydraulic systems. *IEEE Access*, 11, 65903–65915. https://doi.org/10.1109/ACCESS.2023.3298765

15 Sherov, K. T., Sikhimbayev, M. R., Donenbayev, B. S. (2017). Experimental research of rotational-and-frictional boring of big holes in large parts. *Journal of Theoretical and Applied Mechanics,* 47, 2, 67–74. https://doi.org/10.1515/jtam-2017-0018

16 Smakova, N. S., Sherov, K. T., Tusupova, S. O., Buzauova, T. M. (2020). The research of micro-hardness of side surfaces of teeth cylindrical wheels processed by “Shaver-Rolling Device”. *Journal of Theoretical and Applied Mechanics*, 50, 1, 50–56.https://doi.org/10.1515/jtam-2020-0006

17 Zhantlesov, E. Zh., Gruzin, V. V., Togusov, A. K., Zhusupbekov, T. Kh., Zhantlesov, Zh. K. (2024) Scientific and technical substantiation of the parameters of the radiolocation device for the detection of prohibited items. *Eurasian Physical Technical Journal*, 21, 3 (49), 93–98.https://doi.org/10.31489/2024No3/93-98

AUTHORS’ INFORMATION

Smakova, Nurgul Serikovna – PhD, Associate Professor, Kazakh University of Technology and Business named after K. Kulazhanov, Astana, Kazakhstan: https://orcid.org/0009-0002-5754-4001; nuri_5@mail.ru

Pankov, Sergey Vladimirovich – Candidate of Military Sciences, Professor, Leading researcher, National Defense University of the Republic of Kazakhstan, Astana, Kazakhstan; https://orcid.org/0000-0003-3764-3192; sergey.pankov@ndu.kz .

Baisadykov, Bahyt Zhumashevich – PhD, teacher, National Defense University of the Republic of Kazakhstan, Astana, Kazakhstan; https://orcid.org/0009-0003-9234-5945 ; bahyt.baisadykov@ndu.kz.

Zelenkov, Valeriy Viktorovich – PhD, department head, National Defense University of the Republic of Kazakhstan, Astana, Kazakhstan; https://orcid.org/0009-0005-4381-8384; valeriy.zelenkov@ndu.kz

Toibazarov, Daulet Oralbekovich – PhD, Associate Professor, Senior researcher, National Defense University of the Republic of Kazakhstan, Astana, Kazakhstan; https://orcid.org/0009-0000-9135-7360; aldar-kose1@yandex.ru

Karypov, Andrey Andreevich – Candidate of Military Sciences, Chief Specialist, Scientific and Technical Center Almaty Special Design Bureau “Alatau” (LLP “STC ASDB Alatau”), Almaty, Kazakhstan; https://orcid.org/0009-0004-9404-8220; a_kar@bk.ru

EURASIAN PHYSICAL TECHNICAL JOURNAL

2026, Volume 23, No. 2 (56)

https://doi.org/10.31489/2026N2/91-98

Received: 21/02/2026 Revised: 26/05/2026 Accepted: 00/06/2026 Published online: 30/06/2026

Original Research Article

UDC 620.92

SOME METHODS FOR DIAGNOSTICS OF WAKE-INDUCED LAMINAR-TURBULENT TRANSITION

Suprun T.T.

Institute of Engineering Thermophysics, National Academy of Sciences of Ukraine, Kyiv, Ukraine,
*Corresponding author suprun@secbiomass.com

Abstract. *To create a reliable engineering method for calculating local heat transfer of turbine blades, information about the flow regime on the blade surface is necessary. The presence of a wake-induced laminar-turbulent transition on the surface of the blade requires the development of methods for its diagnostics. The object of the study is blade surface under the influence of unsteady periodic wakes from upstream blade rows. The research method is physical modeling of a wake-induced transition initiated by steady wakes behind a still and periodic unsteady wake behind an oscillating cylinder. The article considers some methods for determining the coordinates and extent of a wake-induced transition region. Reliable diagnostics of such a transition is possible only with the help of a combination of developed methods. The presented experimental data allow us to predict the location of a wake-induced transition and the intensification of heat transfer in the preceding pseudolaminar boundary layer, that is, to control the process of such a transition.*

Keywords: wake-induced laminar-turbulent transition, diagnostics of transition coordinates, still and oscillating cylinders.

1. Introduction

The main streamlined surface of thermal power equipment considered in this paper is the turbine blade. Laminar, transitional, and turbulent boundary layers (BLs), as well as separation zones, can coexist on the surface of a turbine blade. One of the primary tasks in turbomachine design is the development of a reliable engineering method for calculating local heat transfer of turbine blades. This method includes both the development of flow regime diagnostic methods and the consideration of the fact that the working fluid in the flow path of turbomachines is highly turbulent. The overall degree of flow turbulence in the gas turbine flow path is determined by both the initial turbulence as it passes through the compressor and combustion chamber, and the flow conditions through the blade cascades of the preceding stages. Such type of flow is formed due to the appearance of stationary and moving wakes behind the trailing edges of the previous rows of blades. These wakes have a significant impact on the development of BL on the blade surface and must be taken into account when calculating the thermal and aerodynamic state of the rotor and stator elements.

Under the influence of unsteady periodic wakes of the upstream blade rows, a transition occurs on the surface of the blades, which is called wake-induced laminar-turbulent transition. In the wake-induced transition, the first stages of the natural transition process are bypassed and the forming turbulent spots immediately merge into turbulent streaks, which then grow and spread downstream. Between these turbulent streaks another type of transition (natural or bypass) may occur. Thus, the transition in gas turbines can occur as multiple transition modes at different distances on the same surface at the same time [1].

The development of improved methods for calculating the intensity of transport processes occurring in the presence of a wake-induced transition requires information about the coordinates and length of this region. The current situation stimulated the continuation of the research started at the IET NASU on the development of new and modification of existing diagnostic methods for the laminar-turbulent transition (LTT). As the results of this work have shown, the methods of diagnosing a bypass transition occurring under conditions of increased turbulence of the external flow can also be successfully used for a wake-induced transition.

2. Analysis of recent research and publications

In recent years, many works devoted to the study of wake-induced transitions have appeared. These works considered various cases of the development of a transition initiated by wakes behind both stationary and moving obstacles; however, the problems of diagnosing such a transition were practically not studied in these works. In particular, review [2] examines models for calculating various types of transitions typical for turbine blade surfaces, including the wake-induced transition. The authors of paper [3] presented the results of calculations using the LES method for the flow around a low-pressure turbine rotor blade with periodically occurring flow wakes. An experimental study of the wake-induced transition using boundary layer flow visualization over a 30P30N multi-element airfoil allows us to detect the formation and subsequent development of Λ-vortices [4]. Paper [5] presents the results of experimental and numerical studies of a low-pressure turbine blade cascade, conducted to analyze wake interaction effects on boundary layer transition. The authors noted that under steady-state conditions, a substantial separated flow occurred on the suction side. Under the influence of the wake generator, this separated flow was reduced, decreasing profile pressure losses by 50%. The influence of the frequency of passage of vortex wakes on the development of transient processes in the boundary layer was considered in [6]. A squirrel cage was used as a wake generator. In experiments, a clear relationship was established: the longitudinal position of the point where the boundary layer becomes fully turbulent shifts upstream with increasing wake vortex frequency. Several papers have been devoted to the experimental study of the transition caused by the wake of a circular cylinder located near the wall using flow visualization techniques [7, 8]. In [9], the flow around a cylinder near a flat wall is numerically investigated for small gap values. Because of the wake-induced transition study, three dynamic vortex motion processes associated with different hairpin vortex generation mechanisms were discovered [9]. These results are consistent with previous data presented in papers [10, 11]. In all the studies cited, methods for diagnosing wake-induced transitions were not considered.

Several methods for diagnosing a wake-induced transition are discussed in the article [12]. The purpose of this paper is to conduct a more detailed study of methods for diagnosing a wake-induced transition initiated by steady wakes behind a still and periodic unsteady wake behind oscillating cylinders.

3. Materials and research methods

The electro calorimetric method was used to study heat transfer. DISA-55M hot-wire system was used to measure the parameters of the internal structure of the dynamic and thermal boundary layers and external flow. Experimental investigations of a flat plate heat and momentum transfer processes in the presence of unsteady flows were carried out in the T-5 wind tunnel of the IET NASU using various wake generators (a still and oscillating cylinders).

The experimental setup diagram of a still and oscillating cylinder (1) with a frequency of 4.4 Hz, as well as a limiting plate (2) in the working section (3) of the T-5 wind tunnel is shown in Fig. 1. In contrast to the case described in paper [12], this study examined the diagnostics of a wake-induced transition in two cases of a still cylinder and an oscillating cylinder. The still cylinder was installed at distances equal to both the amplitude (y_c=20 mm) and the mid-span of the oscillation (y_c=10 mm). The study of heat and momentum transfer processes on a flat plate in the presence of a wake-induced transition was carried out at an external flow velocity $U \approx 9$ m/s.

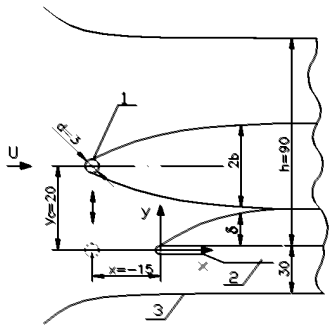

Fig.1. Experimental setup diagram

A total of 4 series of experiments were conducted: in the absence of a cylinder (natural LTT at Tu =0.2–0.4%) (series 1), with two installations of a still cylinder (y_c=20 and 10 mm) (series 2 and 3), and with an oscillating cylinder (series 4).

4. Results and discussion

We will consider the main methods for diagnosing a wake-induced transition using the example of determining the coordinates of transition for the cases of a still and an oscillating cylinder. This study was based on an analysis of distributions of local heat transfer and friction coefficients and the characteristics of dynamic and thermal boundary layers, which are developing along the length of the plate.

1. The traditional method of determining the start and end of the transition by the minimum and maximum points in the distributions of heat transfer and friction coefficients along the length of the plate is unsuitable in case of an oscillating cylinder due to their smoothed nature (Fig. 2a, 2b, symbol 6).

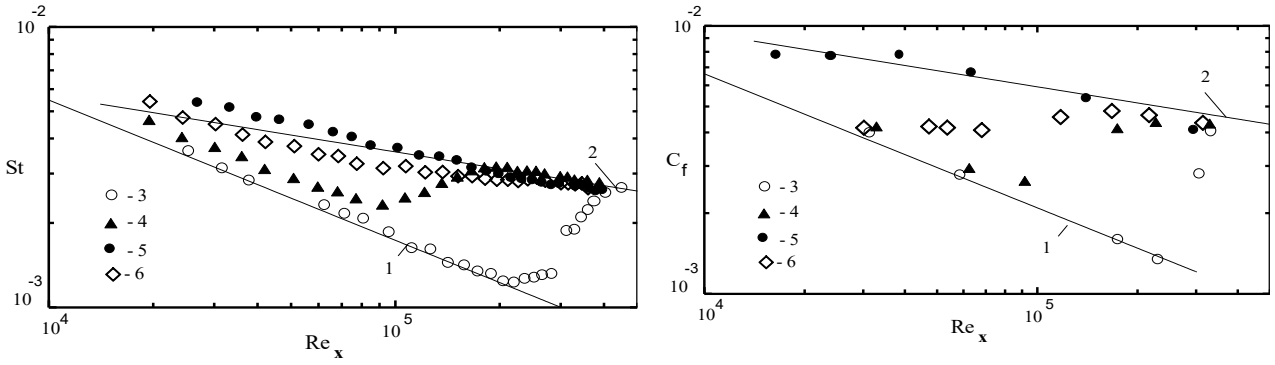

Fig.2. Distributions of local heat transfer (a) and friction coefficients (b):
1 – $St_0 = 0.55 \cdot Re_x^{-0.5}$ (a); $C_{f0} = 0.664 \cdot Re_x^{-0.5}$ (b); 2 – $St_0 = 0.036 \cdot Re_x^{-0.2}$ (a); $C_{f0} = 0.0595 \cdot Re_x^{-0.2}$ (b); 3 – in the absence of a cylinder; 4 - y_c =20 mm; 5 - y_c =10 mm; 6 – an oscillating cylinder

In the absence of a cylinder (series 1, symbol 3 in Fig. 2), the start and end of the LTT region, corresponding to the minimum and maximum of these distributions, are $Re_{x_{st}}$=2·10^5 and $Re_{x_{end}}$=4.5·10^5. The length of the natural transition region was $Re_{x_{end}}/Re_{x_{st}}$ =2.25 (where $Re_{x_{st}}$ and $Re_{x_{end}}$ are the coordinates of the start and end of the LTT, respectively). In series 4 (Fig. 2a, symbol 6), under the influence of an oscillating cylinder, the distribution of local heat transfer coefficients was non-monotonic, and the experimental points were located between series 2 (y_c=20 mm) and 3 (y_c = 10 mm). The intensification of heat transfer in the pre-transitional pseudolaminar BL in series 4 reached ~40% at Re_x= 6·10^4. The distribution of friction coefficients in series 4 (Fig. 2b, symbol 6) also has a smoothed character and is located between series 2 and 3. The intensification of friction in the pre-transitional BL changes from 1.09 in the first measuring section to 1.5 at Re_x =6·10^4. Thus, the intensification of heat transfer at $Re_x = const$ in the pre-transitional BL exceeds the increase in friction for both a still (y_c= 20 mm) and an oscillating cylinder. The reasons for the increase in heat transfer, which outpaces friction, are associated with changes in the internal structure of the pre-transitional BL (primarily with a high degree of correlation between velocity and temperature fluctuations).

As shown by the results of experimental studies of the external flow turbulence when installing a still (y_c = 20 mm, series 2) and an oscillating cylinder (series 4), given in [12], added by additional experiments at y_c= 10 mm (series 3), the degree of turbulence of the external flow gradually increased in series 2, 4, and in series 3 was maximum. Thus, the analysis of the obtained distributions of local heat transfer coefficients along the plate length shows that with increasing turbulence of the external flow caused by the cylinder location (series 1, 2, 4 and 3, respectively), an increase in the heat transfer coefficients in the pre-transition pseudolaminar BL is observed. In the third series, with the cylinder positioned at y_c = 10 mm (symbol 5 in Fig. 2a), the effect of the wake led to a monotonic change in the heat transfer coefficients along the plate length, resulting in a «upper» approach to the turbulent BL characteristics. Such variations of St don't permit to predict the «upper» transition origin and to diagnose the location of its start and end. It should be noted that the distribution of heat transfer coefficients in Fig. 2a of this article coincides with the corresponding distributions in Fig. 2 in the

work [12] for the cases of without cylinder, for installations of a still cylinder y_c=20 mm and an oscillating cylinder.

2. A common method for diagnosing LTT is to determine the start and end of the transition as minimum and maximum points in the dynamic pressure distribution. To implement this method, the total pressure nozzle is moved in the direction of flow at a fixed distance close to the plate surface, which is usually chosen to correspond to the displacement thickness of the laminar BL at the start of the transition region.

3. Less commonly used is the hot-wire anemometer method for determining the transition region. In this method, the hot-wire anemometer probe is also moved along the flow at a fixed distance from the surface. The coordinates of the start and end of the transition can be determined by changes in voltage proportional to the time-averaged velocity or temperature, as well as its longitudinal fluctuations over a wide or fixed frequency band. This method, compared to the previous one, has a number of advantages: the ability to visually observe the nature of disturbances at a given point with low inertia of the measuring system.

4. Diagnostics of the wake-induced transition can be carried out using the temperature distribution on the plate surface or changes in temperature difference: $\Delta t = A \cdot x^n$. Figure 3 clearly shows a break in the temperature difference distribution at $x_{st} \approx 140$ mm, indicating the start of a wake-induced transition. In the pre-transition region, n = 0.28, and in the transition region, n=0.13. Diagnosing the end of a wake-induced transition based on this temperature difference distribution is difficult.

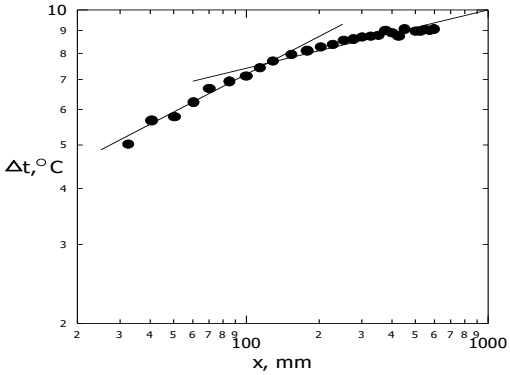

Fig. 3. Distribution of temperature difference along the length of the plate with an oscillating cylinder

5. Determination of the start and end of a wake-induced transition based on the deformation of the velocity profiles in wall law coordinates (Fig.4a).

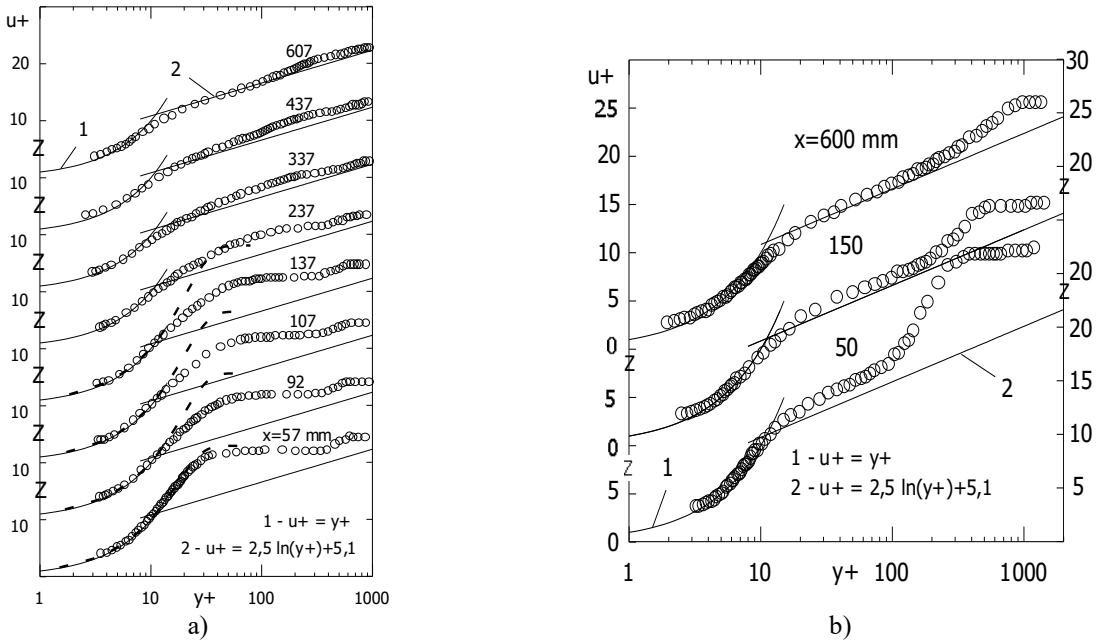

Fig.4. Velocity profiles with an oscillating cylinder (a) and y_c =10 mm (b)

In the first measurement section, at x = 57 mm, the velocity profile for an oscillating cylinder practically coincided with the Blasius profile (dashed line in Fig. 4a). In following sections, at x = 92–137 mm, the velocity distribution in the near-wall region, although different from the Blasius profile, retains its shape. The start of a wake-induced transition is determined by appearance of a flattened portion (an analog of the future region of log-law validity) (Fig.4a, x =237 mm). The end of the transition corresponds to a section in which a velocity profile with a clearly defined region of the logarithmic law is observed (Fig.4a, x =437 mm). This deformation of the velocity profile is characteristic of a bypass transition. The analysis of Fig. 4b shows that when the cylinder is installed at y_c=10 mm, a transitional flow regime is already observed in the section at x =50 mm, which is transformed into a turbulent one, and at x=600 mm the logarithmic law of the velocity distribution occupies the region of y^+ =30-120. This distribution of velocity profiles proves the presence of an «upper» transition in the initial sections of the plate.

6. Diagnostics of a wake-induced transition can be carried out using distributions $\delta/x = f(Re_x)$ and $\delta^{**}/x = f(Re_x)$, where δ^{**} is momentum thickness (Fig.5a, 5b). If we draw two straight lines in these distributions through points lying in the pre-transitional BL and in a wake-induced transition, then their intersection will indicate the coordinate of the start of transition region. The end of the transition cannot be clearly determined using these distributions.

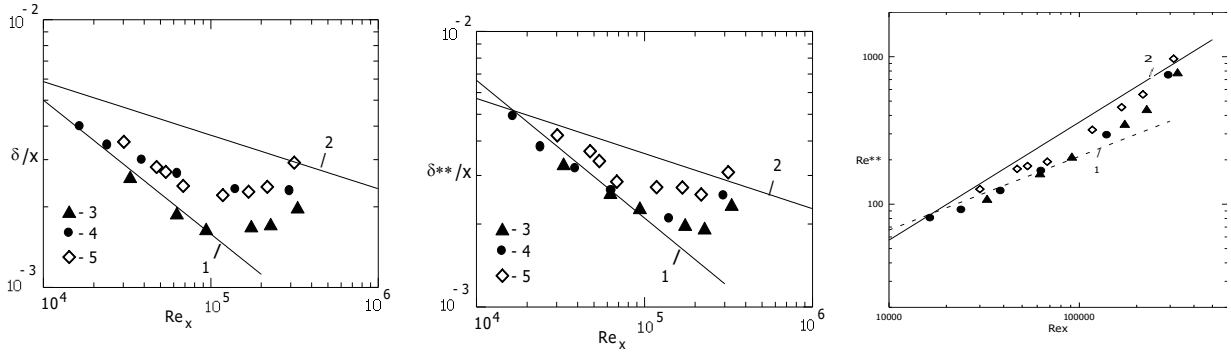

a) b) c)

Fig. 5. Distribution of the thickness of the BL (a) and the momentum thickness (b) along the length of the plate: 1 – $\delta/x = 5/Re_x^{-0.5}$ (a), $\delta^{**}/x = 0.664 \cdot Re_x^{-0.5}$ (b); 2 – $\delta/x = 0.37 \cdot Re_x^{-0.2}$ (a); $\delta^{**}/x = 0.036 \cdot Re_x^{-0.2}$ (b) 3 - y_c =20 mm; 4 - y_c =10 mm; 5 – an oscillating cylinder
c) Distribution $Re^{**} = f(Re_x)$ 1 - $Re^{**} = 0.664 \cdot Re_x^{0.5}$; 2 - $Re^{**} = 0.036 \cdot Re_x^{0.8}$

7. A variation of the previous method is the use of a distribution $Re^{**} = f(Re_x)$ constructed in a logarithmic coordinate system (Fig.5c).

8. The end of a wake-induced transition can be clearly determined from the distribution of the shape parameter along the length of the plate $H = f(Re^{**})$ as the coordinate of the beginning of its linear changes in the region of the turbulent BL (Fig. 6). It should be noted that this distribution is often used to determine the start of LTT. Typically, the start of LTT is defined as the point at which the shape parameter begins to deviate from 2.6, characteristic of laminar BL. This method is unsuitable for diagnosing the start of a wake-induced transition due to the decrease in the shape parameter in the pre-transitional BL (Fig. 6).

9. Diagnostics of a wake-induced transition is possible based on the analysis of velocity and temperature fluctuations. During the transition process, the shape of the longitudinal velocity fluctuations profile is transformed from smooth with a rounded top, characteristic of a pseudolaminar BL, into a pointed shape, typical of a turbulent BL (the first wall peak for an oscillating cylinder in Fig. 7). A characteristic feature of these distributions, which distinguishes them from the fluctuation profiles for still cylinders, is the appearance of a second maximum due to the interaction of wakes. The behavior of the first wall maximum for an oscillating cylinder is characterized by: as it approaches to the transition region, it increases, reaching a value u_m'/U_e =14-15%, and then decreases and approaches the wall in the turbulent BL. The second maximum occurs closer to the outer edge of the BL and in the initial sections is larger in amplitude than the wall peak. Thus, in particular, in the section x=50 mm the wall peak with a maximum u_m'/U_e=12% is located at y/δ =0.2, and the second maximum u_m'/U_e=17.8% - at y/δ=0.6. In following sections of the plate, the amplitude of the second maximum decreases, at the start of the transition it becomes comparable in amplitude to the wall maximum (x =137 mm) and then gradually disappears (x =607 mm).

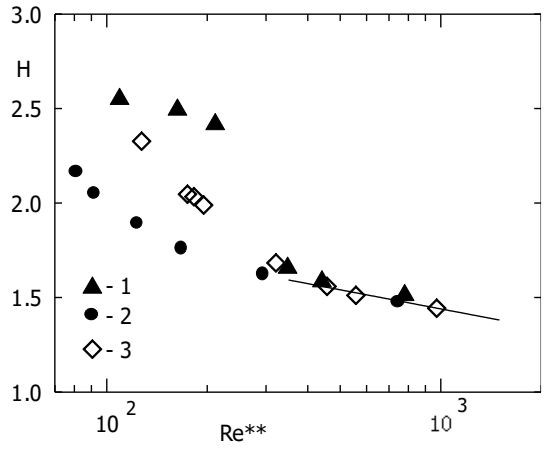

Fig.6. Changing the shape parameter H along the length of the plate: 1 - y_c =20 mm; 2 - y_c =10 mm; 3 – an oscillating cylinder

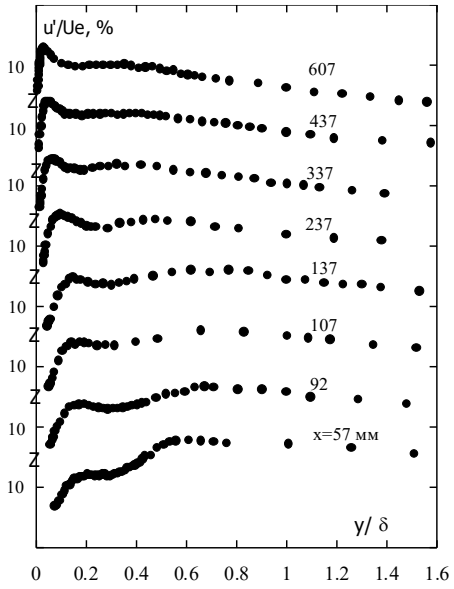

Fig.7. Longitudinal velocity fluctuations profiles with an oscillating cylinder

10. Indicators of the type of BL developing on the surface are the location and amplitude of the longitudinal velocity fluctuations maxima. During the development of the transition, the amplitude of the maximum increases for y_c=20 mm and for an oscillating cylinder (wall peak), reaching a value of $u_m{}'/U_e$ =14-15%, decreasing slightly in the turbulent BL (Fig. 8). The maximum values $u_m{}'/U_e = f(Re^{**})$ in the distribution for an oscillating cylinder are achieved at values Re^{**} smaller than for y_c=20 mm, which confirms the shift of the transition zone upstream in the first case. In addition, which was noted earlier, a distinctive feature of the wake-induced transition, as well as the bypass transition, is the increase in the values of the longitudinal velocity fluctuations maxima in the pre-transition BL with an increase in the external flow turbulence created by the wakes behind the cylinders. The position of the still cylinder at y_c =10 mm turbulizes the external flow so much that the values $u_m{}'/U_e$ are already maximum in the first measurement section and decrease along the length of the plate during a wake-induced transition process. The amplitude of the second maximum for an oscillating cylinder change is similarly. The observed features of velocity fluctuation profiles are in good agreement with results of investigation presented in [12].

A comparison of all the considered diagnostic methods is presented in the table 1.

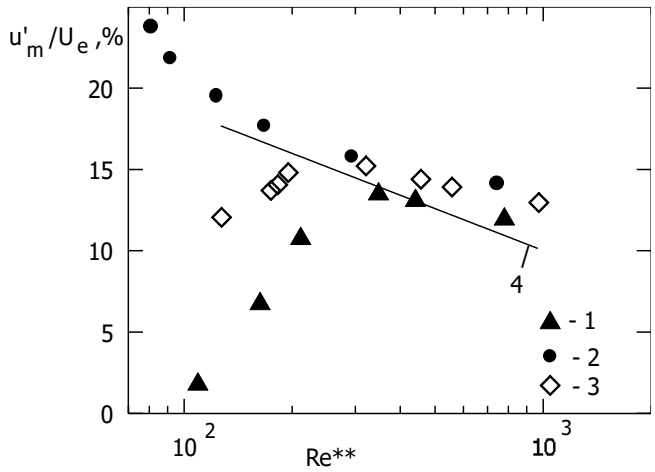

Fig.8. Distributions of the longitudinal velocity fluctuations maxima: 1 - y_c=20 mm; 2 - y_c=10 mm; 3 – wall peak for an oscillating cylinder; 4 – second maximum for an oscillating cylinder

Table 1. Methods for diagnostics of wake-induced transition

Methods	Advantages	Limitations
Distributions of heat transfer and friction coefficients	Suitable for still cylinder (y_c=20 mm)	Unsuitable for still cylinder y_c = 10 mm and an oscillating cylinder
Distributions of dynamic pressure near the plate surface	Simplicity and accessibility of the method	Selecting a fixed distance near the plate surface corresponding to the displacement thickness of the laminar boundary layer
Changing the signal of a hot-wire anemometer near the plate surface	The ability to visually observe the nature of disturbances at a given point with low inertia of the measuring system	Selecting a fixed distance near the plate surface corresponding to the displacement thickness of the laminar boundary layer
Temperature distribution on the plate surface	Simplicity of the method. Suitable for diagnosing the start of a wake-induced transition	Diagnosing the end of a wake-induced transition is difficult
Deformation of the velocity profiles in wall law coordinates	Suitable for still cylinder (y_c=20 mm) and an oscillating cylinder	Diagnosing the region of a wake-induced transition in the presence of an «upper» transition (y_c = 10 mm) is difficult
Distributions $\delta/x = f(Re_x)$, $\delta^{**}/x = f(Re_x)$, $Re^{**} = f(Re_x)$	Suitable for diagnosing the start of a wake-induced transition	The end of the transition cannot be clearly determined
Distribution of the shape parameter	Suitable for diagnosing the end of a wake-induced transition	Unsuitable for diagnosing the start of a wake-induced transition
Analysis of velocity fluctuations distributions including location and amplitude of the longitudinal velocity fluctuations maxima	Suitable for diagnosing the start and end of a wake-induced transition	Diagnosing the region of a wake-induced transition in the presence of an «upper» transition (y_c = 10 mm) is difficult

As the presented methods for diagnosing a wake-induced transition have demonstrated, there is no single, reliable way to determine the start and end of the transition region. Some proposed methods reliably determine the start of the transition, while others only determine the end. This may explain the existing discrepancies in the interpretation of the results of various authors on diagnosing a wake-induced transition. Only a combination of the methods described above allows for the diagnosis of such a transition.

5. Conclusion

The presented results were focused on development of new and modification of existing diagnostic methods for a wake-induced transition initiated by wakes behind a still and oscillating cylinders. The special attention was paid to finding the start and end of its region. It is necessary to use a combination of presented methods to reliably determine the coordinates of a wake-induced transition.

Using a combination of developed diagnostic methods, the coordinates of a wake-induced transition were determined for 4 series of experiments:

– with an oscillating cylinder (series 4): $Re_{x_{st}}$=8.5·10^4, $Re_{x_{end}}$=2.4·10^5, respectively x_{st} ≈140 mm, x_{end} ≈400 mm;

– still cylinder (y_c=20 mm) (series 2): $Re_{x_{st}}$=9·10^4 and $Re_{x_{end}}/Re_{x_{st}}$=2.94;

– still cylinder (y_c= 10 mm) (series 3): $Re_{x_{st}}$=8.2·10^4, $Re_{x_{end}}/Re_{x_{st}}$=2.82.

Increasing the turbulence of the external flow by installing fixed and moving cylinders leads to the fact that a wake-induced transition region shifts upstream in series 2, 4 and 3. These experimentally established facts make it possible to predict the location of the wake-induced transition and the intensification of heat transfer in the pseudolaminar BL, i.e., to control the process of such type transition using wakes behind the still and oscillating cylinders in the range of these experiments parameters. The experimentally discovered fact that with increasing vortex frequency the start of a wake-induced transition region shifts upstream coincides with the conclusions of the previously cited article [6].

Based on the data obtained in the range of parameters in the present experiments, the possibilities of controlling a wake-induced transition are confirmed:

– its location - from x_{st} ≈115 to 155 mm at y_c=10 and 20 mm respectively;

– length - from ($x_{end} - x_{st}$) ~230 to 300 mm at y_c=10 and 20 mm respectively;

– intensification of transfer in the preceding pseudolaminar BL - from ~20% (y_c =20 mm) to ~90% (y_c=10 mm) at Re_x= 6·10^4.

The need to coordinate the efforts of researchers to unify experimental procedures for determining the coordinates of a wake-induced transition region was emphasized.

Conflict of interest statement
The author declares that they have no conflict of interest in relation to this research, whether financial, personal, authorship or otherwise, that could affect the research and its results presented in this paper.

Statement on the use of Artificial Intelligence.
The authors declare that no artificial intelligence tools were used to generate scientific content, results, or conclusions of this article.

Data Availability Statement
The data are available upon reasonable request from the authors.

References

1. Mayle, R.E., Dullenkopf, K. (1989). A theory for wake induced transition. ASME Paper 89-GT-57 1989. https://doi.org/10.1115/89-GT-57

2. Dick, E., Kubacki, S. (2017). Transition Models for Turbomachinery Boundary Layer Flows: A Review. *International Journal of Turbomachinery, Propulsion and Power*, 2(2), 1-45. https://doi.org/10.3390/ijtpp2020004

3. Michelassi, V., Wissink, J. G., Frohlich, J., Rodi, W. (2003). Large-eddy simulation of flow around low-pressure turbine blade with incoming wakes. *AIAA journal*, *41*(11), 2143-2156.

4. Wang, Jiang-Sheng, Wang, Jin-Jun. (2021). Wake-induced transition in the low-Reynolds-number flow over a multi-element airfoil. *Journal of Fluid Mechanics,* 915, A28. https://doi.org/10.1017/jfm.2021.20

5. Stadtmüller, Peter, Fottner, Leonhard, Fiala, Andreas. (2000). Experimental and numerical investigation of wake-induced transition on a highly loaded LP turbine at low Reynolds numbers. *Proceedings of the ASME Turbo Expo 2000: Power for Land, Sea, and Air*. *Volume 3: Heat Transfer; Electric Power; Industrial and Cogeneration*. Munich, Germany. May 8–11, 2000. V003T01A074. ASME. https://doi.org/10.1115/2000-GT-0269

6. Liu, X., Rodi, W. Experiments on transitional boundary layers with wake-induced unsteadiness. *Cambridge University Press*. https://www.cambridge.org/core/journals/journal-of-fluid-mechanics/article/abs/experiments-on-transitional-boundary-layers-with-wakeinduced

7. He, Guo-Sheng; Wang, Jin-Jun. (2015). Flat plate boundary layer transition induced by a controlled near-wall circular cylinder wake. *Physics of Fluids,* 27, 024106. https://doi.org/10.1063/1.4907744

8. He, G., Wang, J., Pan, C. (2013). Initial growth of a disturbance in a boundary layer influenced by a circular cylinder wake. *Journal of Fluid Mechanics,* 718, 116-130. https://doi.org/10.1017/jfm.2012.599

9. Li, Jianghua, Wang, Bofu, Qiu, Xiang, Wu, Jianzhao, Zhou, Quan, Fu, Shixiao, Liu, Yulu. (2022). Three-dimensional vortex dynamics and transitional flow induced by a circular cylinder placed near a plane wall with small gap ratios. *Journal of Fluid Mechanics,* 953, A2. https://doi.org/10.1017/jfm.2022.930

10. He, G.-S., Wang, J.-J., Pan, C., Feng, L.-H., Gao, Q., Rinoshika, A. (2017). Vortex dynamics for flow over a circular cylinder in proximity to a wall. *Journal of Fluid Mechanics*, 812, 698–720. https://doi.org/10.1017/jfm.2016.812

11. Zhou, J., Qiu, X., Li, J., Liu, Y. (2021). The gap ratio effects on vortex evolution behind a circular cylinder placed near a wall. *Physics of Fluids*, 33 (3), 037112. https://doi.org/10.1063/5.0039611

12. Suprun, T. (2016). Heat transfer in the presence of transition induced by wakes of hesitating cylinder. *Eurasian Physical Technical Journal*, 13, 2(26), 93 – 98. http://phtj.ksu.kz/files_phtj/2017.01/13.pdf

---

AUTHORS' INFORMATION

Suprun, Tatiana Tarasovna — Candidate of Technical Sciences, Senior Researcher, Institute of Technical Thermophysics of the National Academy of Sciences of Ukraine, Kiev, Ukraine; Scopus ID: 57200913941; https://orcid.org/0000-0002-5360-388X

EURASIAN PHYSICAL TECHNICAL JOURNAL

2026, Volume 23, No. 2 (56)

https://doi.org/10.31489/2026N2/99-107

Received: 06/01/2026 Revised: 28/05/2026 Accepted: 26/06/2026 Published online: 30/06/2026

Original Research Article

UDC 53.087.4:621.391.63

INTELLIGENT DEVICE FOR DIAGNOSTICS AND FAILURE PREDICTION OF FIBER-OPTIC COMMUNICATION LINES BASED ON DIGITAL MONITORING

Juraeva N.I.*[1], Davronbekov D.A.[2], Boboev A.A.[3]

[1] Karshi state technical university, Uzbekistan
[2] Tashkent University of Information Technologies named after Muhammad Al- Khwarizmi, Tashkent, Uzbekistan
[3] New Uzbekistan University, Tashkent, Uzbekistan
*Corresponding author: juraeva.0878@gmail.com

Abstract. *In the context of intensive growth in the volume of transmitted information and the complexity of telecommunication network architecture, improving reliability of fiber-optic communication lines at the operational stage is becoming particularly relevant. This paper proposes an approach to intelligent diagnostics of fiber-optic information transmission system elements based on the parameters of digital monitoring of optical modules. The feasibility of using diagnostic data on the power of the optical signal, temperature, power voltage, and laser current to assess the current state of the line and identify signs of degradation is analyzed. A structural diagram of a hardware-software device is proposed, providing continuous data collection, their adaptive processing, and the formation of real-time prognostic estimates. For processing diagnostic parameters, a machine learning model adapted for the built-in microcontroller platform and focused on failure risk classification and intelligent diagnostics of line elements. The results of experimental studies based on real operational data confirm the possibility of early detection of potential failures and increasing the reliability of fiber-optic communication lines.*

Keywords: fiber-optic communication lines; digital monitoring; failure forecasting; degradation of optical components; intelligent data processing; technical condition diagnostics; reliability of telecommunication networks.

1. Introduction

The development of digital technologies, the constant growth of the volume of transmitted information, and the increasing demands on communication quality require higher reliability of telecommunication systems. Under these conditions, fiber-optic information transmission systems (FOITS) occupy a special place in modern communication infrastructure, providing high-speed data exchange over long distances [1]. The number of internet users has doubled between 2014 and 2024, which is equivalent to an average annual growth of approximately 7.23% [2]. The constant increase in data transmission speed, the complication of network architecture, and the increased load on communication channels lead to increased failure probability, parameter degradation, and increased requirements for the stable operation of these systems. Fiber optic information transmission systems are placing increasingly high demands on reliability and fault tolerance. To ensure the timely detection of malfunctions and prediction of failures, intelligent diagnostic tools are necessary that can not only record current changes but also make predictions based on accumulated data. Predicting malfunctions is crucial during operation, as it allows for early detection of failures and minimizes downtime. Failure forecasting methods based on the analysis of historical data and intelligent monitoring systems, particularly

machine learning, can analyze failure data volumes, predict possible failures, adapt to changing operating conditions, and eliminate them before they occur [3,4]. This, in turn, allows for early maintenance, automatic parameter correction, and fault-tolerant control of fiber-optic communication systems.

Although the failure forecasting method allows for the detection of possible failures, it is necessary to develop a diagnostic tool that allows for continuous monitoring with adaptive data processing to continuously monitor the state of elements. Of particular interest is the use of DDM (Digital Diagnostic Monitoring) functionality integrated into SFP (Small Form-factor Pluggable) modules, as well as the prospects for their integration with microcontrollers and intelligent algorithms.

A number of works consider various approaches to the diagnosis and monitoring of fiber-optic communication lines and optical modules. The system presented in the work [5] provides power monitoring, channel switching in case of failure, and reflected signal detection, however, the architecture does not support intelligent analysis. An analysis of the reliability of SFP modules was conducted based on long-term monitoring of digital diagnostic monitoring parameters, within which the possibility of using DDM data to assess degradation processes was shown; however, hardware platform diagnostics and failure forecasting have not been implemented and are limited to assessing correlational relationships [6]. A model of a fiber-optic communication line diagnostics device based on the analysis of attenuations and disruptions in the line has been proposed, however, the device does not support digital monitoring functions and does not provide for the application of intelligent data processing algorithms [7]. Modern approaches to free-spatial optical communication and mirror-based optical structures are considered, where the potential of digital monitoring as a tool for monitoring the state of optical systems is noted and the need to supplement it with intelligent analysis tools is emphasized [8]. The architecture and basic capabilities of implementing digital diagnostic monitoring functions in SFP modules are described, while issues of degradation analysis and failure forecasting are not addressed [9]. An optical module for digital diagnostics with real-time measurement of temperature, voltage, current, and optical power is presented, however, parameter processing the module analyzes the data according to a fixed algorithm without implementing prognostic functions [10]. A mechanism for automatic correction of optical power during signal level decrease based on digital diagnostic monitoring data, oriented towards control actions and not providing for the assessment of residual resource and failure probability of communication line elements [11], has been implemented.

Analysis of existing devices and diagnostic methods has shown the need to develop a device designed to diagnose failures in the elements of the SFP module based on diagnostic data obtained from SFP modules with DDM technology for analysis and processing, including predicting the level of fiber degradation, residual service life, and failure probability of elements using machine learning algorithms, and with the possibility of subsequent transmission of forecasting results through the communication module to the user's external devices.

2. Materials and methods of research

The device is designed to collect, analyze, and predict parametric and functional failures of fiber-optic communication line elements based on diagnostic data (Fig. 1). Unlike known solutions, the device allows forecasting the state of network components in real time using a pre-trained machine learning model integrated into the microcontroller system [12].

The operating principle of the device consists of several stages. In the first stage after power supply, the device is activated. The SFP module (1) with the DDM digital monitoring system, is connected to the fiber-optic communication line, transmits and receives the optical signal. The microcontroller (2) acquires diagnostic parameters from the DDM interface of the SFP module system for the $P_{Tx}(t)$ transmitter and $P_{Rx}(t)$ receiver power values, module temperature $T(t)$, power voltage $U(t)$, and bias current $I(t)$ through a standard digital interface (Fig.1). As a microcontroller (2), ESP32 is used, which has an embedded wireless communication module and necessary interfaces for questioning the DDM system, interaction with external modules and data transmission.

The obtained data is structured and transmitted to the adaptive information processing unit (3), where their analysis is carried out using a pre-loaded trained machine learning model obtained from the external learning system (12). The ESP32-S3 microcontroller, which is manufactured by Espressif Systems [13,14], serves as an adaptive information processing module. This product was chosen for its combination of high computing power, energy efficiency, built-in external interfaces, and neural network support (including TensorFlow Lite Micro).

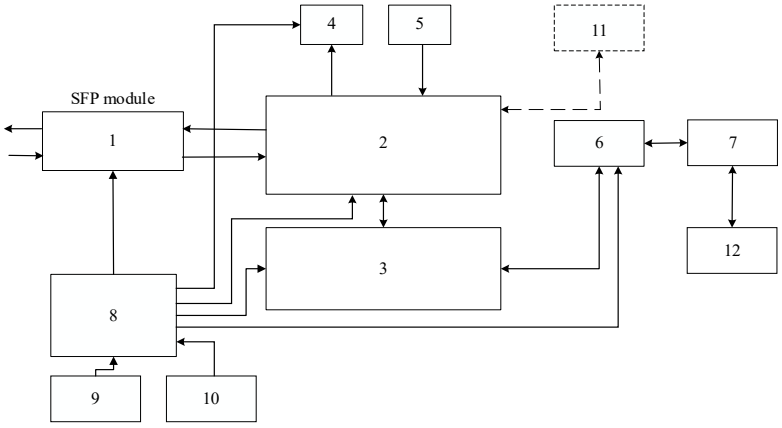

Fig. 1. Structural diagram of the fiber-optic communication line element diagnostics device. 1-SFP Module, 2-microcontroller, 3- adaptive information processing unit, 4- display, 5- control unit, 6- communication module, 7-database, 8- power supply control system, 9- power supply from source, 10- battery, 11- EEPROM (Electrically Erasable Programmable Read-Only Memory), 12-external learning system

The adaptive information processing module, built on the basis of ESP32-S3, represents an intelligent platform for predictive diagnostics of FOITS, capable of analyzing the parameters of optical elements and predicting failures. The forecasting results are displayed on the display (4), and also transmitted through the communication module (6) via a wireless interface to the user's external devices. Simultaneously, the microcontroller stores current diagnostic parameters and forecasting results in EEPROM (Electrically Erasable Programmable Read-Only Memory) (11) and database (7). The user can access the database remotely through a computer or server, view saved data, generate reports, and monitor the line's status. During operation, the control unit (5) coordinates the device's operation, and the power supply control system (8) controls the power supply from source (9) and battery (10), ensuring the device's autonomous operation.

The adaptive information processing module, in which the machine learning model is implemented, is given special attention. The main goal of model training is to form a training model of a machine learning algorithm capable of using diagnostic parameters obtained from the SFP module through the DDM interface (Fig.2). At the initial stage of task formation, the model type is based on the set task. The goal is to determine the failure risk level: low/medium/high and the degradation value, as well as the residual service life. The proposed device architecture supports classification and regression tasks. In this study, only a classification model was implemented and experimentally tested to determine the level of failure risk.

The data should be prepared in a convenient and standardized format for model training. For this, the characteristics are normalized (reduced to a single scale):

$$x_i^{norm} = \frac{x_i - \mu_i}{\sigma_i} \tag{1}$$

where x_i^{norm} - normalized value; x_i - parameter value for the i-th measurement; μ_i - the average value of this characteristic for all data; σ_i - standard deviation of a trait for all data.

Class or predicted value tags are created, for classification:

$$y = \begin{cases} 0; Q(t) < 0,3 \\ 1; 0,3 \le Q(t) < 0,7 \\ 2; Q(t) \ge 0,7 \end{cases} \tag{2}$$

for regression:

$$y = t_{failure} - t \tag{3}$$

Threshold values are selected based on equipment technical passports and preliminary degradation analysis results. The values can be adapted to specific operating conditions.

When choosing a model for implementing predictive diagnostics, it is necessary to consider several important factors, especially those related to the limitations of embedded systems:

- low dimensional size and permissible computational load for the ESP32-S3 microcontroller;
- support for real-time forecasting;

Interpretation of results, necessary for assessing, forecasting, and explaining the causes of identified risks.

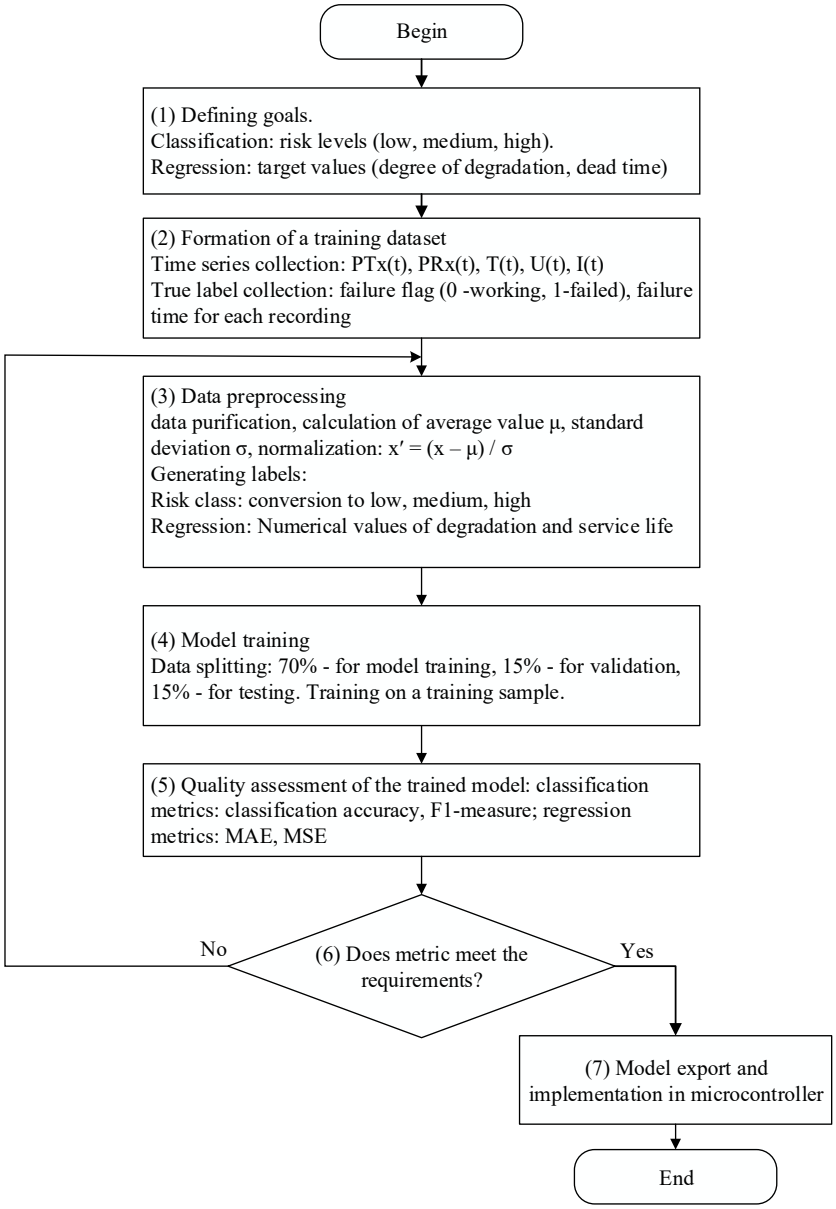

Fig.2. Algorithm for training an ML model for export to a microcontroller

The principle of operation of the device in normal operating mode: after power supply, the microcontroller automatically initiates a sequence of questioning of the DDM SFP module system with an interval of 1 s. With each sample, the laser temperature, power voltage, laser displacement current, as well as the emitted and received optical power are recorded. Data is transmitted to the adaptive information processing module. Based on a pre-trained neural network model, the module forms a forecast of the failure probability of key elements and residual fiber resource; the complete processing cycle —from the moment of sampling to the issuance of the forecast result — does not exceed 5 s. The obtained forecasts are accompanied by a time mark, visualized on a touchscreen in the form of trends and text messages, and simultaneously published through a wireless channel to external user services. In parallel, diagnostic samples and corresponding forecasts are archived in the EEPROM ring buffer and replicated into the internal database. Such an algorithm

ensures continuous ("on-line") observation of the line's state without data loss even with high-frequency parameter fluctuations. In the warning signal mode: when one of the predicted degradation threshold metrics reaches 70% of the critical level by default, the microcontroller generates an alarm event. On the display, a "red" dialog box automatically opens, indicating the reason and the recommended action (for example, "The probability of fiber breaking after ≈72 hours - check the area between points A-B"). Simultaneously, a notification is sent through the communication module via the Web-Push or MQTT-push protocol to the operator's registered devices, indicating the date, time, module identifier, and current statistics. Therefore, the operator receives a warning long before the actual failure and can plan prevention without stopping traffic.

In emergency mode and battery power: in case of sudden loss of external network power or critical hardware error, the power control unit instantly switches the load to the built-in battery. At this point, the device switches to standalone mode: the display lighting and data transmission are switched off, but the collection of diagnostic parameters, forecasting, and logging continue as before. All events recorded during battery operation are marked with a special "backup power" flag. After restoring the main power supply and network connection, the microcontroller automatically discharges the latest archive data, including the time of failure, to the external database, which gives the operator a complete picture of the emergency situation. If necessary, the log file can be manually exported through the user interface.

Such a sequence of modes guarantees the continuity of monitoring, allows for timely warning of impending failures, and ensures data preservation even in emergency situations, thereby increasing the overall reliability of fiber-optic communication lines.

To implement the device failure forecasting function, a trained machine learning model is used, formed based on real diagnostic logs obtained during nine months of operation of twelve fiber-optic communication line main nodes. The dataset consisted of 1,000 labeled samples, each represented by five DDM-based diagnostic features. The data were randomly divided into 70% training and 30% testing subsets. For the MLP classifier, 20% of the training data were internally allocated for validation during the learning process. After training, the network is quantized to 8-bit TensorFlow Lite format, the final file, approximately 180 Kbytes, is signed with the SHA-256 control sum and placed in the protected HTTPS repository of the external training system. The ESP32-S3 microcontroller, when initialized, executes a request to this repository, automatically compares the control sum of the local and available models, and upon the appearance of a new version, uploads the file to the second section of the internal Flash memory; switching to the updated model occurs after re-launching without user intervention. During operation, the input vector for the network is a sliding window from the last fifty samples of diagnostic data (about 50 seconds of observations), supplemented by a sine-cosine representation of the time of day; the hardware neural processing unit of the ESP32-S3 nucleus performs an interference in 4-5 seconds at a clock frequency of 240 MHz, after which the microcontroller compares the obtained probability value with a threshold of 0.8, duplicates the result in the EEPROM and the database, displays it on a touch screen, and publishes it through the wireless channel. Such a software and hardware solution guarantees the reproducibility of the method, provides local forecast calculation without involving external computing resources, and allows for regular improvement of model accuracy through automatic updating from the training system.

Database (7) is an embedded SQLite table placed in the flash memory of microcontroller 3: it does not require a separate hardware unit, but is logically highlighted because it stores a long-term archive of diagnostic samples and forecasts. The MCU (Microprogrammed Control Unit) writes new lines there, and the communication module 6 unloads them to external systems upon request.

The technical result of the developed device is an increase in the reliability of fiber-optic communication lines due to the implementation of diagnostics and forecasting of parametric and functional failures of fiber-optic communication line elements based on the analysis of diagnostic data obtained from SFP modules with the support of DDM technology. The possibility of measuring the transmitter power, receiver power, power voltage, module temperature, laser displacement current is provided, thereby predicting the level of fiber degradation, residual service life, and the probability of element failures. The combination of these effects necessitates a significant increase in the reliability and fault tolerance of fiber-optic communication lines, reduces maintenance costs, and improves the quality of telecommunications services provided.

The diagnostic device for fiber-optic communication line elements with adaptive information processing differs from existing solutions [7-12] in that it additionally contains an adaptive information processing module (3), a display, a communication module, a network power source, a power control unit (Table 1). Microcontroller (2) is capable of transmitting diagnostic parameters from the DDM system to an adaptive information processing module, which is designed to predict parametric and functional failures of fiber-optic

communication line elements using a pre-trained machine learning model. There is also an opportunity to transmit results via a communication module via a wireless channel to the user's external devices in real-time, and diagnostic parameters and forecasting results are stored in energy-independent memory and a database.

Table 1. Devices and methods for diagnosing failures elements in fiber-optic communication lines

Method / System	Method Description	Main Limitations / Advantages	Reference
Integrated semi-active CWDM system with a circulator	Provides optical power monitoring, channel switching in case of failure, and reflected signal detection.	The architecture is limited to CWDM systems, does not include intelligent data analysis.	[7]
Reliability assessment of optical transceivers based on SFP parameter monitoring	Long-term reliability analysis of SFP modules using Digital Diagnostic Monitoring (DDM) parameters.	DDM is used only for correlation analysis without performing predictive diagnostics.	[8]
Optical cable diagnostic device	Analysis of attenuation and disturbances in fiber-optic communication lines.	Does not support DDM and lacks intelligent diagnostic or predictive capabilities.	[9]
Monitoring system for optical SFP transceiver modules	System architecture based on DDM integrated into SFP modules.	DDM functionality is implemented only for parameter monitoring.	[10]
Optical module with digital diagnostic method	DDM-enabled optical module providing monitoring of temperature, supply voltage, laser bias current, and optical power.	Does not include intelligent data processing, employs a fixed diagnostic model, and does not support failure prediction.	[11]
Optical power adjustment method based on the optical module and terminal	Automatic adjustment of optical power using the DDM database.	DDM is used only for operational control; historical data storage, intelligent analysis, and predictive capabilities are not provided.	[12]

3. Results and discussion

Modeling and model training were conducted in the MATLAB environment using neural network modeling tools. The application of the MATLAB software environment made it possible to implement a complete cycle of model construction and verification, i.e., data preparation and architecture selection, visualization of learning convergence, and analysis of quality metrics. comparative experiments were conducted with machine learning models - MLP (Multilayered perceptron), Decision Tree and Random Forest (Table 1). The performance of the evaluated models was assessed using Accuracy, Precision, Recall, F1-score, and ROC-AUC (Table 2), since the dataset was highly imbalanced, with approximately 98.3% of the samples corresponding to the normal operating state and only 1.7% representing fault conditions. Decision Tree and Random Forest models achieved the best overall performance, whereas the MLP classifier demonstrated lower Recall despite its high Accuracy and Precision. Among the evaluated models, the Random Forest classifier achieved the highest ROC-AUC value (0.9986) while maintaining an Accuracy of 99.67%, a Recall of 100%, and an F1-score of 0.9091. Therefore, the Random Forest model was selected for implementation in the proposed intelligent diagnostic device due to its superior predictive performance and robustness.

Table 2. Performance comparison of the evaluated machine learning models

Model	Accuracy	F1-score	Precision	Recall	ROC-AUC
MLP	0.9900	0.5714	1.0000	0.4000	0.9925
Decision Tree	0.9967	0.9091	0.8333	1.0000	0.9983
Random Forest	0.9967	0.9091	0.8333	1.0000	0.9986

The dynamics of training the MLP neural network for loss function is presented in Table 3. As shown in the figure, the training was completed at the 18th epoch as a result of fulfilling the early stop criterion when achieving minimal error in the validation set. The value of the loss function decreased from 0.161 to 0.0115. The gradient decreased from 0.383 to 0.0044, indicating the convergence of the model. The Scaled Conjugate Gradient optimization method was used. This graph confirms the stability of learning and the absence of signs of overtraining.

Table 3. MLP neural network learning dynamics

Parameter	Initial Value	Final Value	Target Value
Epoch	0	18	1000
Elapsed Time	–	00:00:08	–
Performance	0.1610	0.0115	0
Gradient	0.3830	0.0044	1×10^{-6}
Validation Checks	0	6	6

The confusion matrices for the MLP, decision tree, and random forest classifiers shown in Figure 3 provide an analysis of the classification results. The MLP classifier correctly identified most normal samples but failed to detect three fault samples. In contrast, the Decision Tree and Random Forest classifiers correctly identified all fault samples while producing only one false positive.

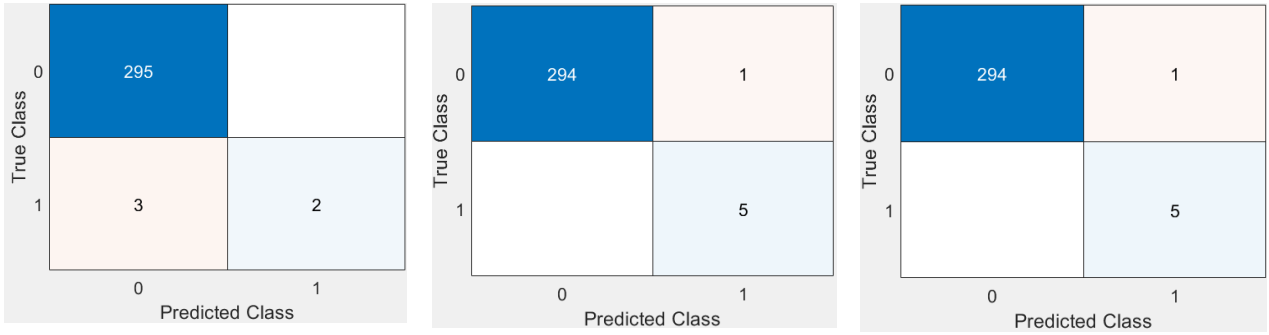

a) b) c)

Fig.3. Confusion matrices: (a) MLP, (b) Decision Tree, and (c) Random Forest

The architecture of a trained MLP neural network used for binary classification of the module's state is shown in Fig.4. A vector consisting of five diagnostic characteristics is fed into the input: transmission power (P_{Tx}), reception power (P_{Rx}), temperature (T), voltage (U), and current (I). The hidden layer contains 10 neurons and utilizes a fully connected structure using the activation function. The result of the hidden layer is transmitted to the output layer, where another linear transformation is performed with the addition of displacements. The output layer consists of two neurons and forms a probability vector of the input data belonging to one of the two classes (correct/failure) using the Softmax activation function.

The conducted experiments showed that this configuration has sufficient generalizability while maintaining low computational load, making it suitable for embedding in the ESP32-S3 microcontroller. Subsequently, the model was trained on labeled diagnostic data and exported to the TensorFlow Lite Micro format, which ensured correct integration into the adaptive information processing module implemented on the target hardware platform. The graph of the change in the loss function during the learning process of the MLP model is shown in Fig. 5. The curves on the graph show a decrease in error in training, validation, and test samples. The minimum error value in the validation sample was achieved in the 12th period (0.029975), marked by the intersection of the green line with the horizontal line "Best." After this point, an increase in validation error is observed, indicating the beginning of retraining. The early stop mechanism automatically completed the training in the 18th era to prevent the degradation of the model's generalizability.

The discrepancy between the validation and testing curves after the 12th era further demonstrates how sensitive the model is to retraining, given the limited training data set. This suggests adding regulation methods and possibly increasing the training set. However, the generalizability obtained from the model may be sufficient for the purposes of developing diagnostic tasks using built-in tools, which is confirmed by the stable behavior of the loss function in the test set until the end of training.

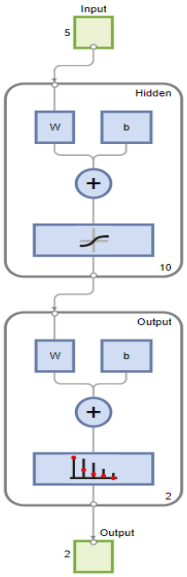

Fig. 4. MLP trained neural network architecture diagram

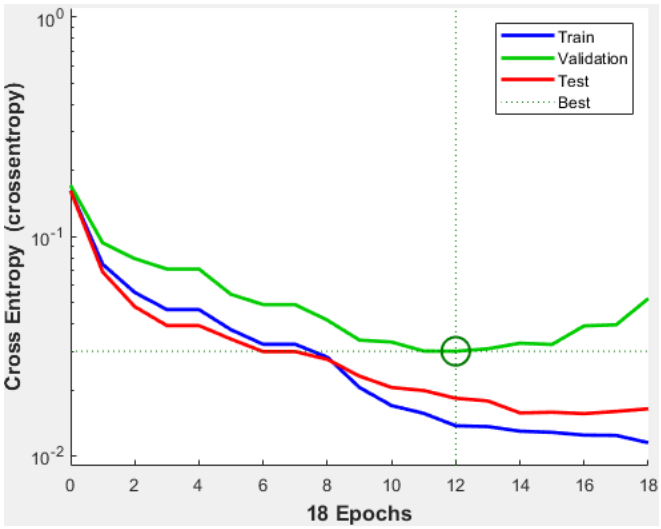

Fig. 5. Reducing errors in training, validation and test samples

4. Conclusion

Analysis of existing devices and methods for diagnosing fiber-optic information transmission systems showed that most of the applied solutions are focused on monitoring current parameters and local adjustment of operating modes, and do not provide failure forecasting and estimation of the residual resource of communication line elements. In this regard, a model of a diagnostic device based on the collection and processing of digital monitoring parameters of optical modules with the support of DDM technology and the integration of intelligent analysis algorithms has been proposed. The developed device architecture includes an adaptive information processing module that implements the assessment of the current technical condition of fiber-optic communication line elements, forecasting the probability of failures through machine-learning-based classification of the technical condition. The proposed device architecture is extensible and can be complemented in future work with regression models for quantitative degradation assessment and remaining useful life prediction. The device operates in real time and provides automatic transmission of diagnostic results to the user, which expands the possibilities of managing the reliability of fiber-optic information transmission systems.

Conflict of interest statement

The authors declare that they have no conflict of interest in relation to this research, whether financial, personal, authorship or otherwise, that could affect the research and its results presented in this paper.

CRediT author statement

Juraeva N.I.: Conceptualization, Methodology, Writing-original draft, Writing - review and editing. **Davronbekov D.A.:** Investigation, Visualization. **Boboev A.A.:** Software, Validation. The final manuscript was read and approved by all authors

Statement on the use of Artificial Intelligence.

During the preparation of this manuscript, artificial intelligence tools were used solely for language editing and grammatical improvement. No AI tools were used to generate scientific content, analysis, results, or conclusions.

Data Availability Statement

For the practical implementation of the developed device, real failure data provided by the telecommunications organization “Uzbektelecom” JSC were employed. In connection with privacy and data protection requirements, original datasets cannot be made publicly available.

Acknowledgements

The author would like to express their sincere gratitude to everyone who provided support in carrying out this study. We are grateful to our colleagues for their valuable advice and suggestions at various stages of our work.

Special thanks to the telecommunications organization that provided data for this work.

References

1. Winzer, P. J. (2023). The future of communications is massively parallel. *Journal of Optical Communications and Networking, 15*, 783–787. https://doi.org/10.1364/JOCN.496992

2. Statista. (2024). *Number of internet users worldwide*. https://www.statista.com/statistics/273018/number-of-internet-users-worldwide/

3. Davronbekov, D., Juraeva, N., & Boboev, A. (2024). Advanced applications of machine learning techniques in FOITS. In *Proceedings of the 4th International Conference on Technological Advancements in Computational Sciences (ICTACS)* (pp. 773–778). Tashkent, Uzbekistan. https://doi.org/10.1109/ICTACS62700.2024.10840715

4. Juraeva, N., Davronbekov, D., & Turdiev, U. (2025). Predicting failures in fiber optic information transmission systems with support of machine learning. *Revista Científica de Sistemas e Informática*, 5(2), e907. https://doi.org/10.51252/rcsi.v5i2.907

5. Zhang, D., Du, Z., Cheng, M., Jiang, M., & Liu, X. (2023). Innovation and demonstration of a new CWDM and circulator integrated semi-active system for 5G fronthaul. *Journal of Lightwave Technology, 41*(4), 1223–1228. https://doi.org/10.1109/JLT.2022.3199470

6. Notaro, P., Palermo, G., & Zanus, D. (2023). An optical transceiver reliability study based on SFP monitoring and OS-level metric data. In *2023 IEEE/ACM 23rd International Symposium on Cluster, Cloud and Internet Computing (CCGrid)*, (pp. 1–12). https://doi.org/10.1109/CCGrid57682.2023.00011

7. Nazarov, A. M., Rakhmonov, A. R., Khurbanbayev, S. Z., Mavlyanov, A. S., & Davronbekov, D. A. (2017). The device for diagnostics of optical fiber cables. *European Journal of Technical and Natural Sciences*, (5), 82–88. https://elibrary.ru/item.asp?id=32378796

8. Pregowska, A., Osial, M., et al. (2020). From mirrors to free-space optical communication. *Future Internet, 12*(11), Article 179. https://doi.org/10.3390/fi12110179

9. Jinlin, Z., et al. (2009). The application and realization of the digital diagnostic monitoring function for SFP optical transceiver module. In *IEEE Conference Proceedings* (pp. 379–382). https://doi.org/10.1109/ICBNMT.2009.5348515

10. China National Intellectual Property Administration. (2024). *Optical module diagnostic system* (Patent No. CN119766321A). https://patents.google.com/patent/CN119766321A/en

11. China National Intellectual Property Administration. (2024). *Automatic optical power correction method* (Patent No. CN118611744A). https://patents.google.com/patent/CN118611744A/en

12. Davronbekov, D. A., Juraeva, N. I., & Xamidov, X. A. (2025). *Adaptiv axborotni qayta ishlash bilan optik tolali aloqa liniyalari elementlarini diagnostika qilish qurilmasi* (Utility Model Patent No. FAP 2865). Ministry of Justice of the Republic of Uzbekistan. https://im.adliya.uz/register/UTILITY_MODEL?page=6

13. Espressif Systems. (2023). *ESP32-WROOM-32E and ESP32-WROOM-32UE datasheet*. https://www.espressif.com/sites/default/files/documentation/esp32-wroom-32e_esp32-wroom-32ue_datasheet_en.pdf

14. Espressif Systems. (2023). *ESP32-S3-WROOM-2 datasheet*. https://www.espressif.com/sites/default/files/documentation/esp32-s3-wroom-2_datasheet_en.pdf

---

AUTHORS' INFORMATION

Juraeva, Nafisa Inoyatovna - Doctor of Technical Sciences, Associate Professor, Faculty of Digital Technologies and Artificial Intelligence, Karshi state technical university, Karshi, Uzbekistan; SCOPUS ID: 26025933700, https://orcid.org/0000-0001-7459-003X; juraeva.0878@gmail.com

Davronbekov, Dilmurod Abdujalilovich - Doctor of Technical Sciences, Professor, Faculty of Technologies of Mobile Communication, Tashkent University of Information Technologies named after Muhammad Al-Khwarizmi, Tashkent, Uzbekistan; Scopus ID: 57193076143; https://orcid.org/0000-0003-1193-7918; d.davronbekov@gmail.com

Boboev, Asilbek Alimardon o'g'li – B.(Sc), Software Engineering, Teaching Assistant, New Uzbekistan University, Tashkent, Uzbekistan; https://orcid.org/0009-0008-9737-8689; asilbekboboyev98@gmail.com

EURASIAN PHYSICAL TECHNICAL JOURNAL

2026, Volume 23, No. 2 (56)

https://doi.org/10.31489/2026N2/108-117

Received: 22/01/2026 Revised: 30/05/2026 Accepted: 26/06/2026 Published online: 30/06/2026

Original Research Article

UDC 533.15:536.25

INVESTIGATION OF MIXING IN BINARY GAS MIXTURES UNDER MECHANICAL EQUILIBRIUM INSTABILITY

Mukamedenkyzy V.[1], Akberdiyev B.E.[2*]

[1] Al Farabi Kazakh National University, Almaty, Kazakhstan
[2] Abai Kazakh National Pedagogical University, Almaty, Kazakhstan
*Corresponding author: bekzhanakberdiyev@gmail.com

Abstract. *Mixing processes in binary and multicomponent gas systems are characterized by a significant variety of observed regimes. The main objective of the study is to determine the boundary between diffusion and convective regimes, as well as to identify the parameters that control the convective regime. The change in modes from "isothermal diffusion" to "gravitational concentration convection" was studied using the ANSYS Fluent software package, which allows investigating the evolution of convective flows at the initial stage of mixing and determining the limits of mechanical equilibrium stability of the system. The observed correspondence between computational and experimental results verifies the proposed method for determining the boundary between diffusion and convective transport in gas mixtures. The novelty lies in reconstructing the spatiotemporal evolution of the isoconcentration fields for binary mixtures at different pressures and relating the convective flow structures to the observed mode transitions. The approach provides a verified method for locating the diffusion–convection boundary and for refining diffusion and thermal-diffusion coefficient measurements.*

Keywords: diffusion, convection, mechanical equilibrium, binary gas mixture.

1. Introduction

The fundamental cause of natural convection in liquids and gases is a disturbance in mechanical equilibrium caused by inhomogeneities in the distribution of density, temperature, and concentration of components [1]. The phenomenon of natural convection underlies many natural processes, such as atmospheric circulation and the transport of water masses in the oceans [2, 3]. The occurrence and development of convection in viscous media is due to the combined action of a number of physical mechanisms. The loss of mechanical equilibrium stability can be explained by various amplifications of hydrodynamic disturbances caused by density fluctuations [1]. Diffusion is a critically important control parameter in a class of problems describing the change in kinetic regimes under the action of simultaneously applied temperature and concentration gradients. Analysis of the stability parameters of the system is necessary not only to determine the boundaries of the growth of hydrodynamic perturbations, but also to predict the areas of their attenuation, since it is in these areas that it is possible to accurately measure the diffusion and thermal diffusion coefficients, which are of great practical importance [4, 5]. This determines the relevance of research in this area, which is valuable both for a fundamental understanding of the physical nature of the effects under study and for solving applied problems. Modeling natural convection requires consideration of a wide range of parameters determined by boundary conditions and system geometry. Models are significantly complicated by the need

to integrate factors such as coupled heat and mass transfer, chemical transformations, internal heat sources, and the presence of phase boundaries [5].

The transition between kinetic mixing modes is determined by the disruption of the mechanical equilibrium of the system. A mode change can be caused by the emergence of density gradients [6], which are formed under the influence of heat flows, composition heterogeneity, or applied external fields. When considering binary mixtures in a system, conjugate temperature and concentration gradients arise [7]. Their interaction causes the development of complex, often unstable, convective modes. The loss of mechanical equilibrium stability in binary gas mixtures is determined by a complex of factors, including spatial temperature gradients, differential compression, and external force fields. When the threshold values of the control parameters are reached, modes are formed in the system that are associated with a change in the dominant transport mechanism from molecular diffusion to convective motion. Under conditions of gravitational stratification, convective flows [8], driven by the difference in the densities of the components, evolve into complex macroscopic structures. Experimental studies [9, 10] have confirmed the validity of approaches [7, 8] for describing regions of non-isothermal diffusion and thermal concentration convection.

It should be noted that studies [5-7,11] considered convection arising from non-isothermal mass transfer and thermal diffusion under the action of a temperature gradient. As shown in [12], during isothermal mixing of multicomponent systems, the difference in diffusion coefficients causes an inversion of the mixture density, which leads to effects that require additional study compared to those presented in works on non-isothermal mixing. In [13], a large number of studies were summarized that were conducted for isothermal cases of multicomponent mixing at the boundary between diffusion and gravitational convection modes under various thermophysical factors.

Numerical studies of the evolution of convective mixing in isothermal mixtures have revealed a variety of transition regimes from diffusion to convection and have determined the characteristic mixing times inherent in diffusion and combined mixing types [14-17]. At the same time, it should be noted that the convective mixing effects recorded in [13-15] are derived from the simultaneous action of several concentration gradients. Therefore, it seems important to study the change in kinetic regimes in the presence of a minimum number of concentration gradients that correspond to binary systems when the condition of increasing mixture density with height is realized. In [9,10,18], the features of convective mixing in isothermal binary mixtures with unstable mixture density stratification were investigated. Within the framework of stability theory [1,7], relations were obtained that register the transition from diffusion to the Rayleigh–Taylor convection analogue [19]. At the same time, studies related to the dynamics of isoconcentration fields at given compositions and pressures have not yet sufficiently established the relationship between the structures of convective flows and the evolution of their development.

Unlike the authors' previous, mainly experimental and stability-theory studies [9, 10, 18], this work uses 3D CFD modelling to reconstruct the spatiotemporal evolution of the isoconcentration fields and to link the structure of the convective flows directly to the mode transitions. The novelty lies in establishing, for isothermal binary mixtures at different pressures, the connection between the spatial organization of convective flows and the "diffusion–convection" and "convection–convection" transitions, including identification of the critical pressure of mechanical-equilibrium instability.

This work proposes to numerically investigate, using the ANSYS Fluent software package [20], the initial stage of the spatial-temporal evolution of concentration fields arising from the instability of the mechanical equilibrium of a gas system at different pressures for isothermal binary mixtures. It is planned to compare the numerical results with experimental data. It is expected that the presented comparison will provide a better understanding of the mechanisms of transition from a diffusion state to a convective state, which will allow recommendations to be developed for a more detailed description of mixing processes in binary systems.

2. Problem formulation and numerical methods

The experimental studies obtained in [9-10] in the pressure range of 0.338–2.5 MPa at a temperature of 298 K using an experimental setup implementing the two-flask method, the diagram of which is shown in Fig. 1, were taken as the objects of study. The diffusion apparatus consisted of two flasks of equal volume $V_u = V_l = 55.6$ cm^3, which were connected by a diffusion channel with a diameter of $d = 0.4$ cm and a length of $L = 6.4$ cm. The duration of the experiments was 17 min, except for the experiments at a pressure of 0.29 MPa, for which the duration was increased to 60 min. The ANSYS Fluent software package provides the ability to

perform three-dimensional modeling of diffusion channels of arbitrary geometry [19], as well as visual visualization of physical processes described by the selected system of equations.

A combined approach to mesh generation was used to discretize the computational domain when modeling a binary gas mixture. The cylindrical elements of the system were approximated by an unstructured mesh based on triangular finite elements, while the diffusion channel was described by a structured mesh of square elements. This mesh generation strategy allows the geometric features of different parts of the installation to be adequately taken into account. The choice of a characteristic mesh cell size of 2 mm ensures correct reproduction of the model geometry and stable convergence of the numerical solution [20]. A mesh sensitivity analysis carried out for a representative case (p = 1.49 MPa) on co-arser and finer grids showed that the predicted nitrogen concentration in the lower flask varied by less than about 1.5% upon refinement, confirming that the results are essentially grid-independent. The mesh of about 385 000 elements was therefore adopted as an optimal compromise between accuracy and computational cost.

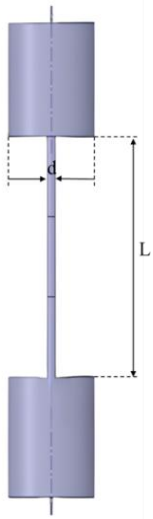

Fig. 1. Three-dimensional model of a diffusion cell and the calculated simulation area

The use of a hybrid mesh combining triangular and square elements provides an optimal balance between modeling accuracy and computational efficiency. The use of triangular cells in cylindrical regions allows for the correct approximation of curved surfaces, while the structured mesh in the diffusion channel significantly reduces computational costs. The proposed approach is consistent with modern practices for constructing computational meshes for numerical modeling of processes in binary gas mixtures, where the choice of element types and sizes is determined by the balance between the geometric complexity of the domain and the accuracy requirements of the calculations.

Mass transfer modeling in the N_2-*He* system was performed under initial conditions, when nitrogen is located in the upper flask and helium in the lower one [10]. This configuration, determined by the difference in molecular weights of the gases, creates a pronounced gravitational stratification of the mixture density, allowing the processes of mechanical equilibrium disruption to be investigated. Within the framework of mathematical modeling, the assumption was made that the physicochemical characteristics of the gas environment are constant. The numerical values of the corresponding parameters were obtained from the built-in database of substances in the ANSYS Fluent software package. Since the process is isothermal at 298 K, the temperature-dependent transport properties remain practically constant within a single run, while the pressure dependence is retained through the binary diffusion coefficient D_{12} (Eq. 6) and the mixture density is computed from the state model as a function of composition; the assumption loses accuracy only under strongly non-isothermal or near-critical conditions.

Since the apparatus is modeled as a closed system, impermeability conditions are set at all its boundaries. This type of boundary condition mathematically excludes the possibility of any mass transfer through the control surface, thereby ensuring the isolation of the system from the external environment in terms of material components. To ensure the isothermal nature of the mixing process, appropriate thermal boundary conditions were used, and the enclosure structure of the apparatus was modeled as a solid wall made of structural stainless

steel whose thermodynamic and strength characteristics were also taken from the standard ANSYS Fluent materials library [18].

Convective flows caused by mechanical equilibrium instability demonstrate complex evolutionary dynamics at the initial stage. The evolution of convective flows includes a sequence of stages: linear growth of small convective perturbations, nonlinear interaction of instability modes, transition to a turbulent regime with the formation of multiscale vortex structures, and other specific features determined by the parameters of the system [21]. To analyze partial flows in media with convective flows of variable intensity, it is advisable to use the k-ω turbulence model [22,23], which allows adequate description of mass transfer processes over a wide range. The initial and boundary conditions were set as follows: at the initial moment of time, the upper and lower chambers of the diffusion apparatus contained different binary gas mixtures. The molar fractions of the components were determined using the patch method for the corresponding grid zones.

In ANSYS Fluent, binary gas mixtures are modeled using component transport equations (mass fractions Y_1 and Y_2) and equations of motion. Mass transfer is described by convective-diffusive equations that take into account molecular and turbulent diffusion, and the density of the mixture is calculated according to the selected state model. The formulas include the transport equation for mass fraction [22-23]:

$$\frac{\partial(\rho Y_1)}{\partial t} + \nabla(\rho\vec{u}Y_1) = \nabla\left(\rho D_{eff}\nabla Y_1\right) + S_1$$
$$\frac{\partial(\rho Y_2)}{\partial t} + \nabla(\rho\vec{u}Y_2) = \nabla(\rho D_{eff}\ \nabla Y_2\ ) + S_2 \quad (1)$$

where D_{eff} is the effective diffusion coefficient, S_1 and S_2 are generalized source terms that account for possible mass sources or sinks of components. In the context of the problem under consideration, there are no additional mass sources.

The standard k–ω model is based on a system of semi-empirical transport equations, including equations for turbulent kinetic energy k and its specific dissipation rate ω, where ω is interpreted as the ratio of turbulent energy dissipation rate ε to k [23]. The standard k–ω model was chosen because, unlike the k–ε family, it integrates directly to the wall without wall functions and retains accuracy at low turbulent Reynolds numbers, so it correctly reproduces transitional and near-laminar regimes and naturally reduces to molecular transport in regions where turbulence production vanishes. This makes it suitable for the present problem, in which the flow evolves from a purely diffusive state through a transitional convective stage to locally developed convection.

$$\frac{\partial}{\partial t}(\rho k) + \frac{\partial}{\partial x_i}(\rho\vec{u}k) = \frac{\partial}{\partial x_j}\left(\Gamma_k\frac{\partial k}{\partial x_j}\right) + G_k - Y_k + S_k + G_k$$
$$\frac{\partial}{\partial t}(\rho\omega) + \frac{\partial}{\partial x_i}(\rho\vec{u}\omega) = \frac{\partial}{\partial x_j}\left(\Gamma_\omega\frac{\partial \omega}{\partial x_j}\right) + G_\omega - Y_\omega + S_\omega + G_\omega \quad (2)$$

G_k – describes the generation of kinetic energy of turbulence caused by average velocity gradients; ρ is the density of the medium; $\vec{u} = (u_x, u_y, u_z)$ – velocity vector; G_ω – characterizes the generation of the specific dissipation rate ω. In the presented system of equations, Γ_k and Γ_ω characterize the effective turbulent diffusion for k and ω, respectively; Y_k and $Y\omega$ are dissipation terms; S_k and S_ω are user source terms, which are assumed to be zero in this work [24]. The indices i, j imply summation over coordinates ($i, j = 1, 2, 3$).

The effective diffusion coefficients for the k–ω model are given by the formulas:

$$\Gamma_k = \mu + \frac{\mu_t}{\sigma_k}$$
$$\Gamma_\omega = \mu + \frac{\mu_t}{\sigma_\omega} \quad (3)$$

Prandtl turbulence numbers σ_k and σ_ω determine the efficiency of diffusion transfer of turbulent kinetic energy and the rate of its dissipation. Within the framework of the model used, constant values $\sigma_k = \sigma_\omega = 2$ are assumed. Molecular viscosity μ is supplemented by turbulent viscosity μ_t, which is a function of k and ω:

$$\mu_t = \alpha^* \frac{\rho k}{\omega} \quad (4)$$

where α^* is a coefficient that dampens turbulent viscosity and has a constant value of $\alpha^*=1$ [23]. Diffusion flows $\overrightarrow{J_1}$ and $\overrightarrow{J_2}$ for substances 1 and 2, respectively, are calculated using the formulas:

$$\overrightarrow{J_1} = -\left(\rho D_{12} + \frac{\mu_t}{Sc_t}\right)\nabla Y_1$$
$$\overrightarrow{J_2} = -\left(\rho D_{12} + \frac{\mu_t}{Sc_t}\right)\nabla Y_2 \quad (5)$$

In the presented model: μ_t is the turbulent viscosity; Sc_t is the Schmidt number, defined as $Sc_t = \mu_t/(\rho D_t)$; the standard value of Sc_t is taken to be 0.7. D_{12} is the binary diffusion coefficient; T is the temperature. It should be noted that in developed turbulent flows, the contribution of turbulent diffusion usually exceeds molecular diffusion. However, in the problem under consideration, corresponding to the initial and transitional stages of mixing, molecular diffusion processes continue to play a significant role.

Binary diffusion coefficient D_{12} is determined within the framework of Chapman-Enskog kinetic theory [25] using the formula:

$$D_{12} = 0.00186 \frac{\left[T^3\left(\frac{1}{M_{w,1}} + \frac{1}{M_{w,2}}\right)\right]^{\frac{1}{2}}}{p_{abs}\sigma_{12}^2 \Omega_D} \quad (6)$$

where M_w - molar mass (g/mol), T - temperature (K), p_{abs} - absolute pressure (atm), Ω_D - dimensionless diffusion collision integral, quantitatively characterizing the intensity of molecular interactions in the system.

An approach based on the pressure method was used for all calculation models. For spatial discretization of computational fluid dynamics equations, the schemes listed in Table 1 were used, which were tested and validated in [23, 26].

The parameters listed characterize the configuration of the numerical solution in the ANSYS Fluent environment, detailing the methods used to discretize the basic equations, approximation schemes, and computational algorithms involved in the modeling process. The PRESTO! (PREssure STaggering Option) scheme computes pressure on staggered face control volumes, avoiding the interpolation errors of standard schemes, and is therefore recommended for flows with strong body forces and steep density gradients, such as the buoyancy-driven concentration convection considered here. The selected and tested combination of discretization schemes guarantees an optimal balance between the accuracy of the numerical solution and computational efficiency, which is particularly critical for problems with the combined influence of convective and diffusion processes, and makes it the preferred choice for this class of problems [24].

Table 1. Solution methods

Quantity	Discretization
Gradient	Least Square Cell Based
Pressure	PRESTO!
Momentum	Second Order Upwind
Turbulent Kinetic Energy	Second Order Upwind
Specific Dissipation Rate	Second Order Upwind
Pseudo Time Method	Off
Transient Formulation	Second Order Implicit

3. Results of numerical studies and comparison with experimental data

Numerical simulation of the dynamics of binary gas mixtures was performed in the ANSYS Fluent 2025 R2 software environment using a Lenovo LOQ 15IAX9 computing complex equipped with an Intel Core i5-12450HX processor, 16 GB of RAM, and an NVIDIA GeForce RTX 3050 graphics accelerator. Depending on the complexity of the calculation scenario and the characteristics of iterative convergence, the duration of

a single computational experiment ranged from 20 to 72 minutes. To assess the reproducibility of the results obtained, each series of calculations was performed three times.

In order to validate the numerical approach adopted to describe the kinetic transition "diffusion–convection" and "convection–convection" over a wide range of pressures, the simulation results were compared with the experimental data presented in [9, 10] and summarized in Table 2. The computational mesh and discretization schemes are described in Section 2.

The experimental data [9,10] presented in Figure 2 illustrate the effect of pressure on the behavior of the N_2–He binary gas mixture. At low pressures, there is good agreement between the concentrations calculated under the assumption of diffusion and the experimental concentrations, which indicates the predominance of the diffusion mechanism of mass transfer. In this pressure range, the binary diffusion coefficient has relatively high values, and density stratification remains stable, as a result of which any local disturbances are effectively suppressed by molecular diffusion. With an increase in pressure starting from a certain critical value (0.518 MPa), the concentration of components increases, which indicates a loss of mechanical equilibrium stability of the system and the emergence of convective currents, i.e., a boundary transition "diffusion-convection" is recorded. This transition is caused by a decrease in the mutual diffusion coefficient with a simultaneous increase in density gradients, as a result of which the characteristic diffusion equilibration time becomes comparable to the growth time of gravity-induced perturbations. At this point, the system reaches a limiting state in which small density and concentration perturbations cease to decay. Further pressure increase leads to an increase in the concentration of components, which corresponds to the convective type of mixing. In the specified pressure range, mass transfer is determined by the development of concentration-driven gravitational convection, leading to intensification of component transfer. However, starting at a pressure of 1.1 MPa, the intensity of convective mixing begins to decrease, and at a pressure of 1.8 MPa, the intensity of mixing decreases, which is typical for diffusion rather than gravitational convection. This behavior may be associated with the restructuring and enlargement of convective structures, as well as with an increase in viscous and stabilizing effects at high pressures, which leads to a decrease in the efficiency of convective mass transfer.

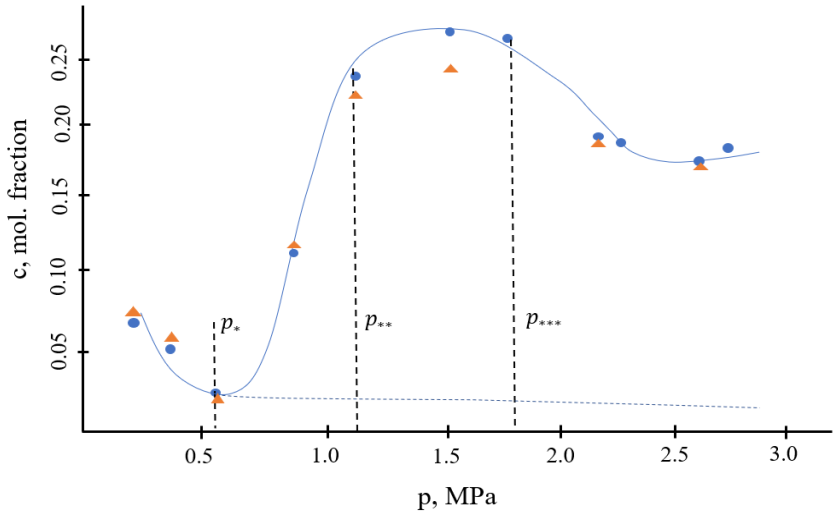

Fig. 2. Pressure dependence of nitogen transfer from upper flask to the lower flask in the N_2-He system: until $p_* \approx 0.518$ MPa – diffusion mode; from p_* to $p_{**} \approx 1.1$ MPa – the occurrence and development of convection; from p_{**} to $p_{***} \approx 1.8$ MPa – transition from one type of convective mixing to another; from p_{***} – decrease in convection intensity. ● – experimental points [9,10], ▲ – Points calculated using Ansys Fluent, solid curve – polynomial approximation, dotted curve – calculation based on Stefan-Maxwell theory

The change of mixing regimes with pressure reflects the competition between the buoyancy forces that drive convection and the diffusive and viscous mechanisms that dissipate it. As the pressure increases, the binary diffusion coefficient decreases (Eq. 6), which weakens the diffusive smoothing of concentration gradients and sharpens the density stratification. Once the solutal Rayleigh number exceeds its critical value, the mechanical equilibrium loses stability and concentration-driven convection sets in. In the range from p=0.52 to 1.1 MPa the driving density gradients dominate over dissipation, and fine-scale plume-like structures analogous to Rayleigh–Taylor fingers develop, providing a large interfacial area and intense convective

transport. At higher pressures, the further reduction of D_{12} is accompanied by an increase in density and in momentum dissipation, so that the characteristic scale of the convective structures grows: the plumes merge into larger and slower circulation cells with a smaller specific interfacial area. As a result, although convection persists, its efficiency decreases and the integral mass-transfer rate approaches values typical of the diffusion regime — this restructuring, rather than a complete suppression of convection, is the physical mechanism behind the "convection–convection" transition.

The table 2 shows experimental and calculated values of concentrations both in the diffusion approximation (according to Stefan-Maxwell equations) and taking into account convective perturbations according to the k-ω turbulence model. Analysis of experimental and numerical data shows good convergence and demonstrates that when critical pressure values are reached in the system, a transition from diffusion mode to concentration convection is observed. The formation of convective flows at certain time intervals is a key indicator of a disturbance in the mechanical equilibrium of the system. The observed process is consistent with the theoretical provisions of convective stability theory. Based on the analysis of the time dependencies of the average molar fractions and isoconcentration isoline maps, two types of transitions were identified: the "diffusion → convection" transition is recorded at the moment of isoline curvature and the appearance of local circulation flows; the "convection → convection" transition corresponds to the restructuring of the flow structure, including due to the action of convective mechanisms. With a further increase in pressure, convection persists, but its nature changes, which manifests itself in the restructuring of the spatial structure of the flows and the stabilization of average concentrations.

Table 2. Concentrations of diffused nitrogen from the upper flask to the lower flask for the *N_2-He* system at various pressures and T=298 K, τ = 17 minutes

P, MPa	$C_{experiment}$	C_{theory}	C_{Ansys}
0,338	0,065	0,064	0,069
0,437	0,051	0,051	0,055
0,518	0,043	0,046	0,040
0,798	0,161	0,030	0,165
1,030	0,244	0,024	0,226
1,490	0,273	0,016	0,239
2,210	0,184	0,022	0,181
2,655	0,173	0,028	0,170

The agreement between the calculated and experimental concentrations was quantified by the relative deviation. The mean absolute relative error over the whole pressure range is about 5.8%, with a maximum of about 12.5% near p = 1.49 MPa, where convective mixing is most intense, this confirms quantitatively the satisfactory predictive accuracy of the model.

The comparison of experimental data with calculated concentration profiles confirms that the initial stage of the diffusion process occurs within a time range that is significant for the overall mixing process. The numerical results obtained demonstrate satisfactory agreement with experimental observations. Figure 3 shows the instantaneous distribution of the concentration field of a binary gas mixture *N_2–He* at a fixed time τ=510 s at different pressure values. This method of data presentation allows us to reveal the influence of pressure on the spatial organization of mass transfer without resorting to integral mixing characteristics.

Analysis of the concentration distributions shown in Fig. 3 shows that when the pressure changes, the structure of the concentration field undergoes a sequential rearrangement—from a quasi-one-dimensional distribution to spatially inhomogeneous configurations. At low pressures, the concentration field is characterized by an ordered structure with a dominant direction of transport along the diffusion channel axis and the absence of pronounced transverse gradients, which corresponds to the distribution shown in Fig. 3a.

As the pressure in the system increases, spatial disturbances intensify, manifesting themselves in the curvature of isoconcentration lines and the formation of local inhomogeneities in the distribution of components (Fig. 3b). These changes indicate a complication of the spatial structure of mass transfer and an increase in the role of transverse concentration redistributions. With a further increase in pressure, the concentration field becomes significantly heterogeneous (Fig. 3c), reflecting the intense spatial redistribution of components within the system and the formation of stable concentration configurations. The further temporal evolution and spatial organization of these structures are shown in Figure 4.

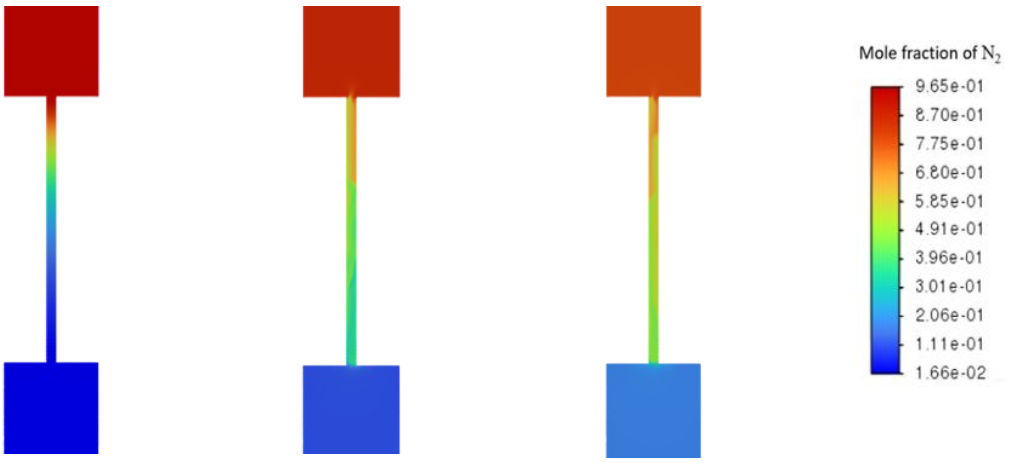

a) b) c)

Fig. 3. Mixing dynamics for the *N_2-He* system at time τ = 510 s depending on mixing modes: a) p=0.437 MPa; b) p=0.798 MPa; c) p=1.49 MPa

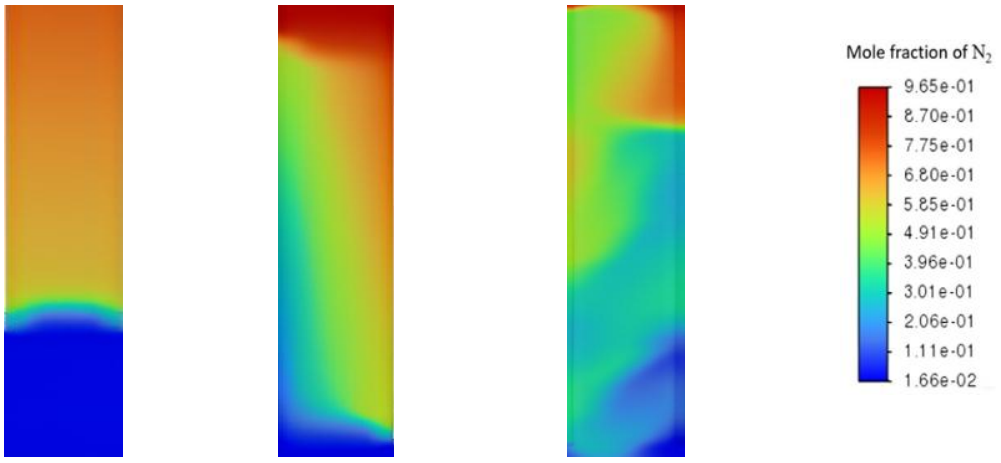

a) b) c)

Fig. 4. Convective flows formed in the diffusion channel for the *N_2-He* system at p=1.49 MPa, T=298 K as a function of time: a) τ = 1 s; b) τ = 2 s; c) τ = 7 s

The sequence of instantaneous distributions allows us to trace the characteristic stages of the evolution of concentration-driven convection after the system loses its mechanical equilibrium stability.

At the initial stage of mixing, the concentration field remains generally ordered, but small distortions of isoconcentration lines occur near the contact region of the components (Fig. 4a). These disturbances reflect the emergence of concentration fluctuations caused by the instability of density stratification and indicate a violation of the pure diffusion transport mechanism. As the process develops, the spatial disturbances intensify, covering the entire cross-section of the channel and leading to a pronounced deformation of the isoconcentration surfaces (Fig. 4b). At this point, diffusion transport is no longer able to compensate for the emerging density inhomogeneities, which leads to a sustained growth of convective motions.

As the process continues, the concentration field acquires a stable spatially heterogeneous structure, reflecting the formation of a developed convective mass transfer regime (Fig. 4c). Convective flows ensure intensive redistribution of components throughout the diffusion channel, and the subsequent evolution of the system is accompanied by complex circulation and maintenance of the quasi-stationary nature of the concentration field.

4. Conclusions

This paper presents a numerical study of mass transfer in a binary gas system *N_2–He* under conditions of isothermal mixing at varying pressure. It is shown that pressure is one of the key parameters determining the stability of mechanical equilibrium and the spatial organization of the concentration field of the gas mixture.

A critical pressure value of $p \approx 0.52$ MPa has been established, at which the diffusion mode of mass transfer loses stability and concentration-driven convection is initiated in the system. In the region of elevated pressures, a developed convective regime is formed, accompanied by an intense spatial redistribution of components and the formation of stable convective structures.

Numerical results obtained using component transport equations and the k–ω turbulence model show good agreement with experimental data and correctly reproduce both the transition from diffusion mode to convection and the subsequent evolution of convective flows. Analysis of the spatiotemporal dynamics of the concentration field revealed the characteristic stages of the process—from the emergence of small concentration perturbations to the formation of stable spatial structures.

The results obtained clarify the physical mechanisms of mechanical equilibrium instability in gas mixtures and can be used in modeling diffusion-convection processes in systems with controlled density stratification.

Conflict of interest statement

The authors declare that they have no conflict of interest in relation to this research, whether financial, personal, authorship or otherwise, that could affect the research and its results presented in this paper.

CRediT author statement

Mukamedenkyzy V.: Conceptualization, Validation, Supervision, Writing - Review & Editing; **Akberdiyev B.E.:** Methodology, Software, Formal analysis, Writing - Original Draft.
The final manuscript was read and approved by all authors.

Statement on the use of Artificial Intelligence.

During the preparation of this manuscript, artificial intelligence tools were used solely for language editing and grammatical improvement.

Data Availability Statement

The data are available upon reasonable request from the authors.

References

1 Landau, L.D., Lifshitz, E.M. (2009). *Fluid Mechanics*. *Course of Theoretical Physics, 6. 2nd Edition*. Butterworth-Heinemann (Elsevier), 539 p. https://www.sciencedirect.com/book/monograph/9780080339337/fluid-mechanics

2 Vailati, A., Xu, S., Aime, S. (2021). Diffusion and convection in nature. *European Physical Journal E*, 44, 145. https://doi.org/10.1140/epje/s10189-021-00148-0

3 Hossam, A., Ashraf, M., Rashad, A.M. (2025). A comprehensive review of convective heat transfer in humid air and its physical perspectives in climate change. *AIP Advances*, 15, 050702. https://doi.org/10.1063/5.0270951

4 Braibanti, M., Artola, P.A., Baaske, P. (2019). European Space Agency experiments on thermodiffusion of fluid mixtures in space. *European Physical Journal E*, 42(7), 86. https://doi.org/10.1140/epje/i2019-11849-0

5 Shevtsova, V., Santos, C., Sechenyh, V., Legros, J.C., Mialdun, A. (2014). Diffusion and Soret effect in ternary mixtures: preparation of the DCMIX2 experiment on the ISS. *Microgravity Science and Technology*, 25(5), 275–283. https://doi.org/10.1007/s12217-013-9349-6

6 Carpenter, J.R., Sommer, T., Wüest, A. (2012). Stability of a double-diffusive interface in the diffusive convection regime. *Journal of Physical Oceanography*, 42(5), 840–854. https://doi.org/10.1175/JPO-D-11-0118.1

7 Drazin, P.G., Reid, W.H. (2004). Hydrodynamic Stability. 2nd Edition. Cambridge Mathematical Library, Cambridge University Press, 605. https://doi.org/10.1017/CBO9780511616938

8 Lyubimova, T.P., Zubova, N.A. (2015). Onset and nonlinear regimes of ternary mixture convection in a square cavity. *European Physical Journal E*, 38(3), 19. https://doi.org/10.1140/epje/i2015-15019-2

9 Kosov, V.N., Zhavrin, Y.I., Ankusheva, N.B. (2008). Convective regimes of mixing in binary systems with mechanical equilibrium instability of a gas mixture. *Journal of Engineering Physics and Thermophysics*, 81, 525–532. https://doi.org/10.1007/s10891-008-0064-x

10 Kulzhanov, D.U. (2002). Stability of mechanical equilibrium in binary gas mixtures at different temperatures. *Bulletin of KazGU. Physics Series*, 2, 115–118. [in Russian].

11 Seleznev, V.D., Kosov, V.N., Poyarkov, I.V., Fedorenko, O.V., Beketaeva, M.T. (2013). Double diffusion in Ar–N_2 binary gas system at constant temperature gradient. *Acta Physica Polonica A*, 123(1), 62–66. https://doi.org/10.12693/APhysPolA.123.62

12 Kossov, V., Krasikov, S., Fedorenko, O. (2017). Diffusion and convective instability in multicomponent gas mixtures at different pressures. *European Physical Journal Special Topics*, 226, 1177–1187. https://doi.org/10.1140/epjst/e2016-60201-1

13 Kossov, V., Altenbach, H. (2023). Diffusion mechanisms of convective instability in liquid and gas mixtures. *ZAMM – Zeitschrift für Angewandte Mathematik und Mechanik*, 103, e202300801. https://doi.org/10.1002/zamm.202300801

14 Kossov, V.N., Mukamedenkyzy, V., Tolepbergen, A., Altenbach, H. (2025). Peculiarities of combined mixing caused by instability of mechanical equilibrium of isothermal ternary gas mixture at diffusion. *International Journal of Chemical Engineering*, 1, 9643371. https://doi.org/10.1155/ijce/9643371

15 Dil'man, V.V., Lotkhov, V.A. (2015). Molecular turbulent evaporation in a gravitational field. *Theoretical Foundations of Chemical Engineering*, 49, 102–106. https://doi.org/10.1134/S0040579515010017

16 Kossov, V., Fedorenko, O., Asembaeva, M., Moldabekova, M., Zhaneli, M. (2023). Diffusion instability in three-component gas mixtures containing greenhouse gas. *International Journal of Thermofluids*, 20, 100495. https://doi.org/10.1016/j.ijft.2023.100495

17 Zhussanbayeva, A., Kossov, V., Fedorenko, O., Magzhan, Z. (2022). Instability of mechanical equilibrium and some features of concentration convection in isothermal ternary gaseous systems. *Physical Sciences and Technology*, 9(1–2), 55–61. https://doi.org/10.26577/phst.2022.v9.i1.07

18 Kossov, V., Fedorenko, O., Zhakebayev, D., Mukamedenkyzy, V., Kulzhanov, D. (2022). Convective mass transfer of a binary gas mixture in an inclined channel. *ZAMM – Zeitschrift für Angewandte Mathematik und Mechanik*, 102(1), e201900197. https://doi.org/10.1002/zamm.201900197

19 Banerjee, A. (2020). Rayleigh–Taylor instability: a status review of experimental designs and measurement diagnostics. *Journal of Fluids Engineering*, 142(12), 120801. https://doi.org/10.1115/1.4048438

20 ANSYS Inc. (2025). ANSYS Fluent User's Guide. Canonsburg, PA, USA. https://www.ansys.com

21 Matyushenko, A.A., Garbaruk, A.V. (2016). Adjustment of the k–ω SST turbulence model for prediction of airfoil characteristics near stall. *Journal of Physics: Conference Series*, 769, 012082. https://doi.org/10.1088/1742-6596/769/1/012082

22 Nouhaila, O., Hassane, M., Scutaru, M.L., Jelenschi, L. (2024). On the accuracy of turbulence model simulations of the exhaust manifold. *Applied Sciences*, 14, 5262. https://doi.org/10.3390/app14125262

23 Abd Halim, M.A., Nik Mohd, N.A.R., Mohd Nasir, M.N., Dahalan, M.N. (2018). Evaluation of k–ε and k–ω turbulence models in modelling flows and performance of S-shaped diffuser. *International Journal of Automotive and Mechanical Engineering*, 15(2), 5161–5177. https://doi.org/10.15282/ijame.15.2.2018.2.0399

24 Kutkan, H., Guerrero, J. (2021). Turbulent premixed flame modeling using the algebraic flame surface wrinkling model: a comparative study between OpenFOAM and ANSYS Fluent. *Fluids*, 6, 462. https://doi.org/10.3390/fluids6120462

25 Qiu, T., Li, C., Zhang, Y., Ge, W. (2025). HS-PPM simulation for diffusion coefficients of binary and multicomponent gas mixtures. *AIChE Journal*, 71(9), e18891. https://doi.org/10.1002/aic.18891

26 Liyanage, R. (2024). Direct comparison of density-driven convective mixing in a three-dimensional porous medium. *Physical Review Fluids*, 9, 043802. https://doi.org/10.1103/PhysRevFluids.9.043802

AUTHORS' INFORMATION

Mukamedenkyzy, Venera – Candidate of Physical and Mathematical Sciences, Associate Professor, Department of Technical Physics and Thermal Physics at Al Farabi Kazakh National University, Almaty, Kazakhstan; SCOPUS Author ID 48561625900; https://orcid.org/0000-0003-3921-2812; mukameden@inbox.ru.

Akberdiyev, Bekzhan Erzhanuly – 3rd year PhD student, Department of Physics at Abai Kazakh National Pedagogical University, Almaty, Kazakhstan; https://orcid.org/0009-0001-2108-9556; bekzhanakberdiyev@gmail.com.

EURASIAN PHYSICAL TECHNICAL JOURNAL

2026, Volume 23, No. 2 (56)

https://doi.org/10.31489/2026N2/118-129

Received: 24/01/2026 Revised: 31/05/2026 Accepted: 26/06/2026 Published online: 30/06/2026

Original Research Article

UDC 538.911

STUDY OF CRYOVACUUM CONDENSATES OF A CARBON MONOXIDE, CARBON DIOXIDE AND METHANE MIXTURES WITH WATER IN A 95:5 RATIO

Chigambayeva N.N.*, Nurmukan A.Y., Aldiyarov A.U., Korshikov E.S., Erlanov T.E.

Al-Farabi Kazakh National University, Almaty, Kazakhstan
*Corresponding author: nurgul050490@gmail.com

Abstract. *In the context of the intensifying greenhouse effect, the search for effective approaches to the capture and retention of greenhouse gases such as CO, CO_2, and CH_4 has become increasingly relevant. The aim of the present work is to experimentally investigate the absorption capacity of water cryocrystals with respect to CO, CO_2, and CH_4 molecules under low-temperature and vacuum conditions, as well as to analyze the effect of phase transitions of water ice on the kinetics of gas impurity release from the standpoint of the prospective application of these systems in decarbonization technologies. This work presents experimental results on the investigation of the absorption properties of water cryocrystals with respect to CO, CO_2, and CH_4 molecules under deep vacuum and ultra-low temperature conditions (13–200 K). Using temperature-programmed desorption (TPD), mass spectrometry (MS), and laser interferometry, the ability of water ice in various phase states (amorphous, cubic, and hexagonal) to efficiently retain and stepwise release gas impurities has been demonstrated. A correlation between the phase transitions of ice (ASW → Ic → Ih) and the desorption behavior of the molecules has been established. The obtained results confirm the potential of water cryostructures for use as passive or controllable sorbents within prospective decarbonization technologies, environmental monitoring, and gas storage applications.*

Keywords: low temperature, temperature-programmed desorption, mass spectrometry, cryogenic conditions, carbon dioxide, carbon monoxide, methane.

1. Introduction

Global climate change is driven by the increase in anthropogenic emissions of greenhouse gases, primarily carbon monoxide (CO), carbon dioxide (CO_2), and methane (CH_4), whose atmospheric concentrations have reached record levels over the entire period of instrumental observations [1]. CO and CO_2 account for the major share of radiative forcing, whereas CH_4 exhibits a significantly higher global warming potential per unit mass, making both gases key targets of climate policy and scientific research [2,3].

According to estimates by the Intergovernmental Panel on Climate Change (IPCC), without additional emission reduction measures, global temperature increases by the end of the 21st century could exceed 3 °C, posing serious risks to sustainable development [4]. According to the International Energy Agency (IEA), global carbon dioxide emissions from the energy sector have exhibited a steady upward trend during the period 2020–2024. After decreasing to 34.2 Gt in 2020 due to reduced economic activity during the COVID-19 pandemic, emissions sharply increased to 36.3 Gt in 2021. In the subsequent years (2022–2024), the growth rate slowed; however, the total emissions reached 37.6 Gt, representing a 9.7 % increase compared to 2020, as shown in Figure 1. This increase is primarily associated with the growth in energy consumption in industry

and transportation, despite the active deployment of renewable energy sources. At the same time, according to IEA estimates, the development of low-carbon technologies has prevented an additional approximately 2.5 Gt of CO_2 emissions per year [5, 6].

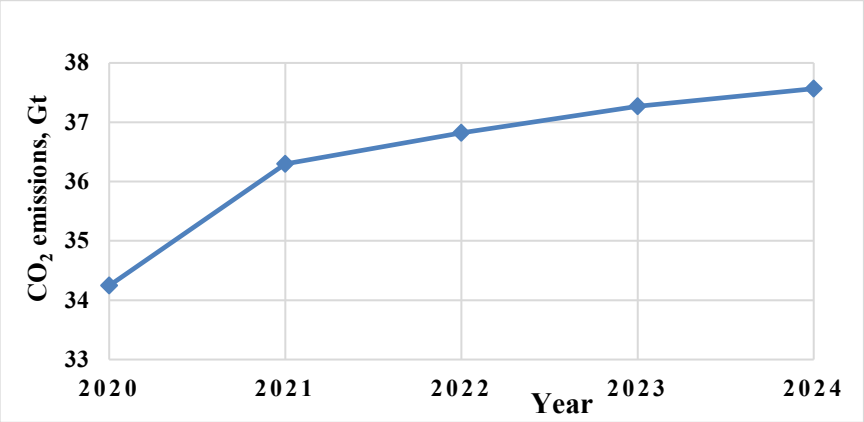

Fig. 1. Analysis of global CO_2 emissions dynamics based on IEA data (2020–2024) [5, 6]

The increase in greenhouse gas emissions observed in recent years indicates that existing measures are insufficient to achieve climate targets, making decarbonization policy particularly relevant. Under current conditions, decarbonization is not only an environmental measure but also a strategic necessity in the context of the escalating climate crisis, requiring active participation of industrial enterprises in reducing their carbon footprint through improved energy efficiency, modernization of technological processes, and implementation of innovative solutions [7]. As noted in [8], an important component of this strategy is the capture, storage, and utilization of CO_2, including its use for biofuel production, which contributes to sustainable development. In this context, alongside the transition to renewable energy sources, carbon capture, storage, and utilization technologies (CCS/CCU) are gaining increasing significance, being considered a necessary and complementary approach within the framework of energy and industrial decarbonization [9, 10].

Traditional methods for capturing CO, CO_2, and CH_4, including chemical and physical absorption, adsorption on porous materials, and membrane technologies, face several limitations related to high energy consumption, material degradation, and significant operational costs [11–13]. This motivates the search for alternative approaches capable of providing high purification efficiency while reducing both energy and economic expenditures [14].

Promising directions include cryogenic methods for gas capture and separation, which are based on phase transitions at low temperatures. Recent studies indicate that cryogenic technologies can be effective when working with gas mixtures containing high concentrations of CO, CO_2, and CH_4, as well as when integrated with gas liquefaction and storage processes [10, 14, 15]. At the same time, the further development and optimization of such technologies are impossible without a detailed understanding of the molecular mechanisms governing gas–condensed phase interactions, as well as an analysis of their phase and structural behavior under cryogenic conditions, which necessitates the use of highly sensitive experimental techniques.

Infrared (IR) spectroscopy methods play a key role in advancing experimental research in low-temperature physics and gas-phase chemistry, as they enable the investigation of the molecular state of substances and their interactions with the condensed phase at cryogenic temperatures. In particular, a low-temperature measurement cell for IR spectroscopy of hydrocarbon materials has been developed and experimentally validated, operating in the temperature range of 77–300 K at atmospheric pressure. This approach makes it possible to obtain new fundamental data on molecular behavior under cryogenic conditions. Such experimental methodologies are also of considerable interest for studying cryovacuum condensates and cryogenic gas capture processes, as they provide precise control over temperature effects, phase transitions, and the spectral characteristics of molecules confined within low-temperature water-based structures [16]. Within this approach, particular interest is drawn to water cryostructures, including cryovacuum condensates and gas hydrates, in which gas molecules are encapsulated within the crystalline lattice of water [17, 18].

Gas hydrate and clathrate systems are actively investigated both for CO_2 capture and storage and for the replacement of methane in natural hydrate deposits, offering opportunities for simultaneously addressing

climate and energy challenges [12, 13, 17]. However, the practical application of these technologies requires a thorough understanding of the processes of gas sorption and temperature-dependent desorption, the phase behavior of water ice, and the kinetics of structural transitions under cryogenic conditions [15, 18].

Recent studies have demonstrated that amorphous solid water (ASW) possesses a highly porous structure capable of effectively trapping volatile molecules within an interconnected network of nanopores. The porosity and gas-retention capacity of ASW are strongly dependent on deposition conditions and thermal history. Upon annealing, ASW undergoes progressive pore collapse, structural densification, and crystallization, all of which significantly influence the release kinetics of trapped gases. Experimental studies have shown that heating ASW results in pore closure, confinement of gases within isolated cavities, and subsequent desorption associated with structural relaxation and crystallization of the ice matrix. These processes are of considerable importance for cryogenic gas storage, the evolution of astrophysical ices, and low-temperature adsorption phenomena. Recent neutron-scattering investigations have provided direct evidence of pore restructuring and densification in ASW during heating, further confirming the strong relationship between ice morphology and the retention of volatile species. Therefore, the study of gas trapping and release in amorphous solid water remains an important research area for understanding the mechanisms of molecular transport and storage in cryogenic water-based systems [19 - 22].

2. Methodology and Experimental Setup

2.1 Experimental Apparatus

In this study, a universal vacuum spectrophotometer was used to perform experiments on cryocondensed films. The working chamber of the setup was evacuated using a rotary vane pump and a turbomolecular pump. A pressure of approximately P ~ 10^{-4} Torr was achieved during preliminary evacuation, while pressures of ~10^{-8} Torr were attained in the high-vacuum measurement mode. A detailed description of the experimental setup used is provided in [23]. The schematic diagram of the experimental setup used in this work is shown in Figure 2. Gradual annealing of the samples was carried out using a DT-670 semiconductor temperature sensor, whose operation was controlled by an LS325 temperature controller (Lake Shore, USA). Experimental data were analyzed using the temperature-programmed desorption (TPD) method. The samples were heated at a constant rate of dT/dt = 0.166 K/s while maintaining high vacuum conditions of approximately ~10^{-8} Torr.

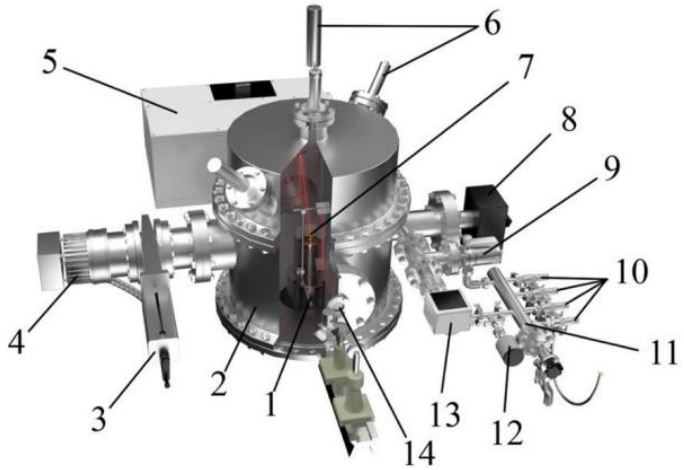

Fig. 2. Schematic diagram of the cryovacuum spectrophotometer setup: 1 – cryostat; 2 – vacuum chamber; 3 – rotary vane pump; 4 – turbomolecular pump; 5 – Fourier-IR spectrometer; 6 – dual-beam laser interferometer; 7 – substrate; 8 – mass spectrometer; 9 – dosing valves; 10 – manometers and pressure sensors [23]

Temperature control was achieved with an accuracy of ±0.1 K over the range of 13–310 K. A copper plate coated with a thin layer of high-purity gold (99.99%) was used as the substrate and cooled to cryogenic temperatures, providing efficient condensation of the gas-phase components. A combination of TPD-MS methods was employed to analyze the desorption of components from cryocondensed films. During programmed heating, the mass spectra of desorbing components as well as the overall pressure change in the working chamber were recorded. This approach allowed us to determine which molecules were released from

the substrate surface and at which temperatures their desorption occurred. The resulting TPD curves reflected the intensity of gas release from the substrate surface as a function of temperature.

2.2 Material

Samples of condensed mixtures of the H_2O–gas system (CO, CO_2, CH_4) were prepared by physical vapor deposition (PVD) at a substrate temperature of T = 13 K and a chamber pressure of approximately P ~ 10^{-4} Torr. The gas mixture was prepared by simultaneously introducing saturated water vapor and the gaseous impurity into the working volume of the chamber through dosing valves. The component ratio in the mixture was 95:5 (H_2O:gas). Distilled water with a residual impurity content of less than 0.005% was used as one of the main components, along with CO_2 of 99.999% purity (ISKHAN TEKHNO-GAZ LLC, Almaty, Kazakhstan), as well as CO and CH_4 with a purity of 99.95%.

2.3 Measurement methodology

The film thickness $d$was determined from the interference pattern recorded by a dual-beam laser interferometer, according to the relation:

$$d = \frac{m\lambda}{2ncos\theta} , \quad (1)$$

where: m — the number of interference fringes, λ= 405 nm — the laser wavelength, n — the refractive index of ice, θ — the angle of incidence of the laser beam.

A dual-beam laser interferometer was used to evaluate the thickness, density, and optical properties of the condensed films. Laser sources with a wavelength of λ = 405 nm were oriented at angles of α_1 = 1° and α_2 = 45° relative to the substrate surface. The geometry of the dual-beam laser interferometer and the arrangement of the laser beam relative to the substrate are shown in Figure 3. Mass spectra were recorded with a time step of 4 s over the mass-to-charge range of m/z = 1–100.

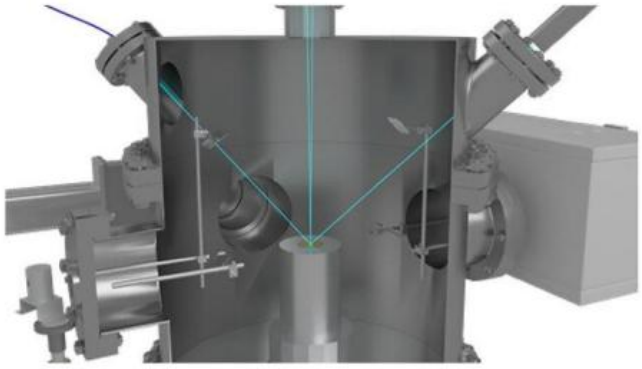

Fig. 3. Three-dimensional model of the experimental setup showing the direction of laser beams [19]

The experimental data were analyzed using the specialized software package EASY, developed for this work. The software enabled signal filtering, automatic peak detection, construction of mass–temperature profiles, and export of processed data for subsequent analysis and visualization. This approach facilitated efficient processing of large datasets and the determination of the quantitative characteristics presented below.

3. Results and Discussion

3.1 Absorption Capacity of Water Cryocrystals for CO, CO_2, and CH_4 Molecules

In this study, the absorption capacity of water cryocrystals with respect to CO, CO_2, and CH_4 molecules was investigated based on the analysis of the temperature-programmed desorption (TPD) of impurities from water ice films during controlled annealing. Two complementary approaches were employed to study the processes of gas molecule retention within the crystalline lattice: a manometric method (recording the total pressure) and a mass spectrometric method (identification of individual components). In parallel with the desorption measurements, optical monitoring of structural changes in the ice matrix was performed, allowing

the correlation between the absorption capacity of ice and its crystalline structure to be established. Each process of impurity molecule retention was considered separately.

Table 1. Comparison of the present results with previously experimental studies on amorphous solid water (ASW)

№	Reference	Ice system	Gas / Sample	Experimental method	Main desorption / structural transition temperature (K)	Main findings
1	This work	ASW + CO, CO_2, CH_4	H_2O–gas mixture	TPD, MS, Laser interferometry	13-200	Three desorption stages associated with ASW - Ic - Ih structural transformations. Excellent agreement between pressure, mass spectrometric and optical measurements.
2	Amato et al. (2025)	Porous ASW	H_2O ASW	Molecular dynamics simulation	15–160	Progressive pore collapse and ice densification during annealing [26].
3	Talewar et al. (2019)	Vapor-deposited ASW	Ar, CH_4, CO_2, He	TPD, Mass Spectrometry	95–185	Identified three gas-release mechanisms: desorption from cracks (>100 K), pore collapse (~125 K), and gas release during crystallization (~155 K) [20].
4	Yuan, Smith & Kay (2016)	ASW films	H_2O	TPD, RAIRS	150–160	Surface-initiated top-down crystallization [24].
5	Mate et al. (2020)	Porous ASW	CH_4/H_2O	FTIR, (QCM), Monte Carlo simulation	42–60	CH_4 diffusion depends on ASW morphology; porous interconnected structures enhance low-temperature gas trapping [25].

Table 1 demonstrates that the results obtained in the present study are consistent with previously reported experimental and computational investigations of amorphous solid water (ASW). Earlier studies have shown that heating ASW leads to progressive pore collapse, structural densification, glass transition, and subsequent crystallization. These structural transformations strongly affect the retention and release of molecules trapped within the ice matrix.

In agreement with these studies, our temperature-programmed desorption experiments reveal that the release of CO, CO_2, and CH_4 occurs in several stages associated with the structural evolution of water ice. The observed desorption behavior confirms that the transformation of ASW into crystalline phases governs the mobility and escape of trapped gas molecules.

Unlike previous investigations, which mainly focused on the structural evolution of pure ASW, the present work examines a multicomponent H_2O–CO–CO_2–CH_4 cryocondensate. This extends the understanding of the relationship between ice phase transitions and gas-release kinetics, providing useful information for cryogenic gas storage, decarbonization technologies, and astrophysical ice analogues.

Figure 4 shows the temperature dependence of the gas pressure recorded during the heating of a thin ice film TPD containing impurity molecules. The curve represents the total desorption signal of all system components and exhibits three clearly defined gas release regions, each corresponding to different desorption processes.

Figure 5 presents the TPD results obtained using cyclic mass spectrometric scanning. Unlike the integral data shown in Figure 4, mass spectrometric analysis allowed the separate contribution of individual components (CO, CO_2, CH_4) to be recorded and enabled precise identification of the desorbing molecules.

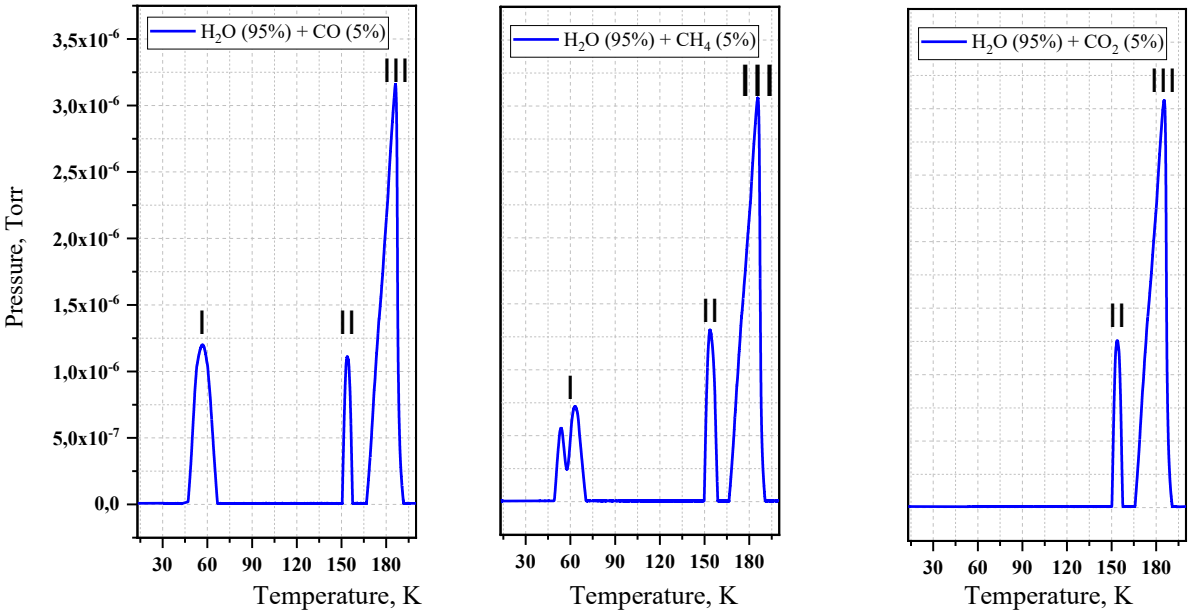

Fig. 4. Temperature-programmed desorption (according to pressure gauge readings) for various mixtures

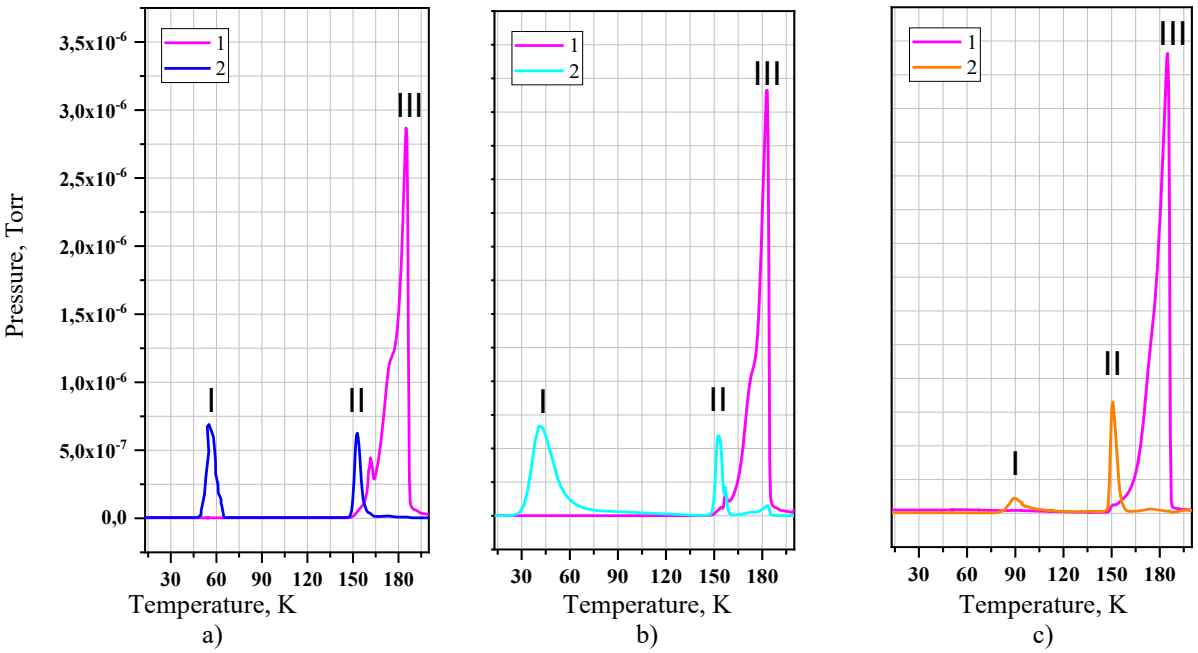

Fig. 5. Temperature-programmed desorption (mass spectrometry analysis, cyclic scanning) for various mixtures: 1 - H_2O (95 %), 2 (blue) – CO (5 %), 2 (cyan) - CH_4 (5 %), 2 (orange) - CO_2 (5 %)

Both applied methods—the manometric and the mass spectrometric—showed complete agreement in the results, revealing three distinctly identifiable regions of impurity molecule desorption from the ice matrix:

– *Low-temperature desorption region – I (40–140 K)*

In the first temperature range, desorption of the most weakly bound molecules are observed. The process includes the removal of physically adsorbed molecules from the ice surface and their release from the open pores of the amorphous ice structure. This stage is recorded by both methods—via manometric measurements (CO, CH_4) and mass spectrometric data (CO, CH_4, CO_2).

– *Medium-temperature range – II (140–160 K)*

This stage corresponds to the release of more strongly bound molecules from crystalline defects and their desorption from closed pores formed during the deposition and relaxation of amorphous ice. The process is

equally well manifested in the curves obtained by both methods, indicating the universality of this desorption process.

– *High-temperature region – III (>160 K)*

This stage corresponds to the desorption of the most strongly retained molecules, associated with the breakdown of residual supramolecular structures during the sublimation of water ice.

The good agreement between the manometric and mass spectrometric measurements confirms the consistency of the obtained desorption data.

3.2 Release of Impurity Molecules during Structural Transformations of Water Ice (ASW(L) → ASW(H))

Figure 6 presents optical study data demonstrating the release of impurity molecules CO, CH_4, CO_2 during the thermally induced densification of low-density amorphous ice. Two pronounced peaks are observed for CO and CH_4, along with a weaker peak for CO_2, indicating differences in the desorption dynamics of these gases. The differences in peak intensities reflect the varying sorption capacities of the water matrix toward these gases. Methane and carbon monoxide exhibit pronounced release at the early stages of heating, whereas carbon dioxide is released from the ice structure in significantly smaller amounts. The presented data clearly demonstrate distinct behaviors of the gas impurities during thermal processing of amorphous water ice. The primary factor determining the sequence of their release is the relationship between the thermal characteristics of the gases themselves and the structural changes in the ice matrix.

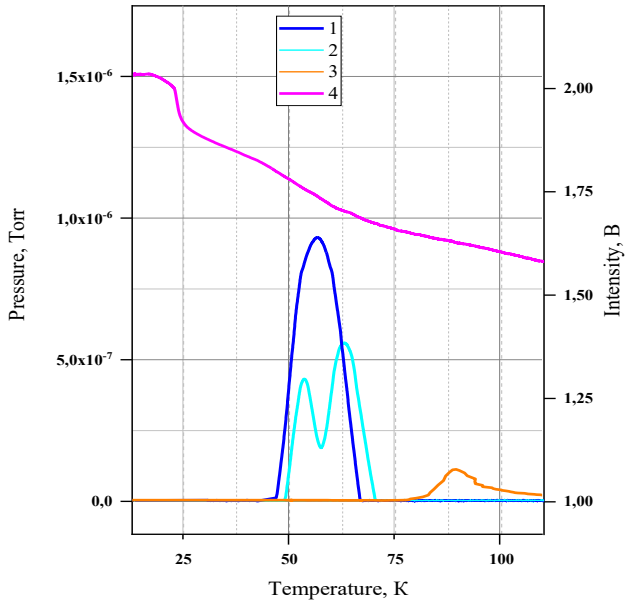

Fig. 6. Optical analysis of impurity molecule release during amorphous ice relaxation:
1 – CO (5 %), 2 - CH_4 ₂ (5 %), 3 - CO_2 (5 %), 4 - H_2O (95 %)

CH_4 and CO exhibit pronounced desorption peaks in the temperature range of 40–70 K. This behavior can be explained by the fact that their sublimation temperatures (34 K for CH_4 and 29 K for CO) are significantly lower than the temperature of intense pore collapse in amorphous ice (~70 K). As a result, these gases are released both through natural sublimation and during the relaxation of the ice structure. CO_2 behaves in a fundamentally different manner, exhibiting only weak signs of desorption within this temperature range. This behavior is due to its significantly higher sublimation temperature (80 K, Figure 7), which exceeds the temperature of intense pore collapse. As a result, CO_2 molecules remain securely trapped within the ice matrix until higher temperatures are reached.

The minor release of CO_2 in the low-temperature region can be attributed to two primary processes. First, surface desorption of molecules weakly bound to the outer layers of the ice film is possible. Second, a certain contribution may arise from the release of molecules from a limited number of macropores that remain after partial collapse of the porous structure. These assumptions are supported by the experimental data (Fig. 7),

which show a sharp, almost instantaneous release of CO_2 upon reaching its sublimation temperature—a behavior that is fundamentally different from the gradual desorption observed for CH_4 and CO.

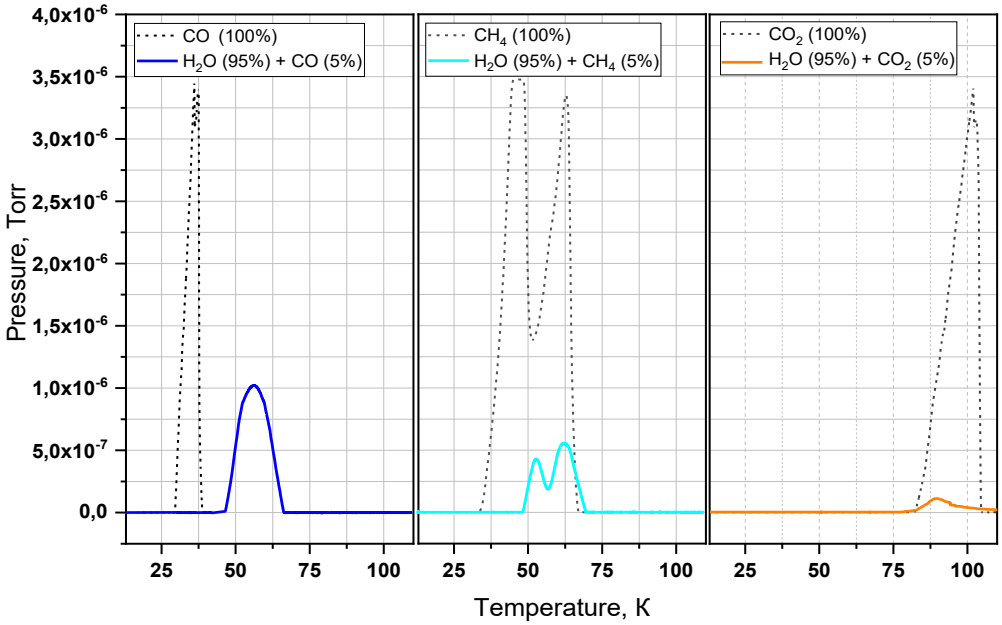

Fig. 7. Comparison of temperature profiles for the desorption of CH_4, CO, and CO_2 from amorphous ice film with the sublimation of pure substances

The results obtained demonstrate that gas desorption is determined by the combined effect of the gas sublimation temperature and structural transformations of the ice matrix. Gases with low sublimation temperatures (Ch_4 and CO) are released in the early stages of heating, while co_2 remains trapped until higher temperatures are reached. During the transition from ASW to Ic, crystallization causes pore compression, reduction of free volume, and elimination of structural defects, which leads to the release of impurity molecules trapped in the ice matrix. It is noteworthy that the desorption kinetics in this temperature range exhibit a complex behavior. In the initial stage of the transition (145–150 K), a gradual increase in the desorption rate is observed, corresponding to the activation of molecular mobility within the amorphous matrix. This is followed by a sharp jump in intensity (150–155 K), coinciding with the main phase of crystallization. During this period, cooperative rearrangement of large ice volumes occurs, leading to the simultaneous release of a significant number of impurities. The final stage of the process (155–160 K) is characterized by a gradual decrease in the desorption rate as crystallization completes.

3.3 Release of Impurity Molecules during Structural Transformations of Water Ice (Ic → Ih) and (ASW → Ih)

This section is devoted to the release of impurities during the structural transitions of water ice from the amorphous to the crystalline phase and during the recrystallization of Ic → Ih.

3.3.1 Optical Studies of Structural Transitions in Ice Films

Figure 8 shows the temperature dependence of the intensity of the laser signal, reflecting the structural transitions occurring in the ice film during heating.

Several key temperature intervals characterizing the structural transitions of ice are highlighted in the graph:

- *Interval I* – water remains in the form of amorphous ice (ASW), with the signal intensity remaining constant;
- *Interval II* – a sharp decrease in the laser signal intensity, associated with the transition of amorphous ice to the cubic modification (ASW → Ic);
- *Interval III* – a reduction in the slope of the curve due to the gradual transition of cubic ice into hexagonal ice (Ic → Ih), resulting from the similarity of their structural parameters.

- *Interval IV* – a sharp decrease in signal intensity, likely caused by the transformation of residual amorphous regions into the hexagonal structure (ASW → Ih), as confirmed by X-ray diffraction results;
- *Interval V* – continued growth of hexagonal ice crystals through the reorganization of remaining cubic regions, accompanied by a linear decrease in intensity;
- *Interval VI* – complete sublimation of the sample, during which the signal returns to its maximum value.

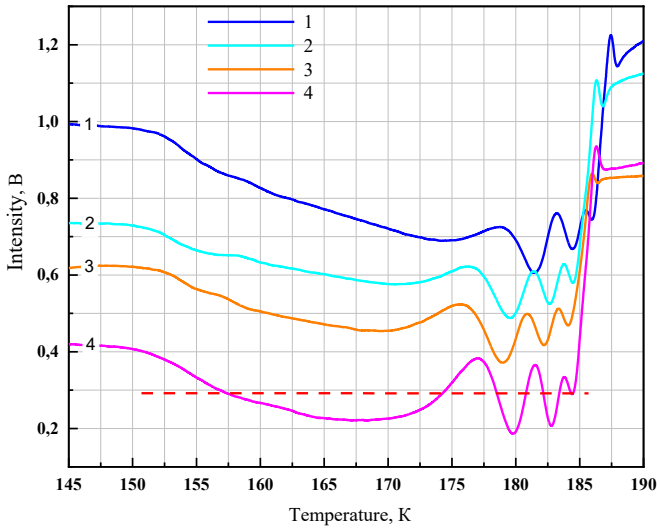

Fig. 8. Laser radiation intensity from the surface with a cryocondensate sample
1 – CO (5 %), 2 - CH_4 $_2$ (5 %), 3 - CO_2 (5 %), 4 - H_2O (95 %)

3.3.2Desorption of Impurities during Heating of the Thin Film

The mass spectrometric data presented in Figure 9 show clearly defined desorption peaks of impurities in the temperature range of 154–163 K (Intervals I and II), which correspond precisely to the regions of structural transitions III and IV in the temperature dependence of the laser signal intensity (Figure 8).

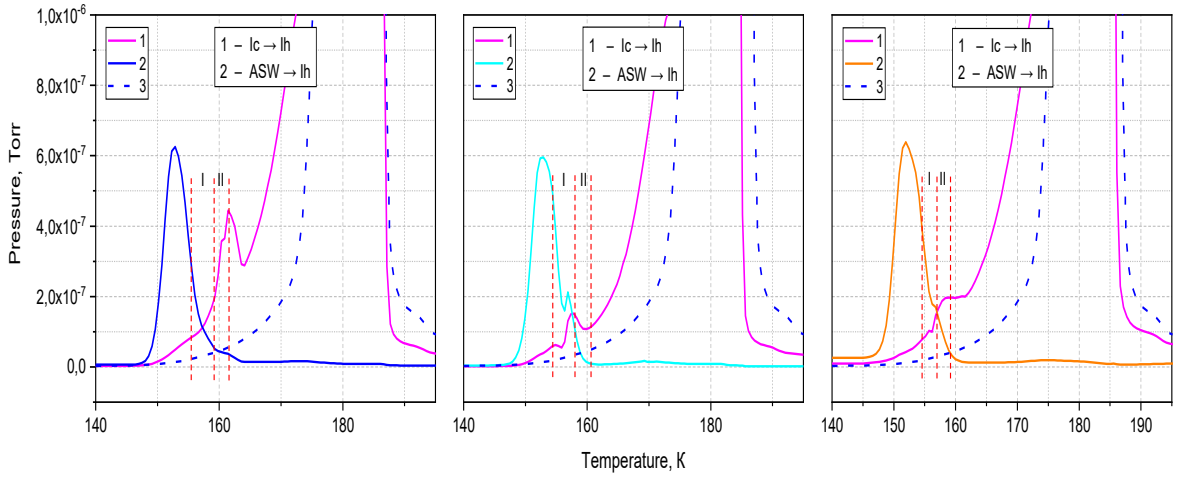

Fig. 9. Mass spectrometry desorption data as a function of temperature for water and various mixtures:
1 - H_2O (95 %), 2 – CO (5 %), 2 - CH_4 (5 %), 2 - CO_2 (5 %), 3 - H_2O (100 %)

The observed correlation indicates a direct relationship between the release of impurity molecules and the structural transformations in water ice during the heating of the thin film. The desorption peaks observed in Intervals I and II are attributed to structural transformations of the ice matrix during the Ic → Ih and ASW → Ih transitions. These processes involve defect elimination and pore collapse, which promote the release of impurity molecules trapped within the ice structure

3.3.3 Influence of the Molecular Mass of Impurities on Structural Transformations of Water Ice

Analysis of the influence of various impurities on the structural transitions of water ice demonstrates the key role of their molecular mass. Light molecules, such as methane (CH_4), due to their high mobility, interact actively with the crystalline lattice of water ice, efficiently transferring energy to it. This leads to localized heating in regions containing impurities, thereby facilitating the initiation of structural transitions. In particular, methane significantly affects the transformation of cubic (Ic) and residual amorphous (ASW) ice into the hexagonal (Ih) phase, accelerating this process within the corresponding temperature range, as confirmed by experimental data showing a shift in the phase transition temperature boundaries in the presence of methane.

Heavier molecules, such as CO_2, although less mobile, possess greater mass, allowing them to transfer more energy per collision; this higher energy transfer compensates for their lower mobility, resulting in a similar influence on ice structural transitions as observed for methane. CO occupies an intermediate position in terms of mass: it is heavier than methane but lighter than carbon dioxide. Consequently, its effect on the water ice structure is less pronounced than that of CH_4 and CO_2, as evidenced by minimal changes in the phase transition temperature boundaries when CO is present. It should be noted that, alongside molecular mass, the specific interactions of impurities with the hydrogen-bond network of ice may also contribute; however, within the scope of this study, the dominant factor is the molecular mass.

3.3.4 Uncertainty Analysis and Experimental Data Reliability

The reliability of the experimental results was assessed based on the stability of the experimental conditions and the consistency of the applied measurement techniques. Temperature control was performed using a DT-670 semiconductor sensor operated by a Lake Shore LS325 controller with an accuracy of ±0.1 K. Throughout all experiments, the heating rate was maintained constant at 0.166 K s^{-1}, minimizing thermal fluctuations during temperature-programmed desorption measurements.

The thickness of the cryocondensed films was determined by laser interferometry. The uncertainty of the thickness determination was mainly associated with interference fringe counting and the optical parameters of the ice film. However, this uncertainty did not affect the determination of desorption temperatures or the qualitative interpretation of the experimental results.

The desorption behavior of the samples was simultaneously monitored by three independent techniques: pressure measurements, mass spectrometry, and laser interferometry. The coincidence of the characteristic desorption temperature ranges obtained by these methods confirms the consistency and reliability of the experimental data. Minor differences in signal intensity are attributed to the different sensitivities of the measuring techniques and do not influence the identification of the desorption stages or the interpretation of the structural transformations of the ice matrix.

Overall, the combination of independent measurement methods, stable experimental conditions, and precise temperature control ensures the high reliability and reproducibility of the obtained results.

4. Conclusion

This study investigates the processes of adsorption and release of CO, CO_2, and CH_4 molecules in structures of cryocondensed water ice, in line with the main objective of the article — to elucidate the physical principles underlying the prospective cryotrapping of gases in water matrices. The use of a combination of manometric, mass spectrometric, and optical methods ensured the reliability and consistency of the obtained data. Gas desorption from the ice matrix occurs as a multistage process across three distinct temperature regions, each corresponding to different impurity retention mechanisms. It was established that structural transformations of water ice play a key role in gas release: transitions from the amorphous phase to cubic and hexagonal forms are accompanied by the collapse of the porous structure and the elimination of crystal lattice defects, resulting in intensive desorption of trapped molecules. The sequence and intensity of desorption are determined by the relationship between ice structural transformation temperatures and the sublimation temperatures of the gases: CH_4 and CO molecules are predominantly released at the early stages of heating, whereas CO_2 remains trapped until higher temperatures.

The precise agreement of desorption temperature boundaries obtained by different measurement techniques confirms the reproducibility of the results, the validity of the proposed desorption model, and the universality of molecular release processes from the ice matrix. Minor quantitative differences in peak

intensities do not affect the qualitative interpretation of the data, and the overall consistency of the experiments provides a reliable basis for analyzing the role of structural transformations of ice in gas desorption processes.

Thus, the obtained results demonstrate the effectiveness of cryocondensed water structures for selective gas capture and can serve as an experimental basis for the development of greenhouse gas cryotrapping technologies within the framework of decarbonization efforts.

Conflict of interest statement
The authors declare that they have no conflict of interest in relation to this research, whether financial, personal, authorship or otherwise, that could affect the research and its results presented in this paper.

CRediT author statement
Chigambayeva N.N.: Investigation, Writing-Original draft preparation, Editing; **Nurmukan A.Y.**: Writing Reviewing, Supervision; **Aldiyarov A.U.**: Conceptualization, Funding acquisition; **Yerlanov T.E.**: Resources, Software, Data curation, Methodology; **Korshikov E.S.**: Investigation, Visualization, Validation, **Erlanov T.E.:** Investigation, Writing-Original draft preparation. The final manuscript was read and approved by all authors.

Statement on the use of Artificial Intelligence.
During the preparation of this manuscript, artificial intelligence tools were used solely for language editing and grammatical improvement. No AI tools were used to generate scientific content, analysis, results, or conclusions.

Data Availability Statement
The data are available upon reasonable request from the authors.

Funding

This research was funded by the Committee of Science of the Ministry of Science and Higher Education of the Republic of Kazakhstan (Grant No. BR34636830).

References

1 World Meteorological Organization. (2022). Greenhouse gas concentrations reach record levels. WMO. https://wmo.int/ru/news/media-centre/koncentraciya-parnikovykh-gazov-dostigla-rekordnogo-urovnya-vnov

2 Lu, G., Zhang, Y., Li, X., Wang, J. (2023). Recent progress in carbon dioxide capture technologies: A comprehensive review. *Int. J. Environ. Sci. Technol. (IJEST)*. 1(1). https://doi.org/10.18686/cest.v1i1.32

3 Irgibayeva, I.S., Nurzhanova, A.K., Kassenova, Z.K. (2022). Climate change and the greenhouse effect. *Bulletin of ENU* 138(1), 18–23. https://doi.org/10.32523/2616-6771-2022-138-1-18-23

4 Intergovernmental Panel on Climate Change. (2018). *Global Warming of 1.5 °C*. Geneva: World Meteorological Organization. IPCC. https://www.ipcc.ch/sr15/

5 International Energy Agency. (2021). *Global Energy Review: CO_2 emissions in 2021*. IEA. https://www.iea.org/reports/global-energy-review-co2-emissions-in-2021

6 International Energy Agency. (2025). *Global Energy Review 2025*. https://www.iea.org/reports/global-energy-review-2025

7 Eurovent Certification. (2023). How do we decarbonise the HVAC manufacturing industry? https://www.eurovent-certification.com/ru/category/article/how-do-we-decarbonise-the-hvac-manufacturing-industry

8 Rahman, F.A., Maniruzzaman, M., Aziz, A., Saidur, R., Bakar, W.A.W.A., Hainin, M.R., Putrajaya, R., Hassan N.A. (2017). Pollution to solution: Capture and sequestration of carbon dioxide (CO_2) and its utilization as a renewable energy source for a sustainable future. *Renew. Sust. Energy Rev.* 71, 112–126. https://doi.org/10.1016/j.rser.2017.01.011

9 Font-Palma, C., Cann, D., Udaeta, M. (2021). Review of cryogenic carbon capture innovations and their potential applications. Carbon Capture Innovations and Their Potential Applications, 7(3), 58. https://www.mdpi.com/2311-5629/7/3/58

10 Kumar, S., Sharma, A., Singh, R. (2022). Review: CO_2 capturing methods of the last two decades. *Int. J. Environ. Sci. Technol. (IJEST)*. 20, 8087-8104. https://link.springer.com/article/10.1007/s13762-022-04680-0

11 Rahman, F.A., Aziz, A., Saidur R. (2017). Capture and sequestration of carbon dioxide and its utilization. *Renew. Sust. Energy Rev.* 71, 112–126. https://doi.org/10.1016/j.rser.2017.01.011

12 Pei, J., Zhang, L., Wang, Q. (2024). CO_2 capture technology based on gas hydrate method: A review. *Front. Chem.,* 12. https://doi.org/10.3389/fchem.2024.1448881

13 Rukh, M., Rahman, Md Sh., Sakib, K M N. (2024). A comprehensive review of semi-clathrate hydrates for CO_2 capture: Characterizations, mechanism and role of promoters. *Sep. Sci. Technol.,* 12, 100217. https://www.sciencedirect.com/science/article/pii/S2772656824000290

14 Tuinier, M.J., Annaland, M., Kuipers, J.A.M. (2010). Cryogenic CO_2 capture using dynamically operated packed beds. *Chem. Eng. Sci.,* 65, 114–125. https://doi.org/10.1016/j.ces.2009.01.055

15 Aneesh, A.M., Ramesh, K., Kumar, S. (2023). A mini-review on cryogenic carbon capture technology. *Frontiers in Energy Research*. https://www.frontiersin.org/articles/10.3389/fenrg.2023.1167099

16 Kenbay, A.A., Yerezhep, D.E., Aldiyarov, A.U. (2025). Development of low-temperature cell for IR Fourier-spectroscopy of hydrocarbon materials. *Eurasian phys. tech. j*., 22(2), 88–96. https://doi.org/10.31489/2025N2/88-96

17 Aminnaji, M., Hassanpouryouzband, A., Yang, J. (2024). CO_2 gas hydrate for carbon capture and storage applications. *Energy* 300, 131579. https://www.sciencedirect.com/science/article/pii/S0360544224013525

18 Wang, Y., Li, X., Zhao, J. (2025). Recent advances in CH_4 recovery from CH_4 hydrate in porous media by CO_2 replacement. *Energies,* 18(21), 5683. https://www.mdpi.com/1996-1073/18/21/5683

19 Amato, Z., Gärtner, S., Ghesquière, P., et al. (2026). Molecular and pore-scale structure evolution in amorphous solid water. Phys. Chem. Chem. Phys. 28, 524–537. https://doi.org/10.1039/D5CP03851K

20 Talewar, S.K., Halukeerthi, S.O., Riedlaicher, R., et al. (2019). Gaseous nanoprobes for detecting gas-trapping environments in macroscopic films of vapor-deposited amorphous ice. J. Chem. Phys. 151, 134505. https://doi.org/10.1063/1.5113505

21 Carmack, R.A., Tribbett, P.D., Loeffler, M.J. (2023). Pore Accessibility in Amorphous Solid Water. Astrophys. J., 942(1), 1. https://doi.org/10.3847/1538-4357/aca76b

22 Fukazawa, H., Kouchi, A., Hama, T., et al. (2025). Crystallization Mechanisms of Porous and Compact Amorphous Solid Water Films. Cryst. Growth Des., 25 (4), 1528-7483. https://doi.org/10.1021/acs.cgd.4c01284

23 Golikov O., Yerezhep D., Akylbayeva A., Sokolov D., Korshikov E., Nurmukan A., Aldiyarov A. (2023). Cryovacuum setup for optical studies of astrophysical ice. *Scientific Reports,* 13, 48541. https://doi.org/10.1038/s41598-023-48541-3

24 Yuan, C., Smith, R.S., Kay, B.D. (2016). Surface and bulk crystallization of amorphous solid water films: Confirmation of top-down crystallization. *Surface Science*, 652, 350–354. https://doi.org/10.1016/j.susc.2015.12.037

25 Mate, B., Cazaux, S., Satorre, M. A., Molpeceres, G., Ortigoso, J., Millan, C., & Santonja, C. (2020). *Diffusion of CH_4 in amorphous solid water*. Astronomy & Astrophysics, 643, A163. https://doi.org/10.1051/0004-6361/202038705

26 Amato, Z., Headen, T.F., Ghesquière, P., Fraser, H.J. (2025). A molecular dynamics study of the effect of annealing temperature on the structure of amorphous solid water. *Physical Chemistry Chemical Physics*, 27, 11186–11195. https://doi.org/10.1039/d5cp00271k

---

AUTHORS' INFORMATION

Chigambayeva, Nurgul Nurbayevna - Doctoral student, al-Farabi Kazakh National University Almaty, Kazakhstan; ORCID iD: 0009-0000-3753-3618; nurgul050490@gmail.com

Nurmukan, Assel Yerzhumayevna - PhD, Senior Lecturer, Department of Thermophysics and Technical Physics, al-Farabi Kazakh National University Almaty, Kazakhstan; SCOPUS Author ID: 57217033769; ORCID ID: 0000-0002-4231-0766; assel.nurmukan@kaznu.kz

Aldiyarov, Abdurahman Ualievich – Candidate of Physical and Mathematical Sciences, Acting Professor, Department of Thermophysics and Technical Physics, al-Farabi Kazakh National University Almaty, Kazakhstan; SCOPUS Author ID: 16201950600, ORCID ID: 0000-0002-5091-7699, Abdurakhman.Aldiyarov@kaznu.edu.kz

Korshikov Yevgeniy Sergeevich - PhD, Senior Lecturer, Department of Thermophysics and Technical Physics, al-Farabi Kazakh National University Almaty, Kazakhstan; Scopus Author ID: 55319247600; ORCID ID: 0000-0002-9479-4192, e.s.korshikov@physics.kz

Erlanov Timur Erlanovich - Master's student, al-Farabi Kazakh National University Almaty, Kazakhstan; ORCID ID: 0000-0003-4034-6981, yerlanovtimur@gmail.com

EURASIAN PHYSICAL TECHNICAL JOURNAL

2026, Volume 23, No. 2 (56)

https://doi.org/10.31489/2026N2/130-138

Received: 14/01/2026 Revised: 25/05/2026 Accepted: 26/06/2026 Published online: 30/06/2026

Original Research Article

UDC 524.527

YOUNG STELLAR OBJECTS IN THE REGION OF DUST BUBBLE N22

Manapbayeva A.B.[1,4], Alimgazinova N.Sh.[1,2], Naurzbaeva A.Zh.[1,2], Kyzgarina M.T.[1,2]*, Abildayev N.E.[2], Sarsenbayeva S.N.[3], Turekhanova K.M.[1,2], Alibek A.A.[4], Omar A.Zh.[1,2], Demessinova A.M.[1,2]

[1] Institute of Experimental and Theoretical Physics, Almaty, Kazakhstan
[2] Al Farabi Kazakh National University, Almaty, Kazakhstan,
[3] Almaty University of Power Engineering and Telecommunications, Almaty, Kazakhstan
[4] Kazakh National Women's Teacher Training University, Almaty, Kazakhstan
*Corresponding author: meir83physics@gmail.com

Abstract. *The study of young stellar objects is one of the priority areas in modern astrophysics, since these objects serve as key indicators of the processes accompanying the formation of stars and planetary systems. In the process of evolution, especially in the conditions of massive star clusters, they generate intense ultraviolet radiation and stellar winds that are capable to scatter the surrounding matter and forming expanding cavities that are infrared bubble structures in molecular clouds. The study of these structures allows us to obtain valuable information about the mechanisms of interaction of stars with their surrounding environment at various stages of evolutionary development. The aim of this work is to study the region of the dust bubble N22 in order to identify and classify young stellar objects. The main observational material was data obtained by the Wide-Field Infrared Survey Explorer space telescope in the near and mid-infrared range: W1 (3.4 μm), W2 (4.6 μm), W3 (12 μm), and W4 (22 μm). As a result of the analysis, new candidates for young stellar objects were identified within the studied region: 15 objects belonging to class I, 7 objects - class II, and 13 objects demonstrating the characteristics of transition disks. For all selected candidates for young stellar objects, color diagrams were constructed displaying their position relative to the characteristic regions of the evolutionary stages of young stars. In addition, spectral indices were calculated and the energy distribution in the spectrum was modeled, which confirmed the classification of objects by evolutionary stages.*

Keywords: dust bubble, infrared radiation, young stellar objects.

1. Introduction

The interstellar medium is the matter and fields that fill the interstellar space within galaxies. The interstellar medium being dynamic and constantly changing, distributed non-uniformly can have different physical and chemical conditions. It consists of hydrogen (about 70%), helium (28%) and heavy elements (2%). In turn, these elements can be neutral or ionized, and can also be collected into molecules. Of all the matter in the interstellar medium, the proportion of atomic ionized matter is 23%, while the proportion of atomic neutral matter is 60%, and the proportion of molecular matter is about 17% [1]. Despite the fact that the interstellar medium is a low-density medium and makes up about 5% of the total mass of stars in the Galaxy, its study is very important for understanding the evolution of the Galaxy. The interstellar medium has everything necessary for the formation of new generations of stars and planets. Stars are formed from interstellar gas, which in the later stages of evolution again give up some of their matter to the interstellar medium. As a result of this exchange, the interstellar medium is enriched with heavy elements created in the

depths of stars. Some of the matter from the interstellar medium is ejected into intergalactic space, and the hot intergalactic gas, with its radiation and pressure, can influence the ionization of the interstellar medium and its dynamics [2]. In our previous studies of the N22 dust bubble [3], Spitzer observations and archival data from the 2MASS, GLIMPSE, and MIPSGAL catalogs were used. Using various classification criteria (L.E. Allen (2004) [4], A. Gutermuth, et al. (2008) [5], and T.P. Robitaille (2008) [6]), around N22 at the early stages of evolution 36 objects were identified that are candidates for young stellar objects (YSOs).

In this paper, in order to identify new candidates and refine the class of previously identified YSOs near the infrared dust bubble N22, we conducted a study using WISE (Wide-Field Infrared Survey Explorer) multi-wavelength observations in the near and mid-infrared range. This choice is due to the fact that in the WISE observation bands, the excess radiation of the cooler circumstellar disk is more significant relative to the stellar photosphere [7].

2. Theoretical part

Data. In our study we used the astronomical database SIMBAD [8] and data from the VizieR catalog: large-scale infrared observation surveys: 2MASS and AllWISE [9, 10]. In this work we used the 2MASS All-Sky Catalog of Point Sources (2003), a catalog of point sources over the entire sky at a wavelength of two microns. From the catalog we selected observations of the sky in the near infrared range of J (1.25 μm), H (1.65 μm), and Ks (2.17 μm), which were obtained using the 2MASS project.

The AllWISE catalog data in the near and mid-infrared range were obtained by WISE, an infrared space telescope of NASA, using a cryogenic five-mirror afocal telescope with a diameter of 40 cm. The telescope is equipped with four cameras. In the near infrared range, the FWHM is 6.0″, and in the mid-infrared range, the FWHM is 12.0″. The catalog contains radiation fluxes in the W1 (3.4 μm), W2 (4.6 μm), W3 (12 μm), and W4 (22 μm) bands. WISE can easily be used as a tool to search for and classify young stellar objects, similar to the work done with Spitzer.

Infrared dust bubble N22. N22 (Fig.1) is one of the northern infrared bubbles created by the expanding HII region, an active star-forming region in our Galaxy, catalogued by Churchwell [11]. N22 is a dust bubble centered at Right Ascension (RA; α) $\alpha 2000 = 276.325^0$, Declination (Dec; δ) $\delta 2000 = -13.176^0$ ($l = 18.254^0$, $b = -0.305^0$) with a radius of about 1.77 pc [12]. N22 was also known as an HII region (G18.259-0.307), and its velocity in the hydrogen recombination line V_{LSR} is ∼50.9 km/s, and for the V_{CO} ∼51.3 km/s [12]. By comparing with the absorption data of HI G18.259−0.307, the kinematic distance was determined to be ∼4.1±0.3 kpc. In the bubble catalog [13], N22 is designated as MWP1G018261-002967. The effective diameter of N22 is 2.09 arcmin, Thickness is 1.88 arcmin, Eccentricity is 0.23, Position Angle is 18 deg.

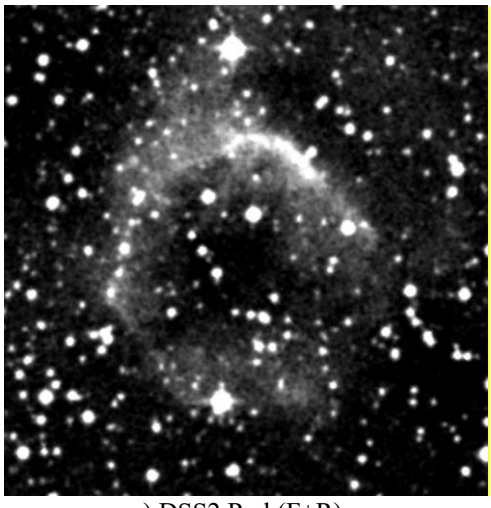

a) DSS2 Red (F+R)

b) IRAC color I1, I2, I4 - (GLIMPSE, SAGE, SAGE-SMC, SINGS)

Fig.1. Image of the N22 dust bubble

Methodology for identification of young stellar objects. In this work the identification algorithm of X.P. Koenig, et al (2014) [7] was used, which consists of several stages.

1st stage. In the VizieR catalog from the AllWISE review, when specifying the center point of an object, a search is made for sources within a circle of a certain selected radius. Here, preliminary cleaning is made for flows that have a zero value and which are also unreliable, since they have a measurement error of more than 0.2 mag.

2nd stage. The previously selected sources need to be cleared of contaminants which also emit in the infrared range. Contamination comes from extragalactic sources such as star-forming galaxies, active galactic nuclei of the broad line (AGN), unresolved knots of shock radiation from outflows colliding with cold cloud material, planetary nebulae, and asymptotic giant branch (AGB) stars (both carbon-rich and oxygen-rich) [14]. To remove contaminants, the criteria described in [15,16] were chosen in this study. Then the sources found in the first stage are tested for the corresponding photometric criteria. In this way, we obtain a list of possible candidates for young stellar objects.

3rd stage. Firstly, the identification of young stellar objects of class I is performed. Infrared radiation sources for which all conditions are met, according to [7], are recorded as possible candidates for young stellar objects of class I.

4th stage. Objects that do not meet the conditions of the third stage are tested for compliance with the criteria for young stellar objects of class II (pre-main sequence stars with optically thick disks). Infrared radiation sources for which all photometric criteria from [7] are met are recorded as possible candidates for young stellar objects of class II.

5th stage. From previously unclassified objects with a non-zero photometric error in the near infrared range according to the 2MASS catalog, according to [7], we separate possible candidates for young stellar objects of classes I and II from young objects of class III and the "transitional disks" class.

6th stage. Infrared emission objects that do not meet the conditions of the fifth stage are tested against the criteria for young stellar objects of the "transition disk" class. Objects of this class have optically thick excess emission at long wavelengths and virtually no excess at short wavelengths. The remaining objects that do not meet the criteria are classified as class III objects.

7th stage. At this stage, criteria using the mid-infrared flux - the W4 band (22 μm) are used. Previously identified objects as AGN candidates are tested to extract possible protostars from them. Infrared emission sources that meet the conditions of [7] are considered as possible protostar candidates.

8th stage. At the last stage, all possible young stellar object candidates selected at the early stages are retested for new photometric criteria that reveal AGN. Objects for which none of the conditions are met are identified as young stellar object candidates of a previously determined evolution class.

3. Results and discussion

The infrared sources of radiation within a radius of 5 arc minutes near the N22 dust bubble were searched (Table 1). A total of 475 objects were detected using the AllWISE survey.

Table 1. Parameters for object search

Region	R.A. Range (deg)	Dec. Range (deg)	Search radius (arcmin)	Number of objects found
N22	276.325≤α≤276.241	-13.176≤δ≤-13.188	5	475

The infrared radiation sources with unreliable flux values comprised 115 objects. The criteria of polluting factors were met by 199 objects. Thus, 161 objects were selected for further study. According to the results of the above-described algorithm for testing objects by evolution classes, the following were identified as candidates for young stellar objects: 16 objects of class I, 30 objects of class II, 102 objects of class III and 13 objects of the "transitional disks" class. Figure 2 shows a "color-color" diagram, in which we see that most objects of class I and II lie in the corresponding area of the diagram, according to work [17], except for objects of the "transitional disks" class - they are located on the diagram to the left of the area. Such an arrangement may indicate that for objects of the "transitional disks" class, the photometric properties and the stage of evolution correspond to a later period than for objects of class I and II. Class III objects are already practically formed young stars, therefore their location corresponds to the region of evolution of stellar objects.

Further, considering that there are currently no unambiguous criteria for identifying young stellar objects, in this work we used several methods to identify true candidates for YSOs. At the next stage of studying the

found YSO candidates, we applied a classification based on the determination of the spectral index, according to [18]. The spectral index is calculated using fluxes in all WISE bands [19]. The distribution of spectral index values by evolution classes is taken in accordance with [20]. We are interested in objects at early evolutionary stages, so further study was carried out only for candidates for I, II, and the "transition disk" class.

Figure 3 shows a diagram showing the quantitative distribution of objects by their spectral index values. For greater clarity, the areas of division by evolutionary stages are shown according to [20].

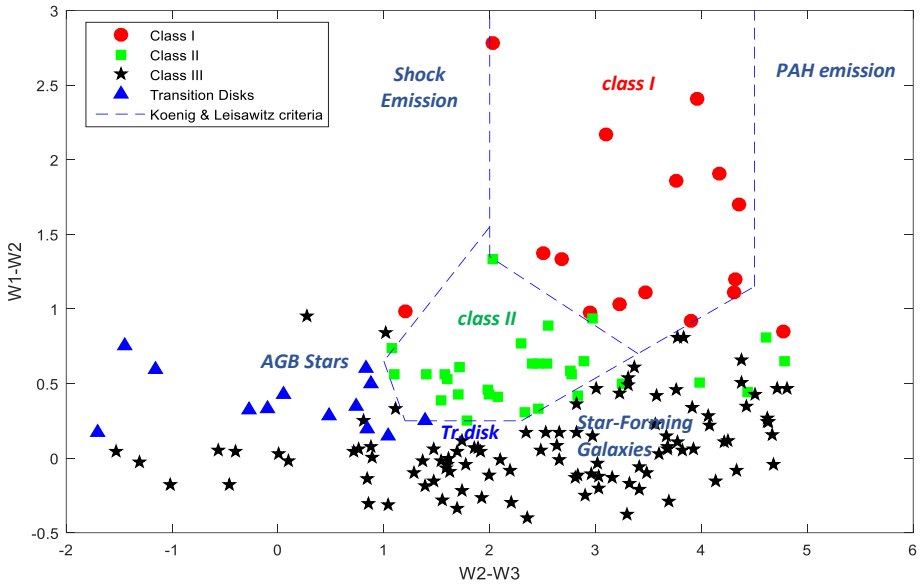

Fig.2. Color-color diagram. Identified candidates for young stellar objects: red squares – class I, green pluses – class II, blue dots – objects with transition disks, black stars – class III

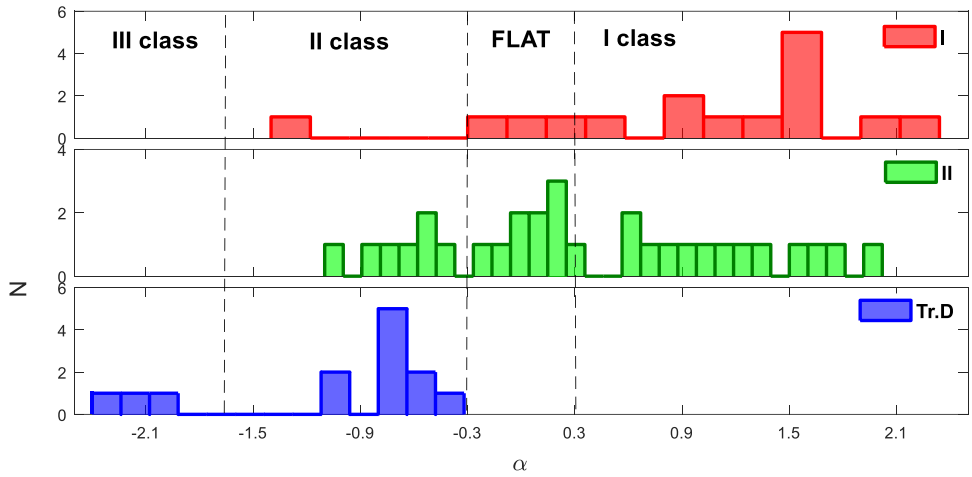

Fig.3. Distribution of the number of objects by spectral index

It's shown that for most objects, their distribution corresponds to the evolution classes that were previously determined using the Koenig X. P algorithm [7]. Of the previously identified candidates for class I YSO, 12 objects have the same evolutionary stage and 3 objects have flat spectra. Of the candidates for class II YSO, only 7 objects have the same evolutionary class, and for transition disks, 10 objects belong to class II evolution by spectral index and 3 objects correspond to class III evolution. Taking this into account, we select as candidates for YSO only those objects that belong to the same class in both cases of identification by evolutionary classes. Now we leave 15 objects as candidates for class I YSO, 7 objects as class II and 13 objects as candidates for the "transition disks" class. The candidates for the YSO selected according to two criteria are presented in Table 2.

At the next stage of the research, we searched for information in astronomical catalogues on objects that we identified by two characteristics. Among 15 objects of the class I, 6 objects have already been assigned

the status of young stellar objects: 4_YSO (2MASS J18252639-1312536 -- Young Stellar Object) [21], 9_YSO (SPICY 83443 -- Young Stellar Object) [22], 11_YSO (SPICY 83447 -- Young Stellar Object) [6], 12_YSO (SSTGLMC G018.2307-00.2427 -- Young Stellar Object) [23], 13_YSO (SPICY 83414 -- Young Stellar Object) [22, 23], 14_YSO (2MASS J18252201-1314449 -- Young Stellar Object) [21,23].

Table 2. Candidates for the YSO

№	_RAJ2000	_DEJ2000	AllWISE	W1	W2	W3	W4	J	H	K
	h:m:s	d:m:s		mag	mag	mag	mag	mag	mag	mag
Class I										
1_YSO	18 25 12.0	-13 10 15.2	J182512.03-131015.1	10,72	9,69	6,46	2,49	16,69	15,68	13,14
2_YSO	18 25 08.8	-13 08 50.4	J182508.77-130850.3	8,97	7,64	4,96	1,93	17,37	14,97	11,33
3_YSO	18 25 07.4	-13 08 59.5	J182507.35-130859.4	10,26	8,35	4,19	0,73			
4_YSO	18 25 26.4	-13 12 51.9	J182526.41-131251.9	11,86	10,49	7,98	6,26	13,43	13,00	12,57
5_YSO	18 25 07.0	-13 08 59.2	J182507.01-130859.1	10,30	8,44	4,69	1,32			
6_YSO	18 25 06.3	-13 09 05.6	J182506.28-130905.6	10,93	8,52	4,56	1,15	14,77	13,65	13,16
7_YSO	18 25 09.7	-13 07 51.5	J182509.68-130751.5	10,74	9,81	5,91	5,28	16,38	15,65	13,12
8_YSO	18 25 03.8	-13 11 19.3	J182503.83-131119.3	10,01	9,16	4,39	0,89	16,13	14,57	13,29
9_YSO	18 25 04.9	-13 08 47.5	J182504.85-130847.5	13,97	11,81	8,71	2,31	14,85	14,05	14,01
10_YSO	18 25 05.7	-13 08 22.1	J182505.74-130822.1	10,34	7,55	5,52	1,53	16,73	14,38	12,45
11_YSO	18 25 05.4	-13 08 07.1	J182505.38-130807.1	11,92	10,22	5,86	2,50			
12_YSO	18 25 01.8	-13 10 00.8	J182501.84-131000.8	10,25	9,05	4,73	0,16			
13_YSO	18 25 01.0	-13 09 42.6	J182500.98-130942.6	10,54	9,43	5,12	1,48			
14_YSO	18 25 22.1	-13 14 46.3	J182522.07-131446.2	11,45	10,48	7,53	4,94	17,99	16,52	13,62
15_YSO	18 25 06.1	-13 13 47.1	J182506.07-131347.1	10,80	9,69	6,22	2,08	17,36	16,79	13,47
Class II										
16_YSO	18 25 05.9	-13 10 16.4	J182505.88-131016.3	10,05	9,80	8,01	5,53	17,90	14,90	11,95
17_YSO	18 25 24.2	-13 07 30.8	J182524.22-130730.8	8,83	8,41	6,41	3,64	17,08	13,23	10,79
18_YSO	18 25 24.3	-13 07 17.1	J182524.30-130717.1	8,67	8,25	6,54	3,90	15,80	11,80	9,86
19_YSO	18 25 22.5	-13 14 12.8	J182522.54-131412.8	11,27	10,34	7,36	6,60	16,30	15,17	12,89
20_YSO	18 25 29.7	-13 07 19.7	J182529.71-130719.6	11,13	10,72	8,65	6,17	17,99	14,78	12,35
21_YSO	18 25 01.3	-13 12 28.0	J182501.28-131228.0	10,13	9,39	8,32	6,01	13,41	12,13	11,27
22_YSO	18 25 28.2	-13 06 25.2	J182528.20-130625.1	9,16	8,59	7,49	4,54	15,24	12,81	10,61
Transition discs										
23_YSO	18 25 15.0	-13 11 15.2	J182515.03-131115.2	8.542	8,37	10,08	2,62	13,52	11,13	9,92
24_YSO	18 25 11.8	-13 11 54.2	J182511.76-131154.2	10.707	10,11	9,28	4,69	17,34	14,74	12,45
25_YSO	18 25 11.3	-13 12 16.7	J182511.34-131216.7	9.534	9,04	8,16	4,34	17,98	13,28	10,88
26_YSO	18 25 31.0	-13 10 02,0	J182531.00-131001.9	9.461	9,31	8,27	4,64	15,94	12,35	10,59
27_YSO	18 25 20.3	-13 06 58.8	J182520.33-130658.8	10.310	9,56	11,00	8,21	15,48	14,46	12,03
28_YSO	18 25 31.1	-13 08 39.4	J182531.12-130839.3	8.609	8,01	9,18	6,32	18,02	12,79	10,08
29_YSO	18 25 29.5	-13 08 05.8	J182529.54-130805.7	10.818	10,54	10,05	5,76	14,99	12,64	11,57
30_YSO	18 25 28.5	-13 07 17.6	J182528.54-130717.6	8.819	8,49	8,59	6,46	16,09	11,96	9,92
31_YSO	18 25 24.9	-13 06 36.5	J182524.85-130636.4	10.918	10,57	9,84	6,65	13,68	12,81	11,69
32_YSO	18 25 01.1	-13 11 37.8	J182501.14-131137.8	10.472	10,15	10,42	4,75	15,60	14,28	11,93
33_YSO	18 25 31.6	-13 07 18.8	J182531.56-130718.7	10.319	9,89	9,84	5,64	17,60	13,76	11,48
34_YSO	18 25 35.2	-13 08 17.7	J182535.24-130817.7	10.552	10,30	8,92	5,74	17,51	13,46	11,52
35_YSO	18 25 12.5	-13 15 08.5	J182512.53-131508.4	10.842	10,65	9,81	5,55	15,92	14,06	12,10

Among 7 objects-YSO candidates of the class II, 1 object has the YSO status: 21_YSO (2MASS J18250127-1312279 -- Young Stellar Object Candidate). This object was studied in [22]. Among 13 objects with signs of transition disks, one object, that is 23_YSO, which is already a formed star 2MASS J18251516-1311139, that is confirmed in [23, 24]. This O-type star is located within the HII region of N22, and was discovered by analyzing radio emission at a wavelength of 20 cm.

The objects in Table 2 with the previously found candidates for YSOs in our work [3]. In the previous study, we studied objects that have infrared fluxes registered by Spitzer were compared. Identification was carried out using the photometric criteria of R. Gutermuth [5]. A total of 36 YSO candidates were identified, information about which is presented in Table 3 of the previous study [3]. Taking into account the fluxes in the near-IR range registered by 2MASS, as well as the coordinates of the sources and their point locations on the integrated maps of the Aladin database, 6 YSO candidates from Table 1 of this study were identified. These are objects No. 15 (4_YSO), No. 24 (9_YSO), No. 29 (11_YSO), No. 32 (12_YSO), No. 33 (13_YSO), No. 35 (14_YSO). As described above, these objects have already been studied and have the status of Young Stellar

Object. Object #2 corresponds to a candidate for a Class III YSO and is presented in astronomical databases as 2MASS J18251320-1310579 -- Young Stellar Object.

Further 10 objects from Table 2 [3] with the initial list of found IR emission objects according to the AllWISE catalog were identified. Objects #6, #9, #11, #13, #21, #25, #26, #28, #31 and #36 were removed at the initial stage of data cleaning because they corresponded to unreliable fluxes in the WISE bands under study. The remaining 19 objects from Table 2 were not reliably identified with the objects found near the N22 bubble.

Previously unstudied objects were selected for further study: 9 objects were candidates for class I YSO, 6 objects for class II, and 12 objects for the "transition disk" class.

Spectral energy distributions (SEDs) were constructed for each previously unstudied YSO candidate, and experimental data for the objects under study were fitted to the model data obtained in [25]. This set of models covers a wide range of evolutionary stages of young stellar objects (YSOs), from the youngest, deeply embedded in the envelope of protostars, to stars before the main sequence with small disks or without them.

Figure 4 shows, as an example, the SEDs for YSO candidates 18_YSO and 17_YSO (dots) and the models with the smallest standard deviation from the observational data (black line). The best model for the object 18_YSO is a model without a shell with a disk mass of ~ 0.01 $M_\odot$, which is typical for a class II YSO. It is also clear from the figure that the parameter

$$\alpha = \frac{d\,log(\lambda F_\lambda)}{d\,log(\lambda)}$$

where α has a value in the range from ≈2 to ≈10 μm that is also characteristic of class II YSOs (-1.5<α<0).

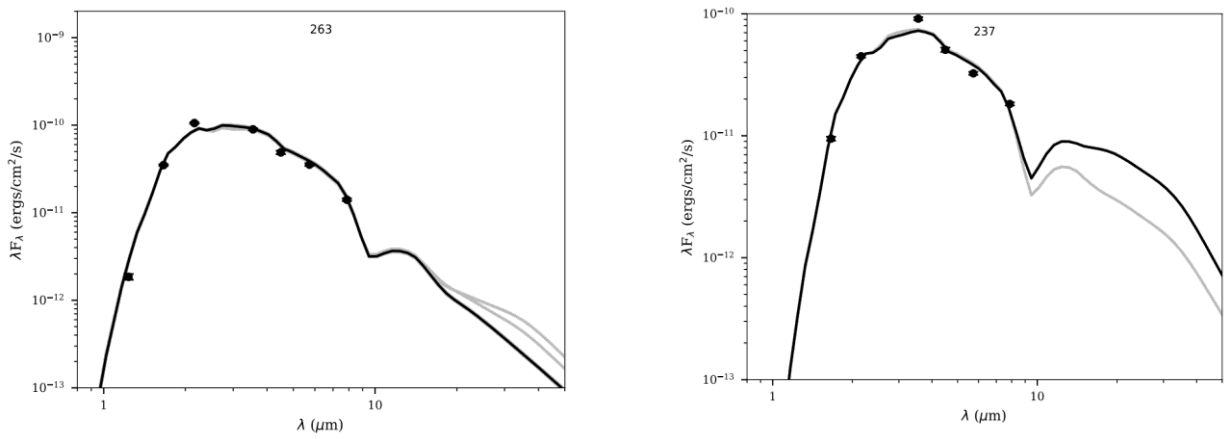

a) b)

Fig.4. Energy distribution in the spectrum of a)18_YSO and b) 17_YSO (dots – observational data, solid line – model [25]

Figure 5 shows an example of a SED for a candidate YSO with a Transition Disk. The best fit for such objects is with models without an envelope with disks of small mass ($\ll 0.01\ M_\odot$), which corresponds to the generally accepted theory about these objects. Such YSOs are at the stage of transition between a full protoplanetary disk and a scattered disk or already cleared space around a star. The values of the parameter α, as shown above, also roughly correspond to an intermediate type between Class II and III. The results of model fitting for other objects generally do not contradict the assumption that they belong to the YSO with a Transition Disk type.

As for the class I YSO candidate objects, no data on fluxes at wavelengths >10 μm were found for the 2_YSO object, so we cannot make a definitive judgment about their belonging to a certain class, but fitting the shorter-wave part of the SED classifies them as class II. The situation is similar for the 1_YSO and 15_YSO objects, but it should be noted that class I models are also close to their SED. For the remaining objects, fitting the models confirms their belonging to class I (Figure 6).

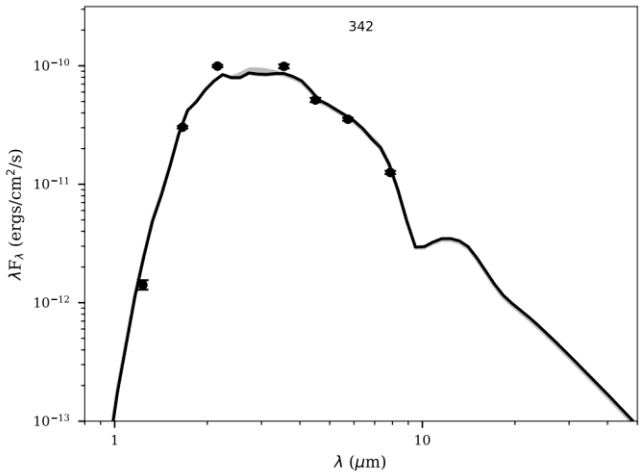

Fig.5. Energy distribution in the spectrum of the object 30_YSO (dots – observational data, solid line – model [25].

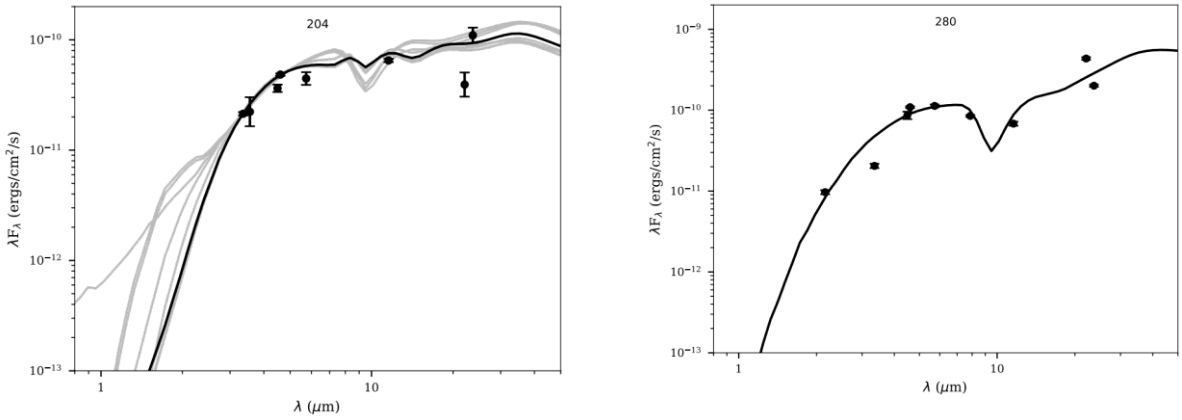

a) b)

Fig.6. Energy distribution in the spectrum of a) 5_YSO and b) 10_YSO (dots – observational data, solid line – model [25].

4. Conclusion

Using multiwavelength studies and archived catalog data, we studied objects emitting in the infrared range around the N22 dust bubble. The technique includes cleaning the sample from contaminants, identifying objects of classes I, II, III and transition disks. The presented approach to identifying YSOs provides a more reliable classification of them by evolutionary stages.

As a result of the study, infrared objects were selected and classified in the vicinity of the N22 infrared dust bubble based on photometry and spectral index criteria. From the list of 475 initial objects identified within a radius of 5', 161 objects were selected for subsequent analysis. Based on the double identification procedure (by color diagram and spectral index), 35 candidates for young stellar objects were identified: 15 objects of class I, 7 objects of class II and 13 objects with signs of transition disks. Comparison with catalogs made it possible to confirm the status of 7 objects as previously known YSOs.

In addition, their SEDs were analyzed by comparing with the model curves developed in the study, which allowed us to more accurately determine the evolutionary stages of the objects.T he results showed that fitting observational data to theoretical models allows us to refine the evolutionary status of some objects, especially for class II objects and those with transition disks. For a number of objects (e.g., 18_YSO), SED confirm their belonging to class II, both by the shape of the spectrum and by the tilt parameter α. However, for some objects, the classification remains uncertain due to the lack of photometric data in the far IR range or a high degree of degeneracy of the models. In general, the obtained SED confirm the preliminary classification of most objects

based on photometric criteria and emphasize the need for further observations with higher sensitivity and spectral coverage, especially in the range >10 μm, to confidently determine the evolutionary class of YSOs. Thus, the conducted study showed that 27 new young stellar objects in the early stages of evolution were identified around the infrared dust bubble N22.

Conflict of interest statement
The authors declare that they have no conflict of interest in relation to this research, whether financial, personal, authorship or otherwise, that could affect the research and its results presented in this paper.

CRediT author statement
Manapbayeva A.B., Alimgazinova N.Sh., Naurzbaeva A.Zh.: conceptualization, methodology, writing – review and editing; **Kyzgarina M.T., Abildayev N.E., Sarsenbayeva S.N., Turekhanova K.M.**: formal analysis, writing – original draft preparation; **Alibek A.A., Omar A.Zh., Demessinova A.M.:** investigation, validation. The final manuscript was read and approved by all authors.

Statement on the use of Artificial Intelligence.
During the preparation of this manuscript, artificial intelligence tools were used solely for language editing and grammatical improvement. No AI tools were used to generate scientific content, analysis, results, or conclusions.

Data Availability Statement
The data that support the findings of this article are openly available.

Funding
This research was funded by the Science Committee of the Ministry of science and Higher Education of the Republic of Kazakhstan (Grant No. AP23489575).

References

1. Klessen, R.S., Glover, C. O. (2014). *Physical Processes in the Interstellar Medium.* Springer-Verlag Berlin Heidelberg, 191 p. https://arxiv.org/pdf/1412.5182
2. Assembay, Zh., Komesh, T., Garay, G., Omar, A., Esimbek, J., Alimgazinova, N.Sh., Kyzgarina, M.T., Murat, S. (2024**).** ALMA observations of the environments of G301.1364-00.2249A. *Cosmic Masers: Proper Motion toward the Next-Generation Large Projects Proceedings IAU Symposium*, 380, 3. https://doi.org/10.1017/S1743921323002624
3. Manapbaeva, A.B., Esimbek, J., Alimgazinova, N.Sh., Kyzgarina, M.T., Atamurat, A.B. (2021). N22 shan kopirshikteri zhanyndagy zhas zhuldyz obektilerin anyqtau. *Izvestija Nacional'noj Akademii nauk Respubliki Kazahstan. Ser. Fiz-mat.*, 3(337), 96-105. https://journals.nauka-nanrk.kz/physics-mathematics/article/view/2078/2447
4. Megeath, S. T., Allen, L. E., Gutermuth, R.A., Pipher, J.L., Myers, P.C., Calvet, N., Hartmann, L., Muzerolle, J., Fazio, J. (2004). Initial Results from the Spitzer Young Stellar Cluster Survey. *The Astrophysical Journal Supplement Series*, 154(1), 367. https://doi.org/10.1086/422823
5. Gutermuth, R. A., Bourke, T.L., Allen, L.E., Myers, P.C., Megeath, S. T., Matthews, B.C., Jorgensen, J.K., Di Francesco, J., Ward-Thompson, D., Huard, T.L. (2008). The Spitzer Gould belt survey of large nearby interstellar clouds: discovery of a dense embedded cluster in the Serpens-Aquila Rift. *The Astrophysical Journal,* 673(2), L151. https://doi.org/10.1086/528710
6. Robitaille, T.P., Meade, M.R., Babler, B.L., Whitney, B.A., Johnston, K.G., Indebetouw, R., Cohen, M., Povich, M.S., Sewilo, M., Benjamin, R.A., Churchwell, E. (2008). Intrinsically red sources observed by Spitzer in the Galactic midplane. *The Astronomical Journal,* 136, 2413-2440. https://doi.org/10.1088/0004-6256/136/6/2413
7. Koenig, X. P., Leisawitz, D. V. (2014). A classification scheme for young stellar objects using the wide-field infrared survey explorer AllWISE catalog: revealing low-density star formation in the outer galaxy. *The Astrophysical Journal,* 791(2), 131. https://doi.org/10.1088/0004-637X/791/2/131
8. SIMBAD Astronomical Database - CDS (Strasbourg). https://simbad.cds.unistra.fr/simbad/sim-fcoo.
9. The VizieR Service for Astronomical Catalogues (CDS, Strasbourg, France). https://vizier.u-strasbg.fr/viz-bin/VizieR-3?-source=II/246&-out.max=50&-out.form=HTML%20Table&-form=sexa
10. AllWISE Source Catalog. https://irsa.ipac.caltech.edu/cgi-bin/Gator/nph-scan?mission=irsa&submit=Select&projshort=WISE
11. Churchwell, E., Povich, M.S., Allen, D., Taylor, M.G., Meade, M.R., Babler, B.L., Wolff, M.J. (2006). The Bubbling Galactic Disk. *The Astrophysical Journal,* 649 (2), 759-778. https://doi.org/10.1086/507015
12. Kolpak, M.A., Jackson, J.M., Bania, T. M., Clemens, D. P., Dickey, J.M. (2003). Resolving the Kinematic Distance Ambiguity toward Galactic H II Regions. *The Astrophysical Journal,* 582 (2), 756. https://doi.org/10.1086/344752

13. Simpson, R. J., Povich, M. S., Kendrew, S. (2012). The Milky Way Project First Data Release: A bubblier Galactic disc. *Monthly Notices of the Royal Astronomical Society,* 424(3), 2442–2460. https://doi.org/10.1111/j.1365-2966.2012.20770.x

14. Alksnis, A., Balklavs, A., Dzervitis, U., Pundure, I. (2001). A general catalogue of galactic carbon stars by C.B. Stephenson. Third edition. *VizieR Online Data Catalog*. *Baltic Astronomy,* 10, 1-318. https://doi.org/10.1515/astro-2001-1-202

15. Koenig, X.P. (2012). Wide-field infrared survey explorer observations of the evolution of massive star-forming regions. *The Astrophysical Journal*, 744 (2),130. https://doi.org/10.1088/0004-637X/744/2/130

16. Turmaganbet, U., Zhexebay, D., Turlykozhayeva, D., Skabylov, A., Akhtanov, S., Temesheva, S., Masalim, P., Tao, M. (2025). Thermal infrared object detection with yolo models. *Eurasian Physical Technical Journal,* 22(2 (52), 121-132. https://doi.org/10.31489/2025N2/121-132

17. Fischer, W. J. (2016). A WISE Census of Young Stellar Objects in Canis Major. *The Astrophysical Journal,* 827(2), 96. https://doi.org/10.3847/0004-637X/827/2/96

18. Verebélyi, E., Könyves, V., Nikolić, S., Kiss, C., Moór, A. (2013). Dense cores in the dark cloud complex LDN 1188. *Astronomical Notes,* 334, 924. https://doi.org/10.1002/asna.201311960

19. Alimgazinova, N.Sh. (2025). Young stellar objects in the region of dust bubble N1. *Recent Contributions to Physics*, 92(1), 50–59. https://doi.org/10.26577/RCPh20259215

20. Komesh, T., Omar, A., Garay, G., Assembay, Zh., Alimgazinova, N.Sh., Zhumabay, N., Kyzgarina, M.T. (2021). ALMA observations of the environments of G333.0162+00.7615. *Proceedings of the IAU,* 17, S373, 35-38. . https://doi.org/10.1017/S1743921323000121

21. Watson, C., Povich, M.S. (2008). Infrared dust bubbles: probing the detailed structure and young massive stellar populations of galactic H II regions. *The Astrophysical Journal,* 681(2), 1341-1355. https://doi.org/10.1086/588005

22. Kuhn, M.A., Souza, R.S. (2021). SPICY: the Spitzer/IRAC candidate YSO catalog for the inner Galactic midplane. *The Astrophysical Journal Supplement Series,* 254(33), 1-31. https://doi.org/10.3847/1538-4365/abe465

23. Ji, W.G., Zhou, J.J., Esimbek, J., Wu, Y.-F., Wu, G., Tang, X.-D. (2012). The infrared dust bubble N22: an expanding HII region and the star formation around it. *Astronomy and Astrophysics,* 544(A39),10. https://doi.org/10.1051/0004-6361/201218861

24. Cutri, R.M., Skrutskie, M.F. (2003). 2MASS All Sky Catalog of point sources. *The IRSA 2MASS All-Sky Point Source Catalog*. http://irsa.ipac.caltech.edu/applications/Gator/

25. Robitaille, T.P. (2017). A modular set of synthetic spectral energy distributions for young stellar objects. *Astronomy & Astrophysics,* 600(A11), 1-16. https://doi.org/10.1051/0004-6361/201425486

INFORMATION'S AUTHORS

Manapbayeva A.B. – Senior Researcher, Institute of Experimental and Theoretical Physics; Senior lecturer, Kazakh National Women's Teacher Training University, Scopus ID: 57205165517, https://orcid.org/0000-0002-0322-1509, e-mail: manapbayeva.arailym@gmail.com,

Alimgazinova N.Sh. – Leading Researcher, Institute of Experimental and Theoretical Physics; Candidate of physical and mathematical sciences, Associate Professor, Al Farabi Kazakh National University, Scopus ID: 35298349000, https://orcid.org/0000-0002-4596-1855, e-mail: Nazgul.Alimgazinova@kaznu.kz

Naurzbaeva A.Zh. – Leading Researcher, Institute of Experimental and Theoretical Physics; Candidate of physical and mathematical sciences, Senior lecturer, Al Farabi Kazakh National University, Scopus ID: 35300380700, https://orcid.org/0000-0001-6653-2948, e-mail: aisha.naur@gmail.com

Kyzgarina M.T. – Senior Researcher, Institute of Experimental and Theoretical Physics; PhD, Senior lecturer, Al Farabi Kazakh National University, Scopus ID: 35146124400, https://orcid.org/0000-0002-4103-7657, e-mail: meir83physics@gmail.com

Abildayev N.E. – bachelor student, Al Farabi Kazakh National University, Almaty, Kazakhstan, https://orcid.org/0009-0009-1934-4907, e-mail: nurlanabildaev833@gmail.com

Sarsenbayeva S.N. — Senior lecturer, Almaty University of Power Engineering and Telecommunications, https://orcid.org/0009-0008-3070-4566, e-mail: ssulukas@mail.ru

Turekhanova K.M. – Senior Researcher, Institute of Experimental and Theoretical Physics; Candidate of physical and mathematical sciences, Associate Professor, Al Farabi Kazakh National University, https://orcid.org/0000-0003-4662-7290, e-mail: kunduz@physics.kz

Alibek A.A. – PhD, Senior lecturer, Kazakh National Women's Teacher Training University, https://orcid.org/0000-0002-5309-347X, e-mail: alibek.akmaral65@gmail.com

Omar A.Zh. – Senior Researcher, Institute of Experimental and Theoretical Physics; PhD, Senior lecturer, Al Farabi Kazakh National University, Scopus ID: 58420497300, https://orcid.org/0000-0002-5604-3742, e-mail: omaruzhan@gmail.com

Demessinova A.M. – Senior Researcher, Institute of Experimental and Theoretical Physics; PhD, Senior lecturer, Al Farabi Kazakh National University, Scopus ID: 57211859262, https://orcid.org/0000-0001-5049-9338, e-mail: aizat.dem@gmail.com

EURASIAN PHYSICAL TECHNICAL JOURNAL

2026, Volume 23, No. 2 (56)

https://doi.org/10.31489/2026N2/139-147

Received: 13/02/2026 Revised: 28/05/2026 Accepted: 26/06/2026 Published online: 30/06/2026

Original Research Article

UDC 53.03; 52-17; 524.7-1/-8

PROBING KING AND PLUMMER DARK MATTER MODELS USING ROTATION CURVES

Kurmanov Ye.[1,2], Konysbayev T.[1,2], Suliyeva G.[1,2,3]*, Urazalina A.[1,2], Oteev T.[4], Rabigulova G.[2], Nurlanbek U.[2], Adil M.[2], Bekmurat B.[2], Tuzen G.[2]

[1] National Nanotechnology Laboratory of Open Type, Almaty, Kazakhstan
[2] Al-Farabi Kazakh National University, Almaty, Kazakhstan
[3] Fesenkov Astrophysical Institute, Almaty, Kazakhstan
[4] Nukus State Pedagogical Institute, Nukus, Uzbekistan
*Corresponding author: g_suliyeva@mail.ru

Abstract. *In this work, we study the distribution of dark matter in the halos of the spiral galaxies ESO3050090, ESO4880049, and ESO0140040 using their observed rotation curves. The analysis adopts spherically symmetric dark matter halos described by the King and Plummer density profiles, neglecting the baryonic component to emphasize the influence of the halo component only. As a first step, the characteristic halo parameters, the central density and the scale radius, are determined through a nonlinear least-squares fitting procedure based on the Levenberg–Marquardt algorithm. These best-fit values are then used as initial conditions for the Markov Chain Monte Carlo method to estimate the parameter space and uncertainties. Subsequently, we compare the results obtained from two specified fitting methods to assess their consistency and robustness. A statistical comparison between the King and Plummer profiles is performed using the Bayesian Information Criterion. The results of this work clarify how effectively the halo models under consideration reproduce the observed kinematics and highlight the ability to distinguish alternative dark matter density profiles.*

Keywords: dark matter, spiral galaxies, rotation curves, King profile, Plummer profile.

1. Introduction

Dark matter (DM) accounts for approximately 27% of the total energy density of the Universe and plays a key role in the formation and dynamical evolution of galaxies and galaxy clusters [1–4]. Its existence is supported by several independent observational probes, including galaxy rotation curves (RCs), strong and weak gravitational lensing, and measurements of the cosmic microwave background. Together, these observations consistently indicate mass distributions that significantly exceed the baryonic component alone [5, 6]. The galactic RCs serving as one of the most direct observational signatures of DM [7] show how the orbital velocity of stars and gas varies with distance from the galactic center. Their analysis allows not only to confirm the presence of DM but also to quantitatively constrain its radial distribution within individual galaxies [8, 9]. This is a fundamental problem in astrophysics, since the DM component governs the gravitational potential and thereby controls the observed galactic dynamics.

A variety of halo density profiles has been introduced in the literature to describe the mass distributions inferred from RC data. Among the most widely used models is the Navarro–Frenk–White (NFW) profile, derived by Navarro et al. [10] from N-body simulations within the standard cold DM framework. In contrast, Burkert [11] introduced a phenomenological cored profile to reproduce the observed RCs of dwarf spiral galaxies. Jimenez et al. [12] demonstrated that a large sample of galaxy RCs can be satisfactorily fitted using

the pseudo-isothermal profile. Brownstein [13] further showed that a core-modified profile with a constant central density provides a good description of the RCs of both high- and low-surface brightness galaxies.

In Refs. [14, 15], the RC data of the low-surface-brightness (LSB) galaxies U11819, U5750, U11454, and U11648 were investigated by some of us, assuming a spherically symmetric distribution of DM. The free parameters of several well-known phenomenological DM density profiles were obtained by fitting the observed RCs using least-squares techniques and the Markov Chain Monte Carlo (MCMC) method. The Bayesian Information Criterion (BIC) was employed to identify the best-fitting models for each galaxy, showing that different density profiles provide the optimal description for different systems.

In addition, in Ref. [16], the RC of the galaxy ESO0140040 was analyzed to investigate the imprint of non-vanishing DM pressure on halo properties. Several phenomenological density profiles were tested using least-squares fitting and information criteria, showing that cored profiles, such as the pseudo-isothermal and Einasto models, provide the most suitable framework for studying the DM equation of state, while cuspy profiles are disfavored.

In Ref. [17], the RCs of the Andromeda galaxy and the Milky Way were analyzed from the central regions to the outer halo within a multi-component mass model. The bulge and disk were described using exponential sphere profiles, while several phenomenological DM halo models were tested in the outer regions. A statistical comparison based on the BIC demonstrated that the exponential sphere profile provides the most consistent description of both galaxies, outperforming cuspy and de Vaucouleurs-type models. The analysis also showed that the choice of the halo profile affects the inferred inner structure and global mass distribution, with the Milky Way found to be less massive than Andromeda, in agreement with independent studies.

Finally, extending these studies to the physical properties of DM, in previous work [18], the DM distribution in the galactic core and inner regions was described by an exponential sphere profile and compared with the Einasto, Burkert, and isothermal halo models. In another work [19], through the statistical analysis for several LSB galaxies, phenomenological profiles were compared to the profiles derived within the framework of Scalar Field Dark Matter (SFDM) model.

In this work, we study the DM distribution in the halos of LSB galaxies ESO3050090, ESO4880049, and ESO014004 based on their observed RCs. LSB galaxies are valuable for halo studies, since their dynamical mass is commonly inferred to be dominated by DM [20, 21]. Moreover, the three galaxies considered here exhibit different RC morphologies and characteristic velocity scales, which allows us to test the ability of the adopted halo models to reproduce distinct kinematic regimes within a single fitting framework.

To model the halo density distribution, we employ King and Plummer density profiles. These two models represent cored density distributions which makes them useful for testing systems where observations indicate finite densities in the inner regions, in contrast to cuspy profiles predicted by cold dark matter (CDM) simulations. Unlike other cored DM profiles (for example, Burkert, pseudo-isothermal, Exponential Sphere, Brownstein profiles), which have been extensively studied in the literature, the King and Plummer profiles have received considerably less attention in this context. And their ability to reproduce observed RCs of LSB galaxies remained poorly constrained.

The observational RC data used in our analysis are taken from Refs. [22, 23]. To compare the results, we apply two complementary fitting techniques: a nonlinear least-squares method based on the Levenberg–Marquardt algorithm and the MCMC approach. The nonlinear fit is first used to obtain preliminary parameter estimates and to identify the minimum χ^2 solution. These values are then adopted as initial conditions and prior ranges for the MCMC analysis, which provides the best-fitting models and reliable uncertainties. On the basis of the resulting density profiles, we subsequently compute the DM mass enclosed within the halos of the galaxies.

This paper is organized as follows. In Section 2, we introduce the DM density profiles adopted in the analysis. Section 3 is devoted to the description of fitting procedures. Section 4 presents the corresponding numerical results and discussion. The main conclusions of the study are summarized in Section 5.

2. Dark Matter halo density profiles

In this section, we present the DM density profiles used in this work. Modeling the mass distribution of galactic DM halos is commonly performed by specifying an analytical form for the density $\rho(r)$, which serves as the starting point for constructing the corresponding gravitational potential and predicted RC. Different profiles correspond to different assumptions about the behavior of the DM density in the central and outer regions of galaxies.

RC data indicate that the DM density is not uniform and varies with radius. To examine how the choice of the profile affects the results, we consider the DM density models introduced below.

King profile [24]:

$$\rho_K(r) = \rho_0 \left(1 + \frac{r^2}{r_0^2}\right)^{-3/2}. \quad (1)$$

Plummer profile [25]:

$$\rho_P(r) = \rho_0 \left(1 + \frac{r^2}{r_0^2}\right)^{-5/2}, \quad (2)$$

where ρ_0 is the central density of DM, and r_0 is the scale radius. These profiles are characterized by smooth behavior at the origin and contain two free parameters ρ_0 and r_0.

The distinction between the King and Plummer models lies in their outer density slopes. At large radii, the King profile decreases as a power law with $\rho_K(r) \sim r^{-3}$. This relatively shallow decline implies an extended halo structure and allows the profile to reproduce slowly varying or approximately flat RCs over a broad radial interval. The Plummer model exhibits a sharper decline at large radii, with $\rho_P(r) \sim r^{-5}$, which leads to a more centrally concentrated halo.

3. Methods

Using the RC data of ESO3050090, ESO4880049 and ESO014004, we examined the properties of their halos by employing two complementary fitting methods.

In the first stage, we applied the nonlinear least-squares procedure (Levenberg–Marquardt) to obtain initial estimates for the free parameters of the selected density profiles. This step helps to identify the region where the χ^2 function is minimized and provides suitable starting values for the subsequent analysis.

We then performed a MCMC study. Unlike the initial fit, the MCMC method explores the parameter space more extensively and allows us to determine statistically reliable intervals for the parameters in both density profiles. The MCMC output refines the preliminary values obtained from the nonlinear approach and shows how accurately each profile follows the observed RCs.

Since the central parts of ESO3050090, ESO4880049, and ESO0140040 remain poorly constrained, we limit the analysis to the halo component and use

$$v_{tot}^2(r) \simeq v_{profile}^2(r), \quad (3)$$

where $v_{profile}(r)$ is the circular velocity of the DM halo.

The circular velocity associated with a given halo mass profile $M(r)$ is

$$v_{profile}(r) = \sqrt{\frac{GM(r)}{r}}. \quad (4)$$

Mass profile is

$$M(r) = 4\pi \int_0^r r^2 \rho(r) dr. \quad (5)$$

Using the density profiles given in Eqs. (1) and 2 and substituting them into Eq. (5), we obtain the corresponding mass profiles for the King and Plummer models.

$$M_{King}(r) = 4\pi r_0^3 \rho_0 \left(-\frac{r}{\sqrt{r^2 + r_0^2}} + \operatorname{arcsinh}\left(\frac{r}{r_0}\right) \right). \quad (6)$$

$$M_{Plummer}(r) = \frac{4\pi \rho_0 r^3 r_0^3}{3\left(r^2 + r_0^2\right)^{3/2}}. \quad (7)$$

To identify which of the two models provides a better description of the RCs of ESO3050090, ESO4880049 and ESO0140040, we compared their fits using the BIC. For each density profile, the value of BIC was calculated as

The Bayesian Information Criterion (BIC) was used to compare the considered dark matter models. For the MCMC analysis, the BIC was estimated as

$$BIC = \chi^2 + k \ln N, \quad (8)$$

where χ is the minimum chi-square value, k is the number of free parameters, and N is the number of observational data points.

For the nonlinear fitting analysis, the BIC values were obtained directly from the built-in Mathematica routine *NonlinearModelFit*, which evaluates the likelihood-based criterion

$$BIC = -2 \ln L_{\max} + k \ln N, \quad (9)$$

where $L_{\max}$ is the maximum likelihood. Assuming Gaussian observational errors,

$$-2\ln L_{\max} = \chi^2 + \sum_{i=1}^{N} \ln(2\pi\sigma_i^2), \quad (10)$$

where σ_i denotes the uncertainty associated with the i-th observational data point. Therefore, the likelihood-based BIC values used in the nonlinear fitting analysis are not necessarily identical to those estimated directly from χ.

The parameter estimation was performed using the Metropolis–Hastings algorithm. Uniform priors were adopted for all free parameters within fixed physically motivated ranges. The prior intervals were chosen to define the allowed parameter space for each model. Initial parameter estimates obtained from the nonlinear least-squares fit were used only as starting values and for selecting reasonable parameter ranges.

For the King profile, the prior ranges were chosen as $\rho_0 \in [1, 250]$ and $r_0 \in [1, 10]$, while for the Plummer profile they were $\rho_0 \in [1, 349]$ and $r_0 \in [1, 13]$. A preliminary MCMC run was used to estimate the proposal covariance matrix, followed by a production chain of 50,000 steps. The initial part of the chain was discarded as burn-in before calculating the final parameter estimates and confidence intervals. Convergence was assessed by inspecting the trace plots of the sampled parameters and the corresponding χ. values.

For practical comparison, we introduce the relative quantity

$$\Delta BIC = BIC - BIC_{min}, \quad (11)$$

where BIC_{min} is the smallest value among all competing models.

For completeness, the likelihood-based BIC values obtained from the built-in Mathematica routine NonlinearModelFit are 74.17and 79.09for ESO0140040, 79.02and 81.30for ESO3050090, and 59.41and 67.80for ESO4880049. The reported ΔBICvalues were computed directly from these likelihood-based BIC values.

For the MCMC analysis, the corresponding BIC values are 9.12 and 13.34 for ESO0140040, 6.59 and 8.87 for ESO3050090, and 7.92 and 16.31 for ESO4880049, obtained using Eq. (8).

Prior to performing the MCMC analysis, we first identified the region where the χ^2 function reaches its minimum by applying the nonlinear Levenberg–Marquardt method. This preliminary step yields a reasonable starting point for the model parameters. In this procedure, the quantity being minimized is

$$\chi^2 = \sum_{i=1}^{N} \left[\frac{v_i^{obs} - v(\rho_0, r_0, r)}{\sigma_{v,i}^{obs}}\right]^2, \quad (12)$$

where v_i^{obs} are the measured rotation velocities and $v(\rho_0, r_0, r)$ is the model velocity computed from the assumed halo profile.

4. Results and discussion

In the left panels of Figures 1, 2, 3, the RCs of the galaxies ESO3050090, ESO4880049 and ESO0140040 are shown together with the model curves obtained from the two halo profiles examined in this work. In all three cases, the blue points represent the observed rotation velocities, and the vertical bars mark the corresponding measurement errors.

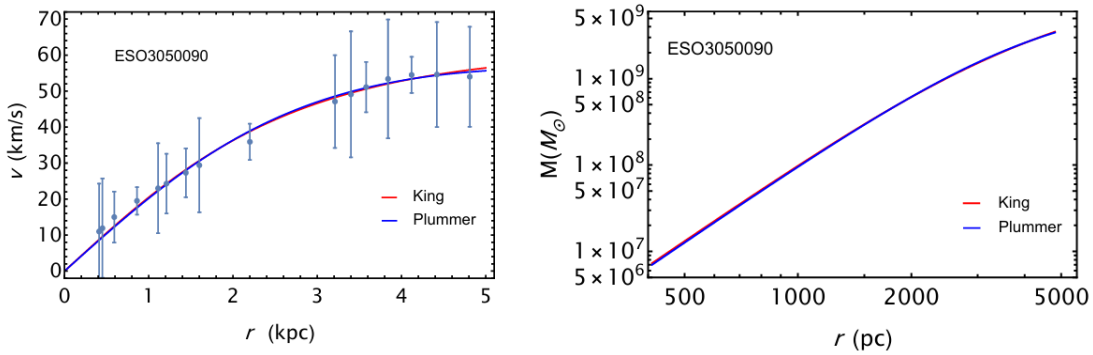

Fig.1. Left panel: Best fit velocity profile for ESO3050090 galaxy. Right panel: Logarithmic mass profiles of DM in the halo in ESO3050090 galaxy.

The solid lines indicate the best-fit King (red) and Plummer (blue) solutions. As the figures show, both halo models follow the general rise of the RCs for each galaxy and reproduce the data within the reported errors over the radial range covered by the observations. This agreement confirms that considered galaxies are

dominated by DM over the observed radial range, and the baryonic contributions are subdominant. In addition, the graphical results show that cored profiles are quite preferable for describing LSB galaxies. Figure 4 shows the contour plots for the parameters ρ_0 and r_0 obtained from the MCMC analysis for the galaxies ESO3050090, ESO0140040 and ESO4880049.

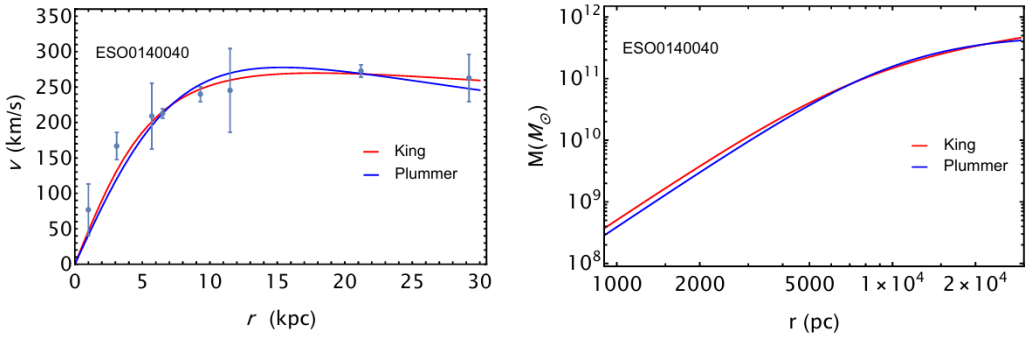

Fig.2. Left panel: Best fit velocity profile for ESO0140040 galaxy. Right panel: Logarithmic mass profiles of DM in the halo in ESO0140040 galaxy.

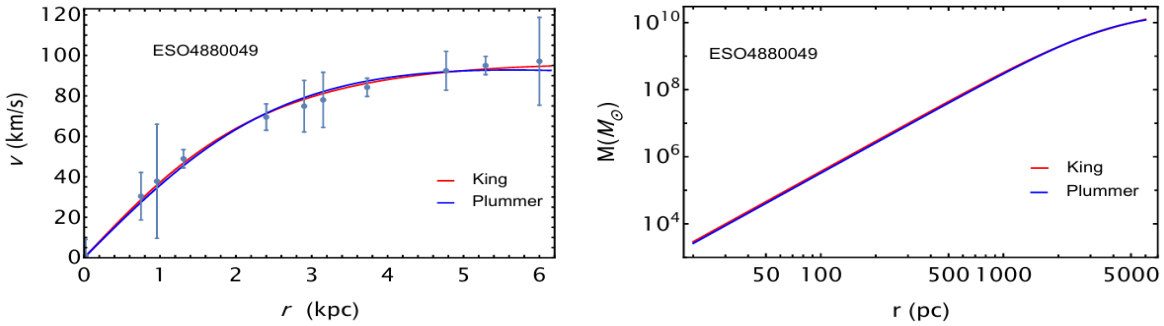

Fig.3. Left panel: Best fit velocity profile for ESO4880049 galaxy. Right panel: Logarithmic mass profiles of DM in the halo in ESO4880049 galaxy.

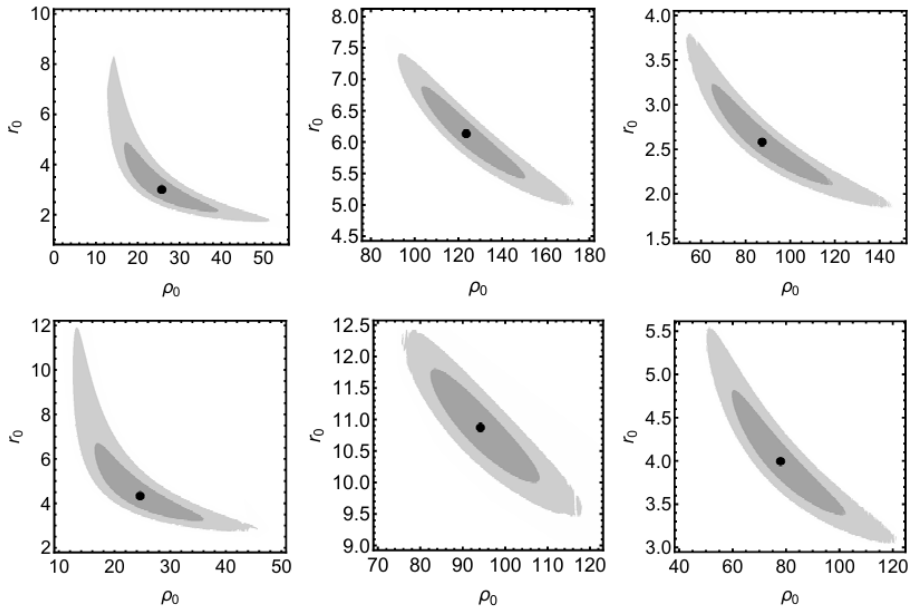

Fig.4. Contour plots of the best-fit parameters (black dots) and the associated 1σ (dark gray) and 2σ (light gray) confidence regions obtained from the MCMC analysis. From left to right, the panels correspond to the galaxies ESO3050090, ESO0140040, and ESO4880049. Top row: King profile; bottom row: Plummer profile.

Each panel corresponds to one of the two halo models considered in this work. The black point marks the best-fit parameter values. The shaded regions indicate the 1σ (dark) and 2σ (light) levels extracted from the

MCMC chains. The shape of the contours reveals an anticorrelation between ρ_0 and r_0, so larger scale radii correspond to lower central densities, and the combination $\rho_0 r^3$ determining the mass scale remains nearly constant. The mass profiles for all three galaxies: ESO3050090, ESO4880049 and ESO0140040 are shown in the right panels of Figures 1, and 2, 3. The functions $M(r)$ were obtained by substituting the King and Plummer density profiles into the integral expression given in Eq. (5). The profiles are plotted on a logarithmic scale, which makes it clear that the enclosed mass increases with radius in both models.

The results obtained from the MCMC analysis for the galaxies considered in this work are summarized in Tables 1, 3 and 5, while the corresponding parameters derived using the nonlinear fitting procedure are reported in Tables 2, 4, and 6. In all tables, we list the central density ρ_0, the characteristic scale radius r_0, the virial mass M_{vir}, and the virial radius r_{vir}, defined as the radius within which the mean density equals 200 times the critical density of the Universe.

Table 1. The parameters of the best-fit model for galaxy ESO0140040 with MCMC.

Profiles	$\rho_0 \pm \sigma_{\rho_0}$ $(10^{-3} M_\odot/\mathrm{pc}^3)$	$r_0 \pm \sigma_{r_0}$ (kpc)	r_{vir} (kpc)	M_{vir} $(10^{11} M_\odot)$	$M \pm \sigma_M^a$ $(10^{11} M_\odot)$	$M \pm \sigma_M^b$ $(10^{11} M_\odot)$	ΔBIC	χ^2
King	$123.58^{+27.18}_{-20.55}$	$6.13^{+0.75}_{-0.71}$	100.96	8.93	4.60 ± 1.6	0.62 ± 0.35	0	4.96
Plummer	$94.17^{+13.94}_{-11.78}$	$10.87^{+0.92}_{-0.87}$	54.26	4.77	4.17 ± 1.12	1.79 ± 0.70	4.22	9.18

Table 2. Best fit model parameters for galaxy ESO0140040.

Profiles	$\rho_0 \pm \sigma_{\rho_0}$ $(10^{-3} M_\odot/\mathrm{pc}^3)$	$r_0 \pm \sigma_{r_0}$ (kpc)	r_{vir} (kpc)	M_{vir} $(10^{11} M_\odot)$	$M \pm \sigma_M^a$ $(10^{11} M_\odot)$	$M \pm \sigma_M^b$ $(10^{11} M_\odot)$	ΔBIC	χ^2
King	123.60 ± 13.62	6.13 ± 0.43	100.96	8.93	4.60 ± 0.89	0.62 ± 0.20	0	4.96
Plummer	94.17 ± 10.18	10.87 ± 0.71	54.26	4.77	4.20 ± 0.85	1.79 ± 0.53	4.92	9.18

Table 3. The parameters of the best-fit model for galaxy ESO3050090 with MCMC.

Profiles	$\rho_0 \pm \sigma_{\rho_0}$ $(10^{-3} M_\odot/\mathrm{pc}^3)$	$r_0 \pm \sigma_{r_0}$ (kpc)	r_{vir} (kpc)	M_{vir} $(10^{9} M_\odot)$	$M \pm \sigma_M^a$ $(10^{9} M_\odot)$	$M \pm \sigma_M^b$ $(10^{9} M_\odot)$	ΔBIC	χ^2
King	$25.73^{+13.44}_{-9.01}$	$2.99^{+1.88}_{-0.90}$	29.11	17.13	3.50 ± 1.86	1.51 ± 0.89	0	0.82
Plummer	$24.59^{+11.42}_{-8.20}$	$4.32^{+2.38}_{-1.12}$	16.26	7.51	3.42 ± 1.62	2.94 ± 1.53	0.13	0.95

Table 4. Best fit model parameters for galaxy ESO3050090.

Profiles	$\rho_0 \pm \sigma_{\rho_0}$ $(10^{-3} M_\odot/\mathrm{pc}^3)$	$r_0 \pm \sigma_{r_0}$ (kpc)	r_{vir} (kpc)	M_{vir} $(10^{9} M_\odot)$	$M \pm \sigma_M^a$ $(10^{9} M_\odot)$	$M \pm \sigma_M^b$ $(10^{9} M_\odot)$	ΔBIC	χ^2
King	25.67 ± 1.69	2.99 ± 0.18	29.11	17.11	3.49 ± 0.39	1.51 ± 0.41	0	0.82
Plummer	24.56 ± 1.62	4.33 ± 0.25	16.27	7.51	3.42 ± 0.40	2.94 ± 0.75	2.28	0.95

Table 5. The parameters of the best-fit model for galaxy ESO4880049 with MCMC.

Profiles	$\rho_0 \pm \sigma_{\rho_0}$ $(10^{-3} M_\odot/\mathrm{pc}^3)$	$r_0 \pm \sigma_{r_0}$ (kpc)	r_{vir} (kpc)	M_{vir} $(10^{10} M_\odot)$	$M \pm \sigma_M^a$ $(10^{10} M_\odot)$	$M \pm \sigma_M^b$ $(10^{9} M_\odot)$	ΔBIC	χ^2
King	$87.37^{+31.76}_{-22.81}$	$2.58^{+0.65}_{-0.45}$	37.82	4.49	1.25 ± 0.74	3.28 ± 3.74	0	0.81
Plummer	$77.94^{+24.34}_{-12.28}$	$3.99^{+0.83}_{-0.63}$	19.16	1.95	1.20 ± 0.64	7.34 ± 6.84	0.92	1.73

Table 6. Best fit model parameters for galaxy ESO4880049.

Profiles	$\rho_0 \pm \sigma_{\rho_0}$ $(10^{-3} M_\odot/\mathrm{pc}^3)$	$r_0 \pm \sigma_{r_0}$ (kpc)	r_{vir} (kpc)	M_{vir} $(10^{10} M_\odot)$	$M \pm \sigma_M^a$ $(10^{10} M_\odot)$	$M \pm \sigma_M^b$ $(10^{9} M_\odot)$	ΔBIC	χ^2
King	87.43 ± 5.14	2.58 ± 0.11	37.83	4.49	1.25 ± 0.12	3.28 ± 0.61	0	0.81
Plummer	78.10 ± 5.85	3.99 ± 0.19	19.14	1.94	1.20 ± 0.15	7.33 ± 1.62	8.39	1.73

[a]The DM total mass is calculated using the last RC data point in the halo for r.
[b]The DM total mass is calculated using the scale radius r_0.

In addition, namely the χ^2 and the BIC, are reported for each halo profile. The quantities obtained from the fits show that ESO0140040 has a more massive halo than the other two galaxies. Its virial mass exceeds

those of ESO3050090 and ESO4880049. This difference explains why ESO0140040 achieves higher velocities and why its RC extends to larger radii.

The statistical analysis of the RCs carried out using both the MCMC approach and the nonlinear fitting procedure leads to conclusion: the King halo profile provides a better fit to the observed RCs than the Plummer model. In the case of ESO0140040, the MCMC results reported in Table 1 show that, for $N = 8$ data points and $k = 2$ free parameters, the BIC yields $BIC = 9.12$ for the King profile and $\mathrm{BIC} = 13.34$ for the Plummer profile. Adopting $\mathrm{BIC}_{min} = 9.12$ as the reference value, the corresponding relative criterion is $\Delta\mathrm{BIC} = 4.22$ for the Plummer model. The nonlinear fitting results reported in Table 2 are consistent with this outcome, as the King profile yields both a lower χ^2 and a smaller BIC than the Plummer model.

A similar behavior is observed for ESO3050090. As shown by the MCMC analysis in Table 3, the BIC yields $\mathrm{BIC} = 6.37$ for the King profile and $\mathrm{BIC} = 6.50$ for the Plummer profile for $N = 16$, corresponding to $\Delta\mathrm{BIC} = 0.13$ for the latter. Although the difference is small, the King halo profile is slightly favored. This behavior is also observed in the nonlinear fitting results reported in Table 4, where the King model yields the lowest BIC value. An analogous result is obtained for ESO4880049. The MCMC analysis summarized in Table 5 yields $\mathrm{BIC} = 5.61$ for the King profile and $\mathrm{BIC} = 6.53$ for the Plummer profile for $N = 11$, leading to ΔBIC=0.92 for the Plummer model. The nonlinear fitting analysis presented in Table 6 leads to the same qualitative conclusion, as the King profile exhibits a substantially lower BIC value than the Plummer model.

Overall, the results presented in the tables enable a clear comparison of the ability of the different halo profiles to reproduce the observed RCs, while the derived virial masses and radii provide a physically meaningful description of the DM halos.

5. Conclusion

In this work we analyzed the RCs of the LSB spiral galaxies ESO3050090, ESO4880049, and ESO0140040 within the two cored DM halo models: the King and Plummer profiles. By combining MCMC method with nonlinear least-squares fitting, we constrained the structural parameters (ρ_0 and r_0), derived the corresponding mass distributions, and performed a comparison of two models using the BIC.

The main result is that both profiles reproduce the observed RCs within the measurement errors over the entire radial range covered by the data. This demonstrates that, these galaxies are dominated by a dark halo component whose gravitational potential alone can account for the observed circular velocities under the assumption $v_{tot}^2 \simeq v_{profile}^2$.

Despite the general similarity of the fitting results, statistical comparison showed that the King profile is preferred over the Plummer profile, with the strength of the preference depending on the galaxy. For ESO0140040, the difference in BIC indicates positive evidence in favor of King, while for ESO3050090 and ESO4880049 the evidence is weaker. In particular, for ESO3050090 and ESO4880049, the MCMC-based ΔBIC values of 0.13 and 0.92 are below the conventional threshold of 2 and should be interpreted as negligible to weak preference. However, the nonlinear fitting yields ΔBIC = 2.28 and 8.39 for these galaxies, lending additional support to the King model. Taken together, both methods consistently favor the King profile, though the strength of this preference varies across the sample.

These results have a following physical interpretation: the shallower outer density decline of the King model ($\rho_K \sim r^{-3}$) implies a more extended mass distribution that better supports the observed velocities at larger radii. It worth noting that galaxies ESO3050090, ESO4880049 and ESO0140040 were previously investigated within the sample of LSB galaxies in the framework of SFDM model [26], brane-world gravity [27] and nearly Newtonian approximation [28]. Although these models imply different physical interpretation (via specific parameters), they produce rotation curves comparable to those obtained in present work. In addition, the derived central densities and characteristic halo radii are consistent with the values inferred here. This agreement indicates that the observational data for given galaxies primarily constrain the overall gravitational potential. However, the divergence between different approaches may become more pronounced in the halos of larger galaxies.

In general, the results of a present work show that cored DM halos provide a self-consistent and adequate description of the kinematics of considered LSB galaxies. The preference for cored profiles found in this work is consistent with the general trend reported in the literature for LSB galaxies, but should not be interpreted as evidence against CDM cuspy profiles. To draw statistically robust conclusions about the preference between cored and cuspy profiles, a direct fitting comparison must be performed on a significantly larger and

morphologically diverse galaxy sample, with high-resolution Rotation Curve data extending to large radii where the two profile families predict the most distinct kinematic signatures.

For a more detailed analysis of different core DM profiles, it would be interesting to construct RCs for galaxies extending to larger radii and to include the impact of their baryonic component and inner structure. These aspects are of our further interest.

Conflict of interest statement

The authors declare that they have no conflict of interest in relation to this research, whether financial, personal, authorship or otherwise, that could affect the research and its results presented in this paper.

CRediT author statement

Kurmanov Ye.: Conceptualization, Methodology, Supervision; **Konysbayev T.**: Software, Validation; **Suliyeva G.**: Formal analysis, Writing - Review & Editing; **Urazalina A.**: Formal analysis, Writing - Review & Editing; **Oteev T.**: Formal analysis, Writing - Review & Editing; **Rabigulova G.**: Investigation, Writing - Original Draft; **Nurlanbek U.**: Investigation, Writing - Original Draft; **Adil M.**: Investigation, Writing - Original Draft; **Bekmurat B.**: Investigation, Writing - Original Draft; **Tuzen G.**: Investigation, Writing - Original Draft. The final manuscript was read and approved by all authors.

Statement on the use of Artificial Intelligence.

During the preparation of this manuscript, artificial intelligence tools were used solely for language editing and grammatical improvement. No AI tools were used to generate scientific content, analysis, results, or conclusions.

Data Availability Statement

The data are available upon reasonable request from the authors.

Funding

This research was funded by the Science Committee of the Ministry of Science and Higher Education of the Republic of Kazakhstan (Grant No. AP23488743).

References

1 Planck Collaboration (2020). Planck 2018 results. *Astron. Astrophys.* 641, A6, https://doi.org/10.1051/0004-6361/201833910, 1807.06209.

2 Lake, G. (1989). Must the Disk and Halo Dark Matter Be Different? *Astronomical Journal*. 98, 1554, https://doi.org/10.1086/115238.

3 Lux, H., Read, J. I., Lake, G., Johnston, K. V. (2012). The Multidimensional Milky Way. *Mon. Not. Roy. Astr. Soc.*, 424(1), L16–L20. https://doi.org/10.1111/j.1745- 3933.2012

4 Deason, A. J., Belokurov, V., Sanders, J. L. (2019). The total stellar halo mass of the Milky Way. *Mon. Not. Roy. Astr. Soc.*, 490(3), 3426–3439. https://doi.org/10.1093/mnras/stz2793, 1908.02763.

5 de Blok, W. J. G. (2010). The Core-Cusp Problem. *Advances in Astronomy*, 789293, https://doi.org/10.1155/2010/789293, 0910.3538.

6 Seo, G., Sohn, J., Lee, M. G. (2020). Tracing Dark Matter Halos with Satellite Kinematics and the Central Stellar Velocity Dispersion of Galaxies. *Astrophys. J.*, 903(2), 130. https://doi.org/10.3847/1538-4357/abbd92, 2010.00693.

7 Rubin, V. C., Ford, Jr. W. K., Thonnard, N. (1980). Rotational properties of 21 SC galaxies with a large range of luminosities and radii, from NGC 4605 (R=4kpc) to UGC 2885 (R=122kpc). *Astrophys. J.*, 238, 471–487. https://doi.org/10.1086/158003

8 Volders, L. M. J. S. (1959). Neutral hydrogen in M 33 and M 101. *Bulletin of the Astronomical Institutes of the Netherlands*, 14, 323. https://scholarlypublications.universiteitleiden.nl/handle/1887/6267.

9 Freeman, K. C. (1970). On the Disks of Spiral and S0 Galaxies. *Astrophys. J.* 160, 811. https://doi.org/10.1086/150474

10 Navarro, J. F., Frenk, C. S., White, S. D. M. (1996). The Structure of Cold Dark Matter Halos. *Astrophys. J.* 462, 563-575. https://doi.org/10.1086/177173

11 Burkert, A. (1995). The Structure of Dark Matter Halos in Dwarf Galaxies. *Astrophys. J. Lett.* 447, L25–L28. https://doi.org/10.1086/309560, astro-ph/9504041.

12 Jimenez, R., Verde, L., Oh, S. P. (2003). Dark halo properties from rotation curves. *Mon. Not. Roy. Astr. Soc.*, 339(1), 243–259. https://doi.org/10.1046/j.1365-8711.2003.06165.x

13 Brownstein, J. R., Moffat, J. W. (2006). Galaxy Rotation Curves without Nonbaryonic Dark Matter. *The Astrophysical Journal*, 636(2), 721. https://doi.org/10.1086/498208.

14 Boshkayev, K., Konysbayev, T., Kurmanov, Y., Muccino, M., G. Z. (2020). Physical properties of dark matter in galaxy U11454. *Physical Sciences and Technology*, 10(3-4), 11–20. https://doi.org/10.26577/PHST.2020.V7.I2.02

15 Kurmanov, Y., Boshkayev, K., Konysbayev, T., Muccino, M., Urazalina, A., Ikhsan, G., Saiyp, N., Rabigulova, G., Karlinova, M., Suliyeva, G., Beissen, N. (2023). Analysis of dark matter profiles in the halos of spiral galaxies. *Physical Sciences and Technology*, 10(3-4), 4–16. https://doi.org/10.26577/PHST.2023.V10.I2.01

16 Boshkayev, K., Konysbayev, T., Kurmanov, E., Luongo, O., Muccino, M. (2020). Imprint of Pressure on Characteristic Dark Matter Profiles: The Case of ESO0140040. *Galaxies*, 8(4), 74. https://doi.org/10.3390/galaxies8040074.

17 Boshkayev, K., Konysbayev, T., Kurmanov, Y., Luongo, O., Muccino, M., Quevedo, H., Zhumakhanova, G. (2024). Numerical analyses of M31 dark matter profiles. *International Journal of Modern Physics D*, 33, 2450016. https://doi.org/10.1142/S0218271824500160, 2212.02999.

18 Boshkayev, K., Konysbayev, T., Kurmanov, E., Luongo, O., Malafarina, D., Mutalipova, K., Zhumakhanova, G. (2021). Effects of non-vanishing dark matter pressure in the Milky Way Galaxy. *Mon. Not. Roy. Astr. Soc.*, 508(1), 1543–1554. https://doi.org/10.1093/mnras/stab2571, 2107.00138.

19 Suliyeva, G., Kurmanov, Y., Konysbayev, T., Boshkayev, K., Urazalina, A., Luongo, O. (2024). Finite temperature effects within scalar field dark matter model. *Eurasian Physical Technical Journal*, 21(2(48)), 92–101. https://doi.org/10.31489/2024No2/92-101.

20 de Blok, W. J. G., McGaugh, S. S., Rubin, V. C. (2001). High-Resolution Rotation Curves of Low Surface Brightness Galaxies. II. Mass Models. *Astronomical Journal*, 122(5), 2396–2427. https://doi.org/10.1086/323450.

21 Mannheim, P. D., O'Brien, J. G. (2012). Fitting galactic rotation curves with conformal gravity and a global quadratic potential. *Phys. Rev. D*, 85(12), 124020. https://doi.org/10.1103/PhysRevD.85.124020, 1011.3495.

22 de Blok, W. J. G., Bosma, A. (2002). High-resolution rotation curves of low surface brightness galaxies. *Astron. Astrophys.*, 385, 816–846. https://doi.org/10.1051/0004-6361:20020080.

23 Barranco, J., Bernal, A., Nunez, D. (2015). Dark matter equation of state from rotational curves of galaxies. *Mon. Not. Roy. Astr. Soc.*, 449(1), 403–413. https://doi.org/10.1093/mnras/stv302

24 King, I. (1962). The structure of star clusters. I. an empirical density law. *Astronomical Journal*, 67, 471. https://doi.org/10.1086/108756

25 Plummer, H. C. (1911). On the problem of distribution in globular star clusters. *Mon. Not. Roy. Astr. Soc.*, 71, 460–470. https://doi.org/10.1093/mnras/71.5.460.

26 Fernandez-Hernandez, L. M., Rodrıguez-Meza, M. A., Matos, T. (2018). Comparison between two scalar field models using rotation curves of spiral galaxies. *Journal of Physics Conference Series*, 1010, 012005. https://doi.org/10.1088/1742-6596/1010/1/012005

27 Garcia-Aspeitia, M. A., Rodriguez-Meza**M** M. A. (2018). Constraining brane tension using rotation curves of galaxies. *Journal of Physics Conference Series*, 1010, 012006. https://doi.org/10.1088/1742-6596/1010/1/012006.

28 Capistrano, A. J. S., Barrocas, G. R. G. (2018). Rotation curves of LSBGs and dwarf galaxies in a nearly Newtonian solution. *Mon. Not. Roy. Astr. Soc.*, 475(2), 2204–2214. https://doi.org/10.1093/mnras/stx2909.

AUTHORS' INFORMATION

Kurmanov Yergali - PhD, Associate Professor, Al-Farabi Kazakh National University, Almaty, Kazakhstan; SCOPUS Author ID: 57695578100, https://orcid.org/0000-0003-3695-0166; ergaly_90@mail.ru

Konysbayev Talgar - PhD, Senior Researcher Associate, Al-Farabi Kazakh National University, Almaty, Kazakhstan; SCOPUS Author ID: 57219800003, https://orcid.org/0000-0001-9476-3700; talgar_777@mail.ru

Suliyeva Gulnara - PhD, Junior Research Associate, Al-Farabi Kazakh National University, Almaty, Kazakhstan; SCOPUS Author ID: 57818572500, https://orcid.org/0000-0001-5072-7898; g_suliyeva@mail.ru

Urazlaina Ainur - PhD, Senior Lecturer, Al-Farabi Kazakh National University, Almaty, Kazakhstan; SCOPUS Author ID: 57076979300, https://orcid.org/0000-0002-4633-9558; y.a.a.707@mail.ru

Oteev Tursinbay - PhD, Teaching Assistant, Nukus State Pedagogical Institute, Nukus, Uzbekistan; SCOPUS Author ID: 57190254652, https://orcid.org/0000-0002-5733-834X; oteevtp@gmail.com

Rabigulova Guldana – PhD student, Al-Farabi Kazakh National University, Almaty, Kazakhstan; SCOPUS Author ID: 58848753900, https://orcid.org/0009-0003-8998-6282; guldanaberikhanovna@gmail.com

Nurlanbek Ulpan - PhD student, Al-Farabi Kazakh National University, Almaty, Kazakhstan; https://orcid.org/0009-0005-7107-5899; ulpan.nurlanbek02@gmail.com

Adil Makhabbat - Master student, Al-Farabi Kazakh National University, Almaty, Kazakhstan; https://orcid.org/0009-0008-2202-4413; adilmahabbat@gmail.com

Bekmurat Bagzhan - Master student, Al-Farabi Kazakh National University, Almaty, Kazakhstan; https://orcid.org/0009-0008-0000-442X; Bagzhan159@gmail.com

Tuzen Galiya - Master student, Al-Farabi Kazakh National University, Almaty, Kazakhstan; https://orcid.org/0009-0001-5083-9395; galiyatuzen@gmail.com

EURASIAN PHYSICAL TECHNICAL JOURNAL

2026, Volume 23, No. 2 (56)

https://doi.org/10.31489/2026N2/148-155

Received: 14/02/2026 Revised: 30/05/2026 Accepted: 26/06/2026 Published online: 30/06/2026

Original Research Article

UDC 539.120

HIGGS INFLATION AROUND THE SYMMETRIC POINT

Berkimbayev D.[1, 2], and Aldabergenov Y.[1, 2, 3]*

[1]National Nanotechnology Laboratory of Open Type, Almaty 050040, Kazakhstan.
[2]Al-Farabi Kazakh National University, Al-Farabi av. 71, Almaty 050040, Kazakhstan.
[3]Fudan University, 220 Handan Road, Shanghai 200433, China
*Corresponding author: aldyermek@gmail.com

Abstract. *A novel generalized Higgs inflation scenario is studied, where inflation takes place near the symmetric point of the "Mexican hat" potential, as opposed to the standard Higgs inflation which takes place at large field values away from the symmetric point. When minimally coupled to gravity, inflation near the symmetric point leads to large tensor-to-scalar ratio which is ruled out by CMB observations, while requiring super-Planckian Higgs VEV which also acts as the axion decay constant (super-Planckian values of the decay constant are theoretically disfavored, for example by the swampland conjectures). It is shown that both of the aforementioned problems can be resolved by considering non-minimal coupling of the Higgs field to the scalar curvature of spacetime. This requires sufficiently large non-minimal coupling parameter, and produces similar results for the scalar spectral index and tensor-to-scalar ratio to the standard Higgs inflation, and the Starobinsky model. The Higgs field under consideration can in principle be identified with the Standard Model Higgs scalar, in which case an extremely large non-minimal coupling is required (in order to reproduce CMB-aligned predictions), which can also be theoretically problematic. A more likely scenario is a hidden sector Higgs-like field, such as the Peccei–Quinn field, where a smaller non-minimal coupling is acceptable. The proposed model offers an alternative to the simplest single-field models of inflation, especially of Higgs and Peccei-Quinn type, while fitting the CMB observations of primordial power spectra. An advantage of such models in the vast landscape of inflationary theories is simplicity: no ad hoc scalar fields are assumed to exist purely to explain inflation, since both Higgs and Peccei-Quinn fields are motivated by particle physics considerations.*

Keywords: cosmology, inflation, Higgs field, spontaneous symmetry breaking

1. Introduction

Cosmic inflation remains the leading paradigm for explaining the observed large-scale homogeneity and isotropy of the Universe and for generating the primordial perturbations that seed cosmic structure. In the slow-roll framework, a scalar field evolving on a sufficiently flat potential produces an approximately scale-invariant power spectrum with a slightly red tilt and a small tensor contribution. These generic expectations are in impressive agreement with the latest CMB constraints, which continue to favor simple, radiatively stable realizations of single-field inflation with suppressed tensor-to-scalar ratio [1].

A particularly attractive direction is to embed inflation into symmetry-based scalar sectors familiar from particle physics. The idea that the Higgs field (or a Higgs-like field such as the Peccei–Quinn field) can act as the inflaton has been explored extensively, most prominently in the Standard Model context with a non-minimal coupling to gravity [2] (see, e.g., [3, 4] for a review). Subsequent studies investigated the impact of

radiative corrections and running couplings on the inflationary regime, clarifying when Higgs-sector potentials can support successful slow-roll dynamics consistent with CMB observables [5, 6]. Some questions still remain, regarding possible violations of perturbative unitarity when the non-minimal coupling of the Higgs field to gravity is large, as required by the standard Higgs inflation scenarios [7–16].

Motivated by these developments, we study an alternative scenario of non-minimally coupled Higgs-like inflation, where inflation takes place around the symmetric point, in contrast to conventional Higgs inflation which happens at large field values and away from the symmetric point of the potential. We consider a simple Abelian symmetry breaking model, where the symmetry can be global or local, as it does not affect inflationary dynamics. Inflation starting sufficiently close to the symmetric configuration shares conceptual features with hilltop inflation scenarios, where slow-roll proceeds near a local maximum of the potential before the system relaxes toward the broken vacuum [17]. If the angular mode (the Goldstone mode of the broken symmetry) remains light during inflation, i.e. no explicit symmetry-breaking terms are generated, axion-like isocurvature perturbations can impose strong constraints on the allowed parameter space [18]. In this respect, gauging the $U(1)$ symmetry provides an appealing option: the axion is absorbed by the gauge field via the Higgs mechanism, which reduces potentially problematic isocurvature contributions.

Investigating inflationary dynamics near the symmetric point of a "Mexican hat" potential provides a crucial alternative to standard large-field scenarios, particularly in addressing the theoretical challenges associated with super-Planckian field excursions and the swampland conjectures [23,27]. By demonstrating that a non-minimal coupling can simultaneously suppress the tensor-to-scalar ratio to observationally viable limits and rescue the model from the swampland, this work establishes a robust framework for a minimal single-field inflation. Furthermore, by utilizing particle-physics-motivated fields like the Higgs or the Peccei–Quinn field, this approach reduces the need for ad hoc cosmological fields, offering a more constrained and well-motivated avenue for connecting early-universe inflation with high-energy particle physics.

The paper is organized as follows. Section 2 presents the minimally coupled Abelian Higgs-like model and discusses the inflationary regime near the symmetric point, where unacceptably large values of tensor-to-scalar ratio, as well as large, super-Planckian VEV of the symmetry breaking field Φ are found. To overcome these drawbacks, in Sec. 3 the same scenario is studied, but in the presence of non-minimal coupling of Φ to the scalar curvature, and find that the aforementioned issues can be resolved for sufficiently large non-minimal coupling. The results are discussed in Sec. 4 and conclusion is given in Sec. 5.

2. Minimal coupling

Consider the Lagrangian for a minimally coupled Abelian Higgs-like field Φ:

$$\sqrt{-g}^{-1}L = \frac{1}{2}R - \partial\Phi\partial\Phi^* - \frac{\lambda}{4}\left(f^2 - 2\Phi\Phi^*\right)^2, \tag{1}$$

where λ is the quartic coupling, and f is the VEV parameter of Φ, which is also the axion decay constant. The complex scalar Φ is parametrized as

$$\Phi = \frac{1}{\sqrt{2}}\phi e^{-i\sigma}, \tag{2}$$

where ϕ is the radial component, and σ is the axion, or the Goldstone boson of a $U(1)$ symmetry. The latter acts on Φ as $\Phi \to \Phi e^{-ic}$, where c is a constant for global $U(1)$, and a function $c(x)$ for local, or gauge $U(1)$ symmetry. The gauging procedure can be done without affecting inflationary dynamics, as in our model inflation is driven by the radial scalar ϕ.

Therefore, we focus on the ϕ -part of the Lagrangian:

$$\sqrt{-g}^{-1}L = \frac{1}{2}R - \frac{1}{2}\partial\phi\partial\phi - \frac{\lambda}{4}(f^2 - \phi^2)^2. \tag{3}$$

For the discussion of inflation it is useful to introduce the potential slow-roll parameters,

$$\epsilon_V \equiv \frac{V_{,\phi}^2}{2V^2}, \quad \eta_V \equiv \frac{V_{,\phi\phi}}{V}, \tag{4}$$

where V is the scalar potential, $V = \frac{1}{\lambda}(f^2 - \phi^2)^2$, and $V_{,\phi}$ denotes its derivative with respect to ϕ. The usual slow-roll inflation requires $\epsilon_V, |\eta_V| \ll 1$. By using these slow-roll parameters one can estimate the inflationary observables consisting of the amplitude of scalar perturbations A_s, their spectral tilt n_s, and the ratio of tensor to scalar perturbations r:

$$A_s \simeq \frac{V}{24\pi^2\epsilon_V}, \tag{5}$$

$$n_s \simeq 1 + 2\eta_V - 6\epsilon_V, \quad (6)$$

$$r \simeq 16\epsilon_V. \quad (7)$$

Their numerical values are calculated at the field value ϕ_* at which the corresponding perturbation exits the Hubble horizon, and compared to the observations of the Cosmic Microwave Background (CMB). The *Planck* and *BICEP-Keck* data suggest the following values [19, 20],

$$A_S = 2.1 \times 10^{-9}, n_s = 0.9668 \pm 0.0037, \ r < 0.036. \quad (8)$$

In addition, the length of inflation can be measured in the number of e-folds ΔN from the horizon exit and until the end of inflation where $\epsilon_V \simeq 1$. It is estimated as

$$\Delta N \simeq \int_{\phi_*}^{\phi_e} \frac{d\phi}{\sqrt{2\epsilon_V}}, \quad (9)$$

where ϕ_e is the value of the inflaton at the end of inflation, which can be found by solving $\epsilon_V(\phi_e) = 1$. For succesful inflation, around $\Delta N = 50 - 60$ is needed, starting from the horizon exit. Then Eq. (9) can be solved for ϕ_* and the observables (5), (6), and (7) at this field value can be estimated.

For the model (3) one obtains

$$\epsilon_V \simeq \frac{8\phi^2}{f^4}, \ \eta_V \simeq \frac{-4}{f^2,} \quad (10)$$

where assume $\phi \ll 1$ is assumed, since inflation is possible only around the hilltop of the potential in this model. Consequently, the length of inflation is calculated as

$$\Delta N \simeq -\frac{f^2}{4}\left(\frac{1}{2} + log\,\frac{\phi_*}{f}\right), \quad (11)$$

so that

$$\frac{\phi_*}{f} = e^{-\frac{1}{2} - 4f^{-2}\Delta N}. \quad (12)$$

By using Eqs. (6), (10), and (12) it can be estimated that $n_s \approx 0.967$ at $\Delta N = 55$ and $f \approx 21$. Next, r is estimated as

$$r \simeq \frac{128}{f^4}\phi^2. \quad (13)$$

At $\phi = \phi_*$ and for $f = 21$ one gets $r \approx 0.036 - 0.043$ for ΔN between 60 and 50, respectively. Our numerical results, however, show even larger values of r (for large f, the approximations (10) and (9) become less and less precise). For example, when $f = 21$ and $\Delta N = 60$, one gets $r \approx 0.057$ (smaller ΔN leads to larger r), which is completely excluded by observations.

In this work, the strategy for obtaining numerical inflationary solutions and the corresponding predictions is the following. First, the equations of motion (27), (28), (29) are solved numerically (for a given field-space metric *G,* which is equal to one in the minimally coupled case, and scalar potential *V;* and using *Mathematica's NDSolve* differential equation solver), in terms of the forward e-fold time *N*. After the solution for the Hubble function *H* is found, one can derive the Hubble-based slow-roll parameters (shown below Eq. (29)) and finally the predictions for n_s and r, calculated via Eq. (30) at the starting time N_* of observable inflation (when the CMB perturbations are generated). In turn, N_* can be found by subtracting ΔN (which ranges from 50 to 60) from the time of the end of inflation N_{end}. The latter is often defined by the condition where the Hubble slow-roll parameter, $\epsilon \equiv \frac{-\dot{H}}{H^2}$, reaches unity (this is set as a condition to stop the numerical integration of the equations of motion).

As for the quartic coupling λ, it can be fixed from (5) by using (8) and (12). One obtains $\lambda \sim 10^{-14}$ for $50 - 60$ e-folds, in line with the standard Higgs inflation [2].

In summary, this section is concluded by noting that the minimally coupled Higgs-like inflation is possible around the symmetric point $\phi = 0$, but (a) it leads to unacceptable values of tensor-to-scalar ratio r, and (b) the VEV parameter (which is also the axion decay constant) is super-Planckian at $f \sim O(10M_P)$, which can be theoretically problematic due to a difficulty of finding consistent UV completions of such a theory [21, 22] (also related to the swampland distance conjecture [23]).

In light of these results, we propose a non-minimally coupled extension of this Higgs-like model. It should be emphasized that in our scenario, inflation takes place at small field values, $\frac{\phi}{f} \ll 1$ (as considered in this section for the minimally-coupled model), as opposed to the usual Higgs inflation, where inflation happens at large field values $\frac{\phi}{f} \gg 1$, or away from the symmetric point.

3. Non-minimal coupling

With the inclusion of non-minimal coupling, the Lagrangian reads

$$\sqrt{-g}^{-1}L = \frac{1}{2}A(\Phi\Phi^*)R - \partial\Phi\partial\Phi^* - \frac{\lambda}{4}(f^2 - 2\Phi\Phi^*)^2 \quad (14)$$

where $A(\Phi\Phi^*)$ is some function of the $U(1)$-invariant product $\Phi\Phi^*$.

By rescaling the metric as

$$g_{mn} \to A^{-1}g g_{mn}, \quad (15)$$

one can bring the Jordan frame Lagrangian (14) to the Einstein frame,

$$\frac{L}{\sqrt{-g}} = \frac{1}{2}R - \frac{1}{A}\partial\Phi\partial\Phi^* - \frac{3}{4A^2}\partial A\partial A - \frac{\lambda}{4A^2}(f^2 - 2\Phi\Phi^*)^2, \quad (16)$$

which extends the kinetic term of Φ by adding the derivatives of $A(\Phi\Phi^*)$, and rescales the potential by A^{-2}.

The simplest choice for the non-minimal coupling function A is linear in $\Phi\Phi^*$:

$$A = \mu^2 + 2\xi\Phi\Phi^* = \mu^2 + \xi\phi^2, \quad (17)$$

where μ is a real parameter which can be eliminated by requiring that $A = M_P^2$ at the vacuum (so that the Einstein–Hilbert term is recovered), or in Planck units,

$$\langle A\rangle = \mu^2 + \xi f^2 = 1. \quad (18)$$

Then $\mu^2 = 1 - \xi f^2$, so that one can write

$$A = 1 - \xi(f^2 - \phi^2). \quad (19)$$

With this, the ϕ -sector of the Lagrangian becomes

$$\sqrt{-g}^{-1}L = \frac{1}{2}R - \frac{1}{2}G\partial\phi\partial\phi - \frac{\lambda\left(f^2-\phi^2\right)^2}{4[1-\xi(f^2-\phi^2)]^2}, \quad (20)$$

where the field-space metric of ϕ, denoted G, is given by

$$G = \frac{1-\xi f^2+(1+6\xi)\xi\phi^2}{[1-\xi(f^2-\phi^2)]^2}. \quad (21)$$

The canonically parametrized scalar φ can be found by solving

$$\frac{d\varphi}{d\phi} = \sqrt{G}, \quad (22)$$

and inverting the solution should give us $\phi(\varphi)$ in order to express the Lagrangian in terms of the canonical scalar. Analytical solutions to (22) and/or the analytical inverse $\phi(\varphi)$ does not always exist, so it can be more convenient to work directly with the non-canonical scalar ϕ.

To understand the impact of the non-minimal coupling on the scalar potential, one can analyze second derivative of the scalar potential of Eq. (20) at $\phi = 0$:

$$V_{,\phi\phi}(\phi = 0) = \frac{-\lambda f^2}{(1-\xi f^2)^3}. \quad (23)$$

This shows that large negative value of ξf^2 can flatten the potential (reduce $V_{,\phi\phi}$) while keeping the negative sign of $V_{,\phi\phi}$ around $\phi = 0$. At the same time the correct sign of the kinetic term of ϕ requires $\xi f^2 < 1$, as can be seen from (20) and (21).

Taking into account Eq. (22), the potential slow-roll parameters can be written in terms of the non-canonical scalar ϕ as

$$\epsilon_V = \frac{V_{,\varphi}^2}{2V^2} = \frac{V_{,\varphi}^2}{2GV^2} = \frac{8\phi^2}{(f^2-\phi^2)^2(A+6\xi^2\phi^2)}. \quad (24)$$

and

$$\eta_V = \frac{V_{,\varphi\varphi}}{V} = \frac{V_{,\varphi\varphi}}{GV} - \frac{G_{,\phi}V_{,\phi}}{2G^2V}, \quad (25)$$

where A is given by (19). For $|\xi|f^2 \gg 1$, ϵ_V is suppressed compared to its expression in the minimally coupled model (10). For η_V in Eq. (25) the situation is more interesting. At $\phi = 0$ (and when $6|\xi|\phi^2 \ll f^2$), it reduces to $\eta_V = \frac{-4}{f^2}$, which is the same value as in the minimally coupled model. Nonetheless, as ϕ moves away from the origin, η can be suppressed once $6\xi\phi^2$ becomes much larger than $|\xi|f^2$ (this can happen while $\frac{\phi}{f}$ is still small if one assumes $|\xi| \gg f^{-2} \gg 1$). These results imply that the non-minimal coupling can help to reduce the value of f, and the value of tensor-to-scalar ratio r (which is proportional to ϵ_V) if the non-minimal coupling is sufficiently large. Let us also estimate the number of e -folds between some small ϕ_1 (start of inflation) and $\phi_2 = f$ (end of inflation):

$$\Delta N \simeq \int_{\varphi_1}^{\varphi_2}\frac{d\varphi}{\sqrt{2\epsilon_V}} = \int_{\varphi_1}^{\varphi_2} d\phi\sqrt{\frac{G}{2\epsilon_V}} \simeq \frac{f^2}{4}\left(log\frac{f}{\phi_1} - \frac{1}{2}\right) + \frac{3}{4}[|\xi|f^2 - log(1+|\xi|f^2)], \quad (26)$$

where $\phi_1 \ll f$ and $\xi = -|\xi|$ are assumed. As can be seen, for large values of $|\xi|f^2$ the number of e-folds is roughly proportional to $|\xi|f^2$, so that f does not need to be large, unlike in the minimally coupled case. In fact, as will be shown, f can be much smaller than one (or much smaller than M_P when restoring Planck mass).

Since the analytical results discussed above can become inaccurate depending on the parameter values and the hierarchies between them, the equations of motion (Klein–Gordon and Friedmann) will be numerically solved and more precise results for the observables n_s and r will be derived. It is convenient to use the number of e-folds N (related to the Hubble function as $\dot{N} = H$) as a time variable when deriving inflationary solutions. The equations of motion for the Lagrangian (20) can be written as

$$\phi'' + (3 - \epsilon)\phi' + \frac{V_{,\phi}}{GH^2} = 0, \tag{27}$$

$$(3 - \epsilon)H^2 = V, \tag{28}$$

$$\epsilon = \frac{1}{2}G\phi'^2, \tag{29}$$

where $' \equiv \frac{d}{dN}$ and $\epsilon \equiv \frac{-\dot{H}}{H^2}$ is the Hubble slow-roll parameter, which can be related to the kinetic term of ϕ via the second Friedmann equation (29). Another useful slow-roll parameter is $\eta \equiv \frac{\dot{\epsilon}}{(H\epsilon)} = \frac{\epsilon'}{\epsilon}$, which shows the rate of change of ϵ. With the Hubble slow-roll parameters one can calculate the spectral index and tensor-to-scalar ratio as

$$n_s \simeq 1 - 2\epsilon - \eta, n_s \simeq 1 - 2\epsilon - \eta, \tag{30}$$

under the slow-roll approximation where $\epsilon \ll 1, |\eta| \ll 1$ (i.e., higher-order terms in ϵ and η are ignored).

After numerically solving the system (27), (28), and (29), the resulting values of n_s and r are plotted in Fig. 1. It can be seen that for $|\xi|f^2 = 90$, the predictions for $n_s$and r differ significantly depending on the value of f. As one increases the effective parameter $|\xi|f^2$, this difference quickly reduces, and for $|\xi|f^2 > 100$ the predictions are practically independent of f as long as f is around Planck mass or smaller (it can be much smaller in principle).

Let us comment on physical interpretation of the parameters and their variation. As mentioned above, the effective parameter $|\xi|f^2$ (assuming negative ξ) flattens the "Mexican hat" potential (in the Einstein frame) near the top, while f controls the VEV of the Higgs (-like) field, and therefore the distance between the top of the potential (symmetric point) and its minimum. As is well-known, flatter potentials (i.e., larger $|\xi|f^2$ in our case) allow the inflaton to travel smaller field-space distances while maintaining the required amount of inflation (50 to 60 e-folds). At the same time, they lead to a decrease in tensor-to-scalar ratio. Given that $|\xi|f^2 \gg 1$ is required in order to sufficiently decrease the value of r, one has $|\xi| \gg f^{-2}$. In addition, $f < 1$ can be required by theoretical motivations, i.e. a sub-Planckian VEV of the inflaton/Higgs field. This necessarily leads to $|\xi| \gg 1$.

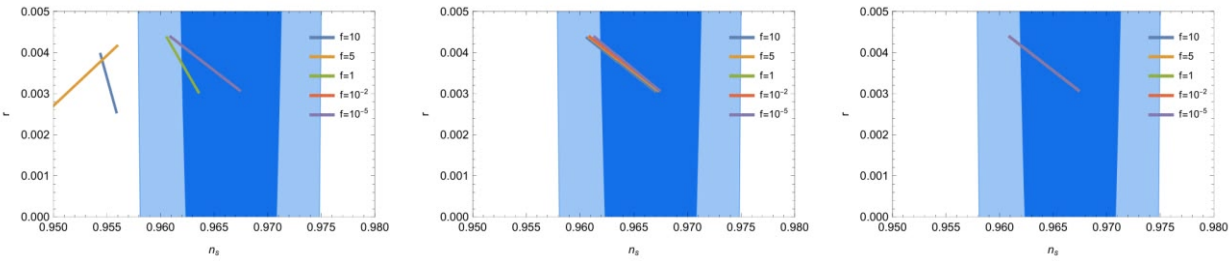

Fig.1. Predictions of Higgs inflation for the spectral index ns and tensor-to-scalar ratio r compared to the Planck constraints [1] (*GetDist* package [28] is use to generate the observational bounds on $n_s - r$ plane). The calculations are done for ΔN from 50 to 60. Values of the composite parameter $|\xi|f^2$ are −90 (left), −200 (middle) and −1000 (right).

4. Results and discussion

This work studies generalized Higgs inflation with non-minimal coupling to gravity, where inflation happens near the symmetric point of the potential. First, inflationary solution without the non-minimal coupling was derived, and it was shown that it leads to large values of tensor-to-scalar ratio that are ruled out by observations. Furthermore, observational constraints on n_s require super-Planckian axion decay

constant/VEV of ϕ, around $f \approx 21M_P$, which is problematic from theoretical point of view, even if the scalar ϕ is not identified with the Standard Model Higgs scalar.

These problems can be resolved by considering large negative non-minimal coupling at least of order $|\xi| \sim \frac{100}{f^2}$. This leads to the predictions for the inflationary observables very close to the Starobinsky model or conventional Higgs inflation, where n_s and r can be approximated as

$$n_s \simeq 1 - \frac{2}{\Delta N}, \quad r \simeq \frac{12}{\Delta N^2}. \tag{31}$$

At the same time the decay constant f can be arbitrarily small, but at the expense of large $|\xi|$ which scales as $|\xi| \propto \frac{1}{f^2}$ if one requires viable inflationary scenario. For the Standard Model Higgs field, $f \sim 100$GeV, or in Planck units, $f \sim 10^{-16}$, leading to an extremely large $|\xi| \sim 10^{34}$. This is problematic from theoretical point of view, in light of unitarity arguments. For example, in the case of the conventional Higgs inflation it has been shown that with the Standard Model Higgs field as the inflaton, the inflationary energy density reaches the perturbative unitarity violation scale unless $|\xi|$ is well below 10^4 [10] (at the same time CMB measurements require $|\xi| \sim 10^4$ or even larger, implying an inconsistency). However, a more careful analysis of tree-level scattering diagrams conducted in [29] (see also more recent works [15,16,30]) has shown that for a single-field case (such as our proposal), the unitarity violation scale is pushed all the way up to the (reduced) Planck mass M_P, so that such models are well-behaved as effective field theories during the inflationary phase, where the energy density is two or three orders of magnitude below the Planck scale.

On the other hand, for a more general Higgs-like field (not from the Standard Model), the VEV f can be close to the Planck scale, or around the possible Grand Unification scale of $10^{15} - 10^{16}$GeV, in which case ξ takes much more reasonable values compared to $|\xi| \sim 10^{34}$. One example of such a model is Peccei–Quinn theory where f can take the values up to the Planck mass in principle [24] (in this case, the axion σ, introduced in (2), can act as dark matter). When f is at the Planck mass (or in Planck units, $f \sim 1$), to satisfy the CMB data, the non-minimal coupling parameter should be of order $|\xi| \sim 100$, which is much below than in the conventional Higgs inflation with $|\xi| \sim 10^4$, making our model somewhat more natural.

5. Conclusion

This work establishes Higgs-type inflation around the symmetric point as a viable candidate for simple single-field inflationary model. By using the example of a complex Higgs-type field with the radial component ϕ, it is found that a non-minimal coupling $\xi\phi^2 R$ to scalar curvature can facilitate the alignment of the model with the CMB measurements as well as reduce super-Planckian field excursions, with the condition that ξ is negative and satisfies $|\xi| f^2 \gg 1$. The novelty of this approach is that it differs in principle from the standard Higgs inflation, which also utilizes the non-minimal coupling, but takes place at large field values, i.e. $\phi \gg f$. By contrast, in our model inflation happens at $\phi < f$, when ϕ is close to the symmetric point $\phi = 0$. Our model belongs to the class of hilltop inflation in a broad sense, where one usually expands the potential around the symmetric point, and discards the corrections which become important near the VEV of the inflaton. More specific hilltop models considered in the literature include specific realizations of string inflation, natural inflation (where the potential is periodic), and some supergravity models (an overview of such models can be found in [17] and Refs. therein). A crucial difference with all these hilltop models is that our approach relies on non-minimal coupling of the inflaton for the flattening of the potential, rather than ad hoc corrections to the potential itself.

In future works it can be interesting to extend our framework by including higher-derivative corrections, such as the Gauss–Bonnet term and Horndeski-type derivative corrections, which can be expected from the effective field theory point of view, without introducing Ostrogradski instability and new degrees of freedom. These corrections can change inflationary dynamics (see, e.g., [25, 26]) and potentially further relax the constraints on ξ and f. On the other hand, more recent activity in the area of inflationary model building is in large part related to the recent Atacama Cosmology Telescope (ACT) results [31] suggesting a mild deviation from the PLANCK constraint on n_s (towards slightly larger values). For instance, in [32] the authors revisit the general hilltop models (minimally-coupled) and further constrain the parameters of the models, while in [33-35] non-minimally coupled Higgs inflation (at large field values) is studied in this context. This also motivates further studies of our model in light of the ACT data, for example, by calculating the effects of the aforementioned Gauss-Bonnet term, along the lines of [36,37].

Conflict of interest statement
The authors declare that they have no conflict of interest in relation to this research, whether financial, personal, authorship or otherwise, that could affect the research and its results presented in this paper.

CRediT author statement
Berkimbayev D.: Investigation, Software, Writing - Original Draft. **Aldabergenov Y**.: Conceptualization, Methodology, Writing - Review & Editing.

Statement on the use of Artificial Intelligence.
The authors declare that no artificial intelligence tools were used to generate scientific content, results, or conclusions of this article.

Data Availability Statement
The data that support the findings of this article are openly available.

Funding
This research was funded by the Science Committee of the Ministry of Science and Higher Education of the Republic of Kazakhstan (Grant No. AP26103695).

References

1 Planck Collaboration (2020). Planck 2018 Results. X. Constraints on Inflation. *Astronomy and Astrophysics*, 641, A10, https://doi.org/10.1051/0004-6361/201833887

2 Bezrukov, F.L., Shaposhnikov, M. (2008). The Standard Model Higgs Boson as the Inflaton. *Physics Letters. B.* , 659, 703-706, https://doi.org/10.1016/j.physletb.2007.11.072

3 Rubio, J. (2019). Higgs inflation. *Front. Astron. Space Sci.*, 5, 50. https://doi.org/10.3389/fspas.2018.00050

4 Cheong, D.Y., Lee, S.M., Park, S.C. (2021). Progress in Higgs inflation. *J. Korean Phys. Soc.,* 78, 897-906, https://doi.org/10.1007/s40042-021-00086-2

5 Barvinsky, A.O., Kamenshchik, A.Y., Starobinsky, A.A. (2008). Inflation Scenario via the Standard Model Higgs Boson and LHC. *JCAP*, 11, 021, https://doi.org/10.1088/1475-7516/2008/11/021

6 De Simone, A., Hertzberg, M.P., Wilczek, F. (2009), Running Inflation in the Standard Model. *Physics Letters B.,* 678, 1–8, https://doi.org/10.1016/j.physletb.2009.05.054

7 Burgess, C.P., Lee, H.M., Trott, M. (2009). Power-counting and the Validity of the Classical Approximation During Inflation. *JHEP,* 09, 103, 1-23, https://doi.org/10.1088/1126-6708/2009/09/103

8 Barbon, J.L.F., Espinosa J.R. (2009). On the Naturalness of Higgs Inflation. *Phys. Rev. D*, 79, 1-9. https://doi.org/10.1103/PhysRevD.79.081302

9 Lerner, R.N., McDonald, J. (2010). Higgs Inflation and Naturalness. *J. Cosmol. Astropart. Phys.,* 04, 015. https://doi.org/10.1088/1475-7516/2010/04/015

10 Burgess, C.P., Lee, H.M., Trott, M. (2010). Comment on Higgs Inflation and Naturalness. *J. High Energy Phys.,* 2010, https://doi.org/10.1007/JHEP07(2010)007

11 Bezrukov, F., Magnin, A., Shaposhnikov, M., Sibiryakov, S. (2011). Higgs inflation: consistency and generalisations. *J. High Energy Phys., 01, 016.* https://doi.org/10.1007/JHEP01(2011)016

12 Giudice, G.F., Lee, H.M. (2011). Unitarizing Higgs Inflation. *Phys. Lett. B,* 694, 294–300. https://doi.org/10.1016/j.physletb.2010.10.141

13 Hamada, Y., Kawana, H., Oda, K.-y., Park, S.C. (2015). Higgs inflation from Standard Model criticality. *Phys. Rev. D,* 91, 053008. https://doi.org/10.1103/PhysRevD.91.053008

14 Escriva, A., Germani, C. (2017). Beyond dimensional analysis: Higgs and new Higgs inflations do not violate unitarity. *Phys. Rev. D*, 95, 123526. https://doi.org/10.1103/PhysRevD.95.123526

15 Ito, A., Khater, W., Rasanen, S. (2022). Tree-level unitarity in Higgs inflation in the metric and the Palatini formulation, *JHEP*, 06, 164. https://doi.org/10.1007/JHEP06%282022%29164

16 Karananas, G.K., Shaposhnikov, M., Zell, S. (2022). Field redefinitions, perturbative unitarity and Higgs inflation, *JHEP*, 06, 132. https://doi.org/10.1007/JHEP06%282022%29132

17 Boubekeur, L., Lyth, D.H. (2005). Hilltop Inflation, *JCAP,* 07, 010. https://doi.org/10.1088/1475-7516/2005/07/010

18 Beltran, M., Garcıa-Bellido, J., Lesgourgues, J. (2007). Isocurvature Bounds on Axions Revisited. *Phys. Rev. D*, 103507. https://doi.org/10.1103/PhysRevD.75.103507

19 Planck Collaboration, Akrami, Y. et al. (2020). Planck 2018 results. X. Constraints on inflation, *Astron. Astrophys,* 641, A10, https://doi.org/10.1051/0004-6361/201833887

20 BICEP, Keck Collaboration, Ade, P. A. R. et al. (2021). Improved Constraints on Primordial Gravitational Waves using Planck, WMAP, and BICEP/Keck Observations through the 2018 Observing Season. *Phys. Rev. Lett.*, 127, 1-22, https://doi.org/10.1103/PhysRevLett.127.151301

21 Banks, T., Dine, M., Fox, P.J., Gorbatov, E. (2003). On the possibility of large axion decay constants. *JCAP,* 1-17, https://doi.org/10.1088/1475-7516/2003/06/001

22 Bachlechner, T.C., Long, C., McAllister, L. (2015). Planckian Axions in String Theory. *JHEP,* 1-36, https://doi.org/10.1088/1475-7516/2003/06/001

23 Ooguri ,H., Vafa, C. (2007). On the Geometry of the String Landscape and the Swampland. *Nucl. Phys. B,* 766, 21–33. https://doi.org/10.1016/j.nuclphysb.2006.10.033

24 Kawasaki, M., Sonoda, E., Yanagida, T.T. (2018). Cosmologically allowed regions for the axion decay constant F_a. *Phys. Lett. B,* 782, 181–184. https://doi.org/10.1016/j.physletb.2018.05.014

25 Aldabergenov, Y., Berkimbaev, D. (2025). Gauss–Bonnet-Induced Symmetry Breaking/Restoration During Inflation. *Universe*, 1-9, https://doi.org/10.3390/universe11030098

26 Addazi, A., Aldabergenov, Y., Berkimbaev, D., Cai, Y. (2025). (Lovelock^2) inflation: explaining the ACT data and equivalence to Higgs–Gauss–Bonnet inflation. https://doi.org/10.48550/arXiv.2512.21167

27 Ooguri, H., Palti, E., Shiu, G., Vafa, C. (2019). Distance and de Sitter Conjectures on the Swampland. *Phys. Lett. B,* 788, 180–184. https://doi.org/10.1016/j.physletb.2018.11.018

28 Lewis, A. (2025). GetDist: a Python package for analysing Monte Carlo samples. *JCAP,* 08, https://doi.org/10.1088/1475-7516/2025/08/025

29 Hertzberg, M.P. (2010). On Inflation with Non-minimal Coupling. *JHEP,* 11, https://doi.org/10.1007/JHEP11(2010)023

30 Antoniadis, I., Guillen, A., Tamvakis, K. (2021). Ultraviolet behaviour of Higgs inflation models. *JHEP,* 08, https://doi.org/10.1007/JHEP11(2010)023

31 Atacama Cosmology Telescope Collaboration. (2025). The Atacama Cosmology Telescope: DR6 constraints on extended cosmological models. *JCAP,* 11, https://doi.org/10.1088/1475-7516/2025/11/063

32 Lynker, M., Schimmrigk, R. (2025). ACT Implications for Hilltop Inflation. https://doi.org/10.48550/arXiv.2507.15076

33 Hell, A., Lust, D. (2025). Aspects of non-minimally coupled curvature with power laws. *JHEP,* 12, https://doi.org/10.1007/JHEP12(2025)091

34 Pallis, C. (2026). Updating GUT-scale pole Higgs inflation after ACT DR6. *Phys.Rev.D,* 113, 015033, https://doi.org/10.1103/h1p2-c333

35 Pallis, C. (2026). Induced-Gravity Palatini-Like Higgs Inflation in Supergravity Confronts ACT DR6. *Astronomy,* 5, https://doi.org/10.3390/astronomy5020009

36 Zahoor, M., Khan, S., Bhat, I.A. (2025). Reconciling Fractional Power Potential and EGB Gravity in the light of ACT. https://doi.org/10.48550/arXiv.2507.18684

37 Zhu, Y., Gao, Q., Gong, Y., Yi, Z. (2025). Inflationary Models with Gauss-Bonnet Coupling in Light of ACT Observations. *Eur. Phys. J. C.*, 85, 1227, https://doi.org/10.1140/epjc/s10052-025-14969-2

AUTHORS' INFORMATION

Berkimbayev, Daulet - MSc, Doctoral Student, Al-Farabi Kazakh National University, Almaty, Kazakhstan; SCOPUS Author ID: 57849492200, ORCID iD: 0000-0003-1410-3150; daulet9432@gmail.com

Aldabergenov, Yermek - PhD, Lead Research Associate, Al-Farabi Kazakh National University, Almaty, Kazakhstan, and Department of Physics, Fudan University, Shanghai, China; SCOPUS Author ID: 56743280800, ORCID iD: 0000-0001-6021-9707; contact information: aldyermek@gmail.com

EURASIAN PHYSICAL TECHNICAL JOURNAL

2026, Volume 23, No. 2 (56)

https://doi.org/10.31489/2026N2/156-164

Received: 27/01/2026 Revised: 07/06/2026 Accepted: 26/06/2026 Published online: 30/06/2026

Original Research Article

UDC: 524.3

VARIABLE STARS IN ARCHIVAL SCHMIDT CAMERA OBSERVATIONS: CROSS-MATCHING AND ML CLASSIFICATION

Izmailova I.*, Shomshekova S., Umirbayeva A., Aktay L.

Fesenkov Astrophysical Institute, Almaty, Kazakhstan
*Corresponding author: izmailova@fai.kz

Abstract. *Digitized archival astronomical observations provide a valuable basis for the study of variable stars and their long-term behavior. This work presents an analysis of variable stars based on archival photometric data obtained with a Schmidt camera at the Fesenkov Astrophysical Institute during the period from 1960 to 1989. The detected objects were cross-matched with existing catalogs of variable stars and modern astrometric and photometric databases, allowing the compilation of an extended set of stellar parameters that had not previously been combined within a single dataset. To complement incomplete catalog information, machine learning methods were applied to classify stellar variability types and spectral classes using available astrometric and photometric features. Several classification models were tested, and the most stable and accurate approach was selected for further analysis. The resulting catalog integrates archival observations, catalog cross-identification results, and predicted stellar characteristics, providing an extended resource for studies of stellar variability and long-term photometric evolution.*

Keywords: archival astronomical data, variable stars, catalog cross-matching, machine learning, photometric observations.

1. Introduction

Digitized archival astronomical data provide a unique opportunity to study long-term variability and evolution of celestial objects. While modern surveys such as Pan-STARRS [1], Gaia [2], and ZTF [3] deliver high-precision measurements over limited time spans, archival observations extend time series to several decades, which is crucial for investigating slowly evolving phenomena [4,5]. Combining archival and modern data enables the detection of long-term luminosity changes and trends that are not evident from contemporary surveys alone, particularly for variable stars. Recent advances in image processing and automation have significantly improved object identification, catalog expansion, and classification accuracy [6]. The development of virtual observatory infrastructures has facilitated access to digitized photographic plates, their cross-matching with modern catalogs, and large-scale automated analysis [7]. Previous studies have demonstrated that scanned plates allow reliable photometry [8] and that historical catalogs can be converted into machine-readable formats suitable for modern workflows [9].

In this work, we analyze archival Schmidt camera observations[1] obtained at the Fesenkov Astrophysical Institute between 1960 and 1989 and published through the Kazakhstani National Virtual Observatory. The data are cross-matched with the General Catalogue of Variable Stars [10], Gaia Data Release 3, and TESS

[1] https://vo.fai.kz/obs_data.php?path=/schmidt_telescope_lc/q/web/form

[11], enabling the refinement of stellar parameters such as galactic height, variability amplitude, and spatial distribution. To complement incomplete catalog information, machine learning methods are applied to predict spectral and variability types. The resulting catalog integrates archival photometry with astrometric, photometric, and physical parameters from modern surveys and includes information on the availability of archival observations. The catalog is published through the virtual observatory framework and is accessible via standard protocols, including the Table Access Protocol [12] and the Simple Cone Search [13].

2. Materials and Methods

This study includes several stages, from processing archival photometric data to the application of machine learning models for stellar classification. The overall workflow of the analysis is shown in Figure 1.

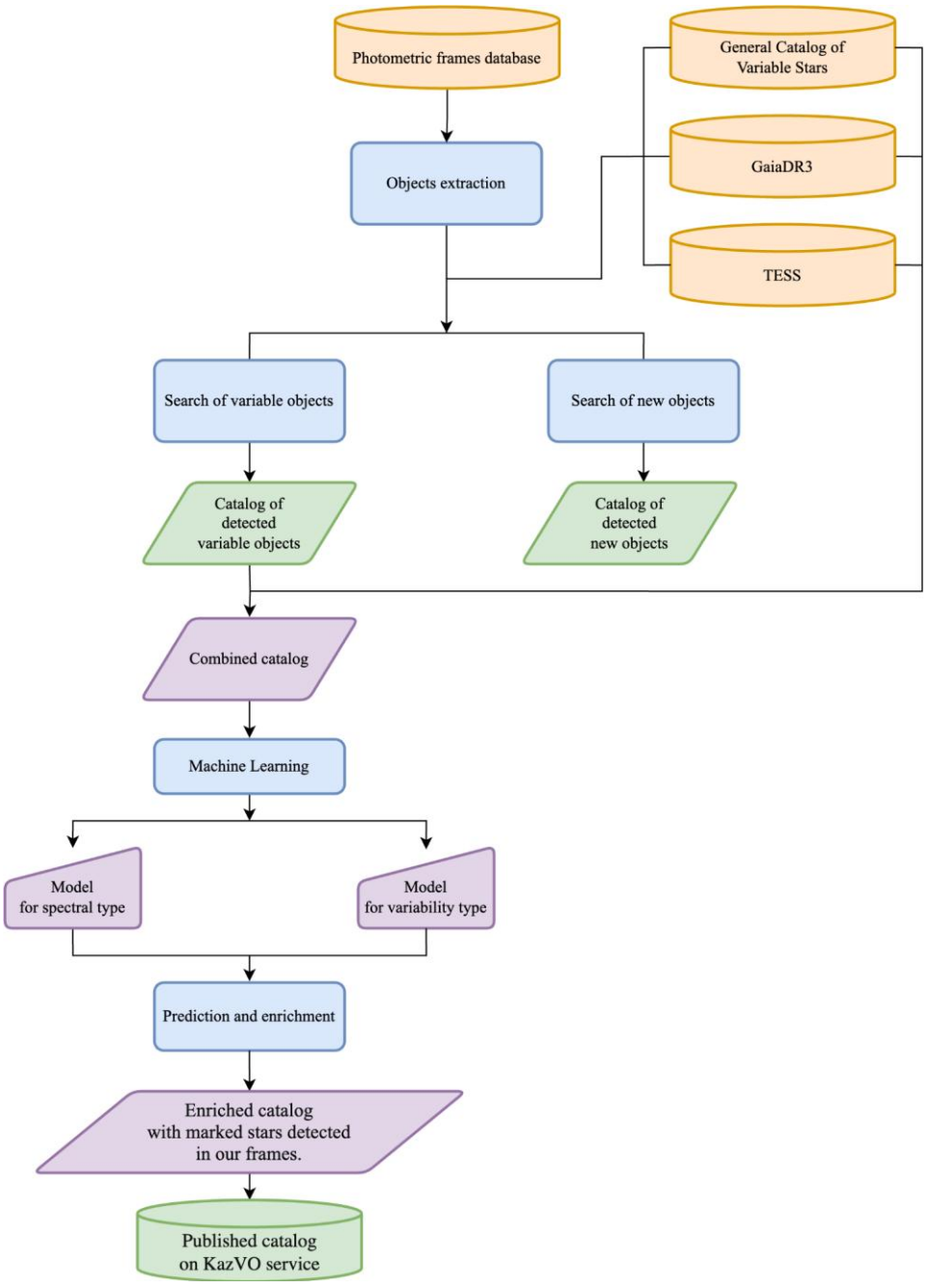

Fig.1. Workflow of the study from archival data digitization to machine learning model training.

2.1. Photometric Data and Coverage

The analysis is based on archival photometric data obtained with the Schmidt camera and published through the Kazakhstani National Virtual Observatory. The digitization and publication procedures have been described in detail in previous studies [14,15]. The spatial coverage of the archival observations is illustrated in Figure 2. The archive contains 1270 Schmidt camera frames covering approximately 74.6% of the sky. The digitized frames represent raw optical density scans and are not photometrically calibrated. Although a limited number of calibration plates are available, their coverage is insufficient to ensure uniform calibration across the dataset. Therefore, photometric measurements derived directly from the plates were not used in this study.

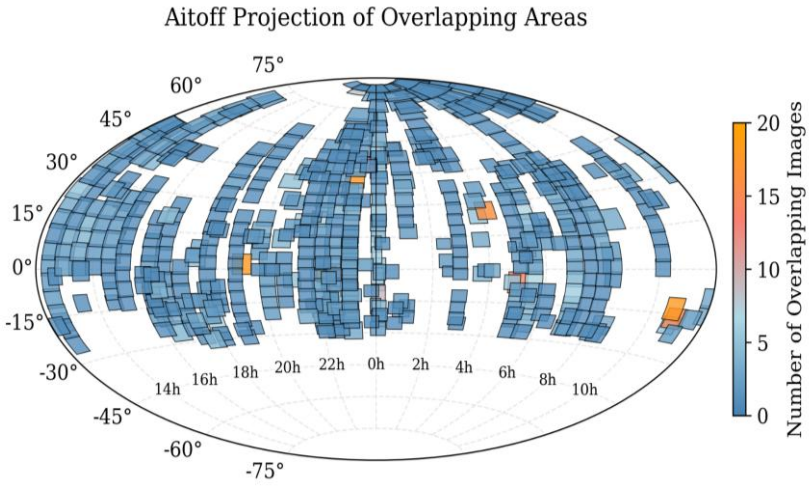

Fig.2. Coverage of photometric observations from the Schmidt camera. Rectangles show observed sky regions; color indicates the number of frames.

Despite this limitation, the extensive sky coverage of the archival material allows reliable coordinate-based cross-identification with modern catalogs and supports the integration of historical observations into contemporary datasets.

2.2. Source Extraction

Source extraction was performed automatically using a custom Python-based pipeline[2] built on the SEP library [16], which implements the Source Extractor algorithm [17]. Background subtraction parameters were optimized by minimizing residual noise and brightness variations, after which background-corrected images were saved in FITS format. Object detection was carried out in image segments to reduce memory usage. Detection thresholds were defined relative to the background, with a minimum object area of nine pixels. Overlapping sources were separated using multi-level segmentation.

For each detected object, coordinates, fluxes, magnitudes, and associated uncertainties were extracted and saved in tabular format. The extraction results were visually validated by overlaying detected sources on the original images. The pipeline supports batch processing, multithreading, and command-line execution, enabling fully automated source extraction for large archival datasets.

2.3. Variable Stars Search

After source extraction and coordinate determination, the detected objects were cross-matched with catalogs of variable stars. The initial step involved transforming the extracted coordinates into a unified reference system compatible with the General Catalogue of Variable Stars. To determine an appropriate matching radius, a test subset comprising the brightest detected objects was cross-matched with the Gaia catalog using a nearest-neighbor approach. The search radius was gradually increased until stable matches were obtained for all test objects, and the resulting coordinate discrepancies were analyzed. Outliers associated with optical distortions were excluded, and the final matching radius was set to 21.75 arcseconds,

[2] https://github.com/ill-i/variable_search (accessed 27 January 2026)

corresponding to a 5-sigma deviation from the mean positional offset distribution as illustrated in the left panel of Figure 3. This value provided a balance between positional tolerance and matching reliability.

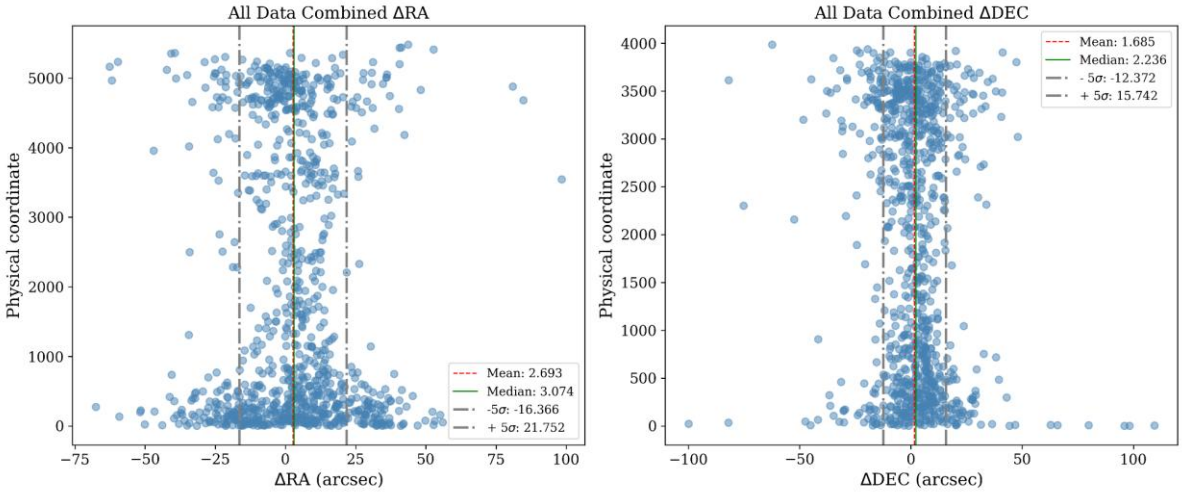

Fig.3. Distribution of coordinate discrepancies in RA (left) and Dec (right) between detected objects and Gaia data. Mean and median values, as well as 5-sigma boundaries, are marked with colored lines.

Using the derived search radius, the full dataset was cross-matched with the General Catalogue of Variable Stars. To improve computational efficiency, the dataset was processed in subsets. The resulting matches were compiled into a unified table containing positional and classification information from both archival detections and reference catalogs.

2.4. Search for New Objects

In addition to identifying known variable stars, a search for objects absent from the Gaia Data Release 3 catalog was performed to assess the consistency of the archival dataset and to identify potential new sources. For this purpose, archival object coordinates were transformed into Cartesian space and indexed using a nearest-neighbor search algorithm. An object was classified as new if no Gaia counterpart was found within the matching radius determined in the previous subsection. To reduce computational complexity, Gaia sources were pre-filtered using the spatial boundaries of individual archival frames. Candidate objects were recorded together with their positional information and frame identifiers. This approach does not account for brightness variability and is therefore not suitable for detecting short-term transient phenomena.

2.5. Machine Learning

To extend the characterization of the identified variable stars, supervised machine learning techniques were applied to classify stellar variability types and spectral classes using parameters derived from modern astronomical catalogs. Since variability and spectral labels are available for different subsets of objects, two independent classification tasks were defined: variability type prediction and spectral classification. This approach allowed the use of the largest possible labeled datasets for each task while preserving classification reliability.

2.5.1 Data Preparation

The input features were compiled from three primary sources: the General Catalogue of Variable Stars, Gaia Data Release 3, and TESS. These catalogs provide variability and spectral labels, astrometric parameters, photometric measurements, color indices, and selected astrophysical and physical stellar properties. Galactic coordinates and galactocentric distances were computed from sky positions and distance estimates. The combined dataset was cleaned by removing invalid entries and converting numerical parameters into a unified format. To reduce scale variance, the variability period was log-transformed. Parameters derived directly from digitized photographic plates were not used for classification due to the absence of reliable photometric calibration; however, the presence of archival observations was retained as metadata.Variability types were grouped into six major classes (eruptive, pulsating, eclipsing, cataclysmic, rotating, and X-ray). Objects with multiple variability types were simplified to a single-label multiclass formulation by retaining only the primary variability type, while ambiguous entries were excluded. Evaluation metrics, including accuracy, were

computed using exact-match criteria for the dominant class. Spectral types from different catalogs were consolidated into broad classes, and uncertain classifications were omitted from model training.

2.5.2 Machine Learning Models

Machine learning models were trained separately for variability type classification and spectral classification using astrometric, photometric, and astrophysical features. Several algorithms were evaluated, including gradient boosting methods, ensemble tree models, and neural networks. The dataset was divided into training and test subsets using an 80/20 split. Missing values were not imputed, as they represent an intrinsic characteristic of observational astronomical data and may introduce systematic biases if interpolated. Hyperparameter optimization was performed using Bayesian optimization minimizing the logarithmic loss function. Hyperparameter tuning and feature selection were conducted strictly on the training subset using k-fold cross-validation. The 20% test subset was isolated and used exclusively for the final metric evaluation presented in Figures 5–6. Feature importance analysis was applied to reduce model complexity while preserving physically meaningful input parameters. The final set of features used in both classification tasks is summarized in Table 1.

Table 1. Input features used for machine learning classification.

Feature group	Parameters	Source
Astrometric parameters	Galactic longitude (LII), Galactic latitude (BII), Parallax (log), Total proper motion, Galactocentric distance (log)	GCVS, Gaia DR3
Photometric and color indices	G-band magnitude, BP–RP, BP–G, G–RP, TESS-band magnitude, Extinction (log), Color excess E(BP–RP)	Gaia DR3, TESS
Variability parameters	Period (log), Cycle period flag	GCVS
Stellar physical properties	Effective temperature (log), Surface gravity (log g), Metallicity [Fe/H], Radius (log), Mass, Stellar density (log), Luminosity (log), Distance (log)	Gaia DR3, TESS

2.6. Predictions and Catalog Enrichment

The optimized models were applied to predict variability types and spectral classes for objects lacking complete classifications in the combined catalog. The trained models were saved for reuse and applied without retraining to ensure reproducibility. As a result, the catalog was enriched with predicted classifications and augmented with metadata indicating the availability of archival observations for each object. The final dataset integrates information from archival observations, modern catalogs, and machine learning predictions. The enriched catalog was published through the Kazakhstani National Virtual Observatory[3] using the DaCHS tool [18] and the TAP service, enabling further analysis and cross-identification.

3. Results and Discussion

This section presents the main results of the archival data analysis and discusses their implications for stellar classification and catalog enrichment.

3.1. Identification of Variable Stars and Archival Coverage

Analysis of the archival Schmidt camera observations resulted in the identification of 20,961 variable objects. Figure 4 illustrates the spatial overlap between the observational frames and variable stars listed in the General Catalogue of Variable Stars. Approximately 36.1% of catalogued variable stars fall within the coverage of the archival observations, demonstrating the significant potential of the digitized archive for extending temporal baselines and refining variability studies.

A search for objects without counterparts in the Gaia Data Release 3 catalog did not reveal reliable transient candidates. This result is primarily attributed to the limited astrometric accuracy of the archival frames, with a positional uncertainty of approximately 21.75 arcseconds, which is insufficient for confident

[3] https://vo.fai.kz/

detection of unmatched sources given the sub-arcsecond precision of Gaia. Consequently, coordinate-based cross-identification proved suitable for catalog consistency checks but ineffective for transient detection.

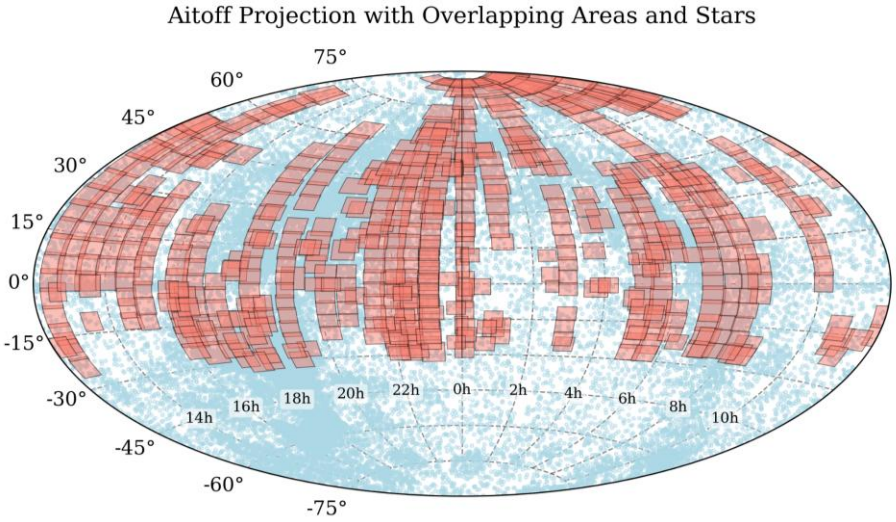

Fig.4. Distribution of variable stars from the GCVS catalog (blue dots) and observational frames obtained with the Schmidt camera (red rectangles).

3.2. Performance of Machine Learning Models

Machine learning methods were applied to classify stellar variability types and spectral classes using catalog-derived features. Among the evaluated machine learning models, XGBoost demonstrated the highest overall performance for both variability and spectral type classification tasks, particularly for rare classes. LightGBM showed comparable results for spectral classification, while Random Forest and neural network models exhibited reduced robustness and generalization capability. The comparative performance of the models for variability type classification is shown in Figure 5.

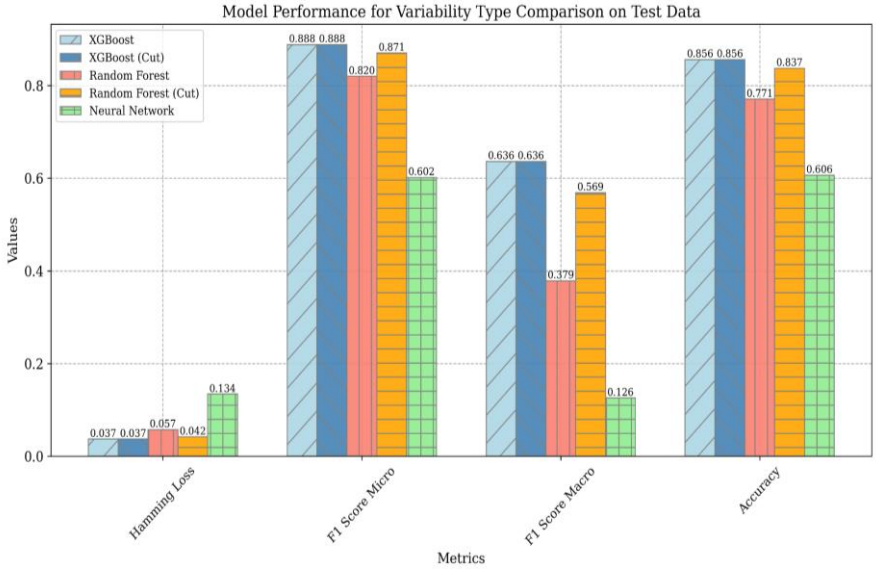

Fig.5. Comparison of machine learning model performance for variability type classification on test data.

As illustrated in Figure 5, feature selection based on individual importance scores led to a systematic decrease in classification performance, indicating the contribution of low-importance features through non-linear interactions. The results of spectral type classification are presented in Figure 6.

Experiments with feature selection indicated that removing parameters with low individual importance consistently degraded classification performance. This suggests that such features contribute through non-linear interactions, and therefore the complete feature set was retained in the final model configuration.

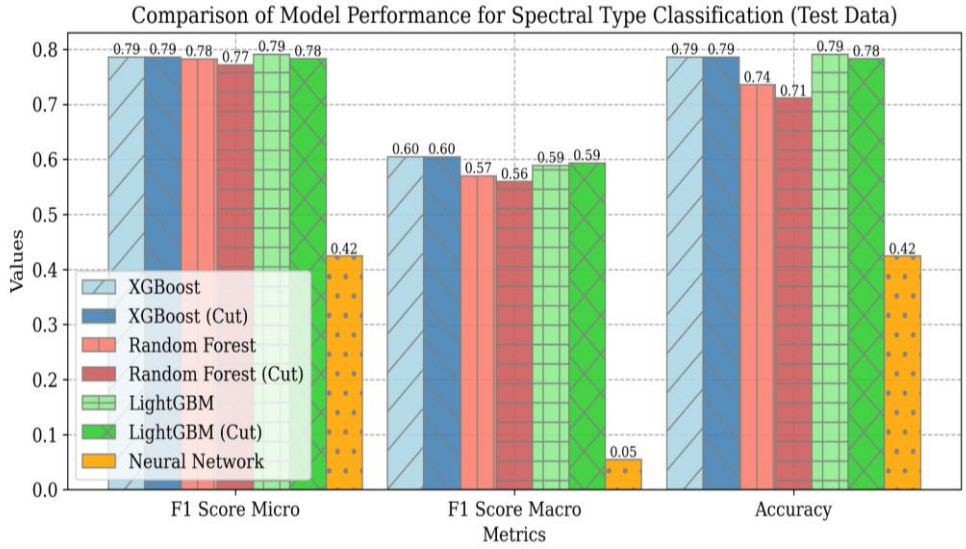

Fig.6. Comparison of machine learning model performance for spectral type classification on test data.

The main instances of model misclassification occur within regions of high interstellar extinction (the Galactic plane), which distorts the color indices, and among variable types with overlapping parameter profiles.

3.3. Catalog Enrichment and Validation

The optimized models were used to predict missing variability and spectral classifications in the combined catalog. As a result, spectral types were assigned to 40,980 stars with previously unknown classifications (99.95%), while variability types were predicted for 477 out of 538 unlabeled cases (88.66%).

Model reliability was assessed using standard performance metrics on held-out test data. The average accuracy of spectral type classification reached 78.9%, with a macro-averaged F1-score of 60%, indicating balanced performance across both common and rare classes. Variability type classification achieved an average accuracy of 86.5%, with micro- and macro-averaged F1-scores of 89.6% and 63.8%, respectively. Lower recall values for underrepresented classes, such as X-ray and rotating variables, reflect their intrinsic rarity in the training data. The spatial distribution of predicted classes follows expected galactic patterns, with late-type stars tracing the Galactic disk and rarer objects exhibiting broader distributions. This consistency supports the physical plausibility of the predictions and indicates the absence of systematic artifacts introduced by the models.

3.4. Publication and Applicability of the Catalog

The enriched catalog[4], integrating archival observations, modern survey data, and machine learning predictions, has been published through the Kazakhstani National Virtual Observatory in compliance with IVOA standards. It is accessible via standard data access protocols, enabling automated queries and integration into further studies of stellar variability and long-term photometric behavior. Future work may focus on incorporating brightness-based variability detection, multi-epoch observations, and probabilistic classification approaches to improve transient sensitivity and uncertainty estimation.

4. Conclusions

This work presents an integrated workflow for processing digitized archival photometric observations and combining them with modern astronomical catalogs, supplemented by machine learning–based

[4] https://vo.fai.kz/obs_data.php?path=/var_star_cat/q/scs/form

classification. Using archival Schmidt camera data obtained between 1960 and 1989, 20,961 variable stars were identified within the observational coverage, which spans approximately 75% of the sky. Cross-identification with contemporary catalogs enabled the extension of their astrometric, photometric, and astrophysical characterization beyond what is available from archival material alone.

The application of supervised machine learning methods allowed the enrichment of the catalog by predicting missing stellar parameters. Spectral types were assigned to 40,980 stars and variability types to 477 objects lacking prior classifications. The achieved classification performance is consistent with results reported in recent catalog-based studies, with average accuracies of 78.9% for spectral types and 86.5% for variability types. The spatial distribution of predicted rare classes, such as white dwarfs and chemically peculiar stars, follows expected Galactic trends, indicating that the models do not introduce artificial clustering or systematic biases. The analysis also demonstrates that coordinate-based cross-matching of archival data is effective for catalog consistency checks but insufficient for reliable transient detection, due to the limited astrometric accuracy and temporal sampling of photographic plate material. This finding is consistent with earlier studies and underscores the need for time-domain photometric information in transient searches.

The resulting catalog, integrating archival observations, modern survey data, and inferred classifications, has been published through the Kazakhstani National Virtual Observatory and made accessible via standard IVOA protocols. Its scientific novelty lies in the systematic integration of historical observations with contemporary catalogs and automated classification techniques. The catalog provides a practical resource for studies of long-term stellar variability, the statistical properties of rare stellar populations, and the planning of targeted follow-up observations. Future work may extend this approach by incorporating calibrated photometry, multi-epoch data, and probabilistic classification methods to further improve completeness and reliability.

Conflict of interest statement

The authors declare that they have no conflict of interest in relation to this research, whether financial, personal, authorship or otherwise, that could affect the research and its results presented in this paper.

CRediT author statement

Izmailova I.M.: Conceptualization, Methodology, Software, Visualization, Writing – Original Draft; **Umirbayeva A.Zh.:** Formal analysis, Validation, Writing – Review & Editing; **Shomshekova S.A.:** Supervision, Project administration, Funding acquisition**; Aktay L.:** Data curation, Investigation. The final manuscript was read and approved by all authors.

Statement on the use of Artificial Intelligence.

During the preparation of this manuscript, artificial intelligence tools were used solely for language editing and grammatical improvement. No AI tools were used to generate scientific content, analysis, results, or conclusions.

Data Availability Statement

The data that support the findings of this article are openly available via the Kazakhstan National Virtual Observatory (KazVO) platform and can be accessed using standard Table Access Protocol (TAP) services.

Funding

This work was supported by the Committee of Science of the Ministry of Science and Higher Education of the Republic of Kazakhstan under Grant No. AP22784884.

Acknowledgements

The authors express their sincere gratitude to Dr. A. Serebryanskiy and Dr. V. Kim (Fesenkov Astrophysical Institute) for their valuable discussions and insightful comments, which contributed to the development of this work.

The authors also acknowledge the Vatican Observatory Summer School (VOSS 2023), where one of the authors gained essential knowledge and practical skills in machine learning that were instrumental for this study.

References

1 Chambers, K.C., Magnier, E.A., Metcalfe, N., Flewelling, H.A., Huber, M.E., Waters, C.Z., Denneau, L., Draper, P.W., Farrow, D., Finkbeiner, D.P., et al. (2016). *The Pan-STARRS1 surveys*. arXiv:1612.05560. https://doi.org/10.48550/arXiv.1612.05560

2 Gaia Collaboration, Prusti T., de Bruijne, J.H.J., Brown, A.G.A., Vallenari, A., Babusiaux, C., Bailer-Jones, C.A.L., Bastian, U., Biermann, M., Evans, D.W., et al. (2016). The Gaia mission. *Astronomy and Astrophysics*, 595, A1. https://doi.org/10.1051/0004-6361/201629272

3 Masci, F.J., Laher, R.R., Rusholme, B., Shupe, D.L., Groom, S., Surace, J., Jackson, E., Monkewitz, S., Beck, R., Flynn, D., et al. (2019). The Zwicky Transient Facility: Data processing, products, and archive. *Publications of the Astronomical Society of the Pacific,* 131(995), 018003. https://doi.org/10.1088/1538-3873/aae8ac

4 Jia, P., Yang, Z., Shang, Z., Yu, Y., & Zhao, J. (2023). Data processing pipeline for multiple-exposure photo-plate digital archives. *Publications of the Astronomical Society of Japan,* 75, 811–824. https://doi.org/10.1093/pasj/psad038

5 Grindlay, J., Tang, S., Los, E., Servillat, M. (2012). Opening the 100-year window for time-domain astronomy. *Proceedings of the IAU Symposium 285: New Horizons in Time-Domain Astronomy*. Cambridge University Press, 29–34. https://doi.org/10.1017/S1743921312000166

6 Kolesnikova, D.M., Sat, L.A., Sokolovsky, K.V., Antipin, S.V., Belinskii, A.A., Samus', N.N. (2010). New variable stars on digitized Moscow collection plates: The field of 66 Ophiuchi. *Astronomy Reports*, 54, 1000–1018. https://doi.org/10.1134/S1063772910110065

7 Shlyapnikov, A.A., Gorbunov, M.A., Gorbachev, M.A. (2020). Archives of CrAO spectral observations. Catalogues of objects and images. *Astronomical Archives Transactions,* 1, 23.

8 Sokolovsky, K.V., Zubareva, A.M., Kolesnikova, D.M., Samus, N.N., Antipin, S.V., Belinski, A.A. (2017). Accurate photometry with digitized photographic plates of the Moscow collection. *Proceedings of the IAU Symposium 339: Southern Horizons in Time-Domain Astronomy*. https://doi.org/10.48550/arXiv.1712.04672

9 Gorbunov, M.A., Shlyapnikov, A.A. (2017). Identification of stars and digital version of E.S. Brodskaya and V.F. *Shajn catalogue of 1958. Astrophysics – Instrumentation and Methods for Astrophysics*, 7 [in Russian] https://doi.org/10.48550/arXiv.1709.08113

10 Samus', N.N., Kazarovets, E.V., Durlevich, O.V., Kireeva, N.N., Pastukhova, E.N. (2017). General catalogue of variable stars: Version GCVS 5.1. *Astronomy Reports,* 61, 80–88. https://doi.org/10.1134/S1063772917010085

11 Ricker, G.R., Winn, J.N., Vanderspek, R., Latham, D.W., Bakos, G.A., Bean, J.L., Berta-Thompson, Z.K., Brown, T.M., Buchhave, L., Butler, N.R., et al. (2015). Transiting Exoplanet Survey Satellite (TESS). *Journal of Astronomical Telescopes, Instruments, and Systems,* 1, 014003. https://doi.org/10.1117/1.JATIS.1.1.014003

12 Dowler, P., Rixon, G., Tody, D., Demleitner, M. (2019). Table Access Protocol, Version 1.1. *IVOA Recommendation, Data Access Layer Working Group*. http://www.ivoa.net/documents/TAP/20190927

13 Plante, R., Williams, R., Hanisch, R., Szalay, A. (2008). Simple Cone Search, Version 1.03. *IVOA Recommendation, Data Access Layer Working Group*. https://doi.org/10.5479/ADS/bib/2008ivoa.specQ0222P

14 Shomshekova, S.A., Izmailova, I.M., Moshkina, S.G., Umirbayeva, A.Zh. (2022). Digitization of cometary photometric astroplates of the Fesenkov Astrophysical Institute. *Proceedings of the National Academy of Sciences of the Republic of Kazakhstan*, 1(341), 137–143. https://doi.org/10.32014/2022.2518-1483.143 [in Russian]

15 Shomshekova, S., Izmailova, I., Umirbayeva, A., Omarov, C. (2022). A method for digitization of archival astroplates of the Fesenkov Astrophysical Institute. *New Astronomy,* 97, 101881. https://doi.org/10.1016/j.newast.2022.101881

16 Barbary, K. (2016). *SEP: Source Extractor as a library. Journal of Open-Source Software*, 1, 58. https://doi.org/10.21105/joss.00058

17 Bertin, E., Arnouts, S. (1996). SExtractor: Software for source extraction. *Astronomy and Astrophysics Supplement Series*, 117, 393–404. https://doi.org/10.1051/aas:1996164

18 Demleitner, M., Neves, M.C., Rothmaier, F., Wambsganss, J. (2014). Virtual observatory publishing with DaCHS. *Astronomy and Computing,* 7, 27–36. https://doi.org/10.1016/j.ascom.2014.08.003

AUTHORS' INFORMATION

Izmailova, Ildana - M.Sc., Junior Researcher, Fesenkov Astrophysical Institute, Almaty, Kazakhstan; ScopusID: 57776936800; ORCID iD: 0000-0001-9878-0989; izmailova@fai.kz

Umirbayeva, Adel - M.Sc., Junior Researcher, Fesenkov Astrophysical Institute, Almaty, Kazakhstan; ScopusID: 57776936900 ; ORCID iD: 0000-0001-9339-4990; umirbayeva@fai.kz

Shomshekova, Saule - Ph.D., Leading Researcher, Fesenkov Astrophysical Institute, Almaty, Kazakhstan; ScopusID: 57208861899; ORCID iD: 0000-0002-9841-453X; shomshekova@fai.kz

Aktay, Laura – Barchelor, Engineer, Fesenkov Astrophysical Institute, Almaty, Kazakhstan; ORCID iD: 0009-0005-5862-4777; aktay@fai.kz